Czech Technical University in Prague

Faculty of Nuclear Sciences and Physical Engineering

Department of Physical Electronics

Wavefront Correction for Mid-IR Laser

Doctoral Thesis

Author: **MSc. Huang Zhou**

Supervisor: **Ing. Martin Smrž, Ph.D.**

Supervisor specialist: **Ing. Jan Pilař, Ph.D.**
Ing. Miroslav Čech, Ph.D.

Bibliographic entry

Author	Ing. Huang Zhou
	Czech Technical University in Prague
	Faculty of Nuclear Sciences and Physical Engineering
	Department of Physical Electronics
Title of Dissertation	Wavefront Correction for Mid-IR Laser
Degree Programme	Application of Natural Sciences
Field of Study	Physical Engineering
Supervisor	Ing. Martin Smrž, Ph.D.
Supervisor Specialist	Ing. Jan Pilař, Ph.D.
	Ing. Miroslav Čech, Ph.D.
Academic Year	2022/2023
Number of Pages	167
Keywords	Wavefront sensing, Wavefront correction, Closed-loop control, Thin-disk lasers, Chirped pulse amplification, Regenerative amplifier

Bibliografický záznam

Autor	Ing. Huang Zhou
	České vysoké učení technické v Praze
	Fakulta jaderná a fyzikálně inženýrská
	Katedra fyzikální elektroniky
Název disertační práce	Korekce čela vlny pro střední infračervený laser
Studijní program	Aplikace přírodních věd
Studijní obor	Fyzikální inženýrství
Školitel	Ing. Martin Smrž, Ph.D.
Školitel-specialista	Ing. Jan Pilař, Ph.D.
	Ing. Miroslav Čech, Ph.D.
Akademický rok	2022/2023
Počet stran	167
Klíčová slova	Snímání čela vlny, korekce čela vlny, řízení s uzavřenou smyčkou, lasery s tenkým diskem, zesílení pulsu, regenerační zesilovač

To my wife Dr. Liyuan Chen and my daughter Shujie Zhou

Declaration

I hereby declare that I have elaborated the doctoral thesis Wavefront Correction for Mid-IR Laser under the supervision of Ing. Martin Smrž, Ph.D., Ing. Jan Pilař, Ph.D. and Ing. Miroslav Čech, Ph.D., and that all sources of information used have been cited. This dissertation is my own work, and all areas where the outcome resulted from collaboration with my colleagues are specified in the text and the Acknowledgements.

In Prague _____

Huang Zhou

Acknowledgements

Finally, I would like to thank everyone who has been helping and supporting me sincerely during the work of this thesis.

First, I would like to thank my supervisor, Ing. Martin Smrž, Ph.D., for his invaluable guidance and advice throughout my study as a Ph.D. student. His absolute support and fruitful discussion provided excellent research conditions - technically and humanly. All my research, as well as this thesis, would not be possible without his continuous support and guidance. I want to thank my supervisor specialist, Dr. Jan Pilař, for sharing invaluable knowledge about Adaptive Optics with me and providing me with much scientific support for his advice and many intuitive and constructive discussions. I also would like to thank my supervisor specialist, Ing. Miroslav Čech, Ph.D., for his supervision and complaisant support during my study at Czech Technical University in Prague. All my research, as well as this dissertation, would not be possible without their continuous support.

I want to thank Dr. Yasuhiro Kamba for sharing his knowledge and experience with ultra-fast regenerative and fiber amplifiers with me. I appreciate his encouragement, guidance, discussion, and pleasant teamwork in the first two years I started my new life and studying in Prague. I want to thank Dr. Michal Chyla for his continuous support during my work on the BIATRI laser project. He was like a “magic bag” where I could get almost anything I needed, from a screwdriver to a thin-disk module. I also want to thank Dr. Jiří Mužík for his discussion and help during building my first thin-disk laser; to Dr. Ondřej Novák for his rigorous research attitude and beneficial discussion of my research about nonlinear effects in CVBG and my manuscript, and for providing information for the mid-IR optical parametric amplification; to Dr. Kohei Hasimoto for his design of my grating mounts for my compressor. I especially wish to thank Prof. Akira Endo for his guidance and supervision on my first research topic on the numerical simulation of ASE in thin-disk lasers. His passing was a great loss to all who knew and loved him.

I appreciate Dr. Tomáš Mocek for providing my wife and me the opportunity to be members of the HiLASE center and work in such great laboratories with many great colleagues. I thank HR manager Olga Lakomá of HiLASE Center for her great help with many of my personal affairs.

I want to thank my wife, Dr. Liyuan Chen, for her love and selfless support during my work

at HiLASE Center, personally and technically. I appreciate her selfless sharing of her experience and resources with me while building my first regenerative amplifier. I want to thank her for caring for our lovely daughter, Shujie Zhou, while I was busy with my project. I appreciate her great encouragement and help when I encounter difficulties.

Last but not least, I thank my parents for their support throughout my studying, working, and living in Prague, for their worldly wisdom in many aspects, and for their benevolence in accompanying me in the first few months after the birth of my daughter, for their endless love.

In Prague

Abstract

This doctoral thesis pursued the developments of the mid-IR Adaptive Optics (AO) system and high-energy ultrafast thin disk laser system for the BIATRI project at HiLASE Center. Laser sources operating in the short-wavelength mid-IR (2 μm to 5 μm) spectral region have numerous applications, such as the generation of attosecond pulses, high-harmonics towards the X-ray range, and medical treatment. High-energy thin disk lasers have recently been widely used as the pumping sources of Optical Parametric Generation (OPG) or Optical Parametric Amplifier (OPA) systems working in the mid-IR spectral range. For decades, wavefront sensing and shaping technologies have been widely used to analyze and diagnose high-power ultrafast laser systems in visible and near-IR spectral regions. In the last decade, the interest in wavefront correction moved towards the mid-IR region as more mid-IR laser sources reached the market and more mid-IR applications appeared. The two topics of this work are: developing an AO system for the short-wavelength mid-IR (2 μm to 5 μm) spectral region and developing a high-energy thin disk regenerative amplifier for OPA pumping.

Chapter 1 briefly introduces mid-IR laser sources within the spectral range of 2 μm to 5 μm and their applications. The need for wavefront correction for this spectral range is discussed at the end of this chapter. The state of the art of wavefront measurement and correction for mid-IR laser sources is investigated and discussed. In the last section, the motivation and goals of this work are introduced.

The theory of Adaptive Optics is introduced and discussed in Chapter 2 according to the primary goal of this work. The Shack Hartmann wavefront sensor (SHWFS) principle and the wavefront reconstruction techniques are introduced, including centroiding techniques and Zernike polynomials widely used to represent the wavefront over a unit circle. Wavefront control techniques, including open-loop control and closed-loop control, are introduced in the last section of this chapter.

In Chapter 3, chirped pulse amplification and thin disk laser technology will be introduced. The principle of regenerative amplification is introduced in the case of thin disk lasers. Rate equations for thin disk regenerative amplification have been introduced, followed by the analytical expression of Amplified Spontaneous Emission (ASE) in a thin disk gain medium. Various kinds of pulse stretching and compressing techniques are introduced at the end of this chapter.

Chapter 4 and Chapter 5 cover the development and experiments of the homemade mid-IR

AO system. Chapter 4 gives the design aspects of the mid-IR Shack-Hartmann wavefront sensor, the algorithm for real-time wavefront measurement, and the development of a typical closed-loop control system. In Chapter 5, the homemade wavefront sensor was calibrated with an absolute calibration method. The wavefront measurement algorithm was verified and calibrated with a commercial wavefront sensor for the wavelength of 1 μm. The thermal properties of the TACHYON 16k camera were studied and improved to get a better signal-to-noise ratio. Laser-induced thermal afterimage of the camera and its impacts on the centroiding and wavefront reconstruction had also been studied. A solution for reducing thermal afterimage has been proposed to minimize the impact. The deformable mirror was then characterized in the closed-loop control system by measuring its influence functions and reproducing the Zernike modes on the mirror. Wavefront correction experiments were carried out. The results were shown and discussed, followed by the conclusion in the last section of this chapter.

In Chapter 6, a thin disk picosecond laser was developed with an all-polarization-maintained fiber front-end as the seeder. Due to the changes in the goal of the BIATRI project, the required pulse energy was changed from 1 mJ to 5 mJ, then to 10 mJ, regardless of the repetition rate. A numerical model was built to simulate the effect on laser performance caused by the Amplified Spontaneous Emission (ASE). It could be used for evaluating the laser performance while designing. Two designs were developed with different seed sources and compressors. In the first design, an all-PM-fiber front-end with the Menlo YLMO oscillator and three fiber pre-amplifiers were built to amplify the seed pulse train. A Chirped Volume Bragg Grating (CVBG) was used to compress the pulse duration. However, strong nonlinearity in the CVBG while compressing pulses with high pulse energy caused pulse duration fluctuations.

Further experiments were carried out to investigate the origin of the temporal fluctuations of pulse duration. It was found that the CVBG can magnify the fluctuations in peak intensity at high Kerr-nonlinearity. In the second design, a new all-PM-fiber front-end was built with home-built All-Normal Dispersion (ANDi) fiber oscillator and one fiber pre-amplifier. A grating pair compressor was designed and built to replace the CVBG compressor to reduce the accumulated nonlinear phase shift experienced by the laser pulses.

The thin disk laser developed in this work provides laser pulses with high performance to be used as the pump of the Optical Parametric Amplifier (OPA) system under development at the HiLASE center. The AO system developed in this work can be easily extended to the mid-IR spectral range (1 ~ 5 μm) thanks to the spectral range of the camera.

Abstrakt

Tato disertační práce sledovala vývoj systému mid-IR Adaptive Optics (AO) a vysokoenergetického ultrarychlého tenkého diskového laserového systému pro projekt BIATRI v HiLASE Center. Laserové zdroje pracující v krátkovlnné střední IR (2 μm až 5 μm) spektrální oblasti mají četné aplikace, jako je generování attosekundových pulzů, vysoké harmonické směrem k rentgenovému rozsahu a lékařské ošetření. Vysokoenergetické tenké diskové lasery byly v poslední době široce používány jako čerpací zdroje systémů optické parametrické generace (OPG) nebo optických parametrických zesilovačů (OPA) pracujících ve středním IR spektrálním rozsahu. Po desetiletí byly technologie snímání a tvarování vlnoplochy široce používány k analýze a diagnostice vysoce výkonných ultrarychlých laserových systémů ve viditelných a blízkých IR spektrálních oblastech. V posledním desetiletí se zájem o korekci vlnoplochy přesunul směrem k oblasti středního IR, protože na trh se dostává více středních IR laserových zdrojů a objevuje se více aplikací středního IR. Dvě témata této práce jsou: vývoj AO systému pro krátkovlnnou střední IR (2 μm až 5 μm) spektrální oblast a vývoj vysokoenergetického regeneračního zesilovače na tenkém disku pro čerpání OPA.

Kapitola 1 stručně představuje střední IR laserové zdroje ve spektrálním rozsahu 2 μm až 5 μm a jejich aplikace. Potřeba korekce vlnoplochy pro tento spektrální rozsah je diskutována na konci této kapitoly. Je zkoumán a diskutován současný stav měření a korekce vlnoplochy pro střední IR laserové zdroje. V poslední části je představena motivace a cíle této práce.

Teorie adaptivní optiky je představena a diskutována v kapitole 2 podle primárního cíle této práce. Je představen princip Shack Hartmann wavefront senzor (SHWFS) a techniky rekonstrukce vlnoplochy, včetně technik centroidingu a Zernikeových polynomů široce používaných k reprezentaci vlnoplochy přes jednotkový kruh. Techniky řízení vlny, včetně řízení s otevřenou smyčkou a řízení s uzavřenou smyčkou, jsou představeny v poslední části této kapitoly.

V kapitole 3 bude představena technologie cvrlikání pulzů a technologie tenkých disků. Princip regenerativního zesílení je zaveden v případě tenkých kotoučových laserů. Byly zavedeny rychlostní rovnice pro regenerativní zesílení tenkého disku, následované analytickým vyjádřením Amplified Spontaneous Emission (ASE) v médiu pro zisk tenkého disku. Na konci této kapitoly jsou představeny různé druhy technik protahování a stlačování pulzu.

Kapitola 4 a Kapitola 5 pokrývají vývoj a experimenty podomácku vyrobeného středního IR AO systému. Kapitola 4 uvádí konstrukční aspekty mid-IR Shack-Hartmann vlnoplochového

senzoru, algoritmus pro měření vlnoplochy v reálném čase a vývoj typického řídicího systému s uzavřenou smyčkou. V kapitole 5 byl podomácku vyrobený vlnoplochý senzor zkalibrován metodou absolutní kalibrace. Algoritmus měření čela vlny byl ověřen a zkalibrován komerčním snímačem čela vlny pro vlnovou délku 1 μm. Tepelné vlastnosti kamery TACHYON 16k byly studovány a vylepšeny, aby bylo dosaženo lepšího poměru signálu k šumu. Byl také studován laserem indukovaný tepelný dosvit kamery a jeho dopady na těžiště a rekonstrukci vlnoplochy. Pro minimalizaci dopadu bylo navrženo řešení pro snížení tepelného dosvitu. Deformovatelné zrcadlo bylo poté charakterizováno v řídicím systému s uzavřenou smyčkou měřením jeho vlivových funkcí a reprodukcí Zernikeových režimů na zrcadle. Byly provedeny experimenty s korekcí vlnoplochy. Výsledky byly ukázány a diskutovány, poté následoval závěr v poslední části této kapitoly.

V kapitole 6 byl vyvinut tenký diskový pikosekundový laser s celopolarizací udržovanou přední částí vlákna jako secím strojem. Vzhledem ke změnám cíle projektu BIATRI došlo ke změně potřebné energie pulzu z 1 mJ na 5 mJ, následně na 10 mJ bez ohledu na opakovací frekvenci. Byl sestaven numerický model pro simulaci účinku na výkon laseru způsobeného zesílenou spontánní emisí (ASE). Mohlo by být použito pro hodnocení výkonu laseru při navrhování. Byly vyvinuty dvě konstrukce s různými secími stroji a kompresory. V prvním návrhu byl pro zesílení sledu pulsů semene zkonstruován celovláknový front-end s Menlo YLMO oscilátorem a třívláknovým předzesilovačem. Ke zkrácení doby trvání pulsu byla použita mřížka CVBG (Chirped Volume Bragg Grating). Silná nelinearita v CVBG při kompresi pulzů s vysokou energií pulzu však způsobila kolísání trvání pulzu.

Další experimenty byly provedeny ke zkoumání původu časových fluktuací trvání pulzu. Bylo zjištěno, že CVBG může zesílit kolísání maximální intenzity při vysoké Kerrově nelinearitě. Ve druhém návrhu byl postaven nový front-end s plným PM vláknem s podomácku vyrobeným vláknovým oscilátorem All-Normal Dispersion (ANDi) a jedním vláknovým předzesilovačem. Kompresor s mřížkovým párem byl navržen a zkonstruován jako náhrada za kompresor CVBG, aby se snížil nahromaděný nelineární fázový posun, ke kterému dochází při laserových pulzech.

Tenký diskový laser vyvinutý v této práci poskytuje laserové pulsy s vysokým výkonem pro použití jako pumpa systému optického parametrického zesilovače (OPA) vyvíjeného v centru HiLASE. AO systém vyvinutý v této práci lze snadno rozšířit na střední IR spektrální rozsah (1 ~ 5 μm) díky spektrálnímu rozsahu kamery.

Table of Contents

Declaration v
Acknowledgements vii
Abstract ix
Abstrakt xi
List of abbreviations xvi
List of symbols xx
Chapter 1 Introduction ..... - 1 -
1.1 Mid-IR laser sources and applications ..... - 1 -
1.2 Adaptive Optics ..... - 2 -
1.2.1 State of the art of AO in the mid-IR spectral region ..... - 2 -
1.3 Motivation and objectives of this thesis ..... - 3 -
Chapter 2 Adaptive Optics ..... - 4 -
2.1 Wavefront sensing and controlling technologies ..... - 4 -
2.1.1 Wavefront sensing: shearing interferometry ..... - 4 -
2.1.2 Wavefront sensing: Shack Hartmann Wavefront Sensor ..... - 6 -
2.1.3 Wavefront sensing: Pyramid Wavefront Sensor ..... - 6 -
2.1.4 Wavefront sensing: in the mid-IR spectral region ..... - 7 -
2.1.5 Wavefront correctors: Bimorph deformable mirror ..... - 8 -
2.1.6 Wavefront correctors: membrane deformable mirror ..... - 9 -
2.1.7 Wavefront corrector: Micro-electro-mechanical system ..... - 9 -
2.2 Shack Hartmann Wavefront Sensing ..... - 10 -
2.3 Modal wavefront reconstruction ..... - 12 -
2.4 Zonal wavefront reconstruction ..... - 13 -
2.5 Zernike polynomials ..... - 14 -
2.6 Centroiding techniques ..... - 17 -
2.6.1 Thresholding Centroid of Gravity ..... - 17 -
2.6.2 Weighted Centre of Gravity ..... - 18 -
2.6.3 Iteratively Weighted Centroiding ..... - 18 -
2.7 Wavefront control technologies ..... - 19 -
2.7.1 Influence functions measurement ..... - 19 -
2.7.2 Zonal and modal control ..... - 22 -

2.7.3 Closed-loop and open-loop control ..... - 23 -
Chapter 3 Thin Disk Laser ..... - 25 -
3.1 Chirped pulse amplification ..... - 25 -
3.2 Thin disk laser concept ..... - 26 -
3.3 Thin disk regenerative amplification ..... - 27 -
3.3.1 The rate equation for pulse amplification ..... - 29 -
3.3.2 Amplified Spontaneous Emission ..... - 30 -
3.4 Pulse stretchers and compressors ..... - 32 -
3.5 Mid-IR Optical Parametric Amplification ..... - 36 -
Chapter 4 Design of Adaptive Optics System ..... - 39 -
4.1 Design of the Shack-Hartmann wavefront sensor ..... - 39 -
4.1.1 TACHYON 16K camera ..... - 39 -
4.1.2 Lenslet array ..... - 41 -
4.2 Algorithm for real-time wavefront measurement ..... - 42 -
4.3 Design of the Adaptive Optics system ..... - 44 -
4.3.1 Deformable mirror ..... - 44 -
4.3.2 Algorithm for measuring the DM Influence Functions ..... - 45 -
4.3.3 Algorithm for the closed-loop control ..... - 48 -
4.4 User Interface of the MATLAB App ..... - 49 -
Chapter 5 Wavefront Correction ..... - 51 -
5.1 Calibration of wavefront sensor ..... - 51 -
5.1.1 Calibration setup ..... - 51 -
5.1.2 Verifying the wavefront reconstruction algorithm ..... - 52 -
5.1.3 Calibration of the mid-IR wavefront sensor ..... - 56 -
5.2 Improving the Signal-to-Noise Ratio ..... - 61 -
5.2.1 Background noise ..... - 61 -
5.2.2 Laser-induced thermal afterimage ..... - 64 -
5.2.3 Impacts on centroiding and wavefront reconstruction ..... - 65 -
5.2.4 Solution for reducing the impacts ..... - 67 -
5.3 Characterization of the Deformable Mirror ..... - 68 -
5.3.1 Experimental setup ..... - 68 -
5.3.2 Measurement of the Influence Functions ..... - 69 -
5.3.3 Reproduction of the Zernike modes ..... - 71 -
5.4 Wavefront correction for mid-IR laser ..... - 73 -
5.4.1 The impacts of the thermally induced error ..... - 73 -
5.4.2 The effects of correcting different modes of aberrations ..... - 78 -
Chapter 6 Thin Disk Chirped Pulse Amplification ..... - 82 -
6.1 Numerical modeling of thin disk regenerative amplifier ..... - 82 -

6.1.1 Simulation results and discussion ..... - 83 -
6.1.2 Conclusion ..... - 85 -
6.2 The architecture of the BIATRI laser system ..... - 85 -
6.3 The first design of the BIATRI laser ..... - 88 -
6.3.1 The first design of all-PM-fiber front-end ..... - 88 -
6.3.2 Thin disk module and pump source ..... - 90 -
6.3.3 Cavity design of the regenerative amplifier ..... - 92 -
6.3.4 Performance of the regenerative amplifier ..... - 95 -
6.3.5 Fluctuation-magnification effect in CVBG compressor ..... - 104 -
6.4 Upgraded version of BIATRI laser ..... - 112 -
6.4.1 Upgraded design of grating pair compressor ..... - 112 -
6.4.2 Upgraded design of the all-PM-fiber front end ..... - 113 -
6.4.3 Laser performance after upgrading ..... - 115 -
Chapter 7 Application of Mid-IR AO: An Outlook ..... - 118 -
Chapter 8 Conclusion ..... - 121 -
8.1 Summary of the results ..... - 121 -
8.2 Contribution to the progress of Adaptive Optics and laser science ..... - 122 -
Appendix 1: Zernike polynomials in polar coordinates ..... - 124 -
Appendix 2: MATLAB codes for Zernike polynomials ..... - 125 -
A 2.1 Zernike polynomials in polar coordinates ..... - 125 -
A 2.2 Matrix of Zernike polynomials ..... - 126 -
A 2.3 Gradient of the Zernike polynomials (Reconstruction Matrix) ..... - 127 -
Appendix 3: MATLAB codes for wavefront reconstruction ..... - 129 -
A 3.1 MATLAB code for generating absolute reference grid ..... - 129 -
A 3.2 MATLAB code for dividing image into equal-sized sub-images ..... - 130 -
A 3.3 MATLAB code for estimating beam profile ..... - 131 -
Appendix 4: Published peer-reviewed papers ..... - 132 -
Publications of the author related to this work ..... - 149 -
List of Figures ..... - 151 -
List of Tables ..... - 156 -
Bibliography ..... - 157 -

List of abbreviations

AC, ACF	Autocorrelation (function)
ANDi	All-normal-dispersion (fiber oscillator)
AO	Adaptive optics
AOM	Acousto-optic modulator
AR	Anti-reflection
a.u.	Arbitrary units
ASE	Amplified spontaneous emission
BBO	Beta barium borate [β-$Ba(BO_2)_4$]
BMC	Boston Micromachines Corporation
BME	Bergmann Messgeräte Entwicklung KG
BIATRI	Project: From mono- to BI- and TRI-chromatic excitation with tailored laser pulses
BW	Bandwidth
CAS	Czech Academy of Science
CCD	Charge-coupled device
CFBG	Chirped fiber Bragg grating
CPA	Chirped-pulse amplification
CuW	Copper-tungsten (mixture)
CMOS	Complementary metal-oxide-semiconductor
CoG	Center of Gravity
CVBG	Chirped volume Bragg grating
CVD	Chemical vapor deposited (diamond)
CW	Continuous-wave
DC	Direct current
DCF	Double-clad fiber
DG	Delay generator
DiM	Dichroic mirror
DM	Deformable mirror
DPSSL	Diode-pumped solid-state laser
DUV	Deep ultraviolet
EO	Electro-optic
ELT	Extremely large telescope
FE	Front-end
FNSPE CTU	Faculty of Nuclear Sciences and Physical Engineering of the Czech Technical University in Prague

FPA	Focal-plane-array
FR	Faraday rotator
FWHM	Full width at half maximum
GaAs	Gallium arsenide
GaInAsSb	Gallium Indium Arsenide Antimonide
GDD	Group delay dispersion
GVD	Group velocity dispersion
HHG	High harmonics generation
HR	High-reflection
HWP	Half-wave plate
IF	Influence functions
IFM	Influence function matrix
IFMs	Influence function matrix in terms of slope
IFMc	Influence function matrix in terms of Zernike coefficients
IR	Infrared
InAsSb	Indium arsenide
InSb	Indium antimonide
ISO	Isolator
IWCoG	Iteratively Weighted Centre of Gravity
KTA	Potassium Titanyle Arsenate ($KTiOAsO_4$) crystal
LD	Laser diode
LMA	Large mode area (fiber)
LSI	Lateral shearing interferometer
LTAO	Laser tomography adaptive optics
MCT	Mercury cadmium telluride
MEMS	Micro-Electro-Mechanical System
METIS	Mid-infrared Extremely Large Telescope imager and spectrograph
MIR	Mid-infrared
MIRAC	Mid-InfraRed Array Camera
ML	Mode locking
MMT	Multiple Mirror Telescope
MMTAO	Multiple Mirror Telescope Adaptive Optics
MOPA	Master oscillator – power amplifier
MPA	Multipass amplifier
NA	Numerical aperture
NIR	Near-infrared
NIT	New Infrared Technologies Company
PBS	Polarization beam splitter

PbSe	Lead selenide
PbTe	Lead telluride
PCC	Plano-concave (mirror/lens)
PCV	Plano-convex (mirror/lens)
PC	Pockels cell
PD	Photodiode
PM	Polarization-maintaining (fiber)
PMN	Lead magnesium niobate
PSF	Point spread function
PTR	Photo-thermo-refractive
PV	Peak-to-valley
PWFS	Pyramid wavefront sensor
PZT	Lead zirconate titanate
O-O	Optical-to-optical (efficiency)
OPA	Optical parametric amplification/amplifier
OPCPA	Optical parametric chirped-pulse amplification
RoC	Radius of curvature
QCW	Quasi-continuous-wave
QCL	Quantum cascade lasers
QE	Quantum efficiency
QWLSI	Quadri-wave lateral shearing interferometry
QWIR	Quantum well infrared (detector)
QWP	Quarter-wave plate
RA	Regenerative amplifier
RMS	Root-mean-square
SCAO	Single conjugate adaptive optics
SCR	Spectral chirp rate
SESAM	Semiconductor saturable absorber mirror
SF	Self-focusing
SH, SHWFS	Shack-Hartmann, Shack-Hartmann wavefront sensor
SMF	Single-mode fiber
SNR	Signal-to-noise ratio
SPM	Self-phase modulation
SSL	Solid-state lasers
SW	Standing-wave (linear cavity)
TCoG	Thresholding Centre of Gravity
TD	Thin-disk
TDM	Thin-disk module

TDL	Thin-disk laser
TFP	Thin-film polarizer
UV	Ultraviolet
VBG	Volume Bragg grating
VPD	Vapor phase deposition
WcoG	Weighted Centre of Gravity
WFS	Wavefront sensor
YAG	Yttrium aluminum garnet ($Y_3Al_5O_{12}$)
ZBLAN	ZrF_4-BaF_2-LaF_3-AlF_3-NaF (fiber)
ZPL	Zero-phonon-line

List of symbols

η	Slope efficiency
η_{abs}	Absorption efficiency
λ	Wavelength
Λ	Grating period
v	Frequency
σ	Cross section
τ	Temporal duration
ϕ	Phase
ρ	Curvature of the wavefront
θ_{max} , θ_{min}	Maximum/minimum detectable wavefront slopes
θ	Angle in polar coordinate
φ	Spectral phase
ω	Angular velocity
∇	Evaluation of gradient in x and y directions
A	Area
$\boldsymbol{A}$	Gradient rectangular matrix
B	B-integral (accumulated nonlinear phase shift)
$\boldsymbol{B}$	Reconstruction matrix for Zernike coefficients
c	Speed of light in vacuum
C_i, $\boldsymbol{c}$	Modal coefficients (matrix) of the polynomials
d	Distance or displacement
dB	Decibels
D_{Airy}	Airy disk diameter
D_{sub}	Sub-aperture diameter
$\boldsymbol{D}$	Large sparse matrix
e	Euler's number
E	Energy
F	Fluence
f	Focal length
G	Gain
G_w	Weighting function
g	Gain coefficient
$\hbar\omega$	Photon energy
I	Intensity of the pixel of sub-image
j	Single index for Zernike coefficients

L	Length
M	Pump passes on the disk
m, n	Nonnegative integers with n ≥ m ≥ 0 denoting the orders of polynomials
N_2, N'_2	Upper-state level density
N_{dop}	Doping concentration
n, n_0	Refractive index
n_2	Nonlinear refractive index
P	Power
P_i	Orthogonal polynomials
PD_{focal}	Power density at the focal spot
Q	The distance between adjacent focal spots
r	Radius in polar coordinate
R_n^m	Radial functions
$\boldsymbol{S}$	Slope vector
$\boldsymbol{S_g}$	Singular value
t	Time
T	Thickness
V	Voltage
w	Beam radius (at $1/e^2$ level)
W, $\boldsymbol{W}$	Wavefront aberrations
Z, $\boldsymbol{Z}$	Zernike polynomials (matrix)

Chapter 1 Introduction

Abstract: This chapter briefly introduces mid-IR laser sources within the spectral range of 2 μm to 5 μm and their applications. The state of the art of wavefront measurement and correction for mid-IR laser sources are investigated and discussed. The motivation and goals of this work are also introduced.

1.1 Mid-IR laser sources and applications

Laser has been widely used in numerous fields, such as material processing, communication, optical storage, medical and beauty technologies, research and military developments, instruments and sensors, entertainment display, and additive manufacturing since it was invented in the 1960s. In recent decades, mid-infrared (mid-IR) laser sources within the wavelength region of 2 - 5 μm are desirable for numerous applications, such as the generation of attosecond pulses, high-harmonics towards the X-ray range [1], and medical treatment [2]. It can also generate powerful broadband few-cycle mid-infrared (mid-IR) radiation [3]. The use of mid-IR semiconductor lasers emitting at room temperature offers rich possibilities for areas such as atmospheric pollution monitoring, industrial process control, leak detection, and aid for the medical diagnosis of disease. The mid-IR (MIR) wavelength region is called the "molecular fingerprint." In particular, the range between 2 - 5 μm is characterized by strong fundamental vibrational absorption lines of atmospheric constituents, vapor, and other gases [4]. These applications all benefit from the development of mid-IR laser sources, which can be primarily attributed to the development of novel laser crystals, nonlinear crystals, and the improving quality of traditional mid-IR materials.

Typical mid-IR laser sources include solid-state lasers, fiber lasers, semiconductor lasers, and nonlinear optical devices. The first mid-IR laser was demonstrated in 1960, soon after the invention of the laser. Uranium (U)-based U^{3+}:CaF_2 flash-lamp-pumped solid-state laser was invented, emitting laser at the wavelength of 2.6 μm [5]. Many mid-IR solid-state lasers and fiber lasers based on trivalent rare-earth ions, such as Tm^{3+} (spectral region of 2.0 – 2.3 μm), Ho^{3+} (spectral region of 2 – 4 μm), and Er^{3+} (spectral region of 2 – 3.5 μm) [6], have been developed with various host materials. So-called mid-IR glasses, including the fluorides [7], tellurites [8], and chalcogenides [9], have lower losses in this spectral region (2 - 5 μm) due to

lower phonon energies. Because of this, mid-IR fiber lasers beyond a wavelength of 2.1 μm typically use fluoride glasses like ZBLAN (ZrF_4-BaF_2-LaF_3-AlF_3-NaF) [10]. Tellurite and chalcogenide fibers have been widely used as mid-IR transport fibers or for spectral-broadening applications.

Nonlinear mid-IR laser sources through nonlinear frequency conversion techniques are also widely used for obtaining tunable sources for various applications. The nonlinear generation takes several forms, such as second-harmonic generation, difference-frequency generation, optical parametric amplifiers, and optical parametric oscillators [11].

Semiconductor mid-IR laser is another commercially developed laser source based on intersubband transitions, which is quantum cascade lasers (QCLs) [12]. The mid-IR interband semiconductor lasers are made using materials such as antimonides [13] (GaInAsSb, InAsSb, InSb) and lead salts [14] (e.g., PbSe, PbTe) that provide emission in the mid-IR due to their small bandgaps (< 0.6 eV).

Thus, interest in detecting and correcting the wavefront of mid-IR laser sources is increasing with the increase in mid-IR applications and laser sources in this spectral range.

1.2 Adaptive Optics

Adaptive Optics (AO) is a well-known technology to detect and correct wavefront distortion. It is a scientific and engineering discipline where the performance of an optical image or laser beam can be improved. This correction of the optical wavefront error is usually performed through a deformable mirror (DM) which adapts to the measured wavefront correcting the distortion or aberration. Since AO also allows for improving the performance of aberrated optical systems or laser sources, it has been widely employed in several other disciplines, such as ophthalmology [15], microscopy [16], free space laser communication systems [17], and endoatmospheric applications [18].

The first original idea of using a deformable optical element for wavefront correction, with a wavefront sensor as feedback of the control loop, was proposed by H. W. Babcock [19] in 1953. It was intended to solve the severe limitations imposed on astronomical observations to compensate for the wavefront error caused by atmospheric turbulence. Since then, various adaptive optics technologies have been developed, including many different wavefront sensors or correctors.

1.2.1 State of the art of AO in the mid-IR spectral region

Mid-IR AO systems have been used in observations for the spectral range of 2 ~ 19 μm. In 2003, a team from the University of Arizona utilized an adaptive secondary AO system for the Multiple Mirror Telescope (MMT) to obtain high-resolution images of AC Herculis and Point

spread function (PSF) of calibration stars [20]. They utilized the 128×128 SiAs blocked-impurity-band 2-20 μm Mid-InfraRed Array Camera (MIRAC3 [21]) for the spectrum of 9.8 μm, 11.7 μm, and 18 μm. The Multiple Mirror Telescope Adaptive Optics (MMTAO) system was updated with a newer version camera, MIRAC4, and will be applied on an Extremely Large Telescope (ELT) [22]. In 2006, a mid-IR AO system was designed for a 30-meter telescope in the spectral range of 5 - 28 μm [23].

A single conjugate adaptive optics (SCAO) system has been developed for the mid-infrared Extremely Large Telescope imager and spectrograph (METIS), covering the wavelength range of (3-19 μm) [24]. It will be further upgraded to a laser tomography adaptive optics (LTAO) system within the same mid-IR wavelength range [25].

Adaptive optics at mid-IR wavelengths appear to be a promising technique that allows for uniquely stable PSF and high Strehls. A high degree of PSF stability will eliminate morphological ambiguities due to poor (seeing-limited) PSF calibrations. Mid-IR AO significantly impacts any field where mid-IR imaging is possible.

1.3 Motivation and objectives of this thesis

With the development of mid-IR laser sources and applications, the demands for mid-IR laser sources with high beam quality are increasing. For example, the wavefront of the fundamental laser beam deteriorates after propagating through numerous optics and nonlinear crystals and being reflected by mirrors in a long beam path (up to a few meters). At the HiLASE center, several Optical Parametric Amplifiers (OPA) are being constructed. In order to improve the beam quality of the OPA systems to achieve higher efficiency or to obtain better results, wavefront correction in the mid-IR spectral range has been proposed.

This dissertation can be divided into two main areas:

1. Providing a solution for the Adaptive Optics System developed for mid-IR laser. To do so, the following objectives should be achieved:
   - Research on the mid-IR detector and choose a suitable detector for the application
   - Design and development of a Shack-Hartmann wavefront sensor with an uncooled Vapor Phase Deposition (VPD) PbSe FPA detector
   - Design and development of the AO system with the homemade wavefront sensor and a silver-coated bimorph piezoelectric deformable mirror, and with a closed-loop control system
   - Wavefront correction experiments on a mid-IR laser beam to verify the AO system
2. Design and development of a high-energy Yb:YAG thin-disk laser system based on chirped pulse amplification (CPA) technology to provide 10 mJ of high pulse energy with ≤ 1 ps of pulse duration for the Optical Parametric Amplification (OPA).
3. Design the application of the mid-IR AO system in the OPA system for future work.

Chapter 2 Adaptive Optics

Abstract: In this chapter, Adaptive Optics, including wavefront sensing and controlling technologies, are introduced and discussed according to the primary goal of this work. The Shack Hartmann wavefront sensor (SHWFS) principle is also introduced in this chapter. Wavefront reconstruction techniques based on the measured wavefront slopes by SHWFS are introduced, including centroiding techniques and Zernike polynomials widely used to represent the wavefront over a unit circle. Wavefront control techniques, including open-loop control and closed-loop control, are introduced in the last section of this chapter.

2.1 Wavefront sensing and controlling technologies

2.1.1 Wavefront sensing: shearing interferometry

Wavefront sensing is essential to the Adaptive Optics (AO) system. Various commercial solutions for wavefront detecting in visible and near-IR spectral regions exist. One of the most widely used wavefronts characterizing techniques is shearing interferometry [26]. The basic idea of the shearing interferometry, as shown in Fig. 2.1, is to use two beams capable of interference, one of which has a perfectly flat wavefront. The interference pattern reveals the deviation of the second beam from the perfect flat reference. One commonly used approach is double-path interferometry, as shown in Fig. 2.1(a). It separates the beam into two different paths to accomplish the interference between the aberrated one and the reference beam. Another approach is the common path interferometry or the Fizeau-type interferometer [27], as shown in Fig. 2.1(b). In this configuration, the beam is self-referencing, which means the reference beam has the same wavefront as the measured one, and both beams follow the same optical path. The advantage of the common path interferometers over the double path ones is mainly the simplification of the experimental setup and low sensitivity to vibration or other environmental influences. The interference pattern of the two beams is not proportional to the wavefront but rather its derivative in the shear direction [28].

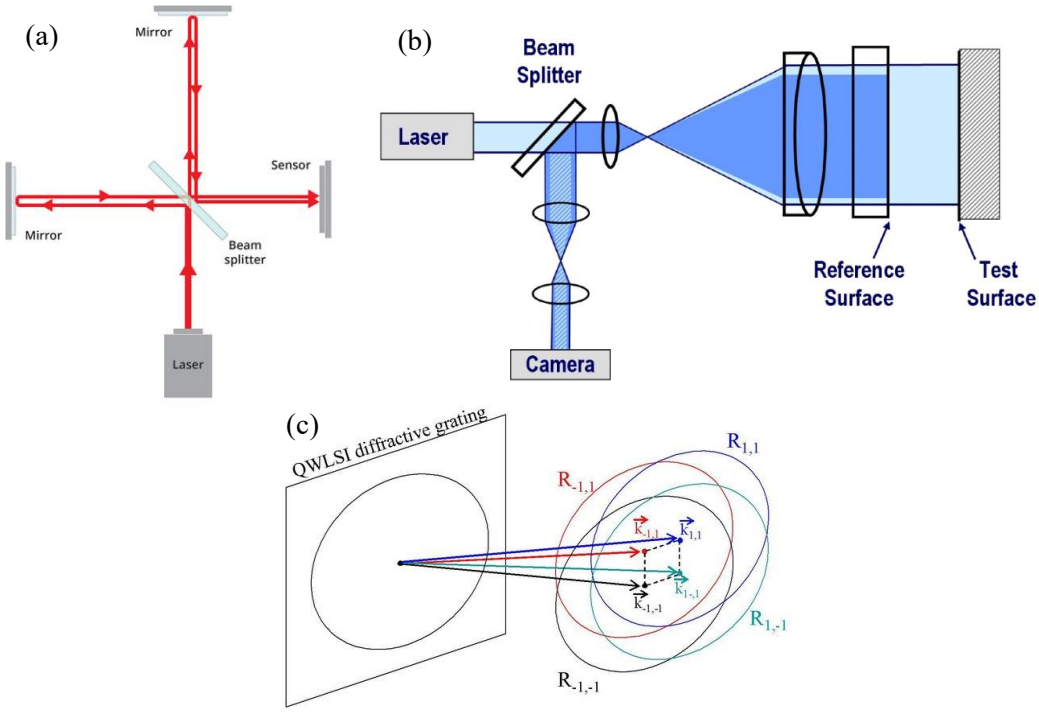

Fig. 2.1 Shearing interferometry wavefront measurements. Principles of (a) double path interferometry, (b) Fizeau type interferometer, and (c) Quadri-Wave Lateral Shearing Interferometry (QWLSI).

One commonly used shearing interferometer for wavefront measurement is called a lateral shearing interferometer (LSI), where the lateral shear is achieved using a beam splitter [29]. It measures the central part of the beam due to the shear; therefore, it can be used to measure symmetrical or spherical aberration [30]. The second type of commonly used interferometer is the radial shearing interferometer [31], where the beam is expanded and used as a reference. Both beams overlap with a common center but a different radial size. If the size of the radial shear is large enough, the measured interferogram becomes the 0^{th}-order derivative [32], which means the measurement is the actual wavefront rather than its derivative. However, it requires large optical elements to construct such an interferometer.

Another type of interferometer is Quadri-Wave Lateral Shearing Interferometry (QWLSI) [33][34][35], known as the modified Hartmann mask technique, as shown in Fig. 2.1(c), where a diffraction grating is applied to generate four beams. The four beams propagate after a few millimeters, and the four replicas overlap and interfere, creating an interferogram on the detector. The phase gradients are encoded in the interference fringe deformation. QWLSI can offer high spatial resolution and large dynamics. Despite QWLSI requiring higher light intensity than other interferometers, it is widely applied in optical metrology or laser wavefront characterization/correction systems [36][37].

2.1.2 Wavefront sensing: Shack Hartmann Wavefront Sensor

Besides interferometry techniques, the Shack-Hartmann wavefront sensor is one of the simplest devices for measuring wavefront. The first Shack-Hartmann wavefront sensor was proposed by Dr. Roland Shack and built by Dr. Ben Platt to measure the wavefront of the image captured from a satellite tracking telescope in the 1960s [38]. Fig. 2.2 shows the optical schematics of an early Hartmann test (left) and the first Shack-Hartmann sensor (right). The first idea of testing the beam quality of a laser with a Shack-Hartmann wavefront sensor was proposed and built by Dr. Ben Platt in the 1970s [39]. In the following decades, the Shack-Hartmann wavefront sensor attracted the interest of various researchers in different fields. Lots of effort has been devoted to improving the dynamic range [40][41][42][43], the sensitivity [44], the centroid detection accuracy [45][46][47], the processing speed [48][49], etc.

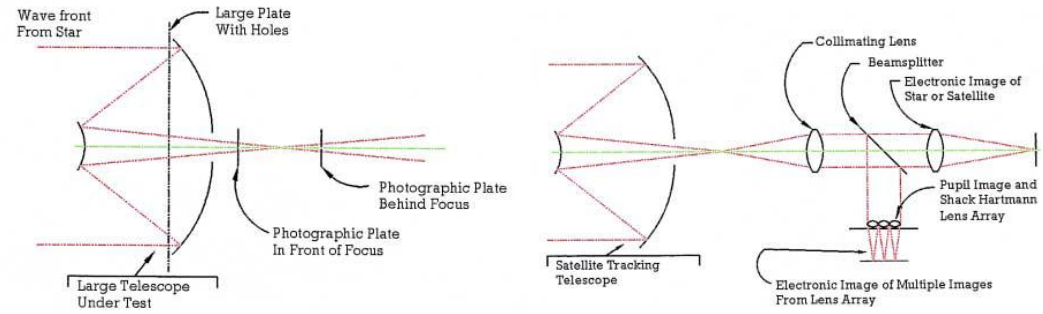

Fig. 2.2 Optical schematics of an early Hartmann test (left) and the first Shack-Hartmann sensor (right).

2.1.3 Wavefront sensing: Pyramid Wavefront Sensor

Another popular wavefront sensor is Pyramid Wavefront Sensor (PWFS) which was proposed by Ragazzoni in 1996 [50]. Its principle is shown in Fig. 2.3 [51]. The sensor uses a refractive pyramidal prism placed inside a Keplerian-type telescope to split the beam into multiple parts at the geometric focus of a lens, i.e., a Charge-coupled device (CCD) sensor. The distribution of light between the four pupil images can be used to reconstruct the wavefront of the incident light. PWFS is highly sensitive to small wavefront aberrations but has limited dynamic range. To increase the range of the sensor, the PWFS is often modulated: the image in the focal plane is moved in a circle around the tip of the pyramid prism [52]. The same effect as the rotation of the prism can be achieved with a fast tip-tilt mirror [53] or a suitable diffuser [54]. The advantage of the PWFS is the relatively high spatial resolution, which is equal to the resolution of the sub-apertures. The sensor's adjustable sensitivity and dynamic range can be used during measurement and optimized to provide the best feedback for the closed loop. A PWFS is successfully deployed [55] or is being deployed at astronomical telescopes [56][57].

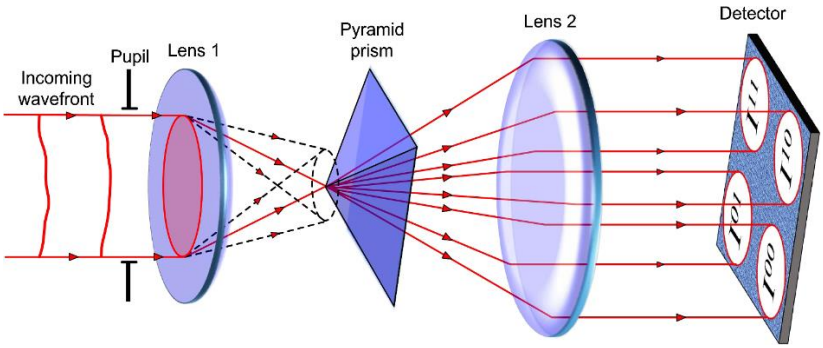

Fig. 2.3 Optical schematic of a pyramid WFS. The circular modulation path is shown in the dashed line.

2.1.4 Wavefront sensing: in the mid-IR spectral region

However, when it comes to the mid-IR spectral region, there are fewer wavefront sensing solutions than in the near-IR spectral region, mainly due to fewer choices of the mid-IR detector. In the mid-IR spectral region, few detectors can be employed to detect the wavefront of mid-IR radiation. The cooled InSb focal-plane-array (FPA) detectors are one of the most commonly used devices for mid-IR radiation detection [58]. To reduce thermal noise, the InSb FPA needs to be cooled down to 77 K. Cooled mercury cadmium telluride (MCT) detector can also be used for the Shack-Hartmann wavefront sensor, which is cooled by a Stirling cooler [59]. Quantum well IR（QWIR) detectors [60] are also well established for long-wave infrared and part of the mid-IR spectral regions. It is based on intersubband transitions in the quantum wells. It is crucial to achieve an operating temperature as high as possible and at least above 77 K to reduce volume and power consumption and improve the detection module's reliability. However, lack of spatial uniformity over a large area still plagues InSb and MCT devices, while QWIRs have larger dark currents and lower quantum efficiency (QE) than the interband devices.

Besides the low-temperature cooled (77 K) detector, the high operating temperature (>120 K) min-IR FPA detector based on type-II InAs/GaSb superlattices [61][62] has high performance in the min-IR spectral region. It has an effective band gap of 3 to 30 μm which is tailored by varying the thickness of constituent layers. This would allow the sensor to detect almost the entire IR region. However, the detectors mentioned above require a complex cooling system. Detectors operating at room temperature are more demanded in many applications. Pyroelectric detectors based on lithium tantalate ($LiTaO_3$), e.g., Pyrocam from Ophir company, is also widely used for the characterization of laser for wavelength longer than 1.5 μm [63]. The pyroelectric devices can operate from 13 nm to 3000 μm. The wavefront sensors based on Quadri-Wave Lateral Shearing Interferometry (QWLSI) technique from PHASICS S.A. company has extended the wavelength range to 2 ~ 16 μm thanks to the use of a broadband microbolometer [64][65][66].

Besides using direct detectors for measuring the wavefront of mid-IR radiation, many

researchers also developed indirect measuring methods. S. Bonora et al. [67][68] developed a wavefront sensing technique by converting the image from mid-IR to near-IR or visible to exploit high-contrast optical switching in vanadium oxide thin-film layers. After the image conversion, the wavefront or beam profile of the mid-IR laser source can be measured by a standard CCD or CMOS (complementary metal-oxide semiconductor) camera with high resolution and low cost. Wavefront distortion induced by mid-IR radiation can also be measured using an indirect probing method [69].

2.1.5 Wavefront correctors: Bimorph deformable mirror

Wavefront correctors, such as bimorph deformable mirrors (DM) [70], membrane DM [71], Micro-Electro-Mechanical Systems (MEMS) [72], and liquid-crystal phase modulators [73][74], are widely used to compensate for the aberrations measured by the wavefront sensor, by changing its surface shape in response to position commands.

Bimorph deformable mirror is usually actuated by piezoelectric or electrostriction material, such as Lead zirconate titanate (PZT) [75] or lead magnesium niobate (PMN) [76], in the form of a disk attached to the back side of a glass substrate with HR coating at the front side. Fig. 2.4 shows the cross-section of a bimorph deformable mirror. It has many advantages, such as large stroke, high damage threshold of laser power, and better correction of low-order aberrations with a given number of actuators. A glass substrate is usually used as the reflective surface of the bimorph deformable mirror; various coatings, such as HR coating or aluminum coating, are allowed. Therefore, it is suitable for high-power laser applications. However, the actuators are mechanically coupled. There is a finite response along the entire surface of the mirror when one actuator moves. As a common feature of the piezoelectric DM, the inherent hysteresis of the piezoelectric material causes a nonlinear relationship between the applied voltage and the mirror deformation response on the order of 10% [77]. The hysteresis would affect the performance of the AO system, such as the bandwidth and residual wavefront error. Despite many model-based solutions that have been applied to compensate for hysteresis, they cannot be fully eliminated. The hysteresis should be considered while designing the AO system.

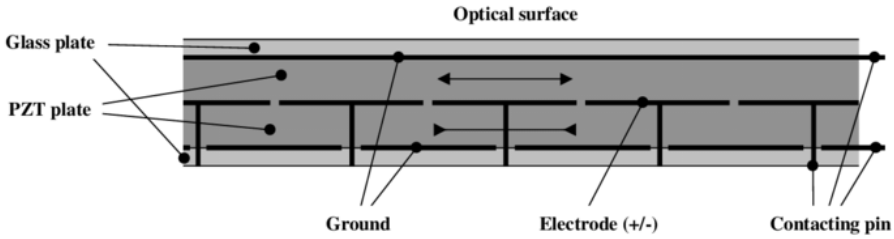

Fig. 2.4 Cross section of a bimorph deformable mirror [78].

2.1.6 Wavefront correctors: membrane deformable mirror

A membrane deformable mirror is one of the most popular deformable mirrors due to its extremely valuable performance, potentialities, ease of use, and low cost. The electrostatic membrane mirror consists of a thin metal (silver or aluminum) coating over a nitrocellulose, polyamide, or silicon membrane, which is pre-tensioned and glued over a metallic frame [79]. The frame is faced the electrode pads utilizing calibrated spacers to maintain the nominal distance between the membrane and electrodes, as shown in Fig. 2.5. However, the membrane deformable mirror exhibits a rather long settling time on the order of several milliseconds. Therefore the usable bandwidth of the AO system is relatively low. The membrane cannot be coated with HR coating as this would cause severe lateral stresses and wrinkling.

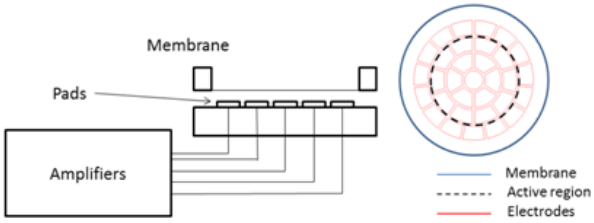

Fig. 2.5 Electrostatic membrane mirror section view and the active membrane region (dashed lines) [80].

2.1.7 Wavefront corrector: Micro-electro-mechanical system

Microelectromechanical systems (MEMS) technology enables the design and fabrication of a new class of deformable mirrors for adaptive optics. As shown in Fig. 2.6, the principle of the MEMS deformable mirrors, the Electrostatic attraction between the energized actuator electrodes and the electrically grounded actuator membrane, deflects the actuators precisely and repeatably, thereby shaping the mirror. It can be used to meet the wavefront control requirements for high-contrast imaging of exoplanets with coronagraph instruments. Boston Micromachines Corporation (BMC) has been one of the most famous companies providing commercially available MEMS DMs since 1999. As demands increases, BMC has produced segmented and continuous mirrors consisting of 32 – 4092 actuators, mirror apertures of 1.5 – 26 mm in diameter, and actuator stroke (maximum linear extension) in the range of 2–8 μm [81]. Thanks to the advantages of MEMS DMs, such as high-actuator density, large stroke, precise control in a small, low-power form factor, and low cost, they have been widely used for space-based wavefront control applications and atmospheric optical communication.

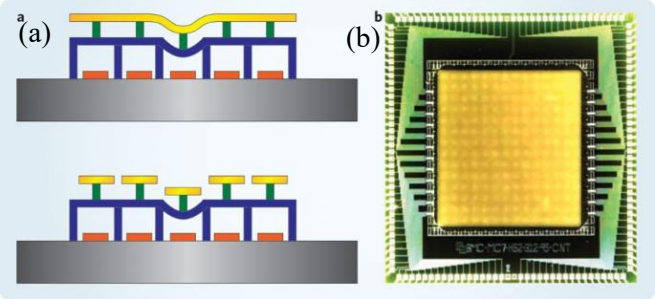

Fig. 2.6 Principles of MEMS deformable mirror A membrane or segmented surface (gold) is attached by silicon actuator posts (green) to an array of locally anchored compliant electrostatic actuator membranes (blue). The actuator is controlled by applying voltages to the rigid silicon actuator electrodes (orange) on the wafer substrate (grey). (b) Photo of a MEMS DM with 140 actuators supporting a continuous DM [82].

2.2 Shack Hartmann Wavefront Sensing

The Shack-Hartmann wavefront sensor (SHWFS) uses a lenslet array to divide the incoming beam into an array of smaller beams, and each beam is imaged onto the camera sensor that is placed at the focal plane of the lenslet array, as shown in Fig. 2.7. The lenslet array focuses the incoming wavefront onto the detector (e.g., CCD). The focal spots at the detector are compared with reference spots, which are usually generated when incoming wavefront comes from surfaces with known profiles. A planar wavefront incident on the Shack-Hartmann wavefront sensor's lenslet array will generate a regularly spaced grid of focal spots. A distorted wavefront will cause individual spots to be displaced from the optical axis of each lenslet.

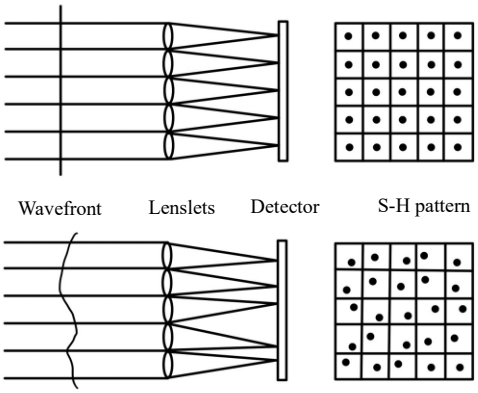

Fig. 2.7 Principle of Shack-Hartmann wavefront sensor. A planar wavefront incident on the Shack-Hartmann wavefront sensor's lenslet array and imaged on the camera sensor will generate a regularly spaced grid of focal spots. A distorted wavefront will cause individual spots to be displaced from the optical axis of each lenslet.

In order to detect the shift of each spot's centroid, the focal spot, i.e., the Airy disk, which describes the best-focused spot of light that a perfect lens with a circular aperture can make, should be larger than the pixel size of the detector. If the Airy disk diameter is smaller than the pixel size, its centroid cannot be detected precisely when it is moving within the range of one pixel, as shown in Fig. 2.8. Due to the small size of each lenslet, we assume a plane wavefront

in each sub-aperture. Therefore, the Airy disk is used to estimate the focal spot diameter ($1/e^2$) as [83]:

$$D_{Airy} = 2 \times 0.82 \frac{\lambda f}{d} \tag{2.1}$$

where λ is the wavelength of the radiation under test, f is the focal length of the lenslet, and d is the width of the sub-aperture (pitch).

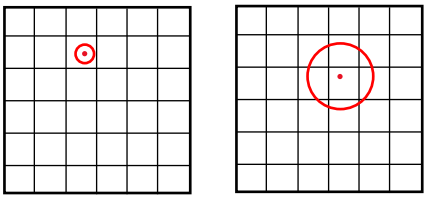

Fig. 2.8 Focal spot (Airy disk, red circle) and its centroid (red dot) on the sub-aperture on the camera sensor. The black grids indicate the pixels in the sub-aperture. On the left, if the Airy disk diameter is smaller than the pixel size, then the centroid cannot be detected precisely. On the right, the Airy disk diameter is larger than the pixel size, so its centroid can be detected and calculated precisely by the Centroid of Gravity algorithm, etc.

The dynamic range [84], which is the maximum detectable wavefront slope, θ_{max}, which is the local tilt of the wavefront at the location of that lenslet, as indicated in Fig. 2.9. It can be calculated by:

$$\theta_{max} = \frac{D_{sub}}{2f} \tag{2.2}$$

where D_{sub} is the sub-aperture diameter. To increase the dynamic range of the sensor, a larger lenslet diameter and/or a shorter focal length lenslet needs to be used. The dynamic range can be increased by shortening the focal length of the lenslet [85].

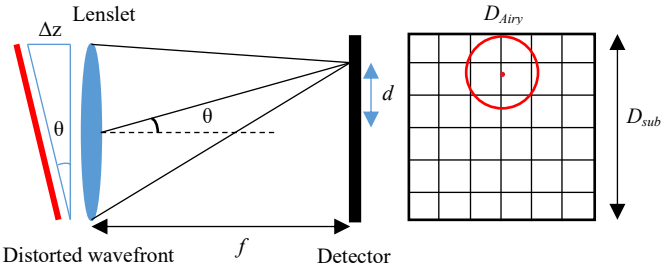

Fig. 2.9 Definition of the dynamic range of the individual lenslet of the wavefront sensor.

However, decreasing the focal length would cause a decrease in measurement sensitivity, which is inversely proportional to the minimum detectable wavefront slope θ_{min}. It could be written as:

$$1/\theta_{min} = \frac{f}{d_{min}} \tag{2.3}$$

where $d_{\min}$ is the minimum detectable spot displacement. Typically, $d_{\min}$ is determined by the photodetector's pixel size, the centroid algorithm's accuracy, and the sensor's signal-to-noise ratio. Therefore, a longer focal length lenslet is needed for better sensitivity if $d_{\min}$ is constant. By combining Eq. (2.2) and Eq. (2.3), the relationship, or the trade-off, between dynamic range

and minimum detectable wavefront slope can be written as:

$$\theta_{min} = \frac{2d_{min}\theta_{max}}{f} \tag{2.4}$$

These quantities are inversely related, which means that increasing the dynamic range of the wavefront sensor results in a decrease in its sensitivity and vice versa for a constant lenslet pitch size, D_{sub}.

Two major methods, modal and zonal wavefront reconstruction methods, are used to reconstruct the wavefront from the measured wavefront slope: the zonal and modal approaches, as introduced in the following sections.

2.3 Modal wavefront reconstruction

The shift of each spot's centroid is proportional to the local slope of the wavefront at the location of that lenslet, as expressed in Eq. (2.5):

$$\frac{\partial W(x,y)}{\partial x} = \frac{1}{f}d_x, \qquad \frac{\partial W(x,y)}{\partial y} = \frac{1}{f}d_y \tag{2.5}$$

where $W(x,y)$ is the wavefront aberration, d_x and d_y are the spot displacement from its reference spot in the x- and y- axes, and f is the effective focal length of the lenslet. The right hands of Eq. (2.5) are the sub-apertures' local slopes, Sx, and Sy.

In the modal method, the wavefront aberration $W(x,y)$ can be decomposed into orthogonal polynomials defined over the pupil area, which is the area where the wavefront is measured, as:

$$W(x,y) = \sum_{i=1}^{M} C_i P_i(x,y) \tag{2.6}$$

where C_i is the modal coefficient of the polynomial, M is the number of orthogonal modes, and $P_i(x,y)$ is the orthogonal polynomial in the pupil area. Legendre polynomials and Zernike polynomials are two complete orthogonal sets of polynomials widely used to describe wavefront aberration. Legendre polynomials are orthogonal on a square or rectangular area [86]. Therefore, it is usually used to describe wavefront aberration in a square or rectangular area [87]. In this work, Zernike polynomials $Z(x,y)$ is selected due to the round shape of the laser beam. More detail about the Zernike polynomials will be discussed in the next section.

Using matrix notation, Eq. (2.6) can be rewritten as

$$\boldsymbol{W} = \boldsymbol{Zc} \tag{2.7}$$

where $\boldsymbol{W}$ is the wavefront aberration matrix, $\boldsymbol{Z}$ is the Zernike polynomial matrix, and $\boldsymbol{c}$ is the modal coefficient vector.

By substituting Eq. (2.6) to Eq. (2.5), the wavefront slopes can be written as:

$$\frac{1}{f}d_x = \sum_{i=1}^{M} C_i \frac{\partial Z_i(x,y)}{\partial x}, \quad \frac{1}{f}d_y = \sum_{i=1}^{M} C_i \frac{\partial Z_i(x,y)}{\partial y} \tag{2.8}$$

Using matrix notation, Eq. (2.8) can be written as

$$\boldsymbol{S} = \boldsymbol{Ac} \tag{2.9}$$

where $\boldsymbol{S}$ is the measured slope vector (x-slopes followed by y-slopes), $\boldsymbol{A}$ is the gradient matrix, or Zernike reconstruction matrix, with M columns and $2N$ rows, where N is the number of focal spots.

$$\boldsymbol{A} = \nabla \boldsymbol{Z} \tag{2.10}$$

where the operator ∇ calculates the gradient evaluation in the x and y directions. Eq. (2.9) is expressed in Fig. 2.10. The modal coefficients of the polynomials can be found using the least square method. Therefore, the Zernike coefficients can be written as:

$$\boldsymbol{c} = \boldsymbol{B} \cdot \boldsymbol{S} \tag{2.11}$$

where

$$\boldsymbol{B} = \left(\boldsymbol{A}^{\boldsymbol{T}}\boldsymbol{A}\right)^{-1}\boldsymbol{A}^{\boldsymbol{T}} \tag{2.12}$$

where $\boldsymbol{A}^{\boldsymbol{T}}$ is the pseudo-inverse matrix of $\boldsymbol{A}$.

The wavefront could be reconstructed when the Zernike coefficients are obtained.

$$\underset{\boldsymbol{S}}{\begin{bmatrix} d_{x1}/f \\ d_{x2}/f \\ \vdots \\ d_{xN}/f \\ d_{y1}/f \\ d_{y2}/f \\ \vdots \\ d_{yN}/f \end{bmatrix}} = \underset{\boldsymbol{A}}{\begin{bmatrix} \frac{\partial Z_1(x_1,y_1)}{\partial x} & \frac{\partial Z_2(x_1,y_1)}{\partial x} & \cdots & \frac{\partial Z_M(x_1,y_1)}{\partial x} \\ \frac{\partial Z_1(x_2,y_2)}{\partial x} & \frac{\partial Z_2(x_2,y_2)}{\partial x} & \cdots & \frac{\partial Z_M(x_2,y_2)}{\partial x} \\ \vdots & \vdots & & \vdots \\ \frac{\partial Z_1(x_N,y_N)}{\partial x} & \frac{\partial Z_2(x_N,y_N)}{\partial x} & \cdots & \frac{\partial Z_M(x_N,y_N)}{\partial x} \\ \frac{\partial Z_1(x_1,y_1)}{\partial y} & \frac{\partial Z_2(x_1,y_1)}{\partial y} & \cdots & \frac{\partial Z_M(x_1,y_1)}{\partial y} \\ \frac{\partial Z_1(x_2,y_2)}{\partial y} & \frac{\partial Z_2(x_2,y_2)}{\partial y} & \cdots & \frac{\partial Z_M(x_2,y_2)}{\partial y} \\ \vdots & \vdots & & \vdots \\ \frac{\partial Z_1(x_N,y_N)}{\partial y} & \frac{\partial Z_2(x_N,y_N)}{\partial y} & \cdots & \frac{\partial Z_M(x_N,y_N)}{\partial y} \end{bmatrix}} \cdot \underset{\boldsymbol{c}}{\begin{bmatrix} a_1 \\ a_2 \\ a_3 \\ \vdots \\ \vdots \\ \vdots \\ a_n \end{bmatrix}}$$

Fig. 2.10 Eq. (2.9) expression using matrix notation

2.4 Zonal wavefront reconstruction

In the zonal approach for a Shack-Hartmann wavefront sensor, the wavefront aberration is determined on a discrete set of points distributed over the local zones which match the lenslet array grid. Some geometries for zonal wavefront reconstruction have been proposed by such as David L. Fried [88] and W. H. Southwell [89]. Due to the lowest error propagation advantage compared to other geometries [90], Southwell geometry, as shown in Fig. 2.11, is more suitable for the Shack-Hartmann sensor.

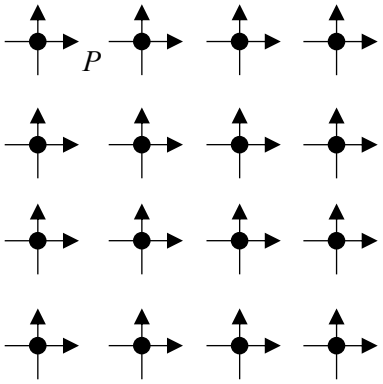

Fig. 2.11 Southwell geometry for wavefront reconstruction. The dots represent phase points (wavefront height), and the arrows represent the measured slopes.

The relation between the measured local wavefront slopes and two adjacent slopes with separation P, which is the pitch size of the lenslet, can be expressed as [89]:

$$\begin{aligned} S^{x}_{col,row} &= \frac{\left[\left(W_{col+1,row} + W_{col+1,row+1}\right)/2 - \left(W_{col,row} + W_{col,row+1}\right)/2\right.}{P} \\ S^{y}_{col,row} &= \frac{\left[\left(W_{col,row+1} + W_{col+1,row+1}\right)/2 - \left(W_{col,row} + W_{col+1,row}\right)/2\right.}{P} \end{aligned} \tag{2.13}$$

where $S^{x}_{col,row}$ and $S^{y}_{col,row}$ are the measured local slopes in x- and y-axes, N is the number of a lenslet in x- and y-axes for a lenslet array consisting of $N \times N$ lenslets, and col = 1, N-1, row = 1, N.

Eq. 2.13 can be written in matrix equation form as [89]:

$$\boldsymbol{DS} = \boldsymbol{A\phi} \tag{2.14}$$

where $\boldsymbol{D}$ is a large sparse matrix that performs the adjacent slope averaging, $\boldsymbol{S}$ is the measured slope vector (x slopes followed by y slopes), $\boldsymbol{A}$ is a rectangular matrix representing the slope model of size N^2 multiplied by the number of measured slopes, $\boldsymbol{\phi}$ is the vector of length N^2 containing the local wavefront value.

The least-square solution for Eq. 2.14 can be written as [89]:

$$\boldsymbol{\phi} = (\boldsymbol{A^T A})^{-1}\boldsymbol{A^T DS} \tag{2.15}$$

2.5 Zernike polynomials

As mentioned above, the Zernike polynomials are a sequence of polynomials widely used in modal wavefront reconstruction with circular apertures [91]. The Zernike polynomials are continuous and orthogonal over a unit circle [92]. The mathematical description of the Zernike polynomials helps define the magnitude and characteristics of the differences between the image formed by an optical system and the original object [93]. F. Zernike first employed it in his phase contrast method for testing circular mirrors [94]. One of the advantages of using the normalized Zernike polynomials to describe aberrations is that the coefficient of each Zernike mode represents the root mean square (RMS) wavefront error attributable to that mode only,

thanks to the orthogonality. Therefore, the already computed or reconstructed wavefront would not be affected by any additional modes added in the sequence.

The wavefront in Eq. (2.6) in terms of the Zernike polynomials Z_n^m that are orthogonal over the entire unit circular pupil can be written as:

$$W(r,\theta) = \sum_{n,m} C_n^m Z_n^m(r,\theta) \tag{2.16}$$

with a double indexing scheme and polar coordinates, as shown in Fig. 2.12. C_n^m denotes the Zernike coefficients. *m* is an integer denoting the angular frequency, and *n* is a nonzero integer denoting radial order. The Zernike polynomials expressed in polar coordinates ($x = r\sin\theta$, $y = r\cos\theta$) are given by the complex combination [93]:

$$\begin{aligned} Z_n^m(r,\theta) \pm iZ_n^{-m}(r,\theta) &= V_n^{-m}(r\cos\theta, r\sin\theta) \\ &= R_n^m(r)\exp(\pm im\theta) \end{aligned} \tag{2.17}$$

where leads to

$$\begin{aligned} Z_n^m(r,\theta) &= R_n^m(r)\cos m\theta \text{ for } m \geq 0, \\ Z_n^m(r,\theta) &= R_n^m(r)\sin m\theta \text{ for } m < 0, \end{aligned} \tag{2.18}$$

where *r* is restricted to the unit circle ($0 \leq r \leq 1$), meaning that the radial coordinate is normalized by the semi-diameter of the pupil, and θ is measured clockwise from the *y*-axis ranged in (0, 2π). This is consistent with aberration theory definitions but different from the conventional mathematical definition of polar coordinates. The radial function, $R_n^m(r)$, can be written as:

$$R_n^m(r) = \sum_{l=0}^{\frac{n-m}{2}} \frac{(-1)^l (n-l)!}{l!\left[\frac{(n+m)}{2}-l\right]!\left[\frac{n-m}{2}-1\right]!} r^{n-2l} \tag{2.19}$$

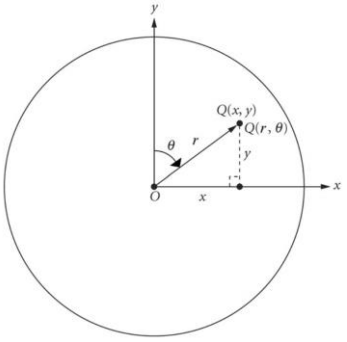

Fig. 2.12 Polar coordinates (*r*, θ) and their relationship with Cartesian coordinates (*x*, *y*) of a point Q in the circular pupil [95].

Therefore, each Zernike polynomial Z_n^m can be written as the product of a radial function and a trigonometric function $\Theta_n^m(\theta)$ as:

$$Z_n^m(r,\theta) = N_n^m R_n^m(r)\Theta_n^m(\theta) \tag{2.20}$$

where trigonometric function $\Theta_n^m(\theta)$ is defined as:

$$\Theta_n^m(\theta) = \begin{cases} \cos m\theta & m \geq 0 \\ -\sin m\theta & m < 0 \end{cases} \tag{2.21}$$

N_n^m is the normalization constant which is chosen to satisfy $R_n^{\pm m}(1) = 1$ for all values of n and m. The normalization constant is described by:

$$N_n^m = \left(\frac{2(n+1)}{1+\delta_{m0}}\right)^{\frac{1}{2}} \tag{2.22}$$

where δ_{m0} is the Kronecker delta ($\delta_{m0} = 0$ for $m \neq 0$).

A double indexing scheme is used in the above equations. A single indexing scheme is also used for describing the Zernike coefficients. Since the polynomials depend upon two indices, n and m, ordering a single indexing scheme is arbitrary. To obtain the single index j, it is convenient to lay out the polynomials in a pyramid with row number n and column number m. The single index j starts from the top, as shown in Fig. 2.13. In the single indexing scheme:

$$Z_j(r,\theta) = Z_n^m(r,\theta) \tag{2.23}$$

where j, n, m satisfies:

$$\begin{aligned} j &= \frac{[n(n+2)+m]}{2} \\ n &= roundup\left[\frac{-3+(9+8j)^{\frac{1}{2}}}{2}\right] \\ m &= 2j - n(n+2) \end{aligned} \tag{2.24}$$

The Algebraic expansion and meaning of the Zernike polynomials are shown in Appendix 1, which is ordered and normalized according to Noll [96]. The relationship between single and double indexing schemes in the third order is shown in the table of Appendix 1. The MATLAB code for the Zernike polynomials and the reconstruction matrix, which is the matrix of the gradient of Zernike polynomials, is attached in Appendix 2.

Zernike polynomials represent classical aberrations [97] that are combined to minimize the aberration variance over the pupil [98] and are widely employed in optical design and adaptive optics. The piston mode is commonly neglected in adaptive optics literature since it does not affect the image. However, in any system with noncircular pupils, the Zernike circle polynomials will not be orthogonal over the whole of the pupil area and thus may not be the ideal polynomial expansion.

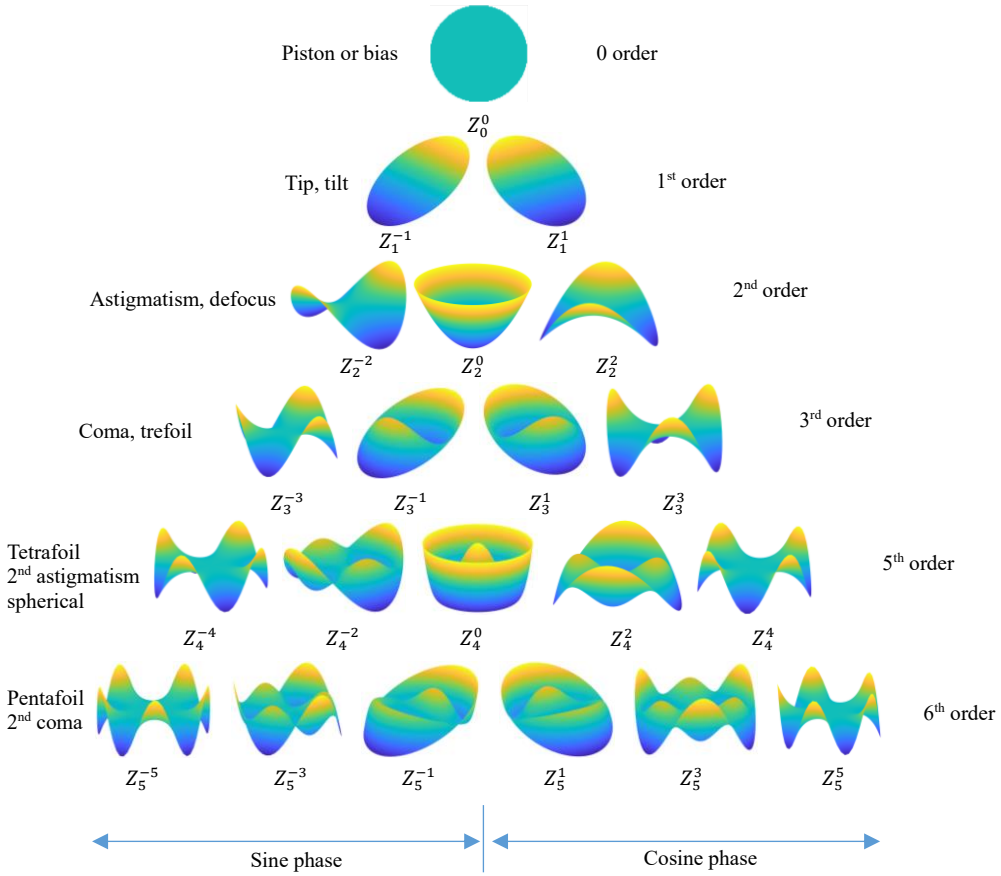

Fig. 2.13 Surface plots of the Zernike polynomial sequence up to 6 orders. The name of the classical aberration associated with some of them is also provided.

2.6 Centroiding techniques

The centroiding techniques to estimate the position of the spots are the key to accurate wavefront measurement. The wavefront is analyzed by measuring, in real-time, the displacements of the centroids of those spots, which are directly proportional to the local wavefront slopes averaged over sub-apertures. Therefore, a reasonable estimation of the wavefront distortion is obtained from a good measurement of the spot positions [99][100]. In this section, three centroiding techniques commonly used in Shack Hartmann wavefront sensing are discussed: Thresholding Centre of Gravity (TCoG) [100], Weighted Centre of Gravity (WCoG) [101], and Iteratively Weighted Centre of Gravity (IWCoG) [102].

2.6.1 Thresholding Centroid of Gravity

The basic centroiding algorithm applied to the sub-image *I* of each sub-aperture is the Center of Gravity (CoG) algorithm, which can be written as:

$$CoG(I_{sub}) = \left(\frac{\sum_{x,y} x \cdot I(x,y)}{\sum_{x,y} I(x,y)}, \frac{\sum_{x,y} y \cdot I(x,y)}{\sum_{x,y} I(x,y)} \right) \tag{2.25}$$

Theoretically, $CoG(I_{sub})$ precisely gives the position of the spot centroid when noise is absent. However, the noise of the detector cannot be neglected. Usually, a threshold $I_{threhold}$ is applied on the sub-image I_{sub} to mitigate the background noise. The threshold value for each sub-image can be determined by:

$$I_{threshold} = [\max(I_{sub}) - \min(I_{sub})] * \eta_{threshold} \tag{2.26}$$

where $\max(I_{sub})$ is the maximum intensity of the sub-image, $\min(I_{sub})$ is the minimum intensity of the sub-image, and $\eta_{threshold}$ is the threshold ratio which is determined by the noise level. Usually, $\eta_{threshold}$ can be set < 10%. Therefore, the Thresholding Centre of Gravity (TCoG) can be written as:

$$CoG(I_{sub}) = \left(\frac{\sum_{x,y} x \cdot (I(x,y) - I_{threshold})}{\sum_{x,y} I(x,y)}, \frac{\sum_{x,y} y \cdot (I(x,y) - I_{threshold})}{\sum_{x,y} I(x,y)} \right) \tag{2.27}$$

2.6.2 Weighted Centre of Gravity

The Weighted Centre of Gravity (WCoG) idea is to give weight to the different pixels depending on their intensities. The contribution of the noisy pixels with minimal signal – outside the core of the spot – is attenuated but not eliminated. The WCoG algorithm can be described as

$$WCoG(I_{sub}, I_0) = \left(\frac{\sum_{x,y} xI(x,y)\, F_w(x,y)}{\sum_{x,y} I(x,y) F_w(x,y)}, \frac{\sum_{x,y} yI(x,y)\, F_w(x,y)}{\sum_{x,y} I(x,y) F_w(x,y)} \right) \tag{2.28}$$

where $F_w(x,y)$ is a weighting function. It is used to damp the side pixels on which there is little of no intensity. We can simply specify a circular window of radius r, $F_w(x,y) = 1$ for $\sqrt{x^2 + y^2} < r$, or square window. Other weighting function, such as the Gaussian weighting function, was introduced to improve the performance of the centroid algorithm, as shown in the literature [103][104]. The WCoG method exists in two versions. The weight $F_w(x,y)$ can either be fixed or recentred on the spot, like thresholding.

2.6.3 Iteratively Weighted Centroiding

Based on the conventional Weighted Centre of Gravity technique, an Iteratively Weighted Centroiding (IWC) technique has been introduced to mitigate the deleterious effects of noise. For a WCoG with a Gaussian weighting function, the process can be iteratively applied to refine the location of the centroid of the Gaussian and minimize the noise.

The weighting function $G_w(x,y)$ can be expressed as:

$$G_w(x,y) = \frac{1}{2\pi\pi^2} e^{-\frac{1}{2\sigma^2}(x-x_c)^2} e^{-\frac{1}{2\sigma^2}(y-y_c)^2} \tag{2.29}$$

where σ is the standard deviation. x_c and y_c are the center of the spot. Eq. (2.29) results in a normalization over all space of unity [102]. The various position moments, up to second order,

can be written as:

$$S_w = \sum_{x,y} I(x,y)G_w(x,y) \tag{2.30}$$

$$S_x = \sum_{x,y} x \cdot I(x,y)G_w(x,y) \tag{2.31}$$

$$S_y = \sum_{x,y} y \cdot I(x,y)G_w(x,y) \tag{2.32}$$

$$S_{xx} = \sum_{x,y} x^2 \cdot I(x,y)G_w(x,y) \tag{2.33}$$

$$S_{yy} = \sum_{x,y} y^2 \cdot I(x,y)G_w(x,y) \tag{2.34}$$

where S_w, S_x, S_y, S_{xx} and S_{yy} represent the different moments of the lenslet spot pattern. The average location of the centroid can be simply written as:

$$x_c = S_x/S_w\,, y_c = S_y/S_w \tag{2.35}$$

For a Gaussian spot, the RMS deviation of position from the mean corresponds to the weighted $(x-x_c)^2 + (y-y_c)^2 = \sigma^2$ or

$$\sigma = \left(\frac{1}{S_w}\right)\sqrt{S_{xx}S_w - S_xS_x + S_{yy}S_w - S_yS_y} \tag{2.36}$$

Eq. (2.29) ~ (2.36) form the basis for the IWC algorithm in which the centroid location and the FWHM of the weighting function can be adaptively changed [102].

In addition, using higher-order moments of the intensity pattern provides an estimation of the FWHM of the Gaussian, which can also be iterated upon along with the centroid of the Gaussian. By allowing the iterative process to occur, however, the algorithm can mitigate the deleterious effects of noise and is ideally suited for use in open-loop applications where the Hartmann spots are far from their unaberrated positions [102].

2.7 Wavefront control technologies

A standard Adaptive optics system utilizes a device capable of controlled phase alteration, such as a deformable mirror, and a controller for such a device. Control algorithms, which need some sort of data feed to perform phase correction, are applied to the controller to drive the deformable mirror (DM) properly. In the AO system developed in this work, the homemade Shack Hartmann wavefront sensor provides the data feed. In this section, several wavefront control technologies have been investigated.

2.7.1 Influence functions measurement

Prior to the control loop, the DM needs to be characterized and calibrated to obtain the control matrix for controlling its surface. Calibration of the deformable mirror is necessary when

implementing an adaptive optics system. During the AO system's calibration procedure, the deformable mirror's properties are characterized by measuring each influence function (IF), which is the characteristic shape produced when a unit control signal is applied to each electrode of all the actuators of the deformable mirror [105].

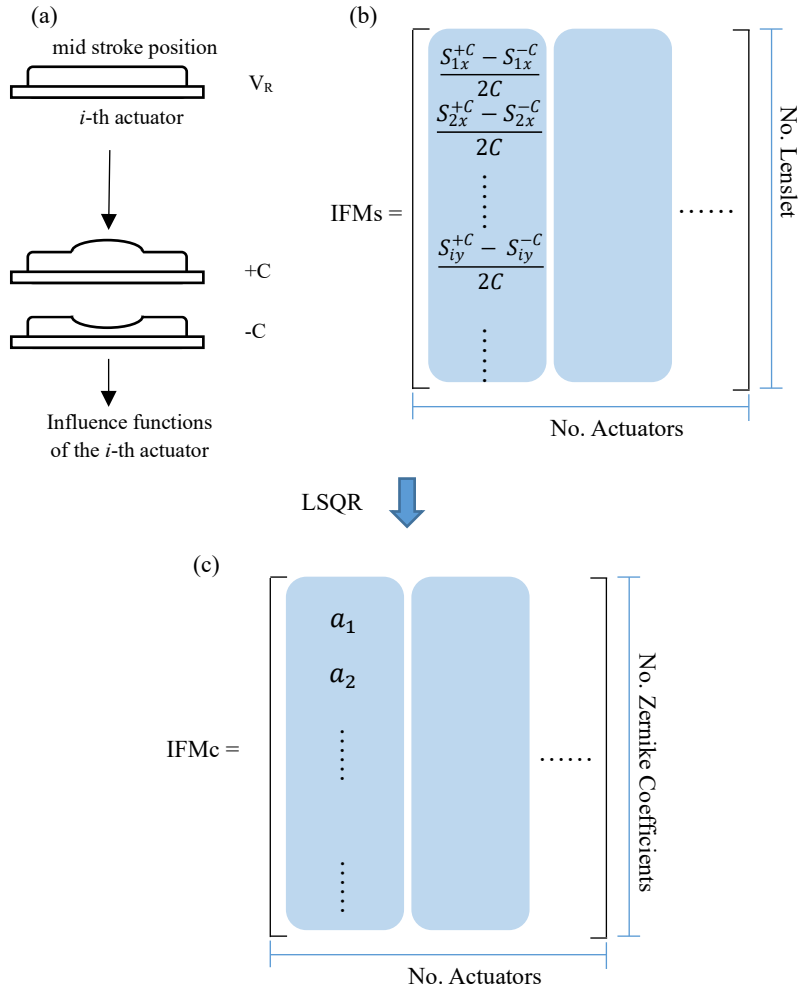

Fig. 2.14 Calibration procedure of the AO system. (a) The positive and negative voltage is applied to each actuator while the reference voltage is applied to the rest actuators. Then the change in the wavefront after applying voltages is measured by SHWFS to obtain the change in slopes or Zernike coefficients per unit control signal, which is the Influence Functions Matrix (IFM) element. Each column of the IFM is the influence function of each actuator. (b) The row of IFMs is the slope of each Zernike aberration mode. (c) A least square method (LSQR) is applied to the IFMs to obtain the Influence Functions Matrix in terms of Zernike coefficients IFMc.

For a piezoelectrically-actuated deformable mirror, the displacement is proportional to the applied voltage onto the actuator, and so does the control signal. Before starting the IF measurement, the DM is set to its mid-stroke position by applying a reference voltage V_R (V_{max} + V_{min})/2, where V_{max} and V_{min} are the maximum and the minimum appliable voltages of the piezoelectric actuator, to all actuators of the DM. This permits the movement of the mirror surface both toward and away from the mid-stroke position. There are two commonly used characterizing methods [106], as shown in Fig. 2.14, for obtaining the Influence Functions Matrix (IFM) of the DM based on different control algorithms, such as zonal control and modal control,

discussed in the next section.

During the characterizing procedure, the control signal set to each actuator is increased and then decreased to poke the actuator positively and negatively relative to the mid-stroke control signal while the other actuators are still set at the mid-stroke position. Then the change in slopes or Zernike polynomial coefficients per unit control signal for modal control can be calculated. The Method I results in Influence Functions Matrix in terms of slopes (IFMs) as shown in Fig. 2.14(b). The element E of the first half of the IFMs is given by:

$$E_{x,IFMs} = \frac{S_{ix}^{+C} - S_{ix}^{-C}}{2C} \tag{2.37}$$

The element E of the second half of the IFMs is given by:

$$E_{y,IFMs} = \frac{S_{iy}^{+C} - S_{iy}^{-C}}{2C} \tag{2.38}$$

where *i* is the lenslet number, S_{ix}^{+C} and S_{ix}^{-C} are the slopes in the x-direction for the *i*-th lenslet when a positive or negative control signal, C, is applied relative to the reference control signal (corresponding to the reference voltage), respectively. The same is true for the y-direction. This process is repeated multiple times for each actuator to obtain an average value of each element of the **IFMs**.

By applying the least square fitting method with the pseudo-inverse of the reconstruction matrix (Eq. 2.12) on the **IFMs**, the Influence Functions Matrix in terms of Zernike coefficients, ***IFMc***, can be calculated as:

$$\boldsymbol{IFMc = B \cdot IFMs} \tag{2.39}$$

Once the influence functions matrix has been obtained, the control matrix, $\boldsymbol{CM = IFM^{+}}$, which is the pseudo-inverse of the **IFM** (including **IFMs**, and **IFMc**). The pseudo-inverse can be obtained using the singular value decomposition (SVD) method [107]. Since the wavefront can be considered the sum of orthogonal Zernike polynomials, the correction capability of the system can be considered as the sum of orthogonal system modes, which result from the SVD of the **IFM**. The system modes are equal in number to the number of actuators. The IFM can be decomposed into three matrices:

$$\boldsymbol{IFM = US_g V^T} \tag{2.40}$$

where the rows of $\boldsymbol{V^T}$ represent mode in actuator space. They can be thought of as mirror modes. The columns of **U** represent the modes as seen by the sensor. The column vector will be a column vector of slopes if the IFMs are used. The column vector will be a column vector of Zernike coefficients if **IFMc** is used. The singular value in the matrix $\boldsymbol{S_g}$ link the modes together. Therefore, the pseudo-inverse IFM^{+} can be calculated as:

$$\boldsymbol{IFM^{+} = V S_g^{-1} U^T} \tag{2.41}$$

Eq. (2.41) shows that the singular values are inverted to become the mirror modes. Small singular values lead to large mirror modes. Therefore, large control signals are required to produce the corresponding mirror mode. However, a large control signal will saturate the

actuator of the DM, i.e., the control signals will reach or exceed their maximum allowed value. In order to avoid saturation of the actuator, those modes can be removed from the final calculation of the control matrix by setting the corresponding gains to zero [108]. The calibrated DM can then be operated in the control loop.

2.7.2 Zonal and modal control

There are two main wavefront controlling or correction approaches: zonal control and modal control. In the zonal control approach, the wavefront is directly and locally corrected using the **IFMs**. The wavefront correction is done in parallel on each sub-aperture of the WFS and/or actuator of the WFC. With the zonal approach, the control signal vector, $\boldsymbol{C}$, for controlling the DM can be calculated directly from the measured slope vector $\boldsymbol{S}$ as:

$$\boldsymbol{C} = (\boldsymbol{IFMs}^{+})\boldsymbol{S} \tag{2.42}$$

The zonal control algorithm is also called the direct slope control algorithm. It is the most direct and flexible method of wavefront control in AO. It allows modifying the control law to accommodate operating conditions and hardware status variations. Zonal control has the advantage of avoiding mode aliasing or cross-coupling [109] in wavefront reconstruction since its objective is to minimize the local slope vector. It also has a relatively good tolerance to small misalignments between the lenslet and the actuators due to the self-calibrating process of measuring the IFMs [110].

The second approach is modal control, which aims to adjust the deformable mirror to the desired wavefront. In the case of modal control, the control signal vector can be written as:

$$\boldsymbol{C} = (\boldsymbol{IFMc}^{+})\boldsymbol{c} \tag{2.43}$$

By substituting Eq. (2.12) and Eq. (2.39) into Eq. (2.43), then it can be rewritten as:

$$\boldsymbol{C} = (\boldsymbol{IFMs}^{+})\boldsymbol{Ac} \tag{2.44}$$

where $\boldsymbol{A}$ is the reconstruction matrix, as mentioned in Section 2.2. With a modal control algorithm, we can control or correct the wavefront with only the set of desired modes by keeping the desired Zernike coefficients and setting the rest to zero in the vector $\boldsymbol{c}$. Modal control has the advantage of allowing the system to control some specific modes.

Usually, the piston mode does not affect the image quality but merely represents a shift in the image location. It can free up the available stroke of the DM for use with the remaining aberrations by not correcting the piston mode. When controlling the DM using a zonal control algorithm, these modes are easily removed by removing the average slopes from the measurements in the x and y directions. When modal control algorithm is used to control DM, the corresponding coefficients can simply be set to zero.

2.7.3 Closed-loop and open-loop control

Various system control techniques have been developed for AO, such as feedback, feedforward [111], and sensorless control. This section focuses on feedback control, usually referred to open-loop control and closed-loop control [112].

The wavefront sensor is placed before the DM in an open-loop control system. Fig. 2.15(a) shows the scheme and block diagram of the open-loop control system. The wavefront sensor measured the wavefront aberration before the DM corrected it. The control signal vector can be calculated by:

$$\boldsymbol{C} = (\boldsymbol{IFM}^{+})\boldsymbol{W} \tag{2.45}$$

where $\boldsymbol{W}$ is the wavefront mode. It could be $\boldsymbol{S}$ in the case of zonal control or $\boldsymbol{c}$ in the case of modal control. The open-loop system is simple and stable but without the benefit of feedback signals.

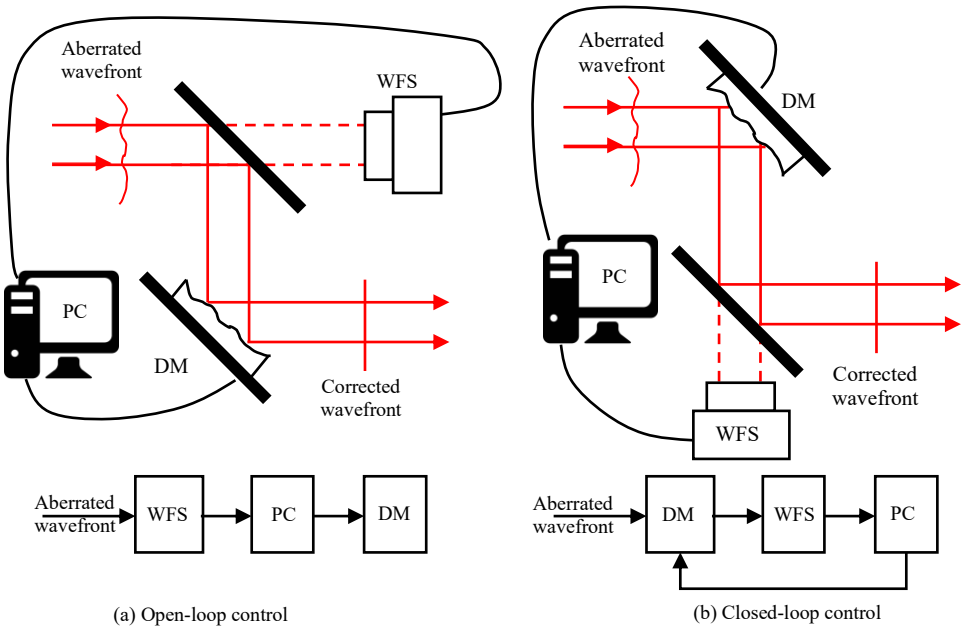

Fig. 2.15 (a) Open-loop control system, (b) Closed-loop control system.

In the closed-loop control, the wavefront sensor is placed after the DM and measures the wavefront aberration after correcting it. Fig. 2.15(b) shows the scheme and block diagram of the closed-loop control system. The closed-loop operation allows the AO system to minimize the residual wavefront aberration. The control signal vector can be simply calculated by:

$$\boldsymbol{C_{new}} = \boldsymbol{C_{current}} + g(\boldsymbol{IFM}^{+})\boldsymbol{W} \tag{2.46}$$

where $\boldsymbol{C_{new}}$ is the new control signal vector sent to the DM, $\boldsymbol{C_{current}}$ is the current control signal vector, g is the gain which is a value between 0 and 1 to limit oscillations in the mirror surface.

The closed-loop control algorithm increases the system accuracy and reduces the sensitivity

of the ratio of the output to input due to variations in system characteristics. It can also sense and correct the nonlinearity in the response of individual DM actuators and their hysteresis characteristics. Compared to the open-loop control system, the closed-loop control system may increase the complexity and cost of the system. However, the closed-loop control system can provide more accurate wavefront correction than the open-loop control system since any non-linearities in the movement of the deformable mirror surface could be inherently compensated [106].

Chapter 3 Thin Disk Laser

Abstract: Since the invention of laser in 1960 by Theodore H. Maiman [113], the world has benefited from its rapid development. Ultrafast pulsed lasers, such as picosecond and femtosecond lasers, have opened new avenues in various fields, such as material processing, biology, chemistry, and spectroscopy research. Research interests in increasing the laser power, repetition rate, pulse energy, and shortening the laser pulse duration have attracted numerous researchers globally. Many fundamental concepts of high-power laser systems have been developed to achieve the goals mentioned above in the past decades, such as solid-state laser, thin disk laser, regenerative amplifier [114], multi-pass amplifier [115], and chirped pulse amplification (CPA) [116].

In this chapter, chirped pulse amplification and thin disk laser technology will be introduced. The principle of regenerative amplification is introduced in the case of thin disk lasers. Rate equations for thin disk regenerative amplification have been introduced, followed by the analytical expression of Amplified Spontaneous Emission (ASE) in a thin disk gain medium. Various kinds of pulse stretching and compressing techniques are introduced at the end of this chapter.

3.1 Chirped pulse amplification

In amplification for ultrashort optical pulses, the optical peak intensity in the amplifier is very high, so detrimental nonlinear effects or destruction of the gain medium or optics may occur in such a situation. In 1985, Gerard Mourou and Donna Strickland developed the Chirped Pulse Amplification (CPA) [116] technique at the University of Rochester's Laboratory for Laser Energetics (LLE). The CPA technique paved the way for more compact and precise high-intensity laser systems.

As shown in Fig. 3.1, the initial ultrafast pulse (e.g., a few hundreds of femtoseconds) is chirped and temporally stretched to longer duration (e.g., hundreds of picoseconds or few nanoseconds) by pulse stretcher, such as Grating pair, prism pair, Chirped Fiber Bragg Grating (CFBG). The stretched pulses are then sent through the optical amplifier, such as a regenerative and stand-wave amplifier. The nonlinear effects in the gain medium or nonlinear medium (such as BBO) during the amplification can be reduced since the long pulse duration reduces the peak

power. After amplification, the amplified pulses are sent to a dispersive compressor (e.g., Grating pair), which removes the chirp of the pulses. The pulse duration is then compressed to a duration similar to the input pulse duration.

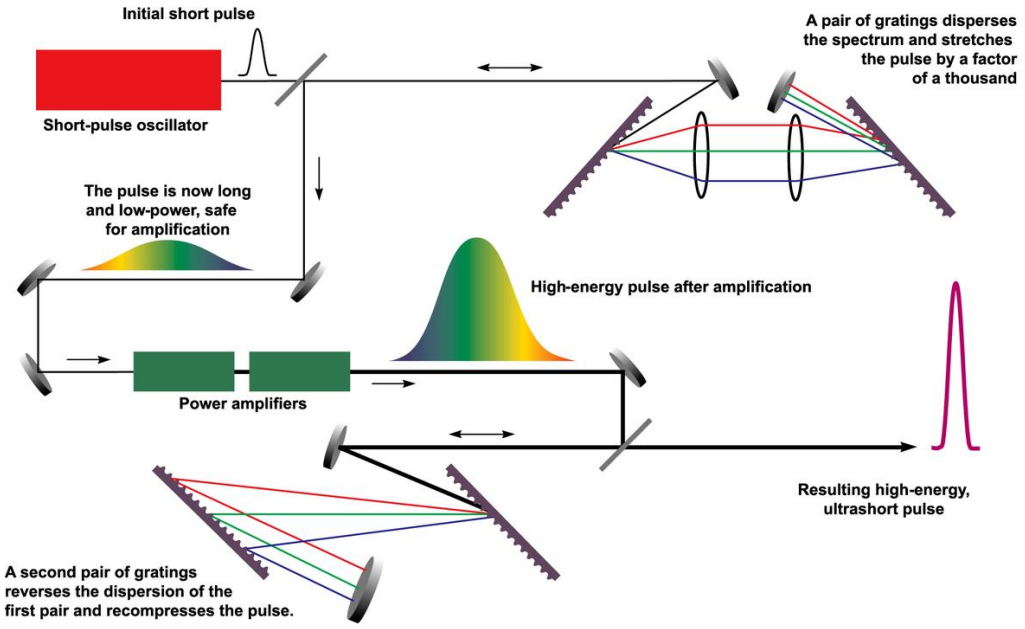

Fig. 3.1 Principle of chirped pulse amplification (CPA) [117].

3.2 Thin disk laser concept

A thin disk laser, invented by A. Giesen and coworkers in 1994 [118] at the Institut für Strahlwerkzeuge (IFSW) of the University of Stuttgart, is a kind of diode-pumped solid-state laser that utilizes a thin gain medium with a typical thickness of 100 ~300 μm. Fig. 3.2 shows the principle of the thin disk laser concept. The gain medium is a thin crystalline disk bonded to a heat sink. The rear side of the disk is highly reflective (HR) coated for both the laser wavelength and the pump wavelength. The pumping optics is designed for a multi-pass transit of the pump beam through the disk to achieve sufficient pump absorption. The thickness of the disk is considerably smaller than its diameter (> 5 mm), which allows the heat generated in the medium to be extracted in the longitudinal direction, which minimizes the thermal lens effect of the disk [119]. Due to the large surface-to-volume ratio, efficient heat dissipation can be achieved, thus allowing operation at extremely high-volume power densities in the medium (up to 1 MW/cm³ absorbed pump power density) [117]. In addition, the temperature gradients are mainly coaxial to the disk surface, thus causing only weak thermal lensing and depolarization loss.

The thermal lens effects are reduced by more than one order of magnitude compared with rod laser systems. The stress-induced birefringence is further reduced and can be neglected for real laser systems. Therefore, stable operation and high beam quality can be achieved over a wide range of pump powers [120].

Since the invention of the thin disk laser technology, the trivalent ytterbium-doped laser materials, such as Yb:YAG and Yb:LuAG, have been widely used as the gain medium for high-power thin disk laser. Thanks to their unique energy structure of Yb^{3+} ion with only two energy level manifolds ($^2F_{7/2}$ and $^2F_{5/2}$), there is no excited-state absorption or up-conversion losses in the medium, although quenching processes can take place for high doping concentrations above 15 at. %.

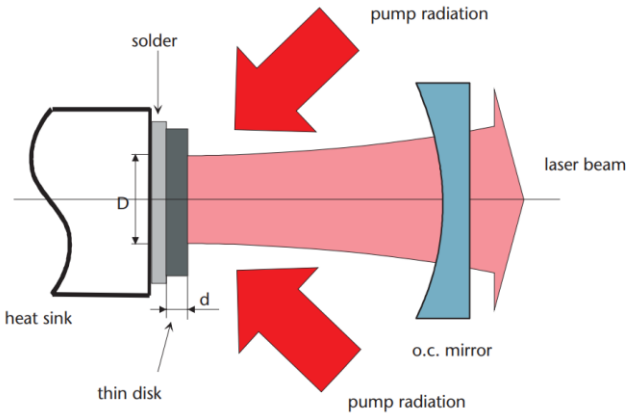

Fig. 3.2 Principle of thin disk laser [121].

However, the levels in both manifolds are much separated, and the thermal population of the higher levels is not negligible. This quasi-three-level behavior of the Yb^{3+} doped medium exhibit a small quantum defect of 5%~9% (depending on the pumping wavelength), which refers to the fact that the energy of a pump photon is generally higher than that of a laser photon, and the energy difference is lost to heat but requires higher pumping intensity for efficient laser emission at room temperature [122] [123] to overcome the reabsorption at the laser wavelength. Thanks to the advantages of Yb:YAG, such as its hardness, high thermal conductivity, and relatively high emission cross-section, it has become the workhorse for high-power ultrafast thin disk lasers or amplifiers for decades.

3.3 Thin disk regenerative amplification

A regenerative amplifier, based on an electronically controlled optical switch (such as Pockels cell, acousto-optic switch) and allows any amplifications to pass through the gain medium, is widely used to amplify low energy level pulses from a mode-locked laser (seed). It can amplify an input seed pulse of only a few nanojoules to multiple millijoules level with a gain greater than 106, even for a thin disk laser with a low single pass gain.

The typical thin disk regenerative amplifier with a linear cavity is shown in Fig. 3.3. The common features of this type of regenerative amplifier cavity are the thin film polarizer (TFP), the quarter-wave plate (QWP), the Pockels cell (PC) and a Faraday rotator (FR) accompanied with a half-wave plate (HWP) to separate the input and output beams. A thin disk is used as the

gain medium, which is CW or pulsed pumped.

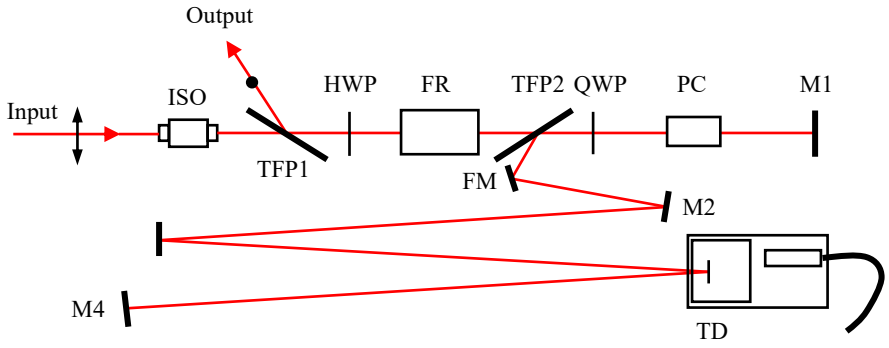

Fig. 3.3 A typical thin disk regenerative amplifier with a linear cavity. The double arrow at the input indicates the horizontal polarization of the seed laser beam. The dot at the output indicates vertical polarization. ISO: optical isolator, TFP: thin film polarizer, HWP: half-wave plate, FR: Faraday rotator, QWP: quarter-wave plate, PC: Pockels cell, M1 ~M4: cavity mirrors, FM: flat mirror, TD: thin disk module.

The operation of such a regenerative amplifier can be explained by distinguishing three operating phases [124]:

(1) ***Pump phase.*** The energy is stored in the TD gain medium during this phase. The voltage of the Pockels cell is set to zero. Thus, laser action is prevented by the QWP and the end mirror (M1) combination, which causes a 90° rotation of the polarization of the seed beam. The horizontally polarized seed pulse from an oscillator passes through the isolator, and the first thin film polarizer (TFP1), experiences a 45° rotation at the HWP, which is then compensated by FR. Therefore, the horizontally polarized seed pulse is injected into the cavity after passing through TFP2. After passing through the QWP and PC with zero voltage, it is reflected by the end mirror M1, then passes through the PC and QWP for the second time. The pulse is rotated again now vertically polarized. It is reflected off the TFP2 and completes one round trip. It is again reflected off by the TFP2 and passes the QWP, the PC, and M1. The pulse is then horizontally polarized when it arrives at TFP2 and passes through TFP2. It experiences a 45° rotation at the FR and a further 45° at the HWP. The TFP1 reflects the now vertically polarized pulse. In a typical thin disk regenerative amplifier configuration, the average power ratio at the output with and without the pump source turned on is the small-signal four-pass gain due to two reflections at the TD in one round-trip.

(2) ***Amplification phase.*** In order to trap a pulse in the cavity for amplification, a λ/4 voltage is applied to the PC as soon as it leaves the QWP after being reflected by the end mirror M1 with vertical polarization and injected into the cavity. It takes around 5 ~ 8 ns to apply the voltage from zero to the voltage required for λ/4 rotation in PC. After applying a λ/4 voltage on the PC, the PC compensates for the polarization rotation caused by QWP. Therefore, the pulse returning from the cavity with vertical polarization non longer experiences a polarization rotation and stays in the cavity. During this phase, the

following pulses from the oscillator no longer experience a polarization rotation for the same reason. They are ejected from the amplifier after reflecting by the end mirror M1. The trapped pulse is amplified to the desired energy during some time, called build-up time. The build-up time is usually more than 100 ns for a thin disk regenerative amplifier with a small single-pass gain.

(3) ***Cavity dump phase.*** After multiple round trips in the cavity, the pulse energy reaches a maximum due to gain saturation. The PC is set to zero voltage in this phase when the pulse leaves the PC. On its last return from the cavity, the pulse experiences a 90° polarization rotation. The horizontally polarized pulse is then ejected through TFP2. The amplified pulse experiences another 90° polarization rotation after passing through the FR and HWP as before and is reflected by the TFP1 to the output port of the amplifier.

3.3.1 The rate equation for pulse amplification

A set of coupled rate equations describes the dynamic behavior of a laser or amplifier with reasonable precision. The longitudinal and radial variations of the radiation within the laser medium are ignored by using a single set of rate equations [124]. In this section, the implementation of pulse amplification is introduced.

The population inversion during the pumping phase can be written by [125]:

$$\frac{dN_2}{dt} = \frac{1}{\hbar\omega_p}\eta_{abs}\frac{I_p}{d} - \frac{N_2}{\tau_f} \tag{3.1}$$

where η_{abs} is absorption efficiency of the pump photons, N_2 is the upper-state level density, $\hbar\omega_p$ is the photon energy of the pump light, I_p is the pump light intensity, d is the thickness of the thin disk, τ_f is the upper state lifetime. The second term is the effect of spontaneous emission, while the first term describes the storage of pump energy. The absorption and saturation effects are considered in the parameter of absorption efficiency η_{abs}, which is written by:

$$\eta_{abs} = 1 - \exp\left[-M_p d\left(\sigma_{abs,p}N_{dop} - \left(\sigma_{abs,p} + \sigma_{em,p}\right)N_2\right)\right] \tag{3.2}$$

where M_p is the number of pump passes on the disk, $\sigma_{abs,p}$ and $\sigma_{em,p}$ are the material's absorption and emission cross-sections at the pump wavelength. N_{dop} is the doping concentration of Yb:YAG material. The small signal gain coefficient can be written by:

$$g = N_2\left(\sigma_{em,l} + \sigma_{abs,l}\right) - N_{dop}\sigma_{abs,l} \tag{3.3}$$

where the $\sigma_{em,l}$ and $\sigma_{abs,l}$ are emission cross-section and absorption cross-section at the laser wavelength, respectively. The seed pulses are coupled into a cavity to extract the stored energy. With the input energy of the seed laser pulse E_{in} and output energy E_{out}, the amplification process can be described by:

$$E_{out} = E_{in} \cdot \sqrt{1 - L} \cdot \exp(g \cdot d) \tag{3.4}$$

where L is the loss factor, which is introduced to describe all losses due to many optics and the

diffraction loss of the regenerative cavity. Then the population inversion after amplification N_2' can be described by:

$$N_2' = N_2 - \frac{(E_{out} - E_{in})}{\hbar\omega_l \cdot d \cdot \pi \left(\frac{D_{pump}}{2}\right)^2} \tag{3.5}$$

where $\hbar\omega_l$ is the photon energy of the laser light, D_{pump} is the diameter of the pump spot. The term $d \cdot \pi \left(\frac{D_{pump}}{2}\right)^2$ in the denominator indicates the volume of the pumped part of the thin disk. The second term on the right-hand side of Eq. (3.5) indicates the reduction of the population inversion due to the extraction of stored energy. N_2' then becomes the initial value in Eq. (3.1) for amplifying the next pulse. The pulse amplification process for the regenerative amplifier can be implemented by repeating this iteration process of Eq. (3.1) ~ (3.5).

3.3.2 Amplified Spontaneous Emission

In the thin disk gain medium, the luminescence or fluorescence from spontaneous emission can be amplified to high power levels when traveling through the excited area of the disk due to the large aspect ratio, which leads to a high possibility of total internal reflection (TIR) and longer propagating optical length in the medium, as shown in Fig. 3.4. The amplified luminescence is called Amplified Spontaneous Emission (ASE), which is one of the major deleterious effects limiting scaling of thin disk lasers [126]. ASE decreases the population inversion in the excited area and limits the energy stored in the thin disk. In extreme cases, such as the edge of the disk causing optical feedback, it can lead to parasitic lasing in the transversal direction and deplete the population inversion even more. The ASE effect is more vital for a quasi-three-level laser gain medium than for a four-level medium.

To avoid ASE, some techniques have been proposed, such as the anti-ASE cap [127][128], which reduces the optical path length in the exited area of the thin disk by suppressing TIR, wedged edge, or cladding the edge [129] of the thin disk which reduced the possibility of optical feedback for parasitic lasing. In principle, ASE leads to additional loss terms in the rate equations. It can be included in Eq. (3.1), and thus it can be rewritten as:

$$\frac{dN_2}{dt} = \frac{1}{\hbar\omega_p}\eta_{abs}\frac{I_p}{d} - \frac{N_2}{\tau_f} - \frac{N_2}{\tau_{ASE}} \tag{3.6}$$

where τ_{ASE} is the ASE lifetime, derived for fast evaluation of ASE, including such effects as reflections of ASE from the boundaries of the gain medium and Lorentzian stimulated emission line shape [130].

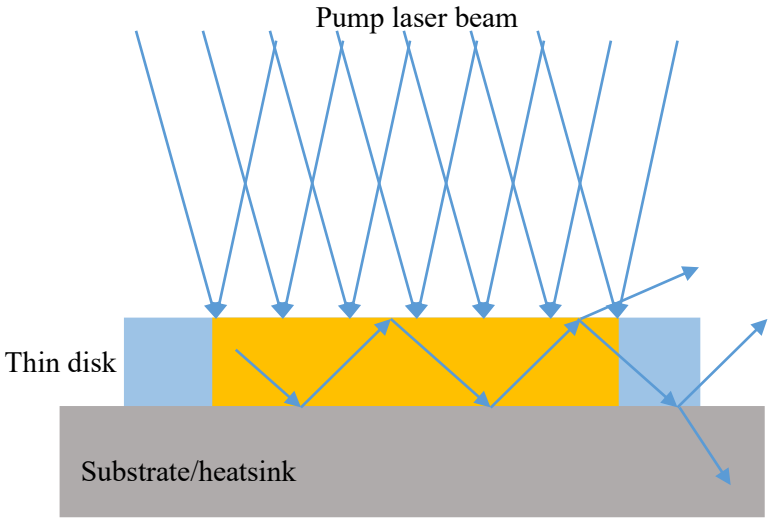

Fig. 3.4 Principle of Amplified Spontaneous Emission (ASE) in thin disk medium. A spontaneously emitted photon gets amplified when traveling through the excited area of the thin disk.

Drew A. Copeland [131] has derived an approximate analytical expression for evaluating the ASE loss rate in a thin disk. The basic idea of this approach is shown in Fig. 3.5. The ASE flux at every "observation" point, emitting from the "source" point in the volume dV, is computed. All the ASE flux at the observation point from all possible points in the laser medium are added to calculate losses of population inversion in the upper-level manifold. Based on this approach, the last two terms of Eq. (3.7) can be merged by introducing an effective upper-level lifetime term τ_{eff}, as written by:

$$\frac{1}{\tau_{eff}} = \frac{1}{\tau_f}\left[1 + \kappa\beta\left\{e^{\frac{1}{2}\beta}\left(I_0\left(\frac{1}{2}\beta\right) - I_1\left(\frac{1}{2}\beta\right)\right) + \int_{\frac{1}{2}\beta}^{\frac{1}{2}\beta\chi} dy \frac{1}{y} e^{y} I_0(y)\right\}\right] \tag{3.7}$$

where

$$\beta = \frac{1}{2} g(\alpha_d d) \qquad \chi = \sqrt{\left(\frac{\alpha_R R}{\frac{1}{2}\alpha_d d}\right)^2 + 1} \tag{3.8}$$

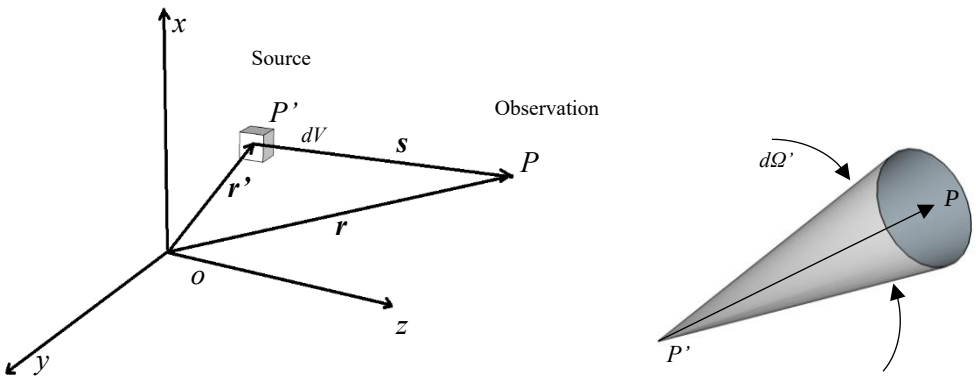

Fig. 3.5 The geometry for computing the ASE flux [126].

While α_R and α_d are radial and height reflective factors, $\alpha_R R$ and $\alpha_d d$ indicates the most extended radial and height paths due to total internal reflection. Due to the geometry of the thin disk, the values of α_R and α_d can be replaced by α for simplicity in our mode. For a standard thin disk without an anti-ASE cap, α can be varied around 2 [132]. The reflective factor will be investigated in detail in the near future for more accurate simulation. $R=D/2$ is the radius of the pumped region of a thin disk in this case, $I_0(x)$ and $I_1(x)$ are modified Bessel functions of the first kind with orders of 0 and 1. ASE effect then is considered by replacing τ_f in Eq. (3.1) with τ_{eff}.

The numerical model is built based on this approach. The results are presented at the conference of *Photonics Devices and Systems VII* [133]. The detail of the results will be discussed in Chapter 6.

3.4 Pulse stretchers and compressors

Various methods exist for temporally compressing an ultrashort laser pulse, i.e., reducing the pulse duration. These methods can be classified into two categories: linear pulse compression and nonlinear pulse compression. Nonlinear pulse compression requires increasing the optical bandwidth with a nonlinear interaction such as self-phase modulation (SPM), leading to chirped pulses. Then the pulse duration can be strongly compressed by linear compression which removes or decreases the chirp. The nonlinear methods fall outside the scope of the work presented in this thesis; therefore, it is not discussed.

The temporal chirp of a laser pulse is usually defined as the time dependence of its instantaneous frequency. A laser pulse can acquire a chirp, e.g., during propagation in a transparent medium, because of chromatic dispersion and nonlinearities. A positively chirped pulse means that the shorter wavelength components in its spectrum lag behind the longer wavelengths during propagation [134], while a negatively chirped pulse is the other way around. The pulse duration of a chirped pulse is longer than the original pulse, and its intensity is reduced accordingly, as shown in Fig. 3.1. By removing or at least reducing the chirp, the pulse duration can be reduced or compressed is also called de-chirping. De-chirping can be accomplished by sending the pulses through an optical element with suitable chromatic dispersion. Various optical components can provide dispersion compensation, such as a pair of diffraction gratings [135-136], a prism pair [137], an optical fiber, a chirped mirror, a chirped fiber Bragg grating (CFBG) [138], or a chirped volume Bragg grating (CVBG) [139]. In this section, three widely used pulse stretching and compressing methods are discussed in this section: chirped volume Bragg grating (CVBG), chirped fiber Bragg grating (CFBG), and grating pairs.

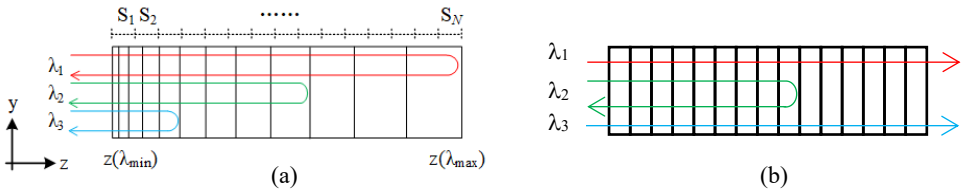

Fig. 3.6 (a) Chirped volume Bragg grating, $\lambda_1>\lambda_2>\lambda_3$. (b) uniform volume Bragg grating (Bragg mirror). Spatial modulation is not in scale.

(1) **CVBG**. Fig. 3.6 shows a chirped volume Bragg grating and a uniform volume Bragg grating (VBG).

A uniform volume Bragg grating (Fig. 3.6(b)) is a phase volume hologram produced by recording the interference pattern of two collimated beams in a photo-thermo-refractive glass [140-141], resulting in a spatial refractive index modulation in it. The modulation, which acts as grating, provides resonant diffraction of a laser beam propagating inside the volume Bragg grating if the Bragg conditions are satisfied [142,143,144]

$$\theta_m = \frac{\lambda}{2n\Lambda} \tag{3.9}$$

where θ_m is the angle inside the PTR glass between a plane of constant refractive index and the direction of beam propagation λ is the wavelength, n is the average refractive index, and Λ is the grating period. If the VBG is positioned as shown in Fig. 3.6(b), it is defined as a reflecting Bragg grating or a Bragg mirror. The laser beam meets the Bragg conditions and can be reflected while the rest propagates through it.

If the interference pattern is produced by interfering a divergent beam with a convergent beam, the grating periods Λ will gradually change in the Z-direction perpendicular to a bisector of the recorded beams. The period varies linearly in the Z-direction only when the convergence and divergence angles are equal. Thus, it can be called chirped reflecting volume Bragg grating, as shown in Fig. 3.6(a). The spectral chirp rate (SCR) can be written as:

$$SCR = \frac{d\lambda}{dz} = 2n\frac{d\Lambda}{dz} \tag{3.10}$$

where $d\Lambda/dz$ is the chirp rate of the grating period, and z is the length along the propagating direction. The total spectral width of a CVBG can be written as:

$$\Delta\lambda = SCR \times T \tag{3.11}$$

where T is the thickness of CVBG along the Z-direction. Different spectral components of a laser pulse would be reflected from a different section of the CVBG. Thus, the total delay time (the maximum compressing) t_s between different spectral components corresponding to the front and back surface of a CVBG can be written as:

$$t_s = \frac{2nT}{c} \tag{3.12}$$

where n is the average refractive index of the CVBG, and c is the speed of light. This delay time determines the temporal delay dispersion (TDD) or group delay dispersion (GDD) of the

CVBG:

$$GDD = \frac{t_s}{\Delta\lambda} = \frac{2n}{cSCR} \tag{3.13}$$

GDD is commonly used for designing a CPA system with a dimensionality of ps/nm. For a given SCR, the GDD for a CVBG recorded in PTR glass with n = 1.5 can be estimated as:

$$GDD, \left[\frac{ps}{nm}\right] = \frac{100}{SCR, [nm/cm]} \tag{3.14}$$

The CVBG can provide a different sign of GDD just by reversing its orientation in the beam path, which means it can be used as a stretcher and compressor, providing almost the exact value of GDD with opposite signs. The CVBG is much compacter than other stretchers or compressors for solid-state CPA systems, and it can be simultaneously used as the stretcher and compressor in one CPA system [141, 145].

(2) **CFBG**. Similar to CVBG, the chirped fiber Bragg grating (CFBG) consists of a quasi-periodic modulation of the refractive index along an optical fiber created by exposing the fiber to UV light interference fringes. Since the laser pulse propagates perpendicular to the length of the optical fiber, the Bragg condition for a uniform fiber Bragg grating (FBG, as shown in Fig. 3.7) can be written as:

$$\lambda_B = 2n\Lambda \tag{3.15}$$

where n is the average refractive index of the fiber. λ_B is called the Bragg wavelength of the uniform FBG. The uniform FBG is also considered a Bragg mirror.

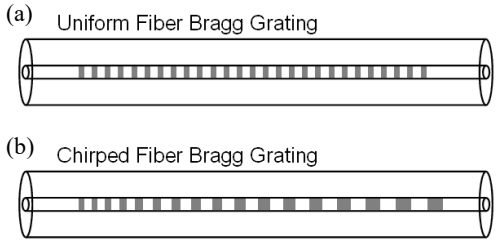

Fig. 3.7 (a) Structure of the refractive index change in a uniform fiber Bragg grating, and (b) chirped fiber Bragg grating.

However, for a CFBG, the Bragg wavelength monotonously varies with position in the fiber, which can be written as:

$$\lambda_B = 2\Delta n\Lambda \tag{3.16}$$

where Δn is the change of the refractive index of the CFBG along the Z axis. It can be written as [146]:

$$\Delta n = \Delta\bar{n}\left[1 + v\cos\left(\frac{2\pi}{\Lambda}z + \varphi(z)\right)\right] \tag{3.17}$$

where $\Delta\bar{n}$ is the average value of the effective refractive index change of the fiber grating core in each grating period; v is the visibility of the refractive index change fringe, which is generally a constant of 0.5 or 1; z is the position in the fiber along the Z-axis; $\varphi(z)$ is the phase of the refractive index change or the chirp of the grating, which can be simplified as $\varphi(z) = C_g z$ with the chirp rate C_g [147]. More detail can be found in the literature [147,148]. Eq. (3.12)

and Eq. (3.13) can still be applied for calculating the time delay or GDD of the CFBG.

(3) **Grating pairs**. Grating-based pulse stretchers and compressors are also used to provide positive or negative dispersion. In a CPA system, the dispersions of the stretcher and compressor must cancel out each other. Because of practical considerations, such as the damage threshold of the gratings, the high-power compressor is usually designed to provide negative dispersion, and the low-power stretcher is therefore designed to provide positive dispersion. Fig. 3.8(a) shows typical designs of Treacy-type compressor [149] providing negative dispersion and Martinez-type stretcher [150,151,152] providing positive dispersion. The GDD introduced by grating pairs, such as the Treacy-type compressor, can be written as:

$$GDD = \frac{d^2\varphi}{d\omega^2} = -\frac{m^2\lambda^3 L_g}{2\pi c^2 \Lambda^2} \cdot \left[1 - \left(-m\frac{\lambda}{\Lambda} - \sin\theta_i\right)^2\right]^{-3/2} \tag{3.18}$$

where m is the diffraction order (usually -1), L_g is the distance between the two parallel gratings and θ_i is the angle of incidence on the first grating. The negative dispersion introduced by this type of compressor can be fine-tuned by adjusting the distance L_g.

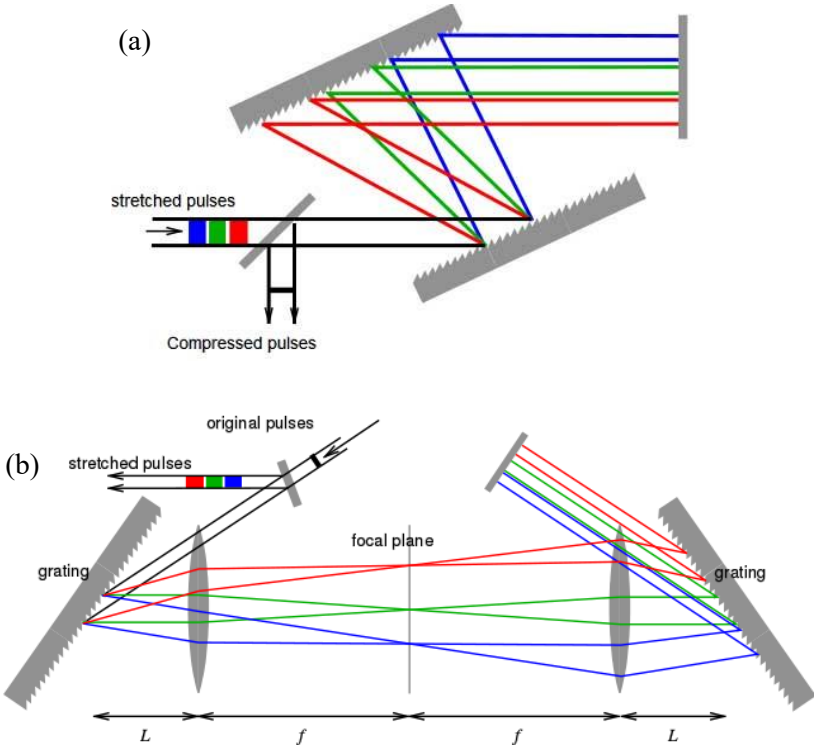

Fig. 3.8 Schematic layouts of (a) the Treacy-type compressor and (b) the Martinez-type stretcher [153].

The Martinez-type grating stretcher involves a focusing lens with the same focal length, *f*, forming a telescope of 1:1 magnification between the two gratings, as shown in Fig. 3.8(b). The lenses are placed at a distance of 2*f* from each other and a distance of *L* from the gratings. In the case of $L < f$, the stretcher provides positive dispersion, Eq. (3.18) can be used with a negative distance L for calculating the positive GDD. In the case of $L > f$, it provides negative dispersion as the Treacy grating compressor, Eq. (3.18) can be directly used for this case. In the

case of $L = f$, it can be used as a pulse shaper [154] with no additional dispersion provided.

3.5 Mid-IR Optical Parametric Amplification

Optical parametric amplification (OPA) is a phenomenon where an optical signal can be amplified using a parametric nonlinearity [155], which is optical nonlinearity with an instantaneous response based on the second-order or third-order nonlinearity of a medium [156], and a pump wave. It transfers photon energy from a fixed frequency pump wave to variable frequency signal photons and the same number of so-called idler photons using second-order nonlinearity in most cases [155] [157] [158] [159]. The energy difference between the photon energies of the pump and signal wave is converted to the photon energy of the idler wave; therefore, the conversion of the pump energy into signal and idler waves is almost 100%, and there is no heat generated in the nonlinear crystal during the process [155].

A simple sketch of the OPA process is shown in Fig. 3.9. In the case of higher pump frequency than the signal and idler frequencies, the energy conversion can be expressed as

$$\hbar\omega_p = \hbar\omega_s + \hbar\omega_i \quad \text{or} \quad \frac{1}{\lambda_p} = \frac{1}{\lambda_s} + \frac{1}{\lambda_i} \tag{3.19}$$

where $\hbar\omega_p$, $\hbar\omega_s$, $\hbar\omega_i$ and λ_p, λ_s, λ_i are the photon energy and wavelengths of the pump, signal, and idler waves, respectively [160]. In addition to energy conversion, the OPA process can be efficient when the phase-matching condition $\Delta\vec{k} = \vec{k}_p - \vec{k}_s - \vec{k}_i = 0$ is satisfied [160], as indicated in Fig. 3.10, where $\vec{k}_p$, $\vec{k}_s$, and $\vec{k}_i$ are the wave vectors of the pump, signal, and idler waves, respectively. Usually, a birefringent nonlinear medium with uniaxial or biaxial optical properties is exploited to fulfill the phase-matching condition. Therefore, the OPA process requires spatial and temporal overlapping signal and pump waves.

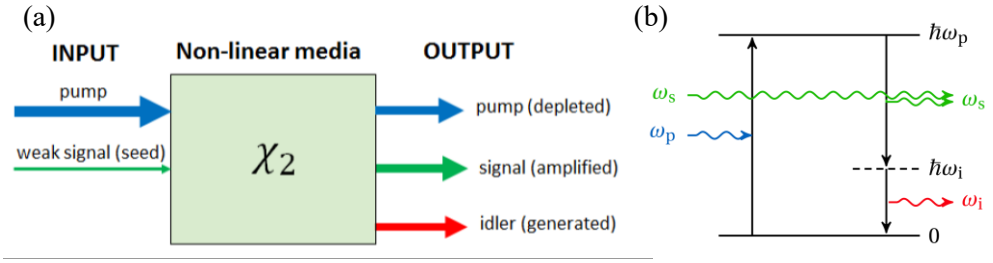

Fig. 3.9 (a) Power flow from the pump wave to signal and idler waves in optical parametric amplification; (b) The OPA process is viewed as stimulated emission of signal and idler photons from a virtual level excited by the pump [161]. ω_p, ω_s, and ω_i are the frequencies of the pump, signal, and idler waves, respectively. $\hbar$ is Planck's constant.

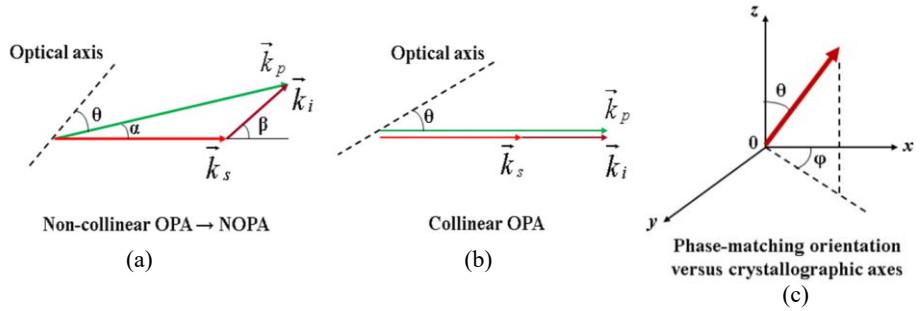

Fig. 3.10 (a) Phase-matching for a non-collinear OPA; (b) Collinear OPA; (c) Phase matching direction versus crystallographic axes [162].

From the laser beam propagation point of view, OPA processes usually can be divided into two types: non-collinear and collinear OPAs, as shown in Fig. 3.10. In the case of non-collinear OPA (NOPA), the phase matching condition is a vector equation which can be rewritten as two scalar equations (Eq. (3.20)) by the projection on two orthogonal axes, as shown in Fig. 3.10(a).

$$\begin{aligned} \frac{n_p(\lambda_p,\theta)}{\lambda_p}\sin\alpha - \frac{n_i(\lambda_i)}{\lambda_i}\sin\beta = 0 \\ \frac{n_p(\lambda_p,\theta)}{\lambda_p}\cos\alpha - \frac{n_s(\lambda_s)}{\lambda_s} - \frac{n_i(\lambda_i)}{\lambda_i}\cos\beta = 0 \end{aligned} \tag{3.20}$$

where α is the angle between the signal and pump waves, θ is the angle between the pump wavevector and the crystal optical axis, β is the angle between the signal and idler wavevectors, and n_p, n_s, and n_i are the refractive indexes of the pump, signal and idler waves in the nonlinear medium, respectively [162]. Note that non-collinear configuration adds one more degree of freedom for optimizing and tuning the OPA process.

In the case of collinear phase matching, $\alpha = 0$, $\beta = 0$, then the phase matching condition becomes scalar equations (Fig. 3.10(b)). Eq. (3.20) can be rewritten as:

$$\frac{n_p(\lambda_p,\theta)}{\lambda_p} - \frac{n_s(\lambda_s)}{\lambda_s} - \frac{n_i(\lambda_i)}{\lambda_i} = 0 \tag{3.21}$$

By substituting Eq. (3.19) into Eq. (3.21), one can obtain the following:

$$\frac{n_p(\lambda_p,\theta) - n_i(\lambda_i)}{\lambda_p} = \frac{n_s(\lambda_s) - n_i(\lambda_i)}{\lambda_s} \tag{3.22}$$

In a particular case that $n_p(\lambda_p,\theta) - n_i(\lambda_i) > 0$ and $n_s(\lambda_s) - n_i(\lambda_i) < 0$, Eq. (3.22) has no solution. This indicates that the phase-matching condition cannot be fulfilled in an isotropic medium with positive dispersion. The same conclusion also holds in an isotropic medium with negative dispersion [160]. Two approaches are usually used to solve this problem: exploit birefringence by propagating the beam with different polarizations or apply periodic modulation to the sign of the nonlinear coefficient, which is called the quasi-phase-matching (QPM) technique [163].

OPA has some advantages, such as (1) scalability to high power levels, (2) tunability of broadband amplification bandwidth and wavelength, (3) high amplification gain over a short distance, (4) good temporal contrast in the signal beam, and (5) small heat load of the nonlinear

medium. All these advantages of short-pulse-pumped OPA require an efficient, reliable, and powerful pump source, which is required to deliver high-energy near-1-ps pulses with near-diffraction-limited beam quality at repetition rates in the kHz to MHz range [164]. In recent years, high-power mid-IR OPAs [165] have attracted much attention as next-generation sources for attosecond science [166] or high harmonic generation [167]. To fulfill the requirements of pump sources with high power, high energy, and high performance for such applications, Yb-doped lasers in thin-disk geometries, which can deliver high-energy, high average power pulses with ps-pulse duration [168], are widely used for pumping mid-IR OPAs [169] [170].

Chapter 4 Design of Adaptive Optics System

Abstract: Tachyon 16K camera is selected as the detector in this work. The design aspects of the mid-IR Shack-Hartmann wavefront sensor are introduced in Section 4.1, followed by the algorithm for real-time wavefront measurement in Section 4.2. This work uses a typical closed-loop control to correct the wavefront error. It is introduced in Section 4.3, including the deformable mirror (DM) selected as the wavefront corrector, the algorithm for DM influence function measurement, and the algorithm for the closed-loop control. At the end of this chapter, the user interface of the wavefront control software developed with MATLAB App Designer is introduced in Section 4.4.

4.1 Design of the Shack-Hartmann wavefront sensor

4.1.1 TACHYON 16K camera

Tachyon 16k camera, which uses Vapor Phase Deposition (VPD) PbSe FPA sensor [171], from New Infrared Technologies (NIT) company [172], is selected as the detector for mid-IR radiation. VPD PbSe FPA detector is monolithically integrated with the corresponding Si-CMOS circuitry. The main advantage of using the VPD PbSe technology is using large sensor size and complex substrates. The camera is shown in Fig. 4.1. The main parameters of this camera are listed in Table 4.1.

Fig. 4.1 Tachyon 16K camera for detecting mid-IR wavelength in the range of 1 – 5 μm.

Table 4.1 Main parameters of TACHYON 16K camera

Detector type	VPD PbSe FPA
FPA format	128 x 128 pixels
Pixel size	50 μm (square format)
Dimension of sensor	6.4 x 6.4 (mm)
Spectral range	Mid-IR 1μm ~ 5 μm
Peak Wavelength of detection	3.7μm
Frame rate (max.)	2000 fps (full resolution)
Cooled housing	Air-cooled housing
Color type	Monochrome

There are many advantages of the VPD PbSe FPA sensor. It combines all the main requirements demanded for volume-ready technology [173]:

1. Fully compatible with plain Si substrates
2. Compatibility with existing Si CMOS technology
3. Compatibility with low-cost packaging
4. Affordable technology
5. Fast imaging
6. Good reproducibility
7. Long term stability
8. Suitable for 2D FPA

The spectral detectivity of VPD PbSe FPA is shown in Fig. 4.2. It is very suitable for detecting mid-IR radiation in the spectral range of from 1 μm to 5 μm.

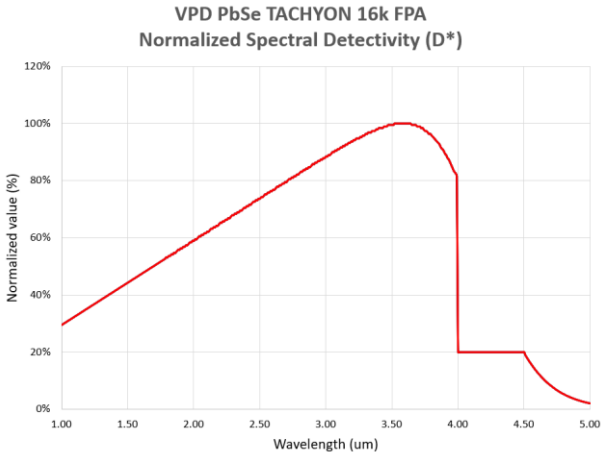

Fig. 4.2 The normalized spectral detectivity of VPD PbSe TACHYON 16K FPA.

4.1.2 Lenslet array

Due to the low spatial resolution of the VPD PbSe FPA, here are some considerations for selecting the proper lenslet array for the mid-IR SHWFS:

(1) the target wavelength is around 2 μm;

(2) the spatial resolution;

(3) the dynamic range, which is the measurable maximum wavefront slope;

(4) the sensitivity, which is inversely proportional to the measurable minimum wavefront slope.

(5) the focal spot diameter of the sub-aperture should be larger than the pixel size (50 μm) to have a detectable focal spot centroid on the sensor.

The main parameters of the selected lenslet array are listed in Table 4.2. Fig. 4.3 shows the internal transmission curves of the IR-grade fused silica.

Table 4.2 Main parameters of lenslet array from Edmund

Type	Lenslet array
Part number	#64 - 467
Type of Optics	Plano-Convex
Lens profile	Spherical
Substrate material	IR Fused Silica
Radius R (mm)	2.35
Thickness (mm)	1.20
Pitch (μm)	300×300
Effective Focal Length (mm)	5.10
Dimensions (mm)	10.0 x 10.0
Wavelength range (nm)	200 – 2200
Coating	uncoated

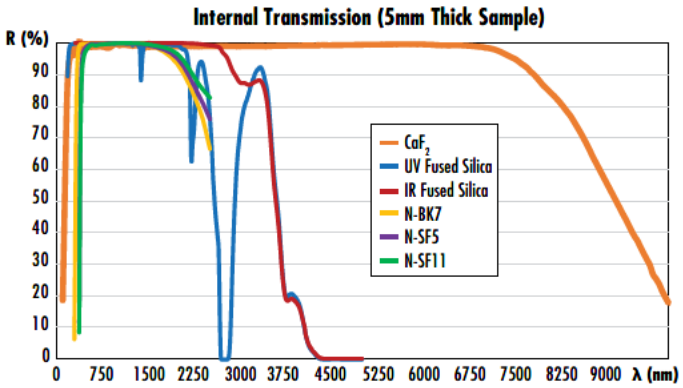

Fig. 4.3 Internal transmission curves for common laser optics materials with no Fresnel reflections [174].

With this lenslet array, the resolution of the SHWFS sub-aperture is 6 × 6 pixels, and the spatial resolution of the SHWFS is 20 × 20 sub-apertures. The total pixels in the active area are 120 × 120 pixels. The Airy disk diameter of the focal spot diameter can be calculated using Eq. (2.1). The focal spot diameter is 54 μm ($1/e^2$) for a 1.94 μm laser beam. The dynamic range calculated by using Eq. (2.2) is 29.4 mrad for λ = 1.94 μm in this design. The minimum detectable wavefront slope, $\theta_{min} = 0.09$ mrad, which is calculated using Eq. (2.3). Typically, d_{min} is determined by the pixel size of the detector and the centroid algorithm. The measurement sensitivity in this work is $1/\theta_{min}$= 1/0.09 mrad^{-1} with a minimum detectable displacement of 0.01 pixel, which is our estimation based on estimations for similar algorithms.

The design and assembly of the mid-IR SHWFS are shown in Fig. 4.4. A mounting tube is designed to mount the lenslet array. The mounting tube also blocks stray light from the environment. A zoom housing (Thorlabs SM1ZM) is used to mount the mounting tube to precisely adjust the distance between the lenslet array and the VPD PbSe FPA sensor. An adaptor (Thorlabs SM1A9) is used to mount the zoom housing to the camera. The camera uses an active cooler for temperature management.

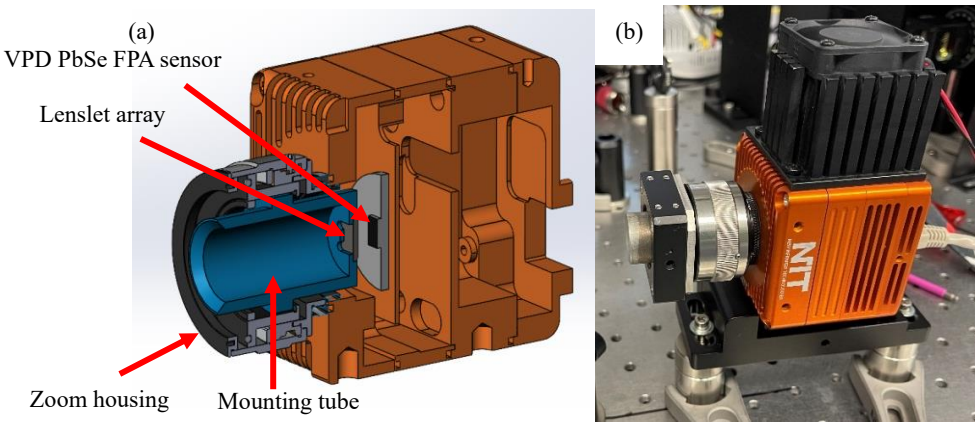

Fig. 4.4 (a) The design of the mid-IR Shack-Hartmann wavefront sensor. (b) Photo of the simple assembly of the homemade mid-IR SHWFS.

4.2 Algorithm for real-time wavefront measurement

The software for the homemade wavefront sensor is developed based on MATLAB App Designer [175]. The algorithm for wavefront measurement is described in the flowchart shown in Fig. 4.5.

When the camera is connected, it is initialized with its default parameters. Once the camera is turned on, one can preview the monochromatic live video stream. It would take about 5 mins to warm up the camera to get a stable thermal noise, a thermal phenomenon resulting from electrons spontaneously generated within the sensor chip without incident light. The thermal noise is mainly dependent on the temperature of the camera. Then the thermal noise image is captured and used in the following image processing procedure. After warming up, the mid-IR laser beam wavefront can be measured.

The image processing procedure will be carried out. A noise filter will be applied to subtract the thermal noise image from the captured Hartmanngram. An absolute reference grid and its centroids (reference centroids) will be generated, assuming an ideal planar wave as a reference wavefront and ideal lenslet array quality for wavefront slope calculation. The MATLAB code for generating the absolute grid and centroids is shown in Appendix 3. A circle will be marked on the captured image to indicate the active area under measurement. The Thresholding Centroid of Gravity (TCoG) algorithm, as introduced in Section 2.5.1, is applied to obtain the centroids of the measured Hartmann-gram.

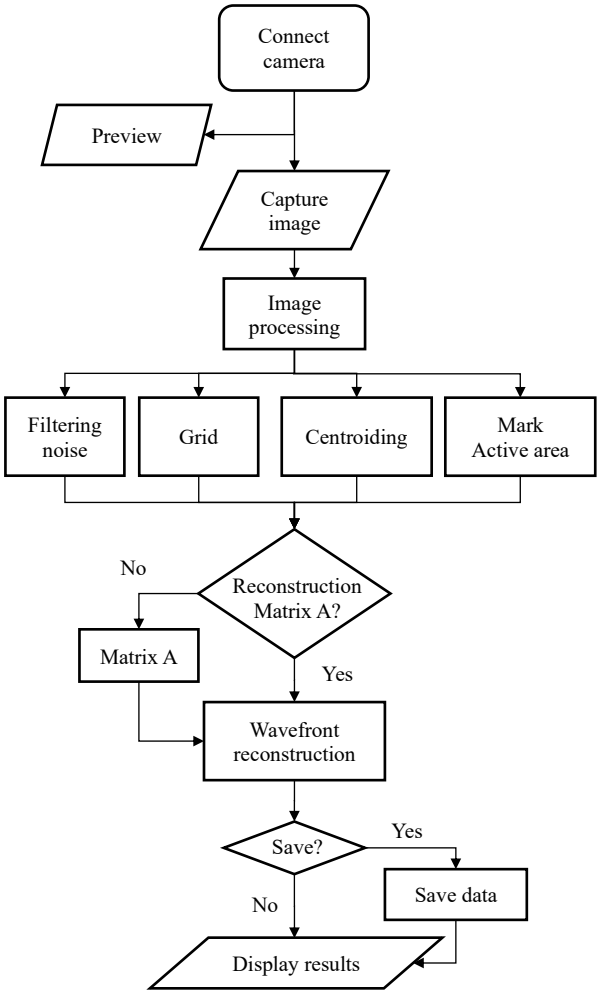

Fig. 4.5 Flowchart of the wavefront measurement algorithm.

The Zernike reconstruction matrix (Matrix A) will be calculated using the reference centroids. In the last step, a modal wavefront reconstruction introduced in Chapter 2.3 will be applied to obtain the wavefront and other data, such as the root-mean-square (RMS) value and peak-to-valley (P-V) value of the wavefront. A 2-dimensional wavefront phase map and a bar plot of the Zernike coefficients are displayed in the user interface, together with the other helpful information. The real-time measurement can be implemented by repeating the procedure from the step of capturing the image to the last step.

In order to speed up the centroiding algorithm, the captured image, after filtering out the

noise, will be divided into 20×20 sub-apertures and saved in a cell whose element consists of 6×6 pixels of each sub-aperture. The detail of the dividing procedure can be found in the reference [176], also cited in Appendix 3 for the reader's convenience. Then the centroiding algorithm will be applied to each cell (sub-aperture) using a single "for…" loop or parallel computing toolbox. The processing time will be reduced from 0.043s with the scanning method for centroiding, which uses two more "for…" loops to scan along both the x- and y-axis of the image, to <0.003 s for one frame.

4.3 Design of the Adaptive Optics system

This work uses a closed-loop control system, as shown in Fig. 4.6, for the mid-IR AO system. The Shack-Hartmann wavefront sensor (SHWFS) measures the incoming wavefront for calculating the control signals sent to the deformable mirror (DM). It provides feedback for the control system, as introduced in Chapter 2.

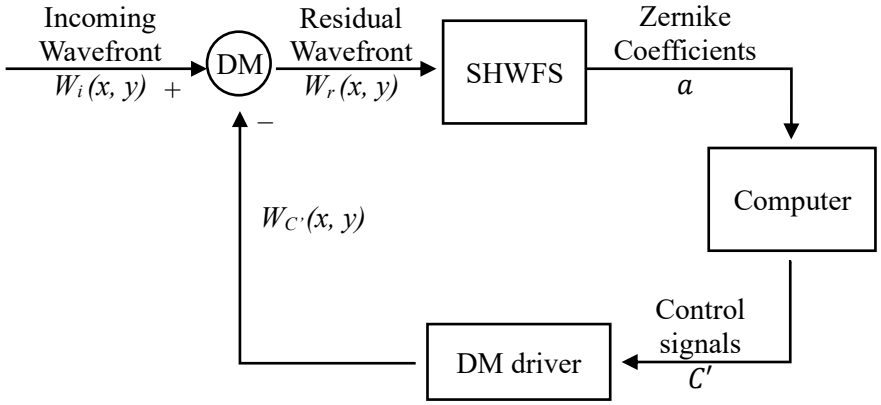

Fig. 4.6 Closed-loop control system for mid-IR AO system.

Table 4.3 Main parameters of the deformable mirror from Dynamic Optics.

Clear aperture size	30 mm
Substrate material	BK10
Coating	Protected Silver
Actuators type	Bimorph
Actuators number	64
Max. actuator voltage	125 V
Min. actuator voltage	-62.5 V
Best flat position voltage	0.06 V

4.3.1 Deformable mirror

Besides the SHWFS, DM is another critical part of the closed-loop control system. A

piezoelectric bimorph deformable mirror from Dynamic Optics is selected as the wavefront corrector in this work. The DM is coated with protected silver coating for wide spectral range applications. A MATLAB driver is provided for controlling DM. The main parameters of the DM are shown in Table 4.3. Fig. 4.7 shows the photo of DM.

Fig. 4.7 The piezoelectric bimorph deformable mirror from Dynamic Optics.

4.3.2 Algorithm for measuring the DM Influence Functions

Before controlling the DM, its Influence Functions, as introduced in Chapter 2, need to be measured. The Algorithm for measuring the DM Influence Functions is shown in Fig. 4.8 following Method III introduced in Chapter 2.

After turning on the wavefront sensor and the deformable mirror, the DM is set to its mid-stroke position by applying reference voltages V_R to all actuators. It can be done by sending a reference command vector $\boldsymbol{C}_{ref}$ to the DM. Then an absolute plane wavefront is generated as the reference wavefront. The reconstruction wavefront matrix A is calculated for wavefront reconstruction or obtaining the Influence Function Matrix in terms of Zernike coefficients. In this work, the mid-stroke position is set when the voltages V_R are set at 31.25 V (reference voltage). After setting the DM at the mid-stroke position, the image containing a Hartmann-gram is captured and saved as $HI_{ref\text{-}pos,}$ which will be used as the reference or background image. Then, a positive voltage V_{pos}(e.g., +100V) is applied to the i-th ($i \in (1:64)$ in this work) actuator by sending a command vector $\boldsymbol{C}_{i\text{-}pos}$ to the DM while the other 64 actuators are still set to the mid-stroke position. A new image is then captured as $HI_{i\text{-}pos}$. By subtracting $HI_{ref\text{-}pos}$ from the $HI_{i\text{-}pos}$, the resulting Hartman-gram $HI'_{i\text{-}pos}$ represents the surface response of the DM while applying a positive voltage to the i-th actuator. Then, the slope vector $\boldsymbol{S}_{i\text{-}pos}$ corresponding to this Hartmann-gram $HI'_{i\text{-}pos}$ can be calculated.

Repeat the same procedure but with a negative voltage V_{neg} relative to the reference voltage V_R for the i-th actuator to obtain the corresponding slope vector $\boldsymbol{S}_{i\text{-}neg}$. Make sure the difference between V_{neg} and V_R should be the same as that between V_{pos} and V_R:

$$V_{pos} - V_R = V_R - V_{neg} \tag{4.1}$$

Therefore, the voltage difference is called the amplitude voltage V_{amp} relative to the reference voltage. The corresponding command value is C_{amp}. Then, the slope response vector per command value $\boldsymbol{S}_i$ for the i-th actuator can be obtained by normalizing the slope changes as:

$$\boldsymbol{S}_i = \frac{(\boldsymbol{S}_{i-pos} - \boldsymbol{S}_{i-neg})}{2 \times C_{amp}} \tag{4.2}$$

Repeat the procedures from step 2 to step 13 in Fig. 4.8 N (N>2) times for the i-th actuator, to obtain the average slope response vector for the i-th actuator:

$$\boldsymbol{S}_{i-avg} = \frac{\boldsymbol{S}_i}{N} \tag{4.3}$$

Repeat the procedures from step 2 to step 14 in Fig. 4.8 for all 64 actuators of the DM, and one can obtain the Influence Functions Matrix in terms of the slope, **IFMs**, as introduced in Section 2.6.1. It should be noted that the impact caused by laser-induced thermal afterimage, which will be introduced and investigated in Section 5.2.2, can be mitigated by repeatedly capturing the reference image whenever mid-stroke voltage is applied to the mirror.

By applying the least square method (LSQR) using Eq. 2.15 and Eq. 2.39 introduced in Chapter 2, one can obtain the Influence Function Matrix in terms of the Zernike coefficients **IFMc**.

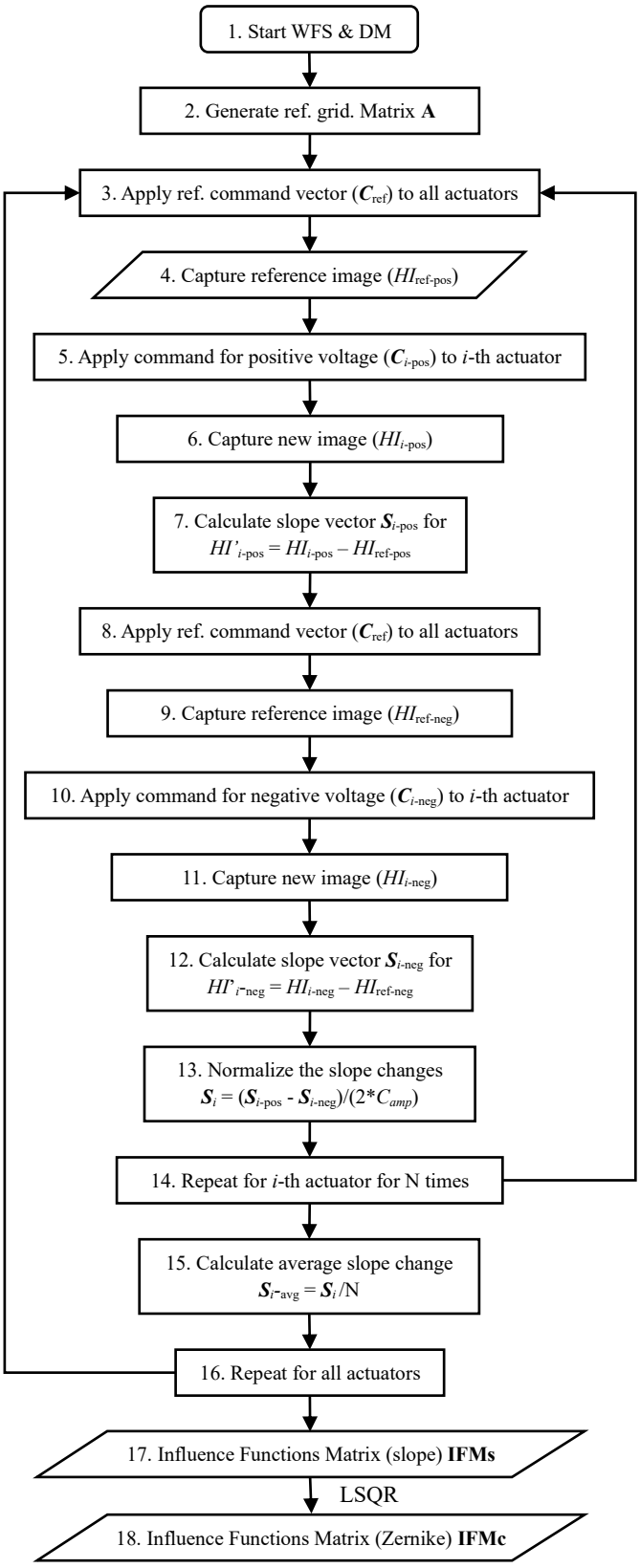

Fig. 4.8 Flowchart of the DM's algorithm for measuring the Influence Functions Matrix.

4.3.3 Algorithm for the closed-loop control

The detailed flowchart of the closed-loop control algorithm is shown in Fig. 4.9. After connecting and activating the wavefront sensor and the deformable mirror, the reference voltage V_R is applied to all actuators by sending a reference command vector $\boldsymbol{C}_{ref}$ to the DM to set the surface of the DM at the mid-stroke position.

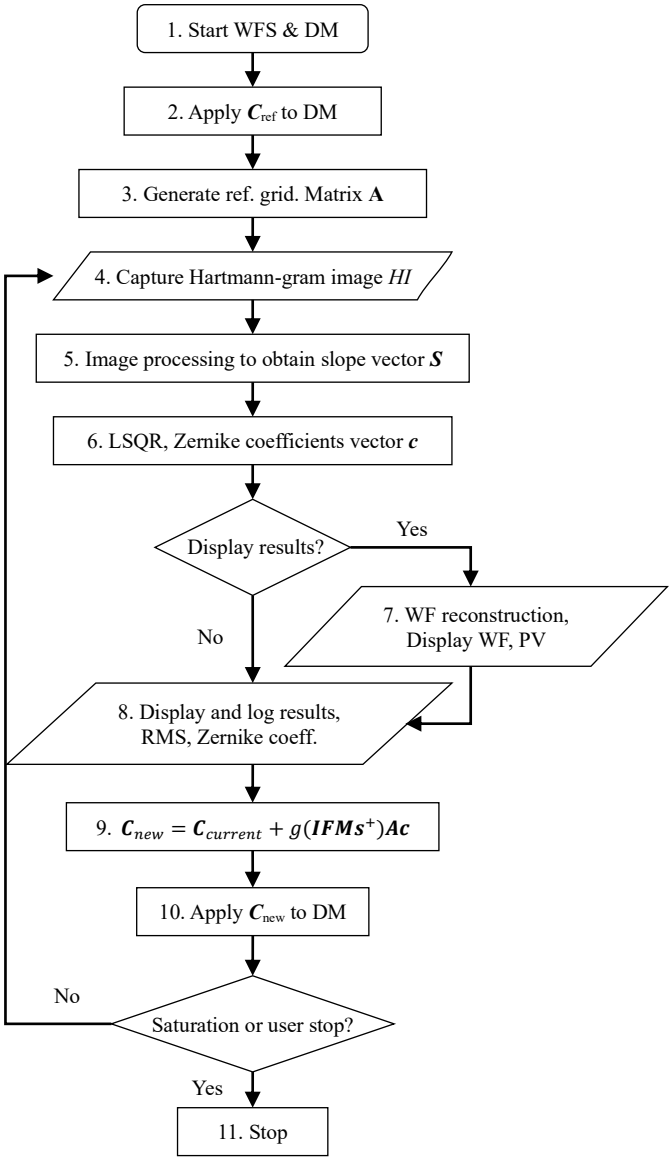

Fig. 4.9 Flowchart of the algorithm for the closed-loop control.

This algorithm assumes an absolute plane wavefront as a reference wavefront. Thus, the reconstruction matrix **A** is calculated. The Hartmann-gram image *HI* is then captured and processed to obtain the slope vector $\boldsymbol{S}$, which will be used to fit the derivatives of the Zernike polynomials to obtain the Zernike coefficients vector $\boldsymbol{c}$ by applying a least square fitting method. Since plotting or surface plotting the results in MATLAB usually slows down the executing speed of the program, a decision can be made by the user whether to display the reconstructed wavefront in real-time or not. If the user decides to display the wavefront, the Zernike

coefficients $\boldsymbol{c}$ will be used to reconstruct the wavefront. The wavefront PV value can be calculated from the reconstructed wavefront. Suppose the user decides not to display the wavefront in real-time. In that case, the Zernike coefficients **c** and the wavefront RMS value can be calculated by calculating the norm of the Zernike coefficients vector $\boldsymbol{c}$ without wavefront reconstruction thanks to the orthogonality of Zernike polynomials [177][178][179][180]. This is one of the main advantages of the Zernike polynomials introduced in Section 2.5. Then the new command vector $\boldsymbol{C}_{new}$ can be calculated from the Zernike coefficients vector and the Influence Functions Matrix IFMs or IFMc obtained during the calibration of the AO system and applied to the DM to compensate for the wavefront distortion. The closed loop will stop if the user stops it or the DM is saturated, meaning any DM actuators reach their limit.

4.4 User Interface of the MATLAB App

The main User Interface of the MATLAB App developed with App Designer is shown in Fig. 4.10. It consists of four parts:

(1) camera setting part (marked by a blue rectangle),

(2) image processing setting part (marked by a green rectangle),

(3) AO controlling part (marked by a red rectangle), the tabs are shown in Fig. 4.11.

(4) Graphical result displaying part (marked by purple polygon).

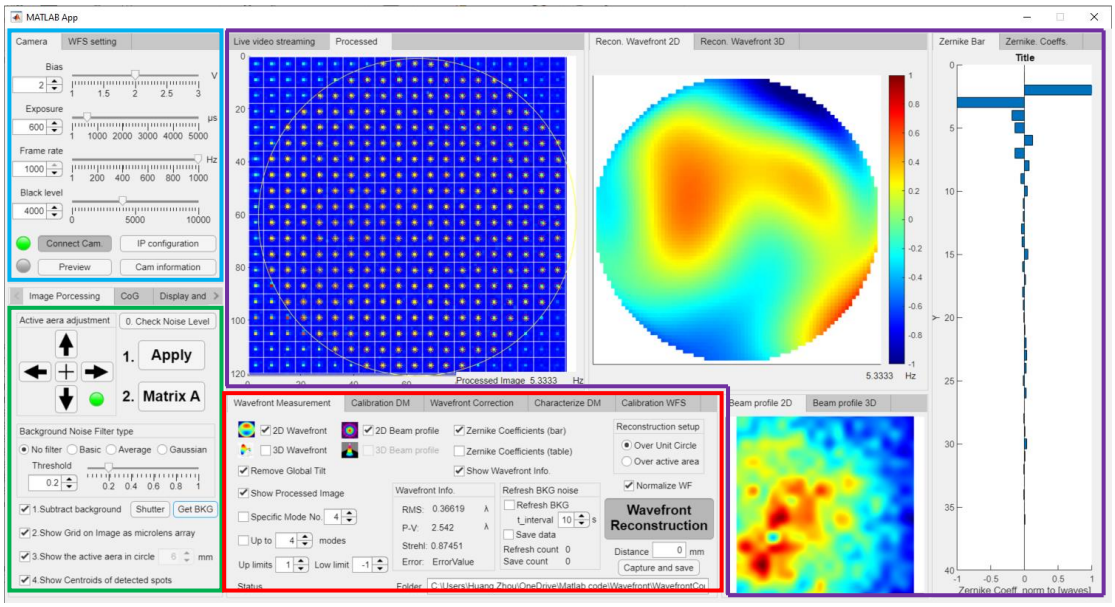

Fig. 4.10 User interface for the wavefront measurement developed with MATLAB App Designer.

The user interface also provides the estimated beam profile for the user's information. A simple method is used to estimate the beam profile. First, sum the intensity value of the 6×6 pixels of each sub-aperture (after filtering the background noise). Then, use the values of each sub-aperture as the elements of an intensity matrix with the size of 20×20. By applying interpolation on the intensity matrix, one can obtain the beam profile, which is not very accurate

but can be used for aligning the AO system. The code for estimating the beam profile can be found in Appendix 3.

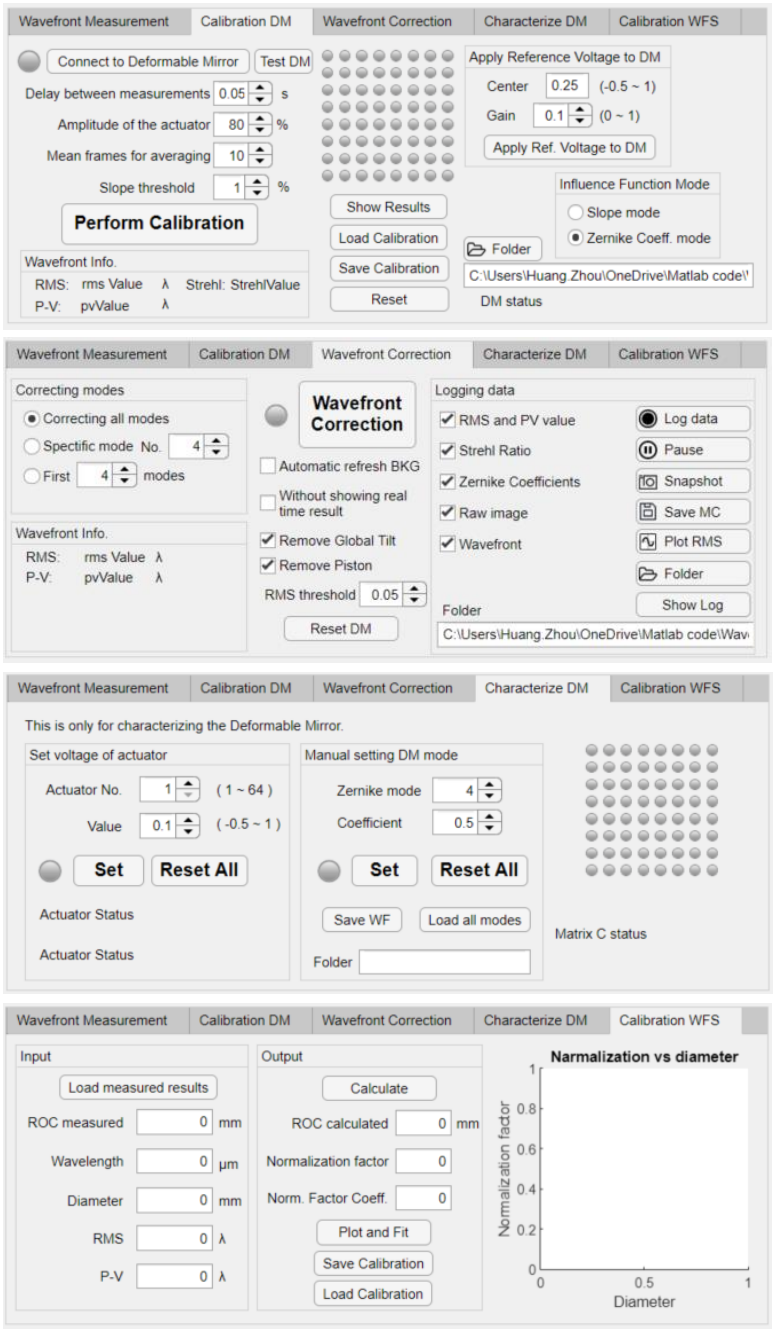

Fig. 4.11 Tabs of the AO controlling part, including “Calibration DM,” where the user can set for DM calibration, “Wavefront Correction,” where the user can start the closed loop to correct the wavefront, “Characterize DM,” where the user can characterize the DM and “Calibration WFS” where user can calibrate the wavefront sensor.

Chapter 5 Wavefront Correction

Abstract: In this chapter, the wavefront reconstructed with my algorithm was verified with the measured wavefront of the commercial wavefront sensor. After verification of the algorithm, the wavefront sensor was calibrated with the absolute calibration method. The thermal properties of the TACHYON 16k camera were studied and improved to get a better signal-to-noise ratio. Laser-induced thermal afterimage of the camera and its impacts on the centroiding and wavefront reconstruction had also been studied. A solution for reducing thermal afterimage has been proposed to minimize the impact.

The deformable mirror was then characterized in the closed-loop control system by measuring its influence functions and reproducing the Zernike modes on the mirror. Wavefront correction experiments were carried out. The results were shown and discussed, followed by the conclusion in the last section of this chapter.

5.1 Calibration of wavefront sensor

5.1.1 Calibration setup

In this section, a calibration setup is designed to calibrate the wavefront sensor with spherical wavefronts [181][182], as shown in Fig. 5.1. The calibration method is called the absolute calibration method and will be introduced in detail in Section 5.1.3. For different measurements, a 1030 nm fiber laser and a 1550 nm fiber laser are used as the optical source (laser 1 in the figure). The maximum power at the single-mode fiber output tip was less than 30mW. In order to minimize the tilt of the wavefront for calibration, it was necessary to align the wavefront sensor precisely. A low-power laser pointer was used as the alignment laser (laser 2 in Fig. 5.1).

First, an alignment laser, a beam splitter, and a flat mirror were used to align the experimental setup. The beam splitter derived the laser beams into two directed beams. The beam splitter was positioned so that one of the beams was precisely positioned at the fiber tip of the fiber laser. The second beam indicated where the center of the sensor should be located. By precisely adjusting the wavefront sensor's position, the alignment laser could be perpendicular to the sensor's surface so that the calibration would be more precise.

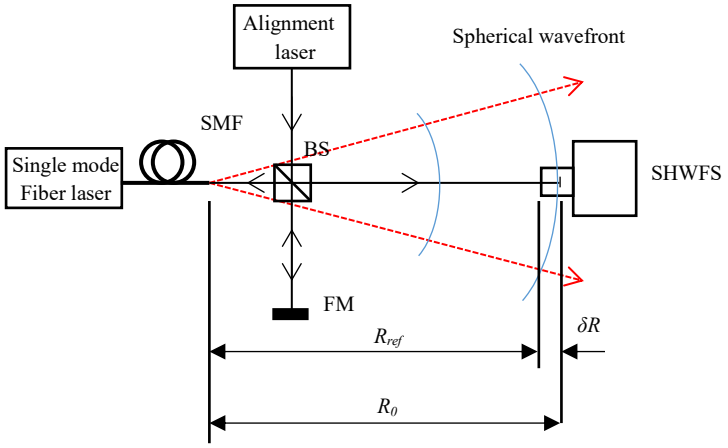

Fig. 5.1 Calibration setup. SMF: single-mode fiber, BS: beam splitter, SHWFS: Shack-Hartmann Wavefront Sensor, FM: flat mirror. R_{ref}: reference radius of curvature of the wavefront, R_0: Actual radius of curvature of the wavefront, δR: the difference between the reference and actual radius of curvature. The blue curves indicate the diverging spherical wave. The red dashed lines indicate the propagating direction of the spherical wave. The alignment laser and BS will be removed during measuring after precise alignment.

5.1.2 Verifying the wavefront reconstruction algorithm

The calibration procedure's first step is verifying the wavefront reconstruction algorithm by comparing the result with that of a commercial wavefront sensor. The wavefront sensor from Dynamic Optics company is used and compared, as shown in Fig. 5.2.

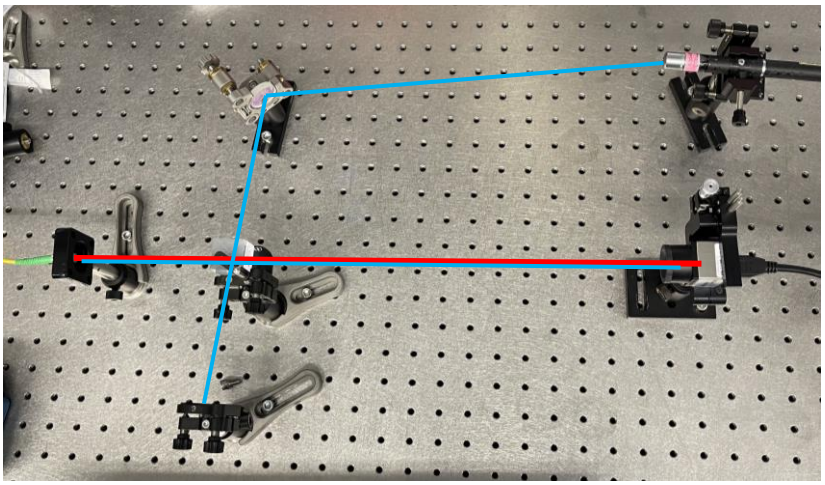

Fig. 5.2 Experiment setup of the spherical wavefront measurement. The beam splitter was removed while measuring the wavefront. Blue lines: alignment beam, red line: 1030 nm fiber laser beam for calibration. (*The alignment laser was not in place when taking photo of the setup*)

According to the spectral detectivity of the NIT TACHYON 16k camera, it should be able to measure the wavefront of the 1030 nm laser beam. However, it was found that the camera had no response to the 1030 nm laser beam. Therefore, the wavefront reconstruction algorithm is verified and calibrated by reconstructing the wavefront of a 1030 nm laser beam from the same Hartman-gram image captured by the Dynamic Optics wavefront sensor.

The experiment setup is shown in Fig. 5.2. A 1030 nm fiber laser is used as the laser source. The beam splitter was removed while measuring the wavefront. Fig. 5.3 shows the captured

Hartmann-gram of the 1030 nm single-mode fiber laser source. Fig. 5.4 shows the snapshot of the PhotonLoop software of the Dynamic Optics wavefront sensor.

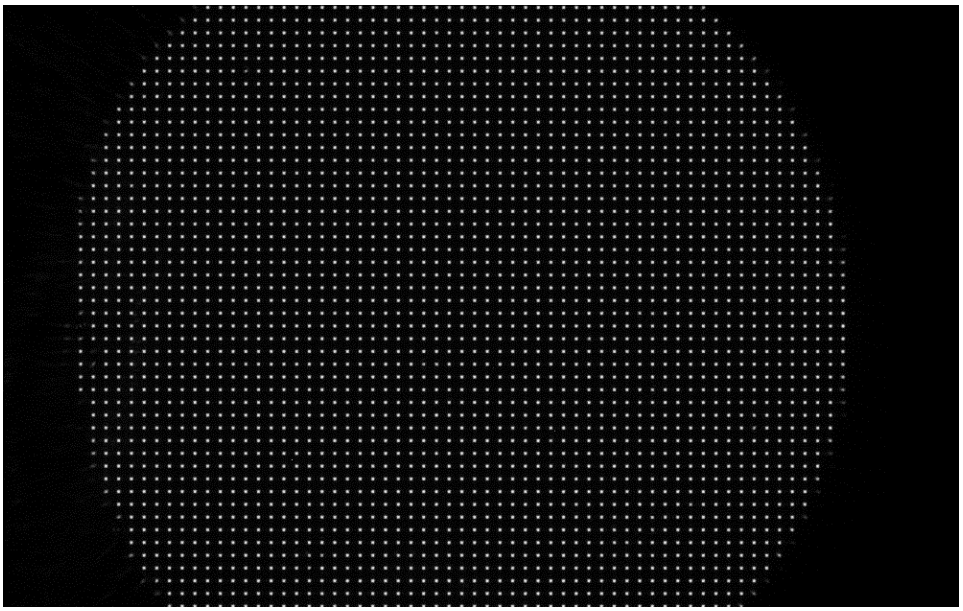

Fig. 5.3 The Hartmann-gram of the 1030 nm laser beam captured by the Dynamic Optics wavefront sensor. Image size: 1216 × 1936 pixels

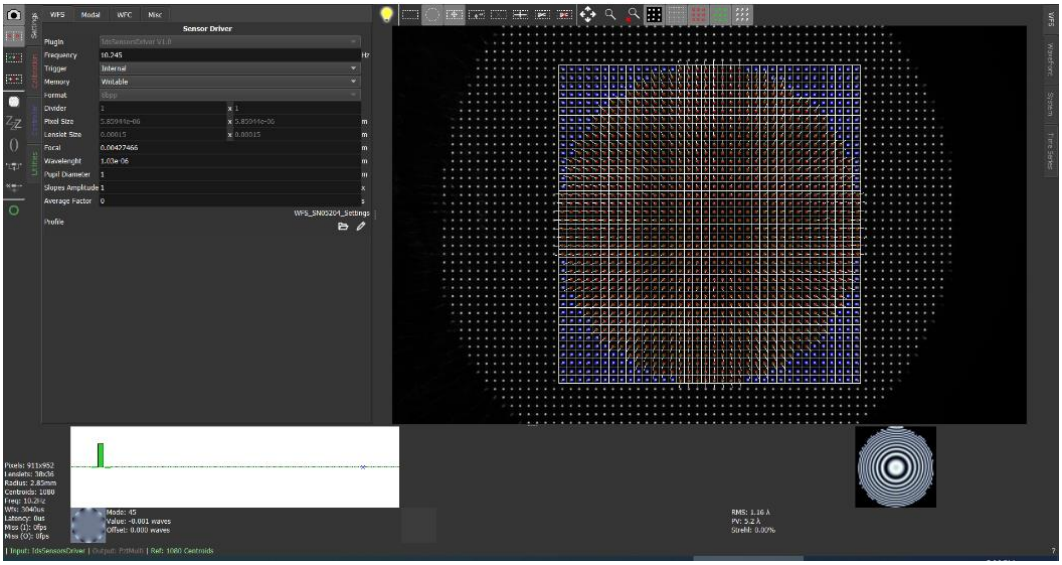

Fig. 5.4 The snapshot of the PhotonLoop software of the Dynamic Optics wavefront sensor.

Fig. 5.5 shows the report of the measured wavefront generated by the PhotonLoop. The measured wavefront on the left of the report indicates the dominant aberration of defocus with a positive sign, which indicates a diverging wavefront. The RMS and the Peak-to-Valley (PV) of the wavefront are 1.16 λ and 5.26 λ as shown in the report, respectively.

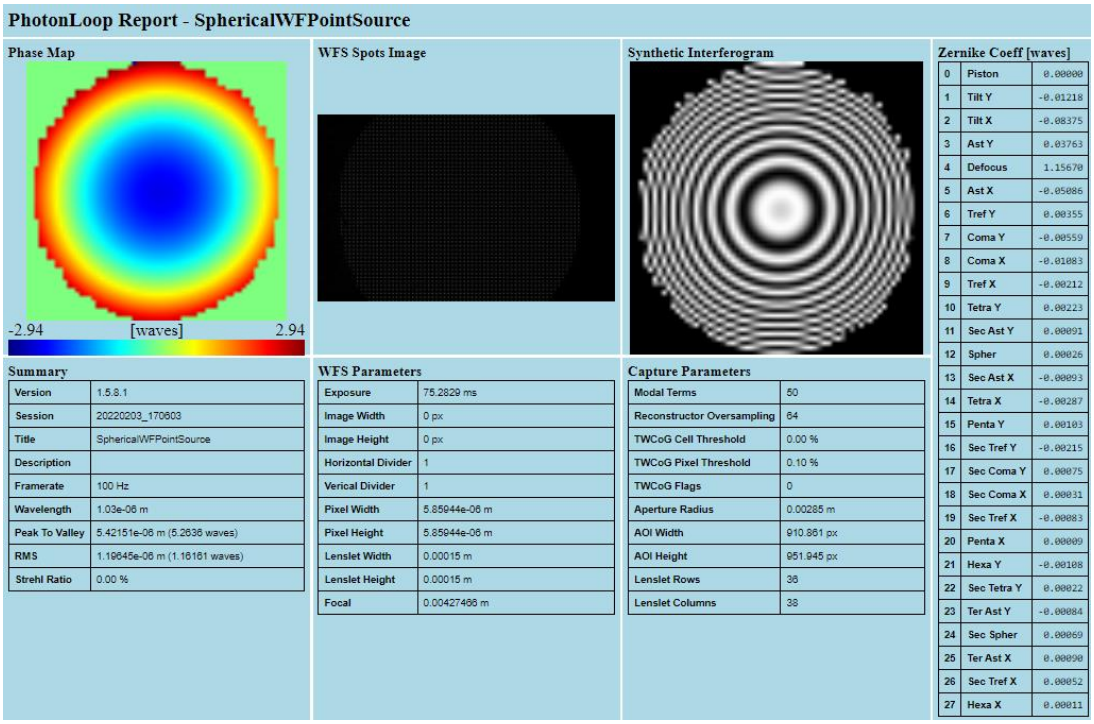

Fig. 5.5 The report of the measured wavefront (left), Hartmann-gram (middle), and synthetic interferogram (right). The Zernike coefficients are also shown in the table.

The Hartmann-gram image captured by the Dynamic Optics WFS was saved, then imported to MATLAB. The wavefront was reconstructed with my MATLAB code using the algorithm introduced in Section 4.2. The captured Hartmann-gram image shown in Fig. 5.3 was processed in MATLAB and shown in Fig. 5.6. The light blue spots indicate the detected focal spots. The white grid indicates the sub-apertures. The big yellow circle indicates the sampling range. The yellow arrows indicate the wavefront slopes at the sub-apertures.

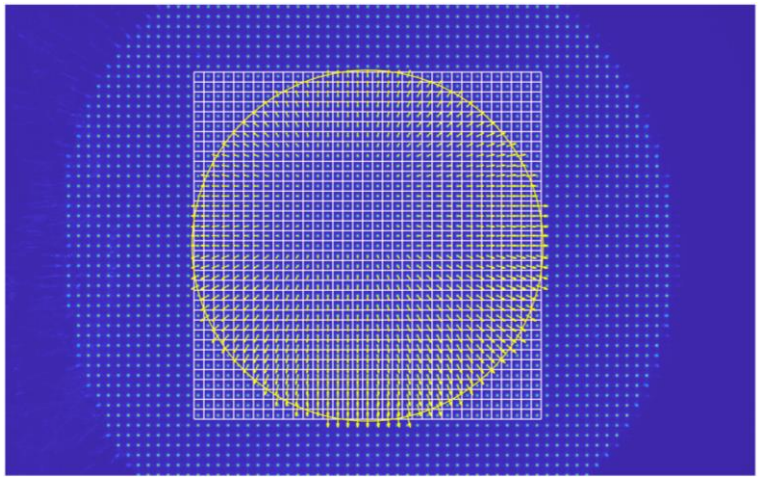

Fig. 5.6 Processed image of the captured Shack-Hartmann spot pattern with my wavefront reconstruction algorithm.

The reconstructed wavefront is shown in Fig. 5.7(b). The wavefront RMS and PV are 1.08 λ and 4.98 λ, respectively. In order to compare the measured wavefronts by different devices, the Zernike coefficients obtained by the Dynamic Optics WFS were imported to MATLAB for

reproducing the results, as shown in Fig. 5.7(a). The difference between them is shown in Fig. 5.8. The difference between the reproduced wavefront and the reconstructed wavefront is mainly caused by different centroiding algorithms between my code and PhotonLoop software.

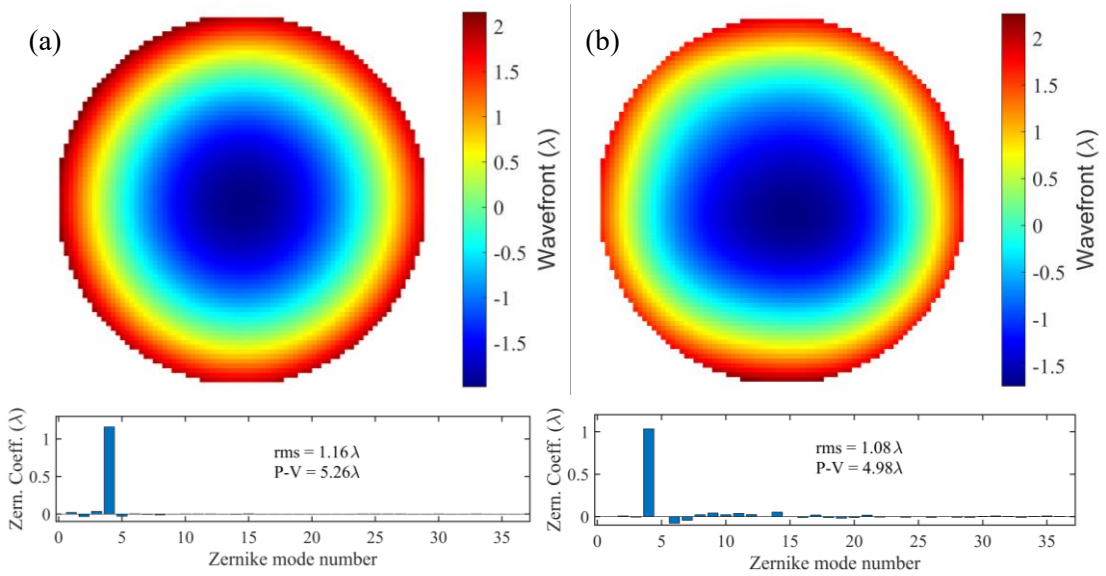

Fig. 5.7 (a) The reproduced wavefront measured by Dynamic Optics WFS, (b) the reconstructed wavefront processed by my MATLAB code. The Zernike modes are indexed in a single indexing scheme, the same for the other figures in this work.

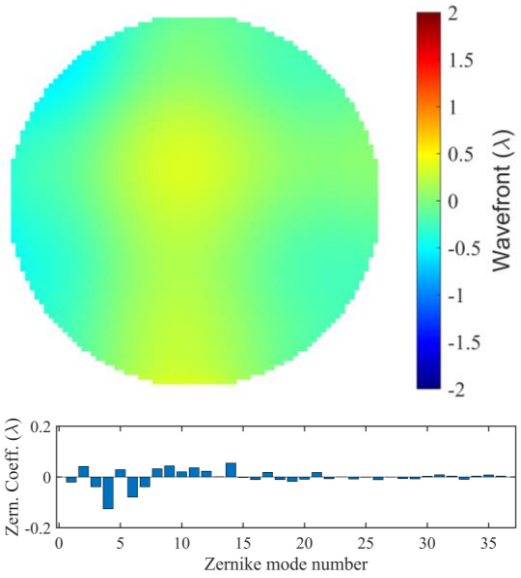

Fig. 5.8 The difference between the wavefront measured by Dynamic Optics WFS and the wavefront reconstructed by my MATLAB code shown in Fig. 5.7.

The RMS of the difference in Zernike Coefficients between the two results can be calculated as:

$$RMS = \sqrt{\frac{\sum_{i=1}^{N}(Z_{i\,Pho} - Z_{i\,My})^2}{N}} \tag{5.1}$$

where N is the number of Zernike Polynomial modes, $Z_{i\,Pho}$ is the Zernike Coefficients fitted

by PhotonLoop, $Z_{i\,My}$ is the Zernike Coefficients fitted by my algorithm. In this case, the RMS of the difference in Zernike Coefficients between the two results was 0.0325 λ.

In order to verify the robustness and repeatability of my algorithm, the above-mentioned comparing procedure is repeated 20 times to obtain an RMS statistic. The difference RMS for 20 measurements is within the range of 0.016 – 0.034 λ, and the average difference RMS is 0.025 λ.

5.1.3 Calibration of the mid-IR wavefront sensor

After verifying the algorithm for wavefront reconstruction, calibration was carried out for the homemade wavefront sensor with a 1.55 μm fiber laser. The experiment setup was the same as shown in Fig. 5.1, except for the fiber laser source and the wavefront sensor, as shown in Fig. 5.9.

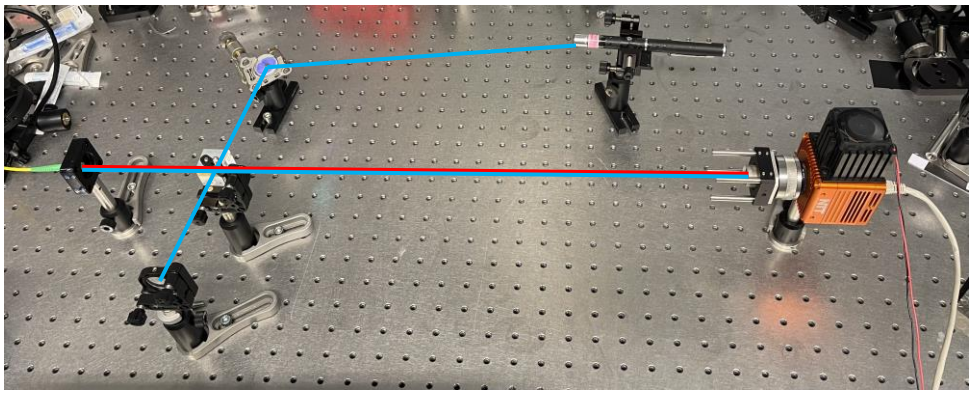

Fig. 5.9 Experiment setup for calibrating the home-mode wavefront sensor with a 1.55 μm fiber laser source. The beam splitter was removed during measurement. (*The alignment laser was not in place when taking photo of the setup*).

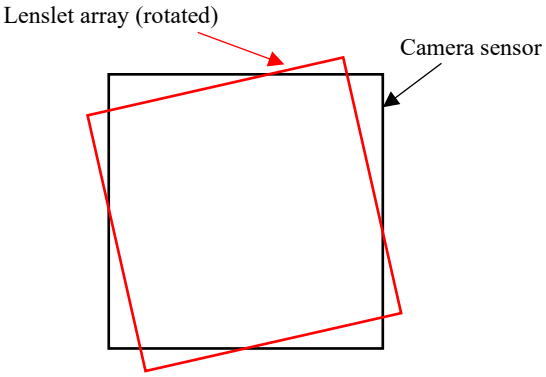

Fig. 5.10 Relative positions (rotation) of the camera sensor and the lenslet array. The black square indicates the position of the camera sensor, and the red square indicates the position of the lenslet array.

It should be noted that the wavefront sensor should be well assembled such that the rotation of the lenslet array matches with the sensor, as indicated in Fig. 5.10. If their relative positions do not match well with each other, the wavefront would be wrongly reconstructed from the measured Hartmann-gram (Fig. 5.11(a)). The focal spots marked by red rectangles in Fig. 5.11(a)

are caused by the mismatching (rotation) between the lenslet array and the sensor. The wrongly reconstructed wavefront is shown in Fig. 5.11(b).

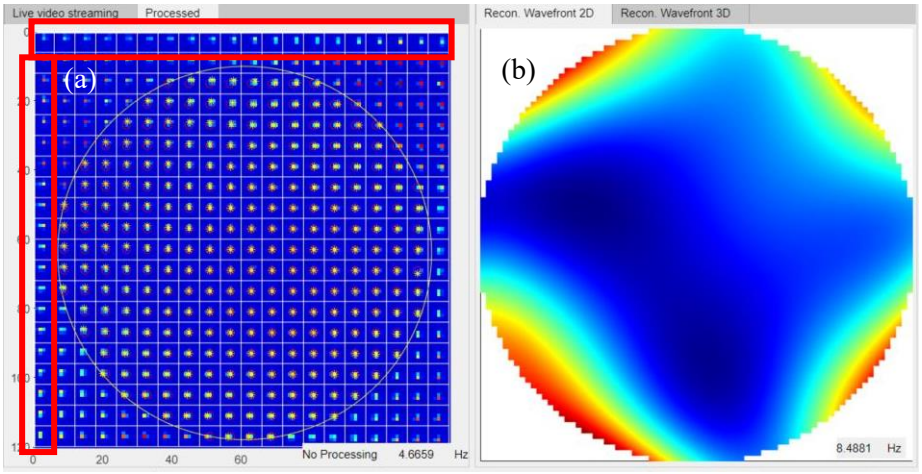

Fig. 5.11 (a) The Hartmann-gram caused by mismatching between the lenslet array and the sensor, (b) the wrongly reconstructed wavefront. (description of axis)

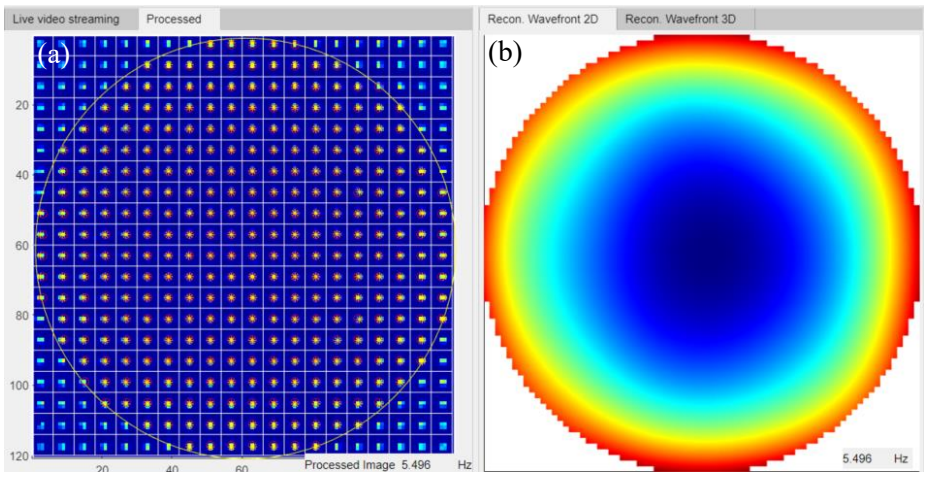

Fig. 5.12 (a) The Hartmann-gram with the precise matching between the lenslet array and the sensor. (b) The correctly reconstructed wavefront.

To correct this, the lenslet array should be rotated and precisely matched with the camera sensor by observing the reconstructed wavefront of a point source until obtaining a symmetric wavefront, as shown in Fig. 5.12(b). The Hartmann-gram captured by the precisely assembled wavefront sensor is shown in Fig. 5.12(a).

Absolute calibration of the wavefront sensor

After precisely assembling the wavefront sensor, the absolute calibration was carried out as instructed in the literature [181][182][183]. The main idea of this absolute calibration is to assume a planar wavefront with the centers of the lenslets of the lenslet array as an absolute reference. By measuring the radii of the curvature of the wavefront at different distances of the sensor from the point light source, the actual geometrical parameters of the SHWFS, such as

the effective focal length, the actual average pitch size of the lenslet array, can be determined using the standard mathematical regression procedure.

The calibration is done by:

(1) measuring multiple wavefronts generated by a single-mode fiber, which can be considered as a point source generating a nearly ideal spherical wavefront,

(2) measuring multiple radii of curvature R_0 of the wavefronts, the distance between the point source (fiber emitting tip), and the lenslet array.

Since the lenslet array is inside the camera housing, as shown in Fig. 4.4, its position cannot be precisely measured. However, it is possible to precisely measure the distance between the fiber tip and a reference point on the camera housing. The measured distance can be named R_{ref}, reference radius of curvature as shown in Fig. 5.1. Then, the measured curvature ρ_{meas} is simply given by:

$$\rho_{meas} = \frac{1}{R_{ref}} \tag{5.2}$$

The difference between the measured curvature ρ_{meas} and the real curvature ρ_{real} can be written as:

$$\delta\rho = \rho_{meas} - \rho_{real} \tag{5.3}$$

Meanwhile, the real curvature ρ_{real} can be obtained by

$$\rho_{real} = (\frac{Q}{P_0} - 1)\frac{1}{f_0} \tag{5.4}$$

where P_0 and f_0 are the real values of the lenslet array's pitch size and the lenslet's focal length, respectively. Q is the distance between adjacent focal spots, independent of the coordinates, as shown in Fig. 5.13, Q = N× S_0, where S_0 is the real value of pixel size. In practice, Q is the average value of the distances between the adjacent focal spots in the areas marked by red rectangles in Fig. 5.14, which shows a processed Hartmann-gram image captured during calibration.

However, the real values of S_0, P_0, and f_0 are now those values are not precisely known. It is necessary to find the small difference between the real values and the values, S, P, and f, given by the specification of the camera and lenslet array, given in Table 4.1 and Table 4.2. They satisfy

$$\begin{gathered} S = S_0 + \delta S, \quad P = P_0 + \delta P, \quad f = f_0 + \delta f \\ \delta S/S \ll 1, \quad \delta P/P \ll 1, \quad \delta f/f \ll 1 \end{gathered} \tag{5.5}$$

where δS, δP, and δf are the difference between the theoretical and the actual values, respectively.

The given values (S, P, and f) can be used to calculate the real values (S_0, P_0, and f_0) by calculating the curvature difference $\delta\rho$ by a Taylor expansion of Eq. 5.4 [181]:

$$\delta\rho = \rho_{meas}^2 \delta R - \rho_{meas}\frac{\delta f}{f_0} - \frac{1}{f_0}(\frac{\delta P}{P_0} - \frac{\delta S}{S_0}) \tag{5.6}$$

Considering the high manufacturing accuracy of the camera sensor, the pixel size can be

assumed to be the theoretical value. That means $\delta S = 0$. Therefore, Eq. 5.6 can be rewritten as:

$$\delta\rho = \rho_{meas}^2 \delta R - \rho_{meas} \frac{\delta f}{f_0} - \frac{\delta P}{f_0 P_0} \tag{5.7}$$

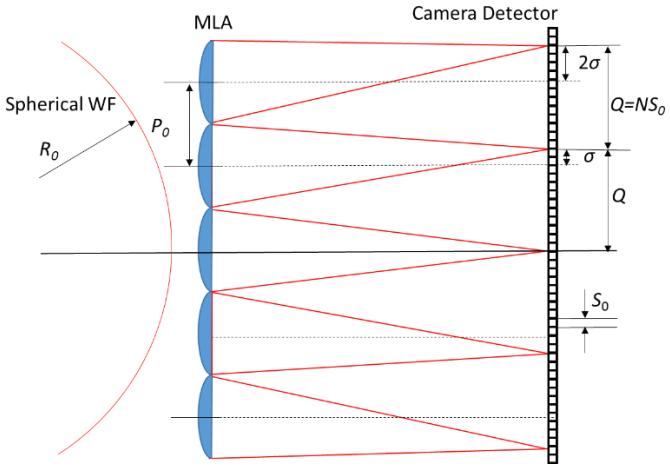

Fig. 5.13 Measuring the curvature of the wavefront [183]

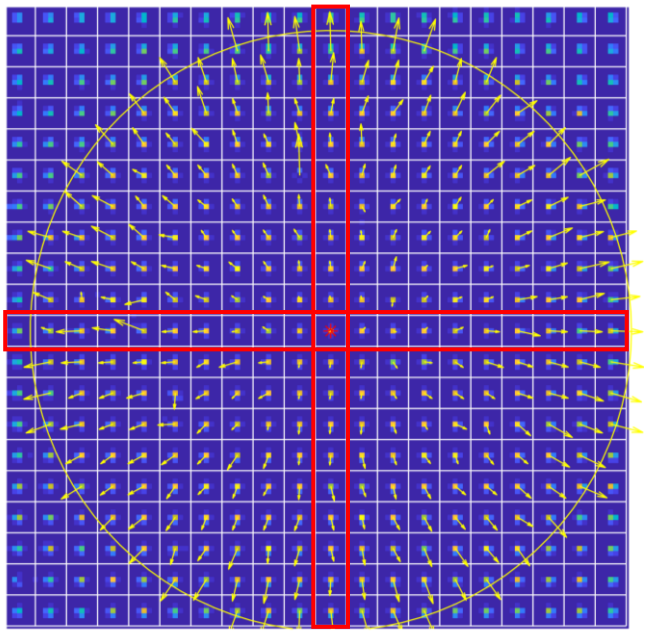

Fig. 5.14 The processed Hartmann-gram image captured during calibration of the wavefront sensor with a 1550 nm fiber laser. The white grid indicates the lenslet array (sub-apertures). The yellow circle indicates the sampled area. The yellow arrows indicate the wavefront slopes in sub-apertures. The focal spots in the areas marked by red rectangles are processed to obtain the distance Q between adjacent focal spots.

By measuring the wavefront at different distances from the fiber laser, multiple values of ρ_{meas} and Q can be obtained.

By fitting the values to Eq. 5.7, as shown in Fig. 5.15, the coefficients of Eq. 5.7 can be obtained. The fitted equation is:

$$\delta\rho = 19.06 \cdot \rho_{meas}^2 - 0.024 \cdot \rho_{meas} - 1.548 \times 10^{-5} \tag{5.8}$$

By comparing Eq. 5.8 with Eq. 5.7, one can obtain the following:

$$\delta R = 19.06$$

$$\frac{\delta f}{f_0} = 0.024$$

$$\frac{\delta P}{f_0 P_0} = 1.548 \times 10^{-5}\ [mm^{-1}]$$

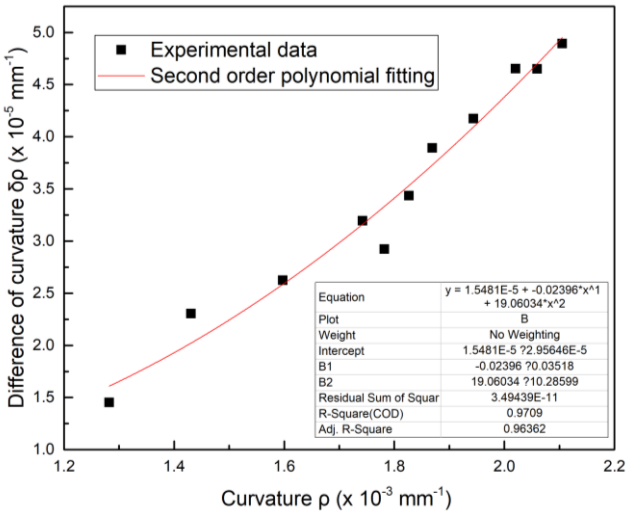

Fig. 5.15 The measured data of the curvatures and its second-order polynomial fitting.

From Table 4.1 and Table 4.2, one could know that f = 5.1 mm, P = 300 μm. Therefore, δf = 0.122 mm, δP = 0.023 μm. The actual focal length of the lenslet is 5.222 mm, and its actual pitch size is 300.023. These values will then be used as the preference of the wavefront sensor. Fig. 5.16 shows one of the measured and reconstructed wavefronts of the 1550 nm fiber laser during the calibration procedure. The defocus term indicates a diverging wavefront. The WFS was ready for wavefront measurement after precise calibration.

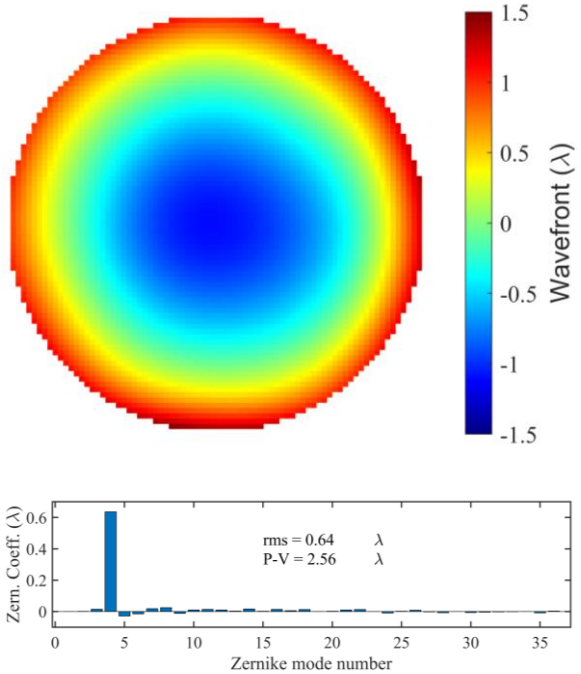

Fig. 5.16 Reconstructed wavefront from the measured Shack-Hartmann pattern and its Zernike Coefficients. Zernike modes are indexed in a single indexing scheme. The defocus term indicates the diverging wavefront.

5.2 Improving the Signal-to-Noise Ratio

Image noise, defined as random variations in the image signal, degrades the image quality. Typically, it is produced by the detector itself, surrounding electronics, dark current, temperature of the detector or system, etc. It should be treated appropriately in order to obtain precise measurement and a high signal-to-noise ratio (SNR), which is defined as the linear ratio of the signal intensity I_{sig} to the standard deviation of the noise σ_{noise} [184][185]. It can be expressed in decibels (dB) with reference to the nominal signal intensity

$$SNR = \frac{I_{sig}}{\sigma_{noise}} \tag{5.8}$$

In this work, laser-induced thermal afterimage, which is an image that continues to appear even after a period of exposure to the original image [186], was observed to decrease the SNR of the image while testing the TACHYON 16k camera with mid-IR irradiation.

In this section, the origins which affect the SNR are divided into two categories for analysis: background noise, including the aforementioned typical noises, and laser-induced thermal afterimage.

5.2.1 Background noise

In this work, all the captured images are converted from the uint8 class to double precision using the Image Processing Toolbox of MATLAB for the convenience of matrix manipulations with MATLAB.

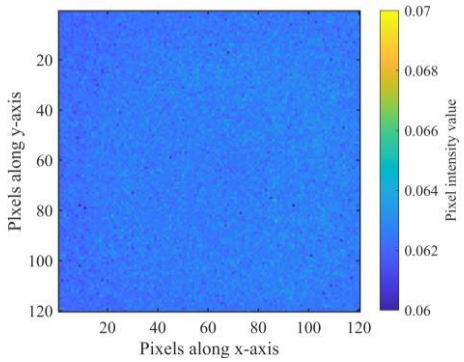

Fig. 5.17 Background noise captured without incident laser beam when the camera was turned on before warming up.

The initial background noise of the camera is captured when the TACHYON 16k camera was first turned on before warming up without incident laser beam, as shown in Fig. 5.17. The color bar indicates the pixel intensity value. The noise is evenly distributed over the sensor.

The Hartman-gram image with an incident laser beam (with laser power of 2 mW) was captured before the camera warmed up and is shown in Fig. 5.18(a). The intensity profile of the spots marked by a red rectangle, as shown in Fig. 5.18(a), is shown in Fig. 5.18(b). The Signal-to-Noise Ratio (SNR) was only 20.43 dB.

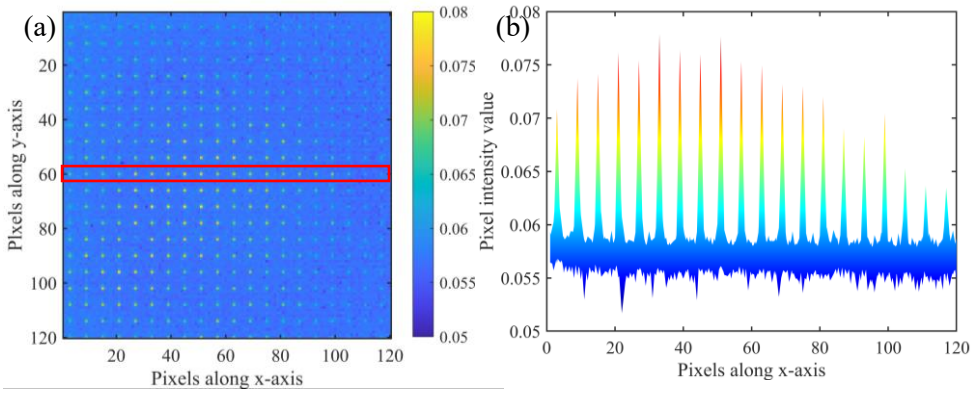

Fig. 5.18 (a) The Hartmann-gram image was captured with an incident laser beam (P = 2 mW) before the camera warmed up. The spots marked by a red rectangle, with coordinates of (60, :) along the axes of the image, were sampled for analysis. (b) the intensity profile of the sampled focal spots. The background noise is not subtracted. SNR = 20.43 dB.

It takes 5 minutes for the camera to reach a thermal stable status without incident laser beam. The background noise without incident laser beam after warming up is shown in Fig. 5.19. Obviously, some parts of the sensor generated more thermal noise after warming up. The thermal noise is unevenly distributed over the sensor. This could be caused by the electronics behind the sensor, such as unevenly distributed chips on the driver circuit.

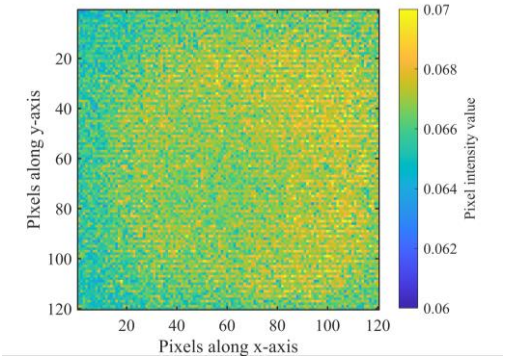

Fig. 5.19 Background noise captured without incident laser beam after warming up.

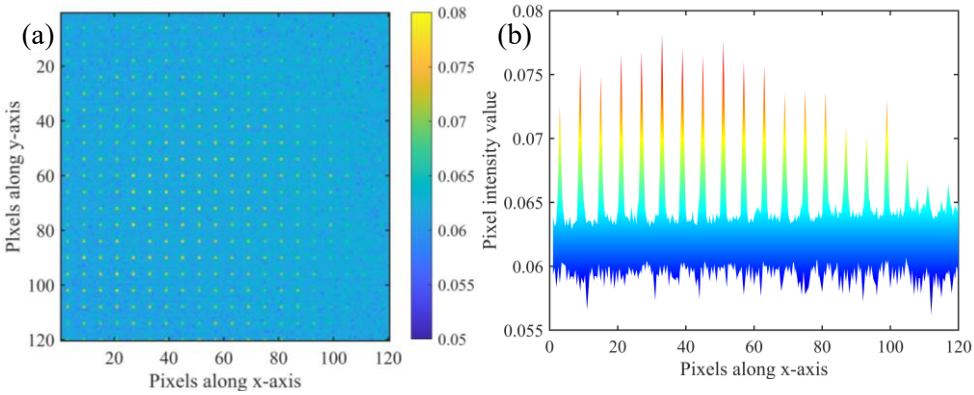

Fig. 5.20 (a) The Hartman-gram image. The spots with coordinates of (60, :) along the axes of the image were sampled for analysis. (b) the intensity profile was captured with an incident laser beam (P = 2 mW) after warming up. SNR = 9.35 dB.

The Hartman-gram image and the intensity profile with an incident laser beam (P = 2 mW) were captured after the camera warmed up and shown in Fig. 5.20. The SNR decreased to 9.35 dB due to increasing the thermal noise of the sensor.

The laser power was then increased to 3.56 mW to increase the SNR, which was increased to 24.24 dB with the same level of thermal noise. Fig. 5.21 shows the Hartmann-gram image and the intensity profile.

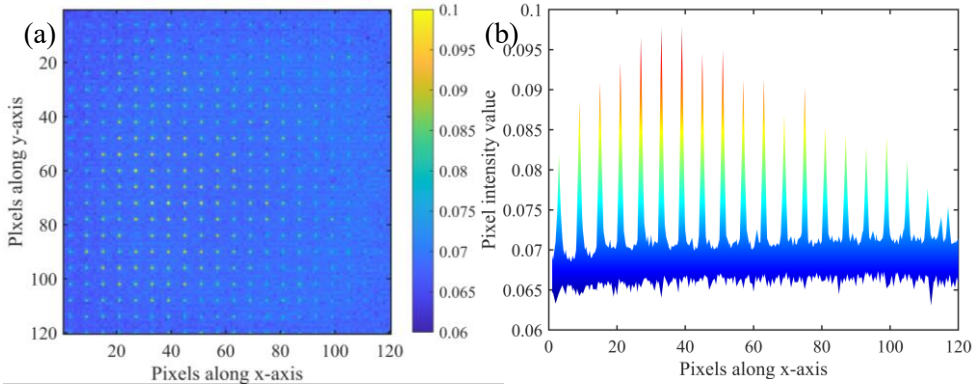

Fig. 5.21 (a) The Hartman-gram image. The spots with coordinates of (60, :) along the axes of the image were sampled for analysis. (b) the intensity profile was captured with an incident laser beam (P = 3.56 mW) after warming up. SNR = 24.24 dB.

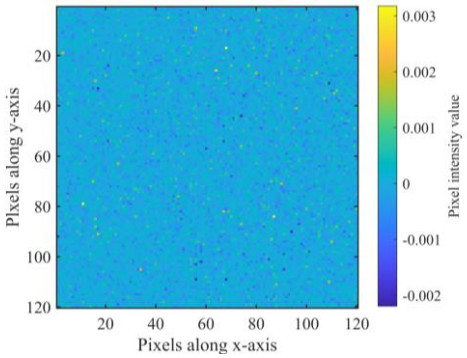

Fig. 5.22 The background image without incident laser input, after subtracting the background noise after warming up

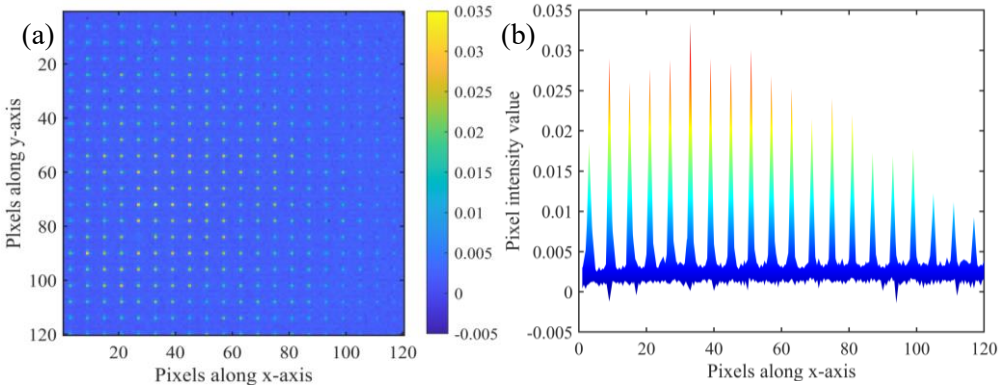

Fig. 5.23 (a) The Hartman-gram image. The spots with coordinates of (60, :) along the axes of the image were sampled for analysis. (b) the intensity profile was captured with an incident laser beam (P = 3.56 mW) after warming up and subtracting the background noise. SNR = 32.21 dB.

The background noise was subtracted from the Hartmann-gram image in order to improve the SNR further. Fig. 5.22 shows the result after subtracting the background noise from the captured image without incident laser beam after warming up.

The Hartmann-gram and the intensity profile captured with the incident laser beam (P = 3.56 mW) after warming up and subtracting the background noise are shown in Fig. 5.23. The SNR increased to 32.21 dB.

5.2.2 Laser-induced thermal afterimage

However, during increasing the incident laser power to increase the SNR, a thermal afterimage was observed after a 10-second laser exposure to the camera. The thermal afterimage is caused by the high intensity of the focal spots. For simplicity's sake, we can assume the incident laser beam is a flat-top beam covering the entire sensor, then the power density at the focal spot on the sensor can be estimated as:

$$PD_{focal} = \frac{P}{N^2 \cdot \pi \, (D_{Airy}/2)^2} \tag{5.9}$$

where PD_{focal} is the power density of the focal spot, N is the number of the lenslet in one axis so that N^2 is the total number of lenslet, D_{Airy} is the diameter of the focal spot.

For the home-made wavefront sensor, N = 20 and D_{Airy} = 80 μm. Thus, the power density PD_{focal} ≈ 100 mW/cm^2 for P = 2 mW, PD_{focal} ≈ 180 mW/cm^2 for P = 3.56 mW. These high-power densities lead to significant heat accumulation at the focal spots. However, by reducing the incident laser power to lower than 2 mW, the SNR will be lower than 10 dB even after subtracting the thermal background noise. Therefore, it is better to keep the power of the incident laser beam lower than 4 mW to obtain sufficient SNR without damaging the sensor.

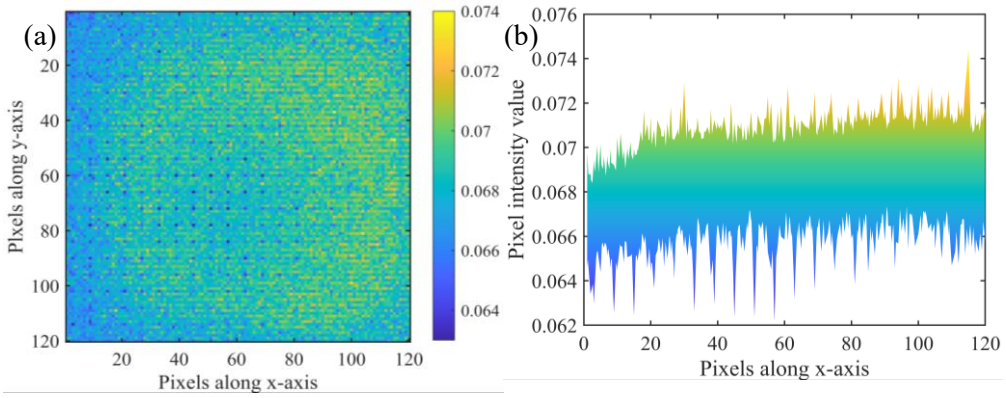

Fig. 5.24 (a) The thermal afterimage captured after a 10-seconds laser exposure to the camera. The spots with coordinates of (60, :) along the axes of the image were sampled for analysis. (b) its intensity profile. The background noise was not subtracted.

Fig. 5.24 shows the laser-induced thermal afterimage and its intensity profile. The background noise was not subtracted from the captured thermal afterimage. The blue spots indicate the positions of the focal spots before blocking the laser beam. It was found that the thermal afterimage was generated in the order of seconds after being exposed to the laser beam. Higher incident intensities of the focal spots lead to shorter accumulating times of the thermal afterimage.

Fig. 5.25 shows the results after subtracting the background noise from the thermal afterimage.

It was found that the maximum SNR, for which those thermal spots were taken as the signal, of the thermal afterimage was 11 dB. Its average SNR was 5.94 dB.

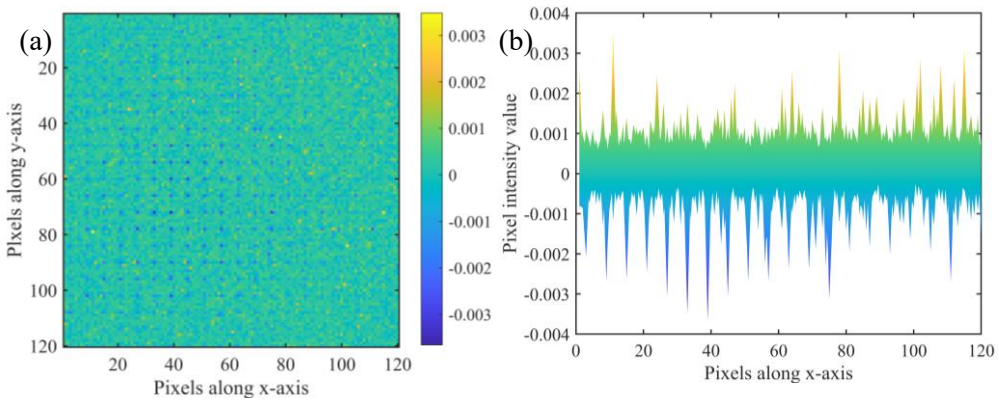

Fig. 5.25 (a) The thermal afterimage captured when blocking the 1.94 μm laser beam (P > 2 mW) after 10 seconds of exposing the camera, with background noise subtracted. The spots with coordinates of (60, :) along the axes of the image were sampled for analysis. (b) its intensity profile. The background noise was subtracted.

5.2.3 Impacts on centroiding and wavefront reconstruction

The thermal afterimage continues to appear on the sensor for a few seconds or more time, which depends on the incident laser power density. It can affect the accuracy of centroid detection. Therefore, the centroids of the focal spots and wavefronts were measured with a time interval of 2 seconds for 120 seconds to see the impacts of the thermally induced afterimage. The sub-aperture marked by the yellow rectangle in Fig. 5.26(a) was chosen for analysis. Fig. 5.26(b) shows the distribution of the focal spot centroids detected during the 120 seconds in that sub-aperture. The change in color of the focal spot centroids is related to the iteration number. It shows the trend of the centroid shifting caused by the afterimage. The centroid distribution RMS is 0.16 pixels and 0.24 pixels for the x- and y-axis, respectively. Fig. 5.27 shows the time development of the x-tilt Zernike coefficient during the 120 seconds. It could be seen that the x-tilt coefficient increased steadily in time.

Fig. 5.28 shows the reconstructed wavefronts of the first and the last measurements. It could be seen that the tilts terms of the Zernike coefficients increased during the thermal afterimage was forming and accumulating. 35 Zernike terms were fitted for wavefront reconstruction (without piston) in this work.

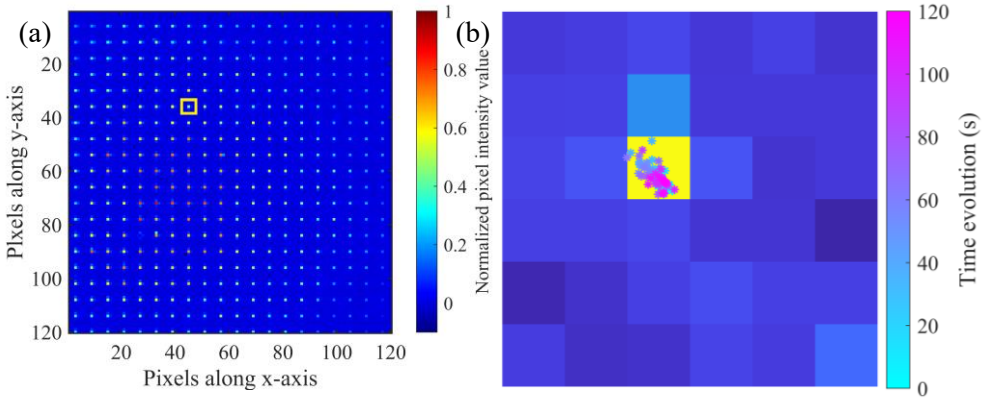

Fig. 5.26 (a) The Hartmann-gram image captured during the measurement. The sub-aperture marked by the yellow rectangle was chosen for analysis. (b) The distribution of the calculated centroids of the focal spots detected during the 120 seconds in the sub-aperture. The background image is the first captured image of the sub-aperture (6 x 6 pixels) in a jet colormap. Each color block indicates one pixel. The colors of the spots varying from cyan to magenta indicate the recording sequence from the first to the last centroids.

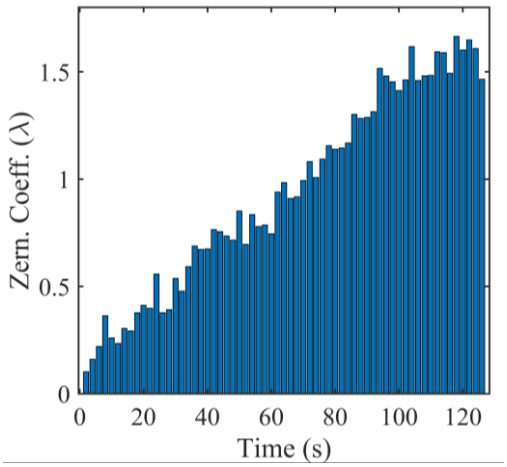

Fig. 5.27 Bar-plot of the Zernike coefficients of the x-tilt term of each reconstructed wavefront as a function of time during the 120 seconds.

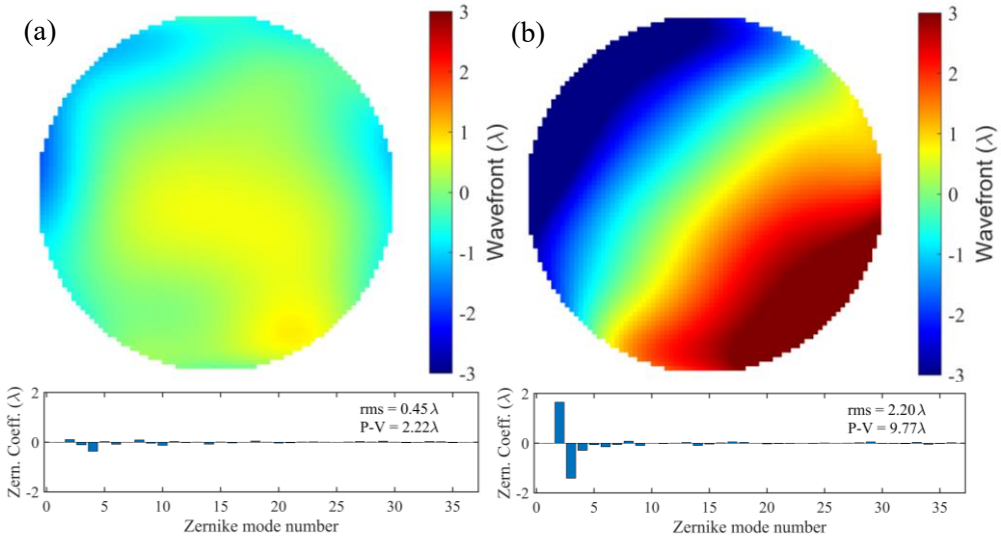

Fig. 5.28 The measured wavefront and the Zernike coefficients of the first (a) and the last (b) capturing during the 120 seconds of measurements.

5.2.4 Solution for reducing the impacts

The TACHYON 16K camera has an integrated physical shutter that can be controlled remotely. This allows easy background updates every few seconds, effectively subtracting the afterimage. The response time of the physical shutter is tested to be about 50 milliseconds, effectively adding a 100 milliseconds delay to the control system for each background update. Therefore, the closed-loop control system would become very sluggish if the time interval for dynamically updating the background is < 1 second. If the time interval is > 5 seconds, the thermal afterimage would not be fully mitigated.

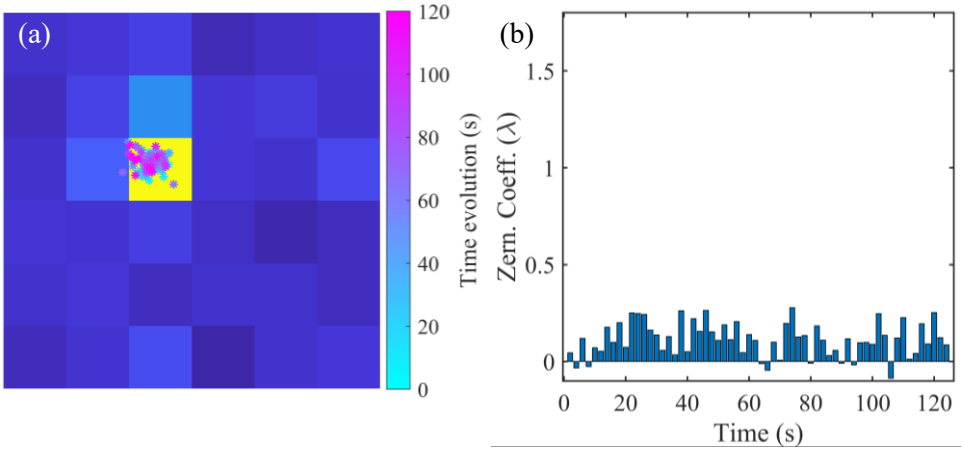

Fig. 5.29 (a) The distribution of the calculated centroids of the focal spots detected during the 120 seconds in the sub-aperture. Each color block indicates one pixel. The colors of the spots varying from cyan to magenta indicate the recording sequence from the first to the last centroids. (b) Bar-plot of the Zernike coefficients of the x-tilt term of each reconstructed wavefront as a function of time during the 120 seconds. Measurements were carried out with dynamic updating of the thermal background with a time interval of 2 seconds.

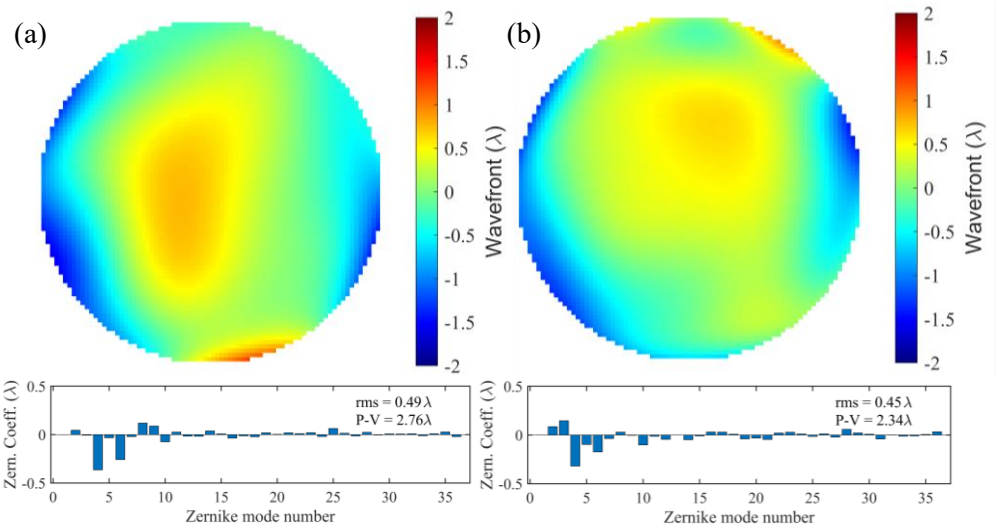

Fig. 5.30 The measured wavefront and the Zernike coefficients of the first (a) and the last (b) capturing during the 120 seconds of measurements, which were done by dynamically updating the thermal background.

With dynamic updating of the thermal background with a time interval of 2 seconds, the detected centroid distribution was more uniform, as shown in Fig. 5.29(a), with RMS reduced

to 0.11 pixels and 0.15 pixels for the x- and y-axis, respectively. The Zernike coefficient of the x-tilt term showed improved stability, as shown in Fig. 5.29(b). The wavefront variations decreased for 120 seconds, as shown in Fig. 5.30(a) and (b). The SNR was improved to 34.17 dB, while the incident laser power was 3.56 mW, as shown in Fig. 5.31.

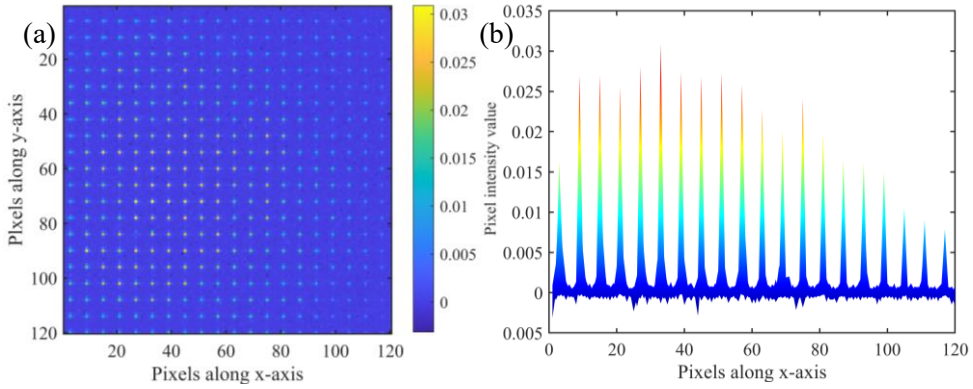

Fig. 5.31 (a) The Hartman-gram image. The spots with coordinates of (60, :) along the axes of the image were sampled for analysis. (b) the intensity profile was captured with an incident laser beam (P = 3.56 mW) after warming up, after subtracting the background noise, with dynamic updating of the thermal background. SNR = 34.17 dB.

5.3 Characterization of the Deformable Mirror

5.3.1 Experimental setup

The experimental setup used for AO system characterization is shown in Fig. 5.32. A closed-loop control scheme [187][188][189] is used in our mid-IR AO system. A Tm fiber laser emitting at the wavelength of 1940 nm was used as the mid-IR source. The Tm-doped fiber laser was collimated with a fiber collimator. An attenuator consisting of a half-wave plate (HWP) and a Polarization Beam Splitter (PBS) was installed after the output to decrease the output power. Two dichroic mirrors (DiM) coated with HR @ 1940 nm and HT @ 780 nm were used to couple out the pump light from the 1940 nm mid-IR laser beam. The residual pump light was present due to the Tm fiber laser specifics. A telescope consisting of two convex lenses with focal lengths of f_1 = 100 mm and f_2 = 800 mm was used to expand the beam diameter to 17 mm ($1/e^2$) to cover most of the center part of the deformable mirror (DM). The DM used in this work was a piezoelectric bimorph mirror with 64 actuators from Dynamic Optics. It is coated with a protected silver coating, suitable for wide spectral range applications, and its clear aperture is 30 mm. The bimorph technology was chosen from various DM technologies based on several aspects. First, it is potentially suitable for high-power laser beams thanks to its ability to integrate multi-layer coating. Second, it is suitable for correcting thermal aberration thanks to its natural flexing properties. Third, it is a cost-effective technology with high-speed control ability. A second telescope formed by two convex lenses with focal lengths of f_3 = 500 mm and f_4 = 200 mm was used as an optical relay system to image the deformable mirror onto the

SHWFS. The beam diameter after the second telescope was 6.8 mm ($1/e^2$). The deformable mirror and the lenslet array of the SHWFS are placed in the conjugated planes of the optical relay system. Two beam splitters were used to get a low-power beam for measurements of the wavefront and the focal spot (far-field). The beam profiler used in this work is WinCamD, based on a broadband microbolometer from DATARAY company. It has a large spectral range from 2 to 16 μm. Its pixel size is 17 × 17 μm^2 and 10.88 × 8.16 mm sensor size. For detailed profile analysis, a plano-convex lens with a focal length of f5 = 1.5 m was used to have a large focal spot size covering more pixels of the beam profiler.

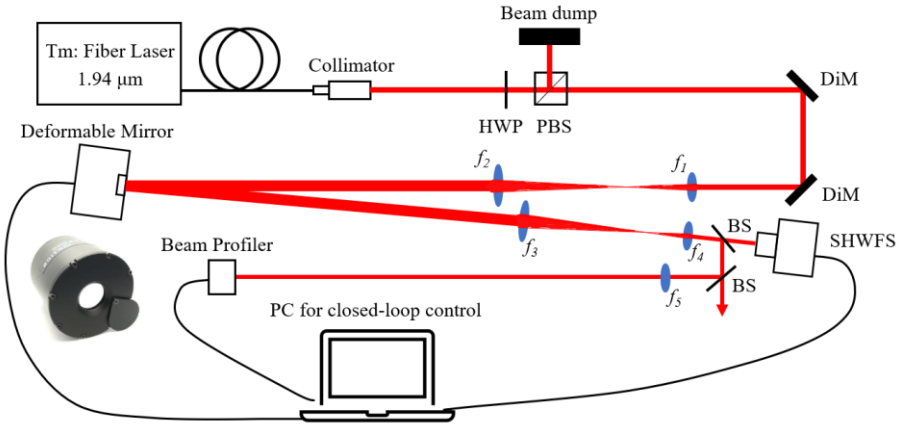

Fig. 5.32 The experimental setup of the Adaptive Optics system for 1.94 μm Tm: fiber laser. HWP: half-wave plate, PBS: polarization beam splitter, DiM: dichroic mirror, SHWFS: Shack-Hartmann wavefront sensor, BS: beam splitter. The inset is a photo of the deformable mirror.

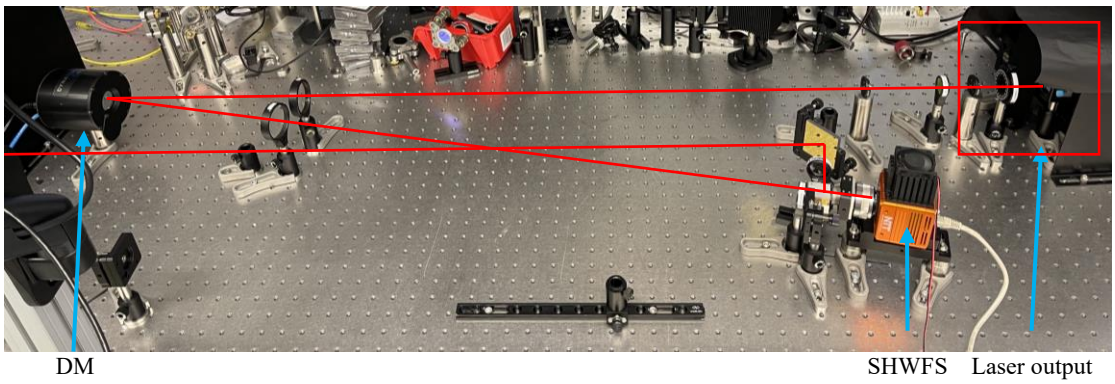

Fig. 5.33 Photo of the experimental setup. The beam profiler is not shown in the photo.

5.3.2 Measurement of the Influence Functions

The Influence Functions of the deformable mirror were measured in this section. The wavefront distortion caused by poking the actuator was obtained by applying a driving amplitude voltage V_{amp} = 74.6 V (80% of the maximum amplitude voltage) from the reference voltage on the actuator, as introduced in Section 4.3.2. N = 15 wavefronts were measured for each actuator, but only the last 10 measurements (N = 10 ~ 15) were taken into the calculation to obtain the mean values to mitigate the impacts caused by the hysteresis of the actuators [190].

Fig. 5.34 shows the DM's produced Influence Functions (surface response) by the action of each actuator over the DM. The actuators are numbered from 1 to 64 as indicated, which is not corresponding to the mapping of the actuators on the DM. During the measurements, 35 Zernike polynomial terms were used for wavefront reconstruction.

It should be noted that precise measurement of the Influence Functions of the DM is essential for controlling the DM in an AO system. An inaccurate Influence Function Matrix in terms of wavefront slope or Zernike coefficients (IFMs or IFMc) leads to saturation of the DM means at least one of the actuators reaches its maximum stroke. The accuracy of the IFMs or IFMc can be affected by many aspects, such as the alignment of the optics and the pointing stability of the laser beam used for Influence Functions measurement. No DM saturation should be observed with properly measured IFMs or IFMc. It is essential to expand the laser beam to cover the clear aperture of the DM and the camera sensor to utilize the full capability of the AO system.

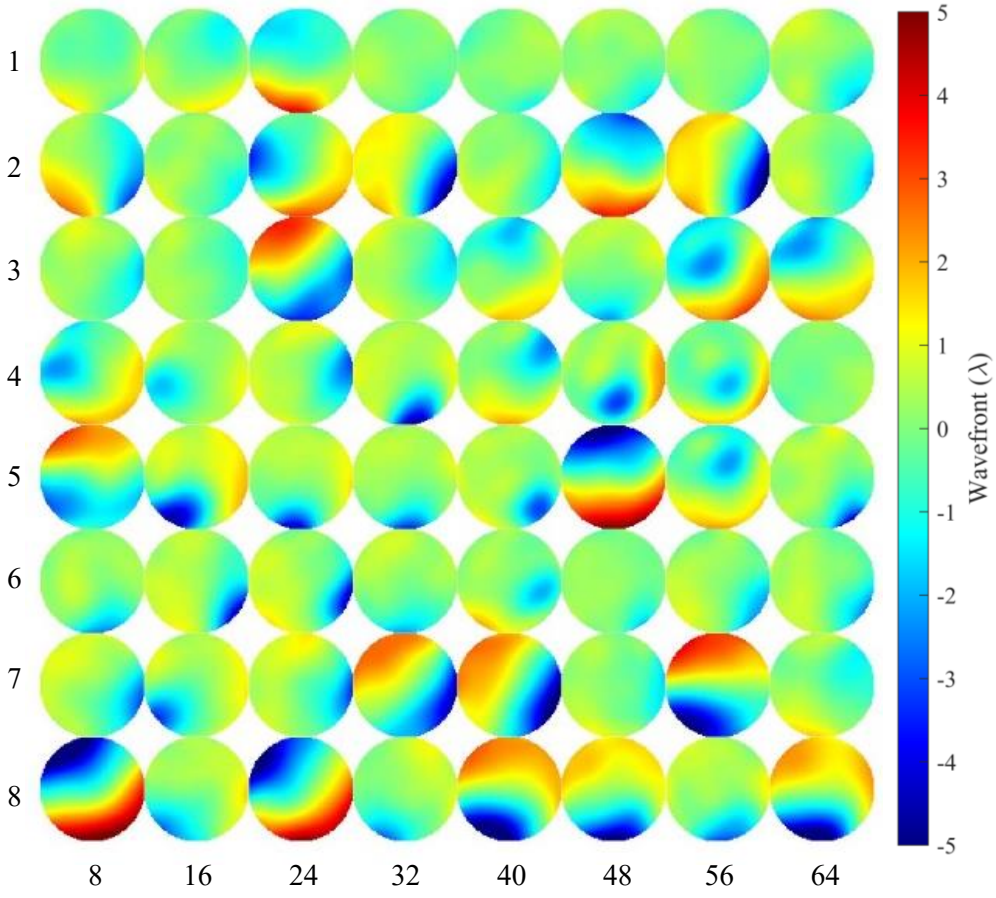

Fig. 5.34 Influence Functions (surface response of the DM) produced by the action of each actuator over the DM. The actuators are numbered from 1 to 64 as indicated, which is not corresponding to the mapping of the actuators on the DM.

5.3.3 Reproduction of the Zernike modes

Specific Zernike modes can be reproduced by setting the corresponding Zernike coefficient at specific values while setting the rest at zero. In such a way, the controlling ability of the AO system can be verified. The data was obtained by subtracting the mirror surface at the mid-stroke position from the reproduced wavefront. The corresponding wavefront PV and RMS values of each reproduced Zernike mode shape and the residual wavefront were calculated to evaluate the performance of the measured Influence Functions of the DM. The experimental reproduction of the first 9 Zernike mode shapes (excluding the piston) is shown in Fig. 5.35. It could be seen that the amplitudes, RMS, and PV, which were the maximal values obtained during the experiments, of the reproduced Zernike mode shapes, decreased as the mode increased. In order to reproduce higher order ($\geq$3) Zernike mode shapes with high accuracy, it is essential to obtain highly accurate Influence Functions of the DM. Therefore, in practice, it is necessary to carry out the calibration procedure (measurements of the Influence Functions) multiple times and verify the IFM by reproducing the Zernike modes. It was also found that it was necessary to make sure the laser beam size cover at least 80% range of the DM clear aperture, and the wavefront sensor should be able to detect the entire laser beam spot. Because the amplitudes, RMS, and PV values of the reproduced Zernike modes would be lower with a smaller laser beam size (covering less than 80% range of the DM clear aperture). Thus, the capability of the AO system would be lower, too.

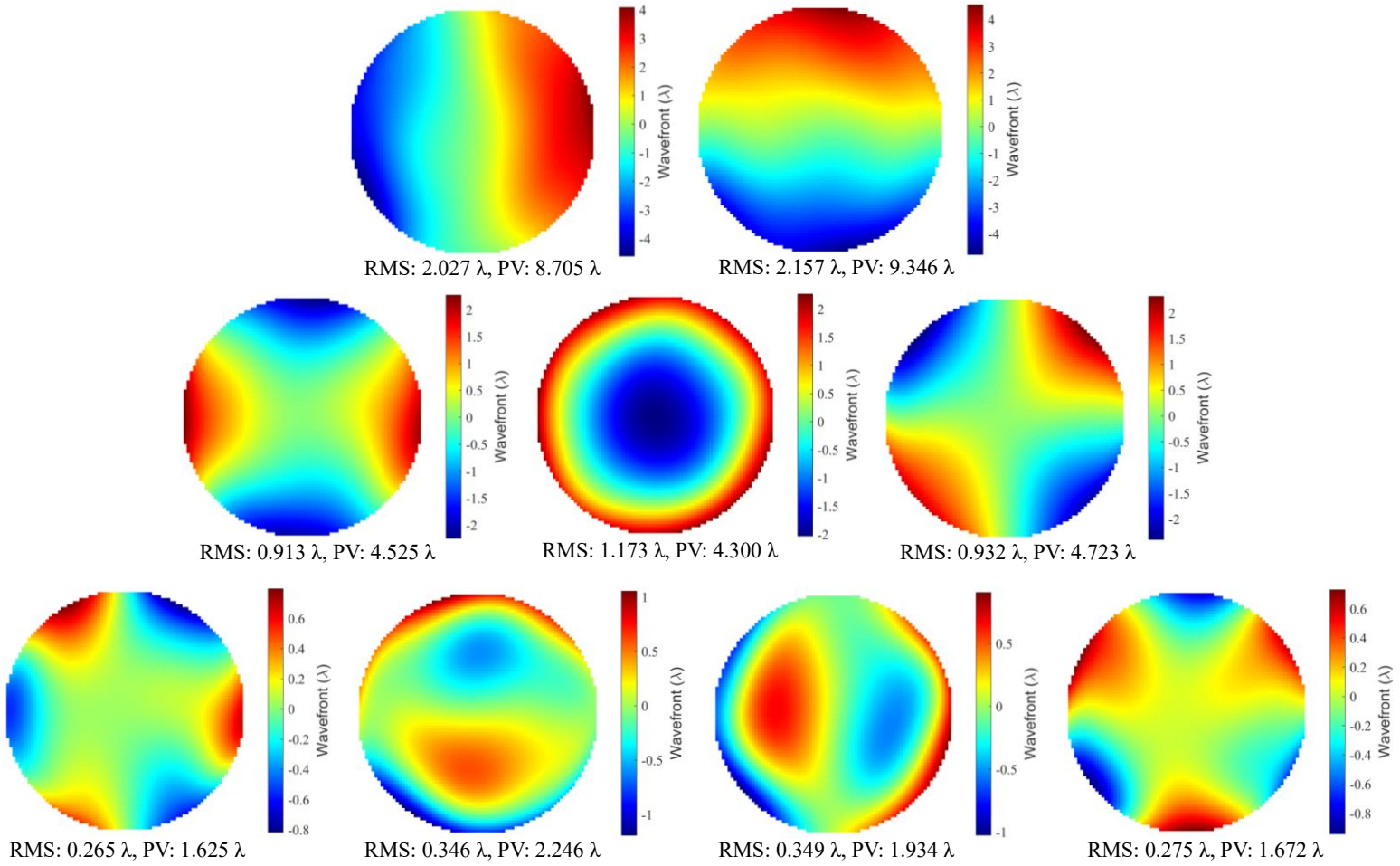

Fig. 5.35 Reproduction of the first 9 Zernike mode shapes (excluding piston) using closed-loop control method. The wavefront PV value and RMS value are indicated for each mode.

5.4 Wavefront correction for mid-IR laser

Prior to starting the AO system, the initial wavefront and the focal spot profile were measured by replacing the DM in the experimental setup shown in Fig. 5.32 with a standard silver-coated mirror with flatness RMS < λ/8 (@632 nm). Fig. 5.36 shows the initial wavefront and the focal spot profile. A focusing lens with a focal length of 1.5 m was selected to obtain a large focal spot so that the beam profiler could measure more detail of the focal spot. The distortion of the wavefront and focal spot profile was mainly caused by the fiber collimator of the laser source and the imperfect alignment of the optical system. The telescopes for the 1.94 μm laser beam were aligned using a mid-IR liquid crystal detector card. The RMS value of the wavefront was 0.68 λ, and Peak-to-Valley (P-V) was 3.75 λ (@1.94μm). The focal spot profile with a dimension of 2.59 mm × 1.2 mm (@1/e^2) and 1.48 mm × 0.42 mm (@FWHM) along the two axes is marked by the solid white line and dashed line.

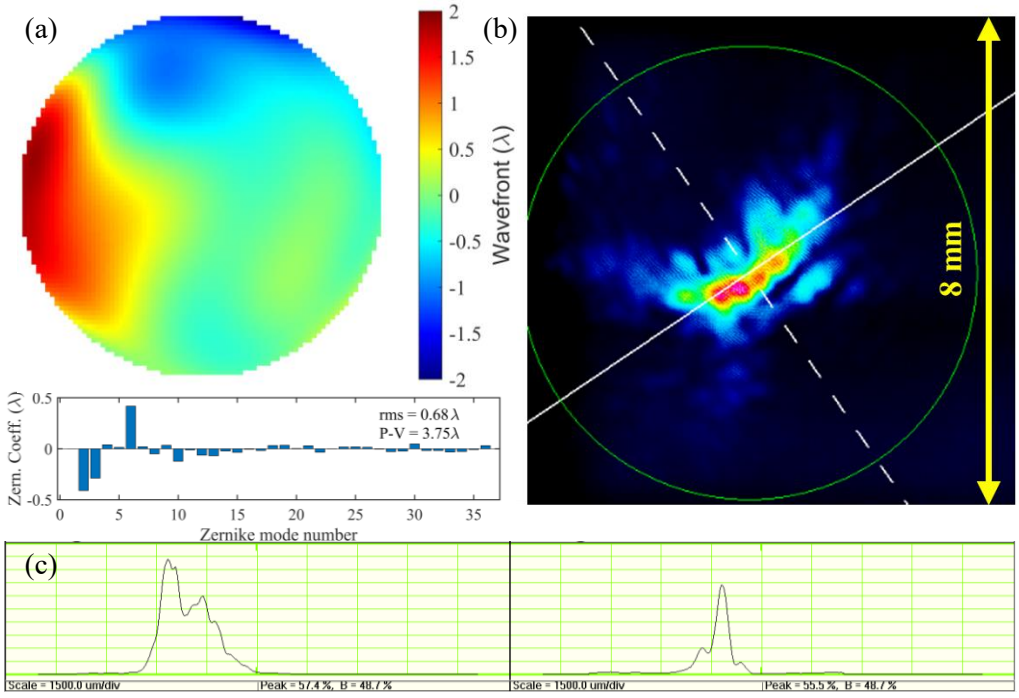

Fig. 5.36 (a) The initial wavefront and its Zernike coefficients of the 1.94 μm laser beam with the wavefront RMS was 0.68 λ, P-V was 3.75 λ (@1.94 μm), and (b) the focal spot profile with a dimension of 2.59 mm × 1.2 mm (@1/e2) and 1.48 mm × 0.42 mm (@FWHM) along the two axes marked by a solid white line and dashed line, (c) the 2D profiles of the focal spot along two axes. Results were measured when replacing the DM with a flat silver-coated mirror.

5.4.1 The impacts of the thermally induced error

After the characterization of the initial wavefront and the focal spot profile, the DM was installed back into the AO system. Then, the AO system was calibrated to obtain the control matrix, the pseudo-inverse of the Influence Function Matrix, as introduced in Section 2.7.1. The closed loop was then started, and the RMS of the residual wavefront was logged as a

function of the time/iteration number. We compared the case without dynamic updating of the thermal background with the case where the thermal background is updated during the closed loop.

(1). Without dynamic updating of the background, correcting 35 Zernike terms

Fig. 5.37 shows the wavefront RMS evolution for 650 iterations. During the measurements, the wavefronts and data were shown in real time for observation. So, the system was running at a low processing speed of 5~10 Hz, as explained in Section 4.4. The speed could be increased up to 40 Hz by disabling the displaying of the results in real-time.

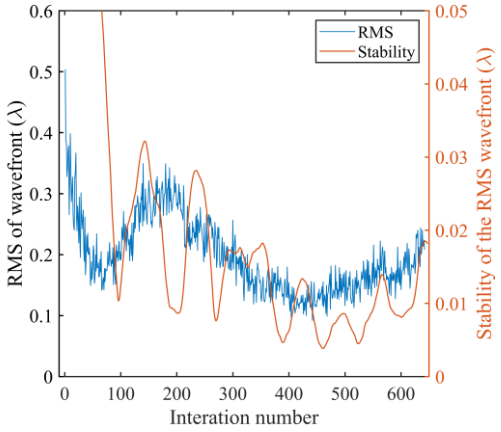

Fig. 5.37 The residual wavefront RMS was logged as a function of the iteration number of the AO system, without dynamic updating of the background, with correcting all the 35 Zernike terms. The gain was set at 0.1. The orange curve shows the stability of the control system performance by calculating the standard deviation of every 50 values of the wavefront RMS.

It could be seen that without dynamic updating of the background but with correcting all the 35 Zernike terms, the residual wavefront RMS initially decreased to 0.16 λ after 70 iterations (about 7 seconds). However, it did not remain stable and continued to fluctuate, presumably due to the thermal error buildup as indicated by the RMS stability curve, which was performed by calculating the standard deviation of every 50 values of the wavefront RMS.

Fig. 5.38 shows the focal spot profile and the residual wavefront after running 650 iterations. The residual wavefront RMS was 0.29 λ, P-V value was 2.05 λ (@1.94μm). The focal spot diameter was 2.6 mm (@$1/e^2$) and 0.51 mm (@FWHM) with a lens of focal length f_5 = 1.5 m. It could be seen that the broad bases of the 2D profiles, marked by the red arrow in Fig. 5.4.3(c), lead to a large $1/e^2$ focal spot diameter.

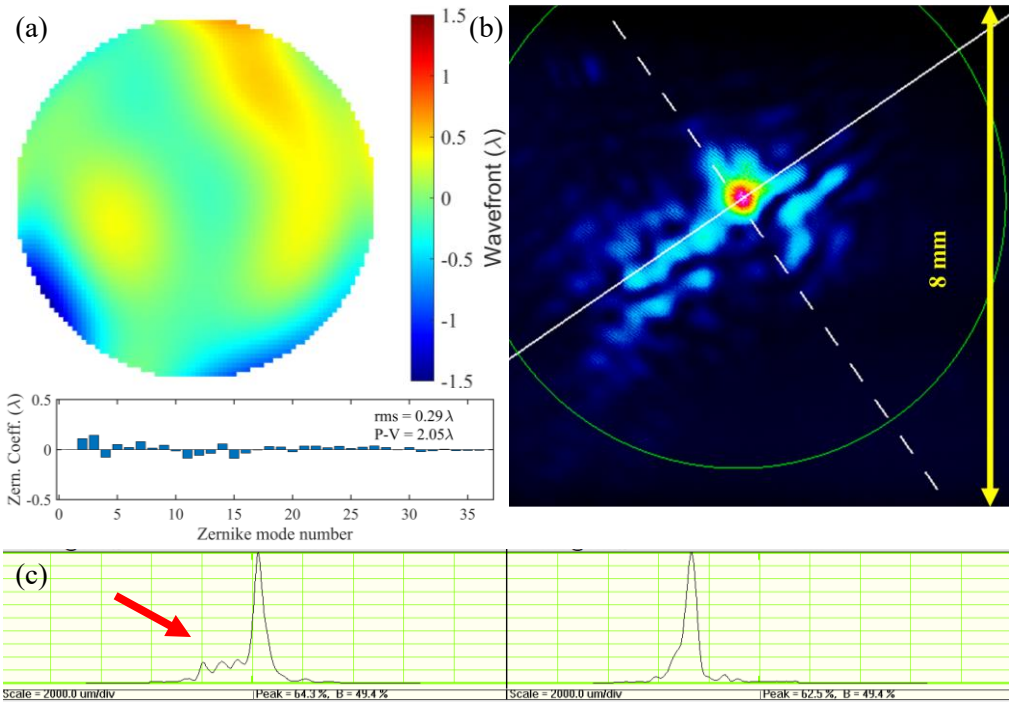

Fig. 5.38 (a) Residual wavefront RMS and its Zernike coefficients after running 650 iterations without dynamic updating of the background. The wavefronts RMS was 0.29 λ, P-V was 2.05 λ (@1.94 μm) (b) Focal spot profile with a diameter of 2.61 mm (@$1/e^2$) and 0.51 mm (@FWHM), (c) 2D beam profiles along the two axes marked by a solid white line and dashed line.

(2). With dynamic updating of the background, a time interval of 2 seconds, correcting 35 Zernike terms

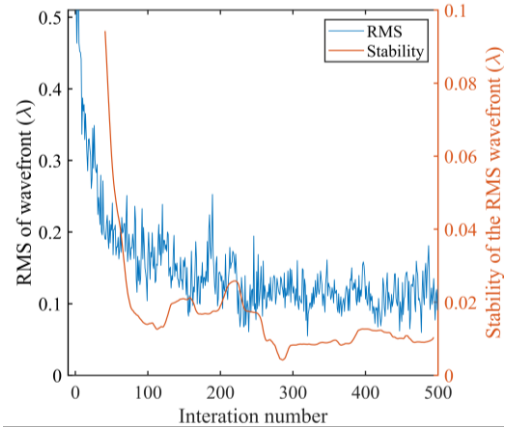

Fig. 5.39 The residual wavefront RMS was logged as a function of the iteration number of the closed-loop control system, with dynamic updating of the background with the time interval of 2 seconds, with correcting all the 35 Zernike terms. The gain was set at 0.1. The orange curve shows the stability of the control system performance.

Wavefront correction experiments were carried out with dynamic updating of the background with a time interval of 2 seconds. All 35 Zernike terms were corrected in this measurement. Fig. 5.39 shows the wavefront RMS evolution for 500 iterations. The residual wavefront RMS decreased from 0.54 λ to 0.15 λ after 100 iterations (about 12 seconds). The RMS was stable within the range of 0.1 λ – 0.18 λ after 220 iterations (about 25 seconds). The stability curve

indicates stable performance with fewer oscillations. The equidistant ripples on the stability curve were caused by the background updates every 2 seconds. The system stability was improved after 300 iterations.

Fig. 5.40 shows the focal spot profile and the residual wavefront after running 500 iterations. The residual wavefront RMS was 0.11 λ, P-V value was 0.71 λ (@1.94μm). The focal spot diameter was 1.26 mm (@$1/e^2$) and 0.52 mm (@FWHM). The bases of the 2D profiles became decreased.

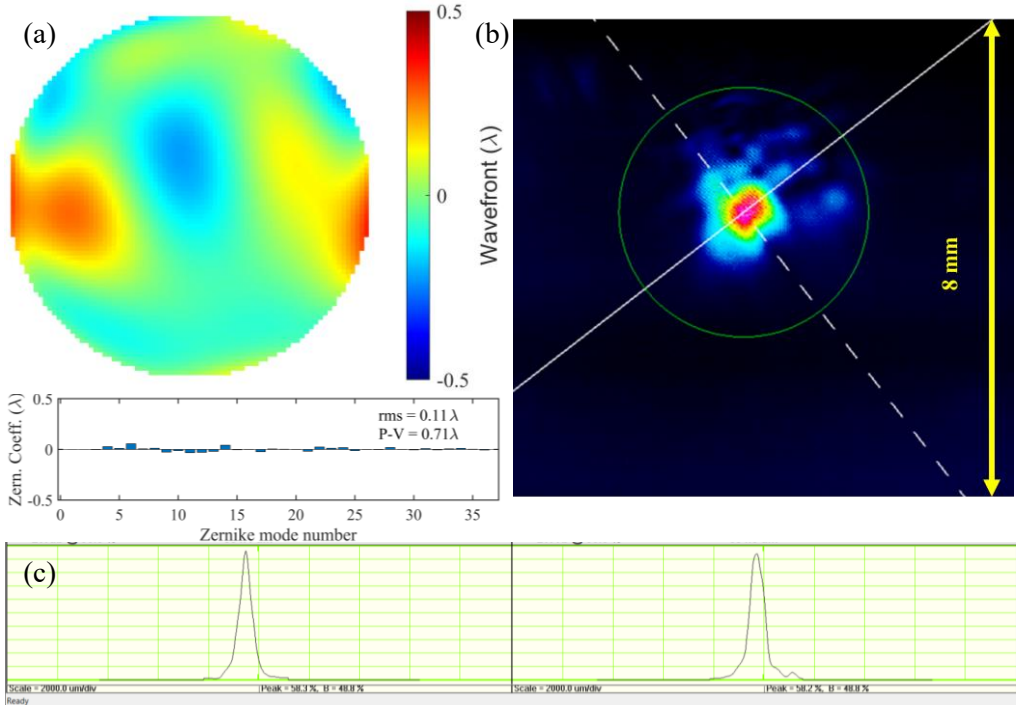

Fig. 5.40 (a) the residual wavefront RMS and its Zernike coefficients after running 500 iterations, with dynamic updating of the background with the time interval of 2 seconds, with correcting all the 35 Zernike terms. The wavefront RMS was 0.11 λ, P-V was 0.71 λ (@1.94 μm) (b) The focal spot profile with a diameter of 1.26 mm (@$1/e^2$) and 0.52 mm (@FWHM), (c) the 2D beam profiles along the two axes marked by a solid white line and dashed line.

(3). With dynamic updating of the background, a time interval of 5 seconds, correcting 35 Zernike terms

Wavefront correction experiments were carried out with dynamic updating of the background with a time interval of 5 seconds. All 35 Zernike terms were corrected in this measurement.

Fig. 5.41 shows the wavefront RMS evolution for 430 iterations. The residual wavefront RMS decreased from 0.41 λ to 0.12 λ after 100 iterations (about 12 seconds). The RMS was stable within the range of 0.1 λ – 0.15 λ after 120 iterations (about 14 seconds). The stability curve indicates stable performance with fewer oscillations. The equidistant ripples on the stability curve were caused by the background updates every 5 seconds. It could be seen that the stability curve was increasing slowly with more extended time intervals. That is because more thermal noise was accumulated with more extended time intervals.

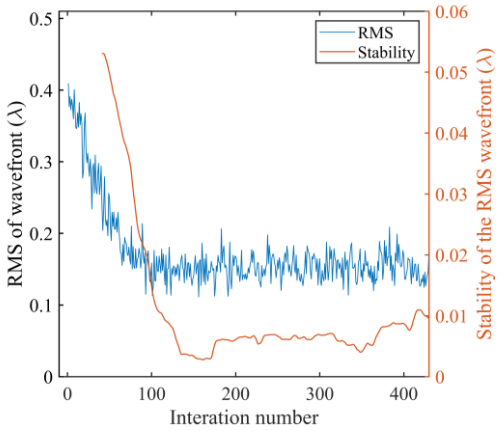

Fig. 5.41 The residual wavefront RMS was logged as a function of the iteration number of the closed-loop control system, with dynamic updating of the background with the time interval of 5 seconds, with correcting all the 35 Zernike terms. The gain was set at 0.1. The orange curve shows the stability of the control system performance.

Fig. 5.42 shows the focal spot profile and the residual wavefront after running 430 iterations. The residual wavefront RMS was 0.10 λ, P-V value was 0.72 λ (@1.94μm). The focal spot diameter was 1.33 mm (@$1/e^2$) and 0.54 mm (@FWHM). There was still some base on the 2D profiles.

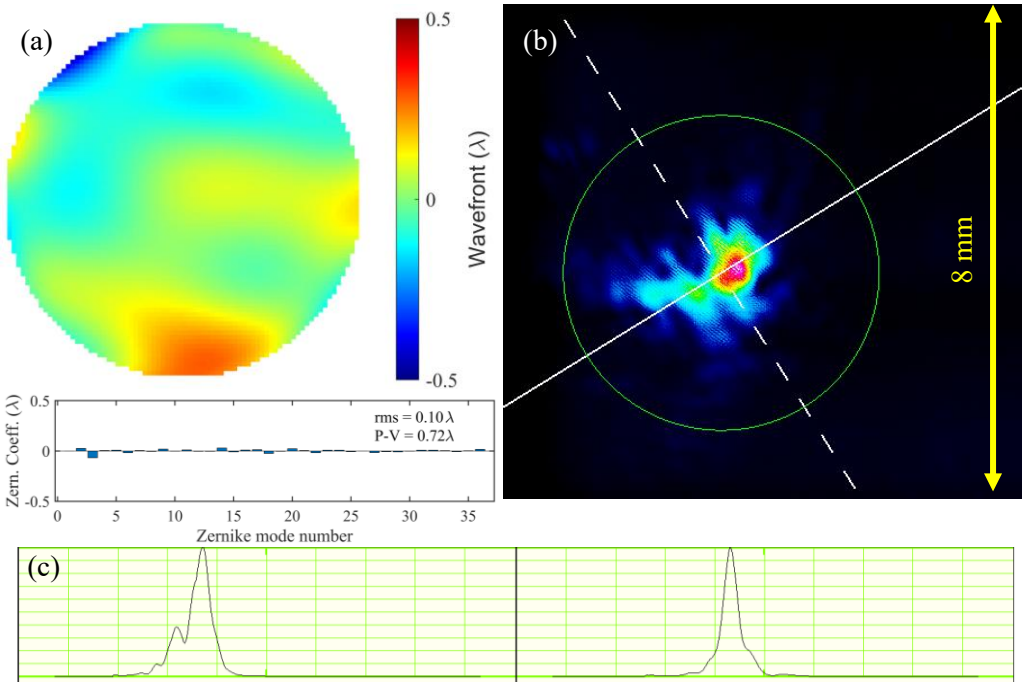

Fig. 5.42 (a) the residual wavefront RMS and its Zernike coefficients after running 400 iterations, with dynamic updating of the background with the time interval of 5 seconds, correcting all the 35 Zernike terms. The wavefronts RMS was 0.1 λ, P-V was 0.72 λ (@1.94 μm) (b) The focal spot profile with a diameter of 1.33 mm (@$1/e^2$) and 0.54 mm (@FWHM), (c) the 2D beam profiles along the two axes marked by a solid white line and dashed line.

5.4.2 The effects of correcting different modes of aberrations

As shown in Fig. 5.36(a), the first 15 Zernike terms contributed most to the wavefront aberrations. Wavefront correction experiments with correcting fewer Zernike terms had been carried out to investigate the influence on the performance of the AO system. During the experiments, all 35 Zernike terms (without piston) were fitted in the wavefront measurement procedure to ensure the same level of fitting error. The experiments were conducted with dynamic updating of the thermal background with a time interval of 2 seconds.

(1). With dynamic updating of the background, correcting the first 15 Zernike terms

Fig. 5.43 shows the wavefront RMS evolution for 400 iterations, with dynamic updating of the background with the time interval of 2 seconds, with correcting the first 15 Zernike terms. The residual wavefront RMS decreased from 0.46 λ to 0.14 λ after 80 iterations (about 8 seconds). The residual wavefront RMS was stable within the range of 0.1 λ – 0.13 λ. The stability curve indicates stable performance with fewer oscillations than correcting all the 35 Zernike terms. However, there was still a rise in the stability curve from the iteration number of 150. The equidistant ripples on the stability curve decreased much.

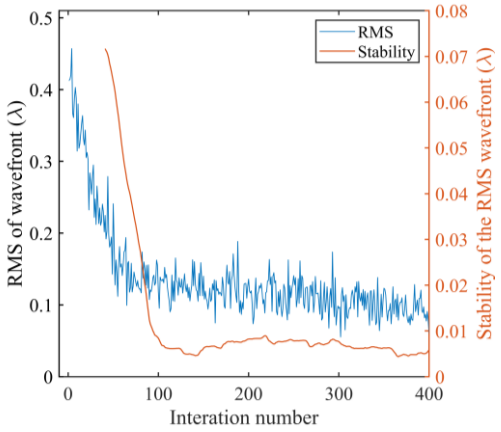

Fig. 5.43 The residual wavefront RMS was logged as a function of the iteration number of the closed-loop control system, with dynamic updating of the background with the time interval of 2 seconds, with correcting the first 15 Zernike terms. The gain was set at 0.1. The orange curve shows the stability of the control system performance.

Fig. 5.44 shows the focal spot profile and the residual wavefront after running 400 iterations. The residual wavefront RMS was 0.13 λ, P-V value was 0.69 λ (@1.94μm). The focal spot diameter was 0.96 mm (@$1/e^2$) and 0.53 mm (@FWHM).

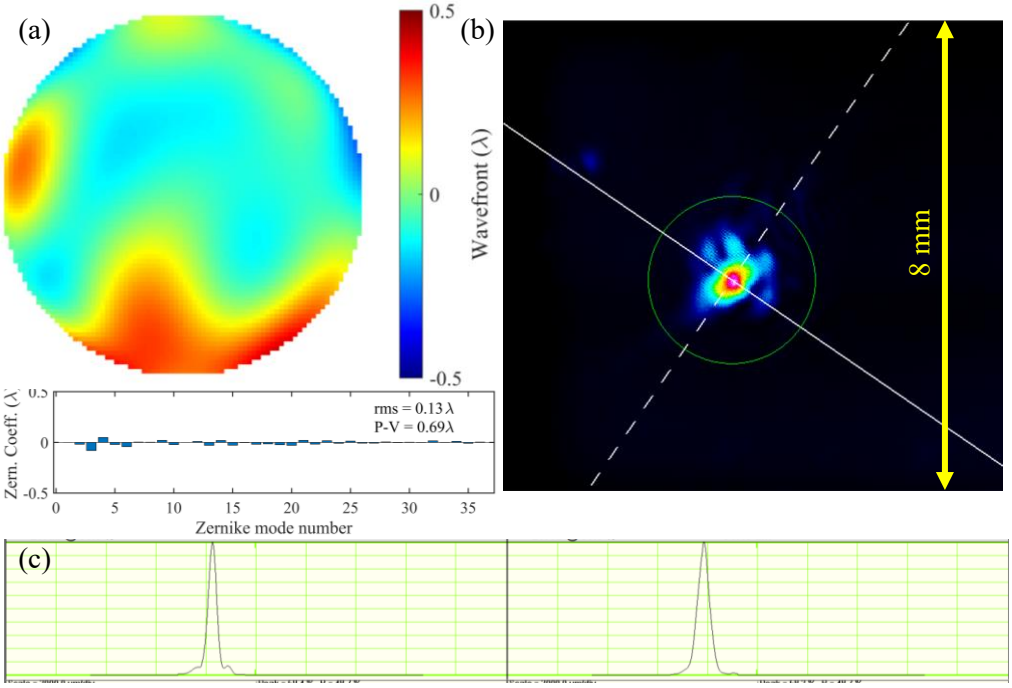

Fig. 5.44 (a) the residual wavefront RMS and its Zernike coefficients after running 400 iterations, with dynamic updating of the background with the time interval of 2 seconds, with correcting the first 15 Zernike terms. The wavefronts RMS was 0.13 λ, P-V was 0.71 λ (@1.94 μm) (b) The focal spot profile with a diameter of 0.96 mm (@$1/e^2$) and 0.53 mm (@FWHM), (c) the 2D beam profiles along the two axes marked by a solid white line and dashed line.

(2). With dynamic updating of the background, correcting the first 10 Zernike terms

Fig. 5.45 shows the wavefront RMS evolution for 300 iterations, with dynamic updating of the background with the time interval of 2 seconds, with correcting the first 10 Zernike terms. The residual wavefront RMS decreased from 0.5 λ to 0.11 λ after 76 iterations (about 7.6 seconds). The residual wavefront RMS was stable within the range of 0.1 λ – 0.15 λ. The stability curve of the AO system became flattered after about 80 iterations. There was no rise in stability except for small ripples, as in the previous case.

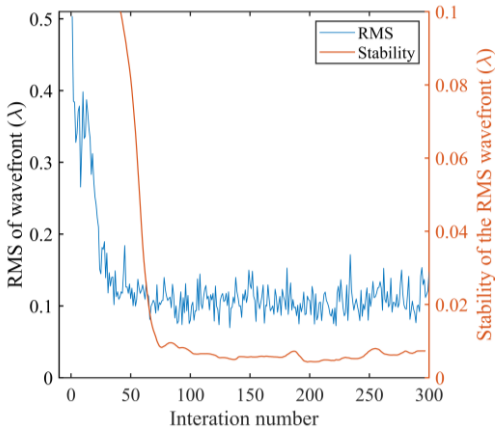

Fig. 5.45 The residual wavefront RMS was logged as a function of the iteration number of the closed-loop control system, with dynamic updating of the background with the time interval of 2 seconds, with correcting the first 10 Zernike terms. The gain was set at 0.1. The orange curve shows the stability of the control system performance.

Fig. 5.46 shows the focal spot profile and the residual wavefront after running 400 iterations. The residual wavefront RMS was 0.11 λ, P-V value was 0.66 λ (@1.94μm). The focal spot diameter was 0.97 mm (@$1/e^2$) and 0.54 mm (@FWHM).

The reasons are that the higher order Zernike coefficients are in the noise level, mainly caused by the residual thermal afterimage, the fluctuating laser beam, and the system delay due to dynamic updating of the background. The thermal afterimage cannot be fully mitigated by dynamic updating of the background. The residual thermal afterimage still introduced fitting errors, especially for the higher-order aberrations. Correcting higher-order Zernike terms, in this case, would lead to the wrong response of the DM surface trying to correct the noise.

Therefore, an optimal focal spot can be obtained by correcting the first 10 - 15 Zernike terms. The stability of the AO system can also be improved with less oscillation and smaller ripples than by correcting all the 35 Zernike terms. Especially for the case of correcting the first 10 Zernike terms, the stability curve was flatter with no rising after 80 iterations than that of correcting the first 15 Zernike terms. The AO system reached stable status faster when correcting fewer Zernike terms.

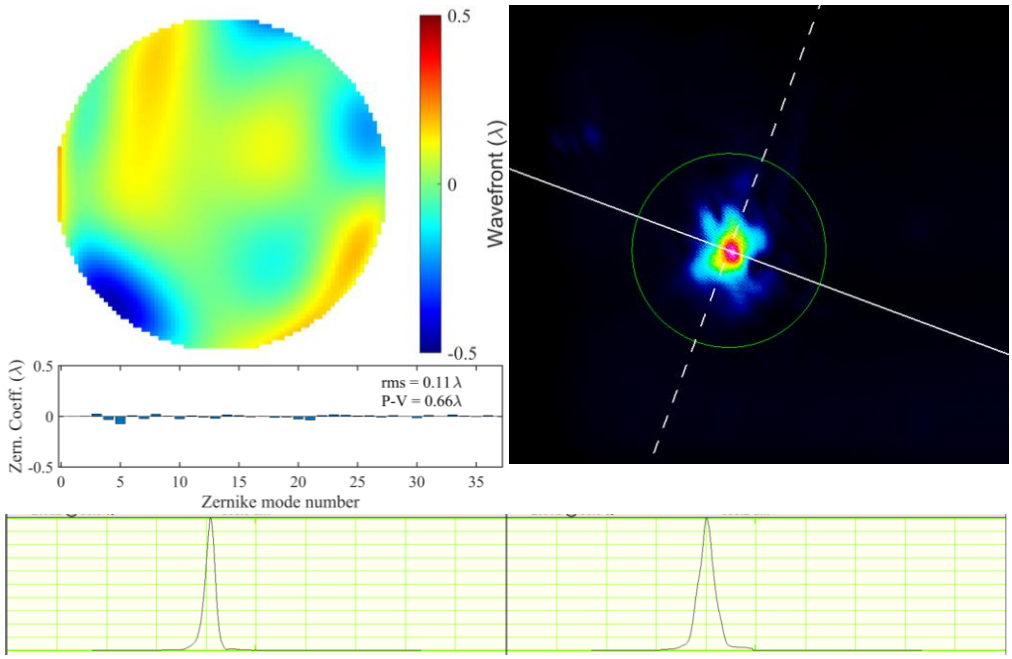

Fig. 5.46 (a) the residual wavefront RMS and its Zernike coefficients after running 300 iterations, with dynamic updating of the background with the time interval of 2 seconds, with correcting the first 15 Zernike terms. The wavefronts RMS was 0.13 λ, P-V was 0.71 λ (@1.94 μm) (b) The focal spot profile with a diameter of 0.97 mm (@$1/e^2$) and 0.54 mm (@FWHM), (c) the 2D beam profiles along the two axes marked by a solid white line and dashed line.

In conclusion, the thermal character of the laser causes an afterimage to be formed on the sensor, especially in the positions of the lenslet-generated focal spots. It introduces a significant error to the centroid detection and causes errors in wavefront reconstruction. The afterimage effect can be effectively mitigated by dynamic background updating. The time interval was selected to be 2 seconds as a compromise between the ability to mitigate the thermal afterimage and keeping the loop speed high. Using this approach, the residual wavefront RMS was reduced

from 0.29 λ to 0.11 λ, and the focal spot diameter was reduced from 2.6 mm to 1.26 mm (@$1/e^2$) while correcting 35 Zernike terms. The stability curve of the AO system was also improved with less oscillation. By correcting the first 10 – 15 Zernike terms, the focal spot diameter was further improved to be around 0.97 mm (@$1/e^2$) while the residual wavefront RMS was still around 0.11 λ – 0.13 λ. That was because the higher-order Zernike terms at the noise level were abandoned from wavefront correction to avoid the wrong response of the DM surface. The stability curves of the AO system reached stable status faster with less oscillation when correcting fewer Zernike terms.

Chapter 6 Thin Disk Chirped Pulse Amplification

Abstract: This chapter describes the design, development, and performance of the BIATRI thin disk laser system, developed for the project "Advanced designing of functional materials: From mono- to BI- And TRI-chromatic excitation with tailored laser pulses" (Acronym BIATRI). A numerical model was built to simulate the effect on the performance of the thin disk regenerative amplifier caused by Amplified Spontaneous Emission (ASE) in the first section. The design detail and experiment results are introduced in the following sections.

6.1 Numerical modeling of thin disk regenerative amplifier

An analytical model has been developed to simulate the output energy characteristics of the regenerative or multi-pass amplifier and to analyze the dynamics of pulse amplification in different configurations based on the theory introduced in Section 3.3. The layout of the thin disk regenerative amplifier can be simplified as shown in Fig. 6.1. The Yb:YAG thin disk with a thickness of d is pumped in the center region to obtain population inversion. During the pumping phase, energy is stored in the thin disk, and spontaneous emission is amplified, forming Amplified Spontaneous Emission (ASE). The seed pulses are then coupled into the thin disk's pumped region. The stored energy is extracted, and the seed pulses are amplified. The process is repeated during the amplification phase.

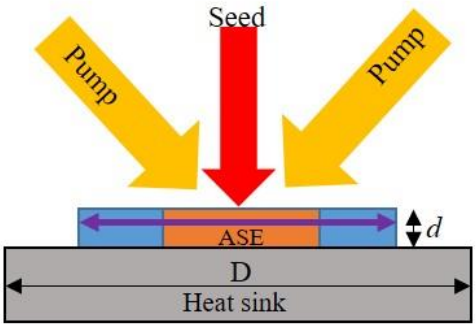

Fig. 6.1 Simplified layout of the thin disk regenerative amplifier used in the model.

The schematic block diagram used to illustrate the amplification process is shown in Fig. 6.2. The influence of ASE is considered within the pumping phase. Since the time scale (in nanosecond scale) of the amplification phase is concise compared to the time scale in between the pulses (in microsecond scale), the influence of ASE does not need to be considered during the amplification phase [191]. The dynamics of ASE decrease the population inversion in the

upper state level manifold, reducing the effective lifetime of the upper state level manifold. Therefore, ASE's influence is considered the effective lifetime of the upper state level manifold during the pumping phase.

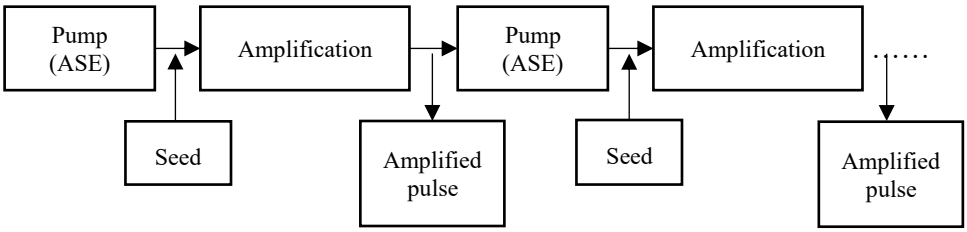

Fig. 6.2 The schematic block diagram of the simulation.

A numerical model was developed with MATLAB to simulate the regenerative amplifier regardless of its cavity design. The parameters used in our model are shown in Table 6.1. For the analysis, specific parameters were fixed, and only variable parameters were varied from case to case. In order to reduce the complexity of the model and to achieve fast simulation, the temperature was assumed to be T = 293.15K in this case.

Table 6.1 Parameters used in the model

	Item	Symbol	Value	Units
Fixed parameters	Temperature	T	293.15	K
	Pump photon energy	$\hbar\omega_p$	2.11×10^{-19}	J
	Pump absorption cross-section	$\sigma_{abs,p}$	3.97×10^{-25}	m^2
	Pump emission cross-section	$\sigma_{em,p}$	8.39×10^{-26}	m^2
	Seed photon energy	$\hbar\omega_l$	1.93×10^{-19}	J
	Seed absorption cross-section	$\sigma_{abs,l}$	1.29×10^{-25}	m^2
	Seed emission cross-section	$\sigma_{em,l}$	2.16×10^{-24}	m^2
	Reflective factor	α	2	
	Upper lever state lifetime	τ_f	951	μs
Variable parameters	Number of pump passes	M_p	24	
	Pump delay	Δt	100~800	μs
	Pump power	P	50 ~ 380	W
	Pump spot size	D	2.8	mm
	Frequency of seed pulse	f	100	kHz
	Thickness of thin disk	d	220	μm
	Doping concentration	N_{dop}	7	%at.
	Number of roundtrips	M_r	90	
	Loss factor	L	0.001	

6.1.1 Simulation results and discussion

The model mentioned above explores the scaling limits imposed by ASE on the thin disk regenerative amplifier, calculates the required pump energy for reaching specific output pulse energy, and predicts the performance of the thin disk regenerative amplifier under different

conditions. Therefore, the model should be calibrated based on experimental results. In this section, the simulated results are fitted with the experimental data of the regenerative amplifier developed at the HiLASE center. The regenerative amplifier was pumped by CW 969 nm diode at 380 W pump power, and 0.95 mJ pulses at 100 kHz repetition rate were delivered successfully. It had a cavity length of 3 m.

Moreover, the roundtrip number was set at 90, i.e., 180 double passes through the Yb:YAG disk to extract the stored energy efficiently. Part of the laser parameters is shown in the variable parameters of Table 6.1. More detail about its configuration can be found in reference [192].

Fig. 6.3(a) shows the simulated pulse build-up at a pump power of 380 W. The ASE effect has been considered in the simulation. The experimental data is shown in Fig. 6.3(b). A good agreement between the numerical model and experimental results was obtained. For example, we obtained simulated output energy of 1.01 mJ (i.e., output power 101 W) compared to experimental output energy of 0.95 mJ (i.e., output power 95 W) when the loss factor L was set at 0.16, which corresponds to the loss rate per one roundtrip of about 8.35% according to equation (4). The large loss rate of the simulation is caused by temperature-independent presumption. All the losses caused by heat in the thin disk are accumulated into the loss factor in our model. In order to use this model to predict the performance of the regenerative amplifier, the relationship between the loss factor and pump intensity also needs to be known. For this purpose, the loss factor was adjusted to match the simulated output energy of the regenerative amplifier with the experimental data measured at different pumping powers.

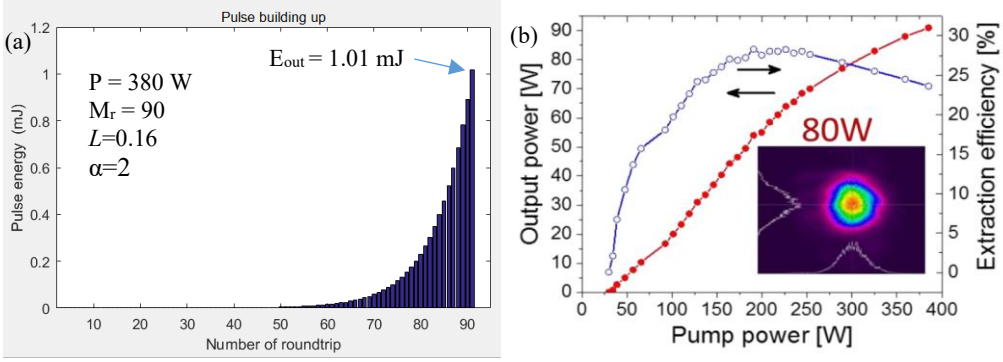

Fig. 6.3 (a): Simulated pulse building up in the regenerative amplifier for a pump power of 380 W, roundtrip number of 90, loss factor of 0.16, and reflective factor of 2. The simulated output energy was 1.01 mJ. At the given pumping intensity, the experimental maximal output energy was 0.95 mJ. (b): the experimental output power as a function of the pump power, taken from the reference [192].

Fig. 6.4(a) shows the experimental and simulated data with different loss factors. It is seen that output energy increases nonlinearly with the pump intensity mainly due to the increasing thermally induced diffraction losses at higher pump intensities. However, at a constant loss factor value, the simulated output energy increases linearly with the pump intensity. Thus, a single value of the loss factor cannot be used to describe the dynamic performance of the regenerative amplifier. Furthermore, we calculated the loss factors of the regen according to the experimental data. The loss factor was estimated separately at each pumping intensity, as shown in Fig. 6.4(b). We found that the loss factor does not change linearly with increasing pump intensity. The loss factor L increased from 0.01 at 0.8 kW/m^2 to 0.16 at 6.6 kW/m^2. Many

reasons cause the nonlinearity of the dynamic loss factor. We believe the main reason is the thermally induced diffraction losses, which increase nonlinearly with pump intensity.

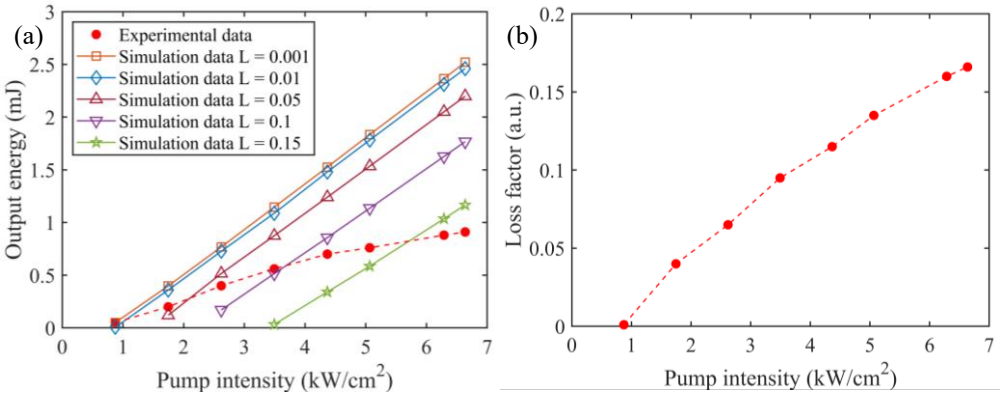

Fig. 6.4 (a) The experimental data and the simulated data with different loss factors, (b) the loss factor increased nonlinearly with pump intensity.

In order to predict the dynamic performance of the regenerative amplifier using the presented model, the following steps need to be taken: 1) Calculate the pump intensity. 2) Estimate the loss factor according to pump intensity. The estimated loss factor can then be used to simulate the regenerative amplifier. Although the estimated loss factor cannot be very accurate, the simulated results can be close to the experimental data with a proper estimation of the loss factor.

6.1.2 Conclusion

In conclusion, a practical numerical model of a thin disk regenerative amplifier has been built in this section. The effect of ASE has been considered in the model in terms of the effective lifetime of the upper-level state manifold in the rate equations. In order to verify the numerical model, the simulated results were fitted with experimental data of the regenerative amplifier built at the HiLASE Centre. By fitting the simulated results with experimental data, we have obtained a general way of using this model to explore the scaling limits imposed by ASE to predict or analyze the dynamic output performance of regenerative amplifiers under development at the HiLASE Centre.

6.2 The architecture of the BIATRI laser system

In this section, the details were introduced on the design, development, and performance of the BIATRI laser, which was the other main research interest during my Ph.D. study. The BIATRI laser system was initially designed as the laser source with 100 W of average power, 1 ps of pulse duration at 100 kHz of repetition rate with high beam quality ($M^2 < 1.3$) for the 6-year project entitled “Advanced designing of functional materials: From mono- to BI- And TRI-chromatic excitation with tailored laser pulses” (Acronym BIATRI), which was granted under the Operational Programme of Research, Development, and Education (OP VVV) of the

Ministry of Education, Youth and Sports, Czech Republic. During the development, the target parameters, mainly the pulse energy, of the BIATRI laser system were changed multiple times due to the requirements of the following laser applications of the project. The higher pulse energy was required. Therefore, some design features of the laser system were optimized to ensure high energy output.

In the following sections, the overview of the laser system will be first introduced, followed by the implementation of all fiber-based front ends (including the fiber pre-amplifier), the main thin disk regenerative amplifier, and the pulse compressors. The design aspects and experimental details are included in the relevant sections.

Overview of the laser layout

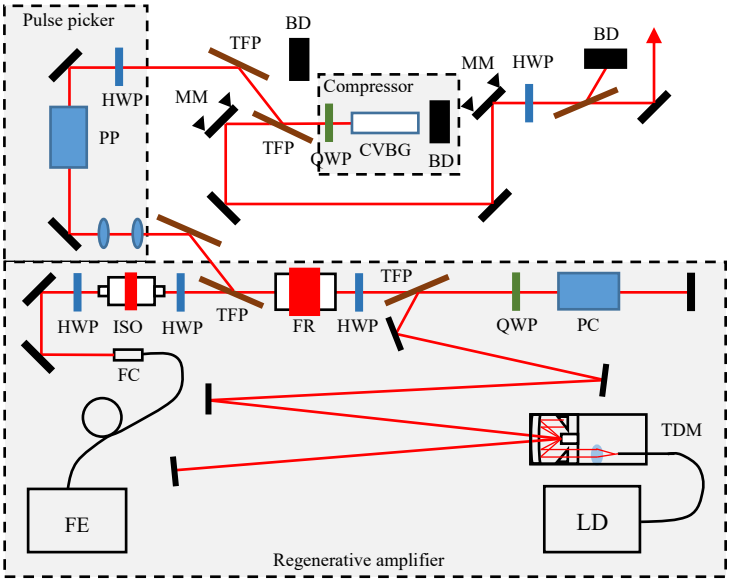

Fig. 6.5 The schematic overview of the first design of the BIATRI laser system, with a regenerative amplifier and CVBG pulse compressor. FE: Front-end, FC: Fiber collimator, HWP: Half-wave plate, ISO: Isolator, TFP: Thin film polarizer, PC: Pockels Cell, TDM: Thin disk module, LD: Laser diode, PP: Pulse picker, MM: Motorized mirror mount, CVBG: Chirped Volume Bragg Grating, BD: Beam dump.

The schematic overview of the first design of the BIATRI laser system is shown in Fig. 6.5, together with a regenerative amplifier and a Chirped Volume Bragg Grating (CVBG) as the pulse compressor. An all-PM-fiber-based front-end was used to seed the main regenerative amplifier with a stretched laser pulse of 500 ps pulse duration, 1 MHz repetition rate, and 1 μJ pulse energy (introduced in Section 6.3). The thin disk regenerative amplifier then amplified the seed laser beam to 93.9 W of average power with 0.94 mJ of pulse energy operating at 100 kHz repetition rate (completion in March of 2019). Due to the need of the BIATRI project, the pulse energy was scaled up to 5.5 mJ with 55 W of average power operating at 10 kHz of repetition rate (completion in June of 2019). In the first design (until December 2020), the beam was expanded by a telescope after ejecting it from the main amplifier. A pulse picker was designed to reduce the repetition rate and pulse picking. Then the pulses were compressed by a

CVBG compressor. The laser beam was stabilized by a Beam Stabilization System consisting of two motorized mirror mounts and two cameras (not shown in the figure), followed by a laser beam attenuator consisting of a half-wave plate and thin film polarizer.

Due to the need of the BIATRI project, 10 mJ of pulse energy was required regardless of the repetition rate. The BIATRI laser system was re-estimated and upgraded without damaging the optics in the laser. After precise calculation and simulation, it was found that this cavity was able to deliver pulse energy up to > 20 mJ without causing serious nonlinear effects, such as self-phase modulation (SPM) and self-focusing (SF), in the laser cavity. In December 2020, the upgraded laser was accomplished to deliver laser pulses with 50.6 W of average power, 300 ps of pulse duration, 20 mJ of pulse energy, and 2.5 kHz repetition rate before pulse compression. The repetition rate was initially set at 5 kHz. It was reduced to 2.5 kHz due to significant bifurcation with very high pulse train contrast (> 100:1). A pair of gratings were used to compress such a high-energy laser pulse. The upgraded design is shown in Fig. 6.6. At last, the laser was running at 25 W of average power, 10 mJ of pulse energy, 2.5 kHz of repetition rate (with bifurcation), and 1 ps of pulse duration for the Nonlinear Optics Team led by Dr. Ondrej Novak.

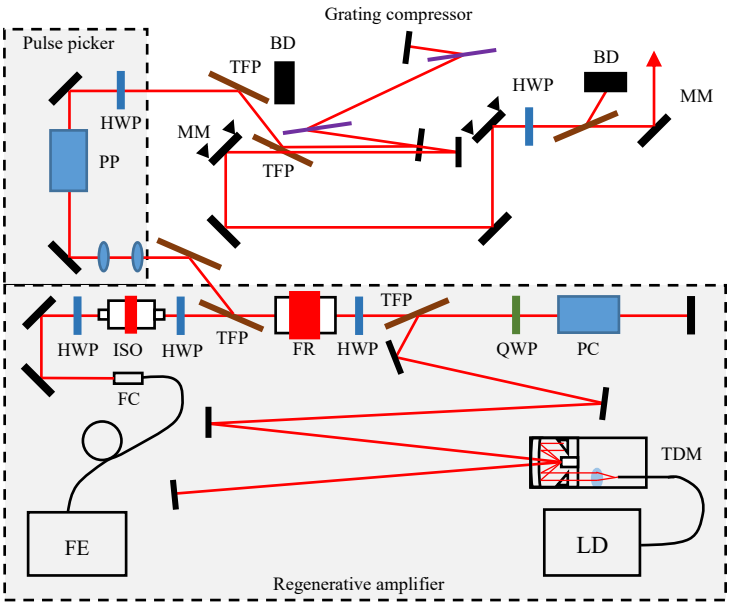

Fig. 6.6 The schematic overview of the upgraded design of the BIATRI laser system, with a regenerative amplifier and CVBG pulse compressor. FE: Front-end, FC: Fiber collimator, HWP: Half-wave plate, ISO: Isolator, TFP: Thin film polarizer, PC: Pockels Cell, TDM: Thin disk module, LD: Laser diode, PP: Pulse picker, MM: Motorized mirror mount, BD: Beam dump.

6.3 The first design of the BIATRI laser

6.3.1 The first design of all-PM-fiber front-end

Fig. 6.7 shows the layout of the first design of the all-PM-fiber-based front-end. All the fiber components used in this front end were polarization-maintained. A commercial fiber oscillator (YLMO from MenloSystems company, as shown in Fig. 6.8(a)) was used as the seed pulse generator. The spectrum and the pulse width of the seed pulse from the oscillator are shown in Fig. 6.8(b) and (c), respectively. The bandwidth (FWHM) was 13 nm, and the pulse duration (Gaussian fitting) was measured to be 28.6 ps (FWHM). The spectrum was measured with an integrating sphere (Thorlabs integrating sphere IS236A-4). However, apparent periodical modulation was still observed on the spectrum. More details regarding the issues of the YLMO oscillator will be discussed in Section 6.3.5.

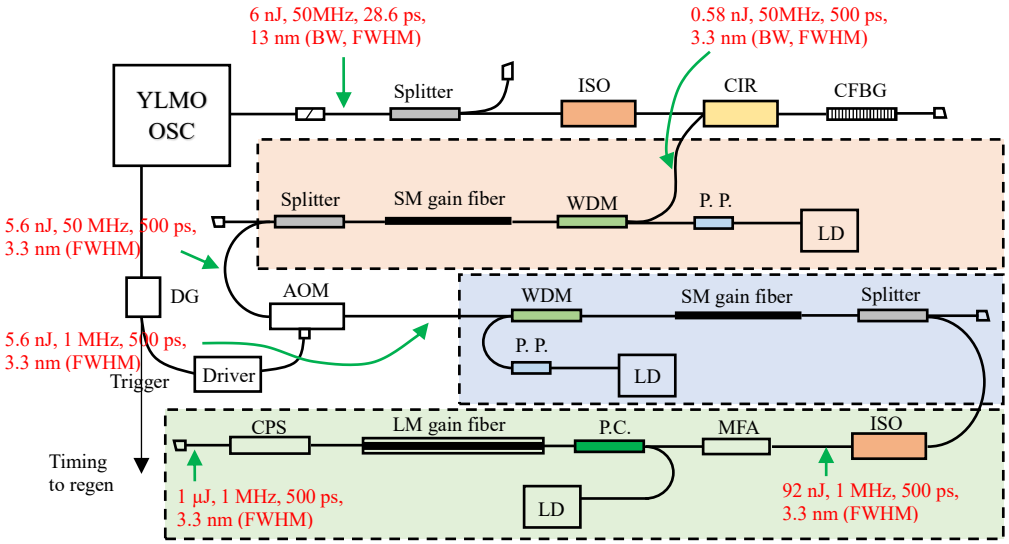

Fig. 6.7 The schematic overview of the first design of the all-PM-fiber-based front end. All the fiber components used in this front end were polarization maintained. OSC: Oscillator, ISO: Isolator, CIR: Circulator, CFBG: Chirped Fiber Bragg Grating, WDM: Wavelength Division Multiplexing, P.P.: Pump protector, SM: single mode, AOM: Acoustic Optic Modulator, MFA: Mode field adaptor, LM: Large mode, CPS: Cladding power stripper.

A fiber optical isolator was used to protect the oscillator. A chirped fiber Bragg grating (CFBG) stretcher, type TPSR-1030V-3.3F[204M-2.5-(204)]-0P1-0T from Teraxion with a tunable dispersion coefficient of -204 ± 38 ps/nm, stretched the laser pulse duration from 28.6 ps to 500 ps. The nominal center wavelength of this stretcher was located at 1030.3 nm with a bandwidth of 3.3 nm (FWHM) and reflectivity of 47.6%. Therefore, about 88% of the pulse energy from the oscillator was lost after stretching, since the stretcher only reflected the target spectrum of the seed pulse. Then the stretched seed pulse was amplified by a single-mode fiber, which consisted of a single-mode PM gain fiber (length of 1 m, type PM-YSF-HI-HP from Nufern), WDM, pump protector, and a single-mode fiber-coupled laser diode (980 nm, 3S Photonics 1999CHP) as the pump source. The repetition rate of the pulse train was reduced

from 50 MHz to 1 MHz by a 200 MHz fiber Acoustic Optic Modulator (AOM) (T-M200-0.1C2G-3-F2S from Gooch&Housego) acting as a pulse picker. The average power of the seed pulses decreased to 5.6 mW.

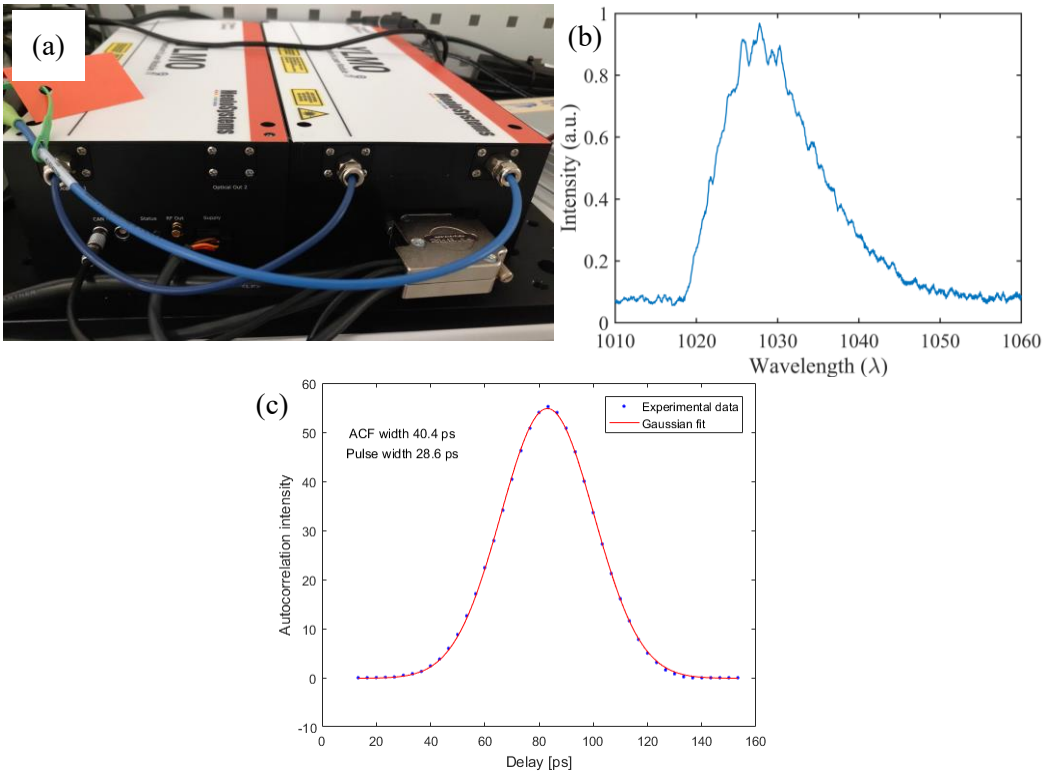

Fig. 6.8 (a) YLMO oscillator from Menlo Systems company, (b) Spectrum of the YLMO oscillator with a bandwidth (FWHM) of 13 nm, (c) Pulse duration of the YLMO oscillator with a pulse duration of 28.6 ps (Gaussian fit, FWHM).

A second single-mode fiber amplifier, the same as the first fiber preamplifier, was used to boost the laser power to 92 mW. The mode field of the laser beam was then enlarged by and Mode Field Adaptor (MFA) to match the large mode double cladding fiber since a third fiber preamplifier, which consisted of a large mode double cladding gain fiber (length of 1 m, type PLMA-YDF-10/125-VIII from Nufern), was used to amplify the seed pulse furthermore.

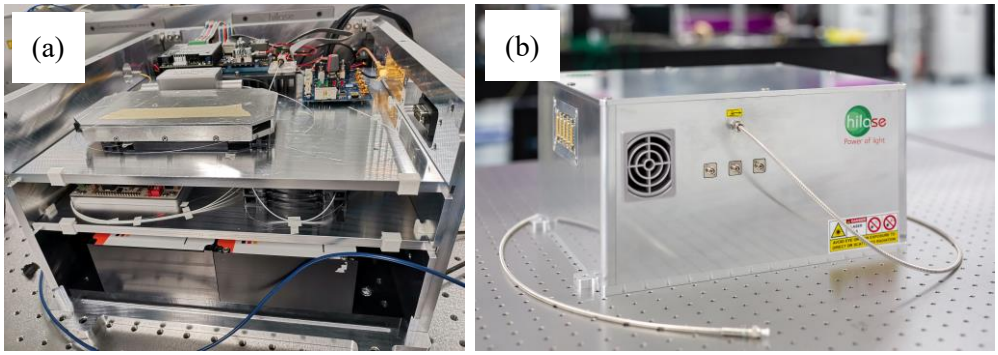

Fig. 6.9 (a) The first design of the front end, including the oscillator and three stages of fiber preamplifiers, and (b) the final build of the first design of the front end.

The laser pulse was amplified to 1 µJ of pulse energy and ejected from the fiber after stripping the residual pump light with a Cladding Power Stripper (CPS). Multiple fiber splitters with a

splitting ratio of 98:2 were used in the front end to sample the laser light to monitor the oscillator's status or preamplifiers. Fig. 6.9 shows the photos of the front end.

Performance of the front-end

Amplified seed laser beam was obtained with 1 W of average power, 1 MHz of repetition rate, 3.3 nm of bandwidth (FWHM) centered at the wavelength of 1030.3 nm, and 494 ps of pulse duration. The warming-up time for the front end was 1 hour. The long-term stability of the front-end output power was measured to be 0.36% for 5 hours after warming up. The results are shown in Fig. 6.10, respectively.

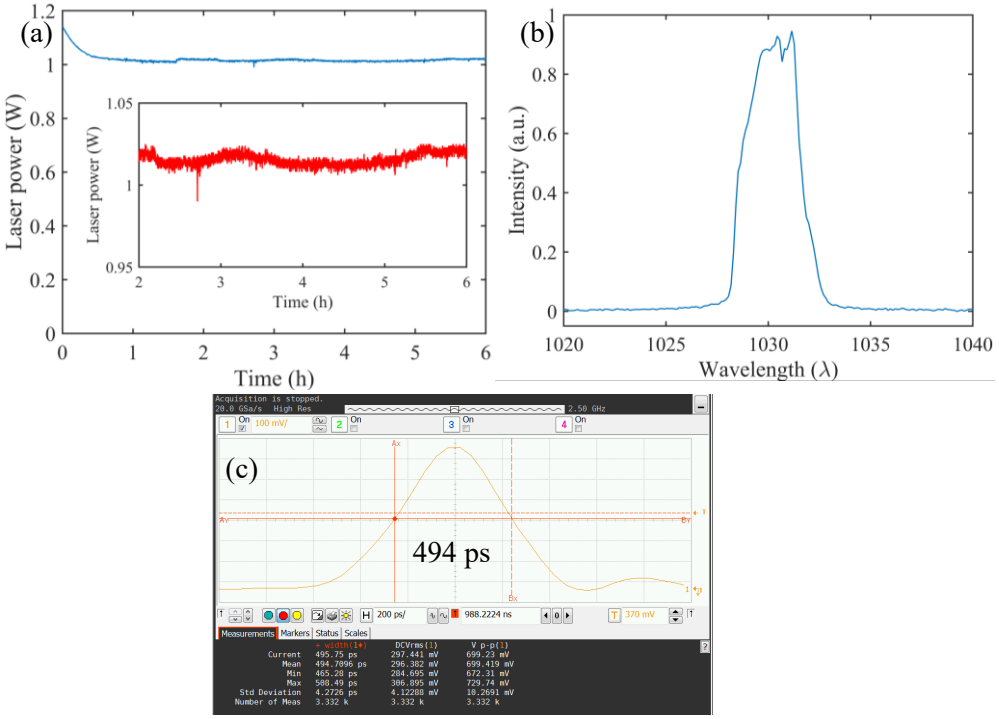

Fig. 6.10 (a) Long-term stability (RMS) of the average power of the front-end for 6 hours. It took the front end 1 hour to get warm. After warming up, the RMS stability is 0.36% for 5 hours. (b) The spectrum of the front-end measured at full power after warming up, with a bandwidth of 3.3 nm (FWHM) centered at 1030.3 nm. (c) The pulse duration of 494 ps, measured at full power after warming up.

6.3.2 Thin disk module and pump source

The critical component of the regenerative amplifier is the thin disk gain medium which is mounted in a pump chamber (thin disk module) and pumped by a laser diode, as introduced in Section 3.2. This section briefly introduces the thin disk module and the pump source.

As shown in Fig. 6.11 (a) Yb:YAG thin disk used in the regenerative amplifier, (b) and (c) photos of the thin disk module TDM 1.0 from Dausinger+Giesen GmbH.(b) and (c), the thin disk module used in this work was TDM 1.0 manufactured at Dausinger + Giesen GmbH. The gain medium was Yb:YAG thin disk, as shown in Fig. 6.11(a), with 7 at.% of doping concentration, 12 mm of diameter, and 215 μm of thickness. The front side of the disk was

coated with anti-reflective (AR) coating for both the pump and emission wavelengths. The back side was coated with a highly reflective (HR) coating for both wavelengths. The disk was bonded to a CVD diamond heatsink of 16 mm in diameter and 2 mm in thickness, with high thermal conductivity of 1200 – 2250 W/(m·K) [193]. The disk had a concave surface shape with a radius of curvature of 3.8 m. The thin disk was wedged by about 0.1° to prevent the etalon effect. The disk was cooled with 18 °C water at the flow rate of 2 l/min with a water pressure of 2.3 bar.

With this pump chamber, 24 passes (i.e., 12 reflections) of pump light through the disk can be realized to achieve sufficient absorption (>93% of absorption efficiency [194]). The thin disk module was configured with a high-power laser fiber with 1 mm of core diameter and 0.22 of Numerical Aperture (NA). The pump spot diameter was 2.7 mm with a proper collimator. In order to handle a high average power, the pump chamber, the pump optics, the collimator mount, and the fiber holder were cooled with water with a 1 l/min flow rate from a parallel branch of the thin disk's cooling circuit. The maximum allowed pump intensity on the thin disk was specified as 6 kW/cm^2 without damaging the disk.

Fig. 6.11 (a) Yb:YAG thin disk used in the regenerative amplifier, (b) and (c) photos of the thin disk module TDM 1.0 from Dausinger+Giesen GmbH.

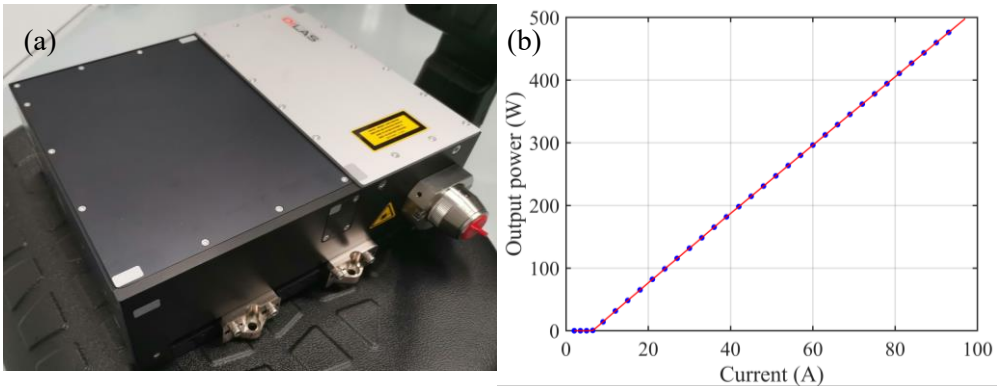

Fig. 6.12 (a) DILAS IS45.4MP pump diode laser, (b) output power vs. current

Zero-phonon-line pumping was preferred to reduce the quantum defect of the thin disk [195][196]. A diode laser DILAS IS45.4MP with a VBG-stabilized wavelength of 969 nm (FWHM bandwidth of 0.3 nm) was used to implement the zero-phonon-line pumping. Its maximum output power was 500 W. Fig. 6.12 shows the photo of the pump diode laser and its power

curve. The diode laser was cooled with 25 ℃ low-conductivity (< 3 μS/cm) water at a flow rate of 7 l/min.

6.3.3 Cavity design of the regenerative amplifier

A highly stable laser cavity is essential for obtaining diffraction-limited ultrafast laser pulse. The performance of the thin disk regenerative amplifier, such as power stability, optical efficiency, and beam quality, highly depends on the laser cavity design. The laser cavity was designed with the reZonator software [197], which is developed based on the ABCD matrix formalism [198][199].

Here are the considerations for designing the laser cavity:

1. The maximum output power is 100 W after compression; therefore, the uncompressed power should be around 120 W assuming compression efficiency of > 80%，
2. After compression, the maximum pulse energy is 1 mJ (for the first design before upgrading). Therefore, the maximum energy of the uncompressed pulse should be around 1.2 mJ,
3. The intracavity pulse duration is 500 ps (FWHM),
4. The thin disk's Radius of Curvature (RoC) was 3.8 m when it is not pumped. According to the previous experiments on other thin disk laser systems developed in our laboratory, the concave shape of the thin disk becomes flattered with increasing pump laser power due to the thermal expansion of the thin disk and its substrate [200]. For the thin disk with a diamond heatsink used in this work, the RoC would increase only by about a few centimeters (< 0.5 m) when pumped by a 969 nm diode laser with 4.5 kW/cm^2 intensity on the thin disk according to our experience.
5. The Eigenmode diameter on the thin disk should be around 2 mm (75% of the pump spot diameter, which is 2.7 mm. The optimum overlap of the pump spot and the eigenmode for fundamental mode operation of a thin disk laser is recommended to be 70% ~ 80% [201][202]. In this work, I decide to use the overlapping ratio of 75%) for optimal energy extraction efficiency and single transverse (fundamental) mode operation of the thin disk laser,
6. Eigenmode diameter on the optical elements, such as mirrors, waveplates, etc., should be large enough to avoid damaging their coating,
7. The beam diameter in the BBO crystal should be large enough to minimize the B-integral, which is the accumulated nonlinear phase shift of the laser light, to avoid nonlinear effects, such as Self-Phase Modulation and Self-focusing, in the BBO crystal. The dimension of the BBO crystal, which was planned to be used in this work, was 8x8x25 mm^3. Therefore, the beam diameter should not exceed 3.2 mm (40% of the width of the BBO crystal. Laser beam with a larger diameter would get cropped by the

crystal and lead to the increased insertion loss of the laser cavity),

8. The cavity length should be longer than 1.2 m (depending on the rising time of the driver for Pockels cell. In this work, a Pockels cell driver bpp5d3, which provides a maximum high voltage of 10 kV with a rising time of 8 ns, from BME KG company. Thus, the cavity length L = (Rising time × speed of light) / 2). Therefore, the laser pulse would not be clipped by the Pockels cell after one roundtrip in the cavity.

The evolution of beam radius of the eigenmode of the designed cavity is plotted and shown in Fig. 6.3.7. A flat turning mirror (angle of incidence: 45°) was used after the TFP to fold the cavity during construction of the laser cavity. The eigenmode diameter on the thin disk was 2.1 mm when not pumped, about 78% of the pump spot diameter. The eigenmode diameters on the optical components were kept within 2 ~ 2.2 mm except that on the only plano-convex mirror (marked as PCV in Fig. 6.13), where the eigenmode diameter was only 1.56 mm. In the case of the highest considered pulse energy of the amplifier output of 1.25 mJ, the maximum pulse fluence on those optical components in the cavity was less than 0.06 J/cm^2, which is far lower than the damage threshold fluence (4 – 6 J/cm^2 for picosecond pulse specified by the manufacturer LAYERTEC [203]) of the mirror used in the laser cavity.

The cavity length was 2.84 m, resulting in a cavity roundtrip time of 18.9 ns.

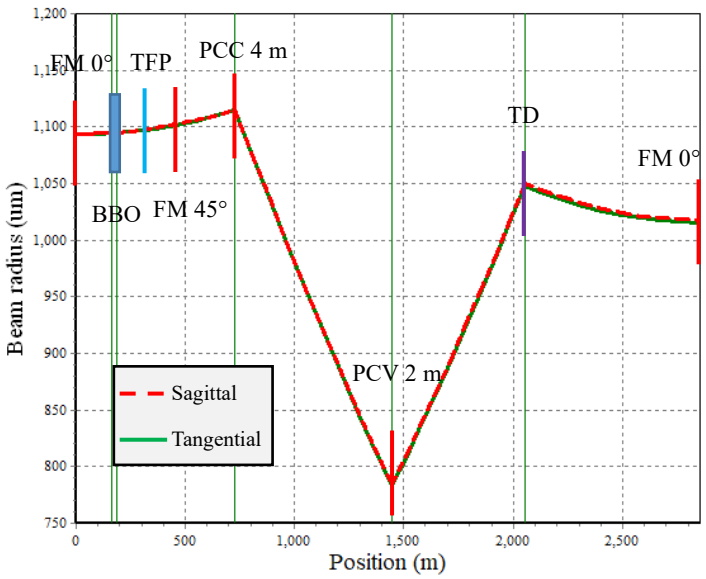

Fig. 6.13 The evolution of the eigenmode's beam radius along the regenerative amplifier's laser cavity. The RoC of the thin disk was assumed to be 3.8 m (concave shape). FM: flat mirror, TFP: thin film polarizer, PCC: plano-concave mirror, PCV: plano-convex mirror, TD: thin disk. The eigenmode beam radii in both the sagittal and tangential planes overlap, indicating high ellipticity (> 0.98) of the eigenmode of this cavity.

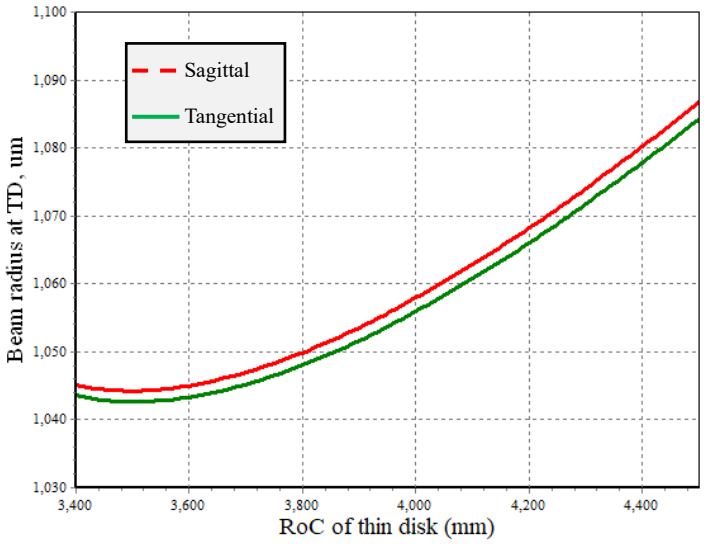

Fig. 6.14 The eigenmode beam radius on the thin disk as a function of the RoC of the thin disk.

Fig. 6.14 shows the thin disk's eigenmode radius against the thin disk RoC from 3.8 m to 4.5 m, corresponding to the increase of the pump laser intensity from 0 kW/cm^2 to more than 4.5 kW/cm^2. It could be seen that the eigenmode diameter on the thin disk increased from 2.1 mm to 2.17 mm.

The stability parameter of this cavity is defined as (A+D)/2 from the cavity roundtrip matrix introduced in literature [198] plotted versus the RoC of thin disk and shown in Fig. 6.15. The condition of $-1 < (A+D)/2 < 1$ should be fulfilled to obtain a stable cavity. It could be seen from Fig. 6.15 that the cavity was stable for thin disk RoC varying from 3.8 m to 4.5 m.

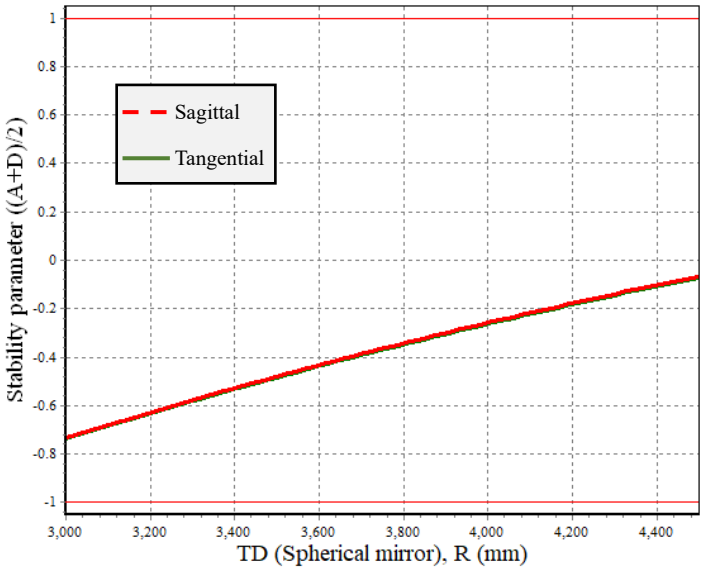

Fig. 6.15 The stability parameter of the laser cavity plotted vs. RoC of the thin disk. Values of ±1 represent the limits of the stability region.

6.3.4 Performance of the regenerative amplifier

CW performance

The laser cavity was then constructed and optimized, as shown in Fig. 6.16. During the optimization process, the distances between the last cavity mirror and the thin disk were tuned to obtain the highest slope efficiency and stability of the laser output in continuous wave (CW) operation mode.

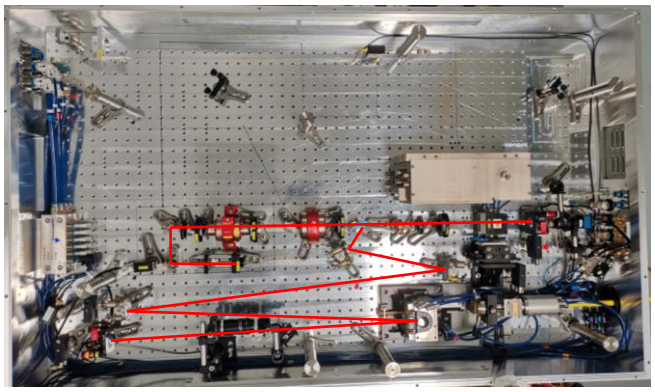

Fig. 6.16 The constructed laser cavity for testing.

The Pockels cell was inserted into the cavity and precisely aligned during the test. A maximum 112 W of average output power was obtained from this cavity in CW operation mode after optimization. Fig. 6.17 shows the average output power and optical-to-optical (O-O) conversion efficiency plotted versus the pump power. The O-O efficiency was 52.3% at 213 W pumping with a pump intensity of 3.72 kW/cm^2 on the disk. The slope efficiency was 58.6%. The inset in Fig. 6.17 is the output laser beam profile measured at full output power. It could be seen from the O-O efficiency that the laser was still not saturated yet.

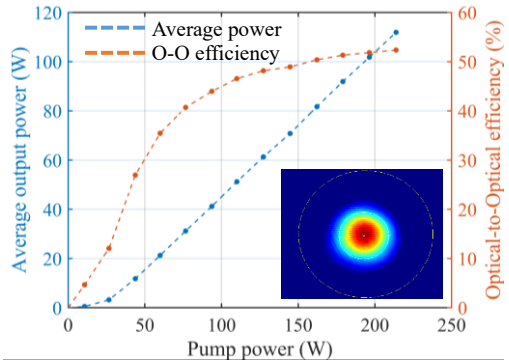

Fig. 6.17 Average output power and optical-to-optical (O-O) conversion efficiency are plotted as functions of the pump power for CW operation mode. The maximum output power was 112 W with maximum O-O the efficiency of 52.3% and slope efficiency of 58.6%. The inset is the beam profile of the laser output measured at full output power.

Pulse energy scaling up to 5 mJ

In March 2019, a new task was requested by the BIATRI project that 5 mJ of pulse energy of

the fundamental laser was needed for the OPA system. Thus, the laser cavity was re-estimated. For obtaining 5 mJ output pulse energy with the same laser cavity, the maximum pulse fluence on the plano-convex mirror in the cavity was about 0.24 J/cm^2, which was still far lower than the damage threshold fluence (4 – 6 J/cm^2). The pulse energy can be increased by reducing the repetition rate of the laser. Since the average power was not essential for the BIATRI project, we decided to run the laser at 10 kHz with an average power of around >50 W.

Since pulse energy needed to be increased by about 5 times, the accumulated nonlinear phase shift of the laser pulse, referred to as the B-integral, should be considered. The B-integral can be calculated by

$$B = \frac{2\pi}{\lambda}\int_0^L n_2(z)I(z)\,\mathrm{d}z \tag{6.1}$$

where λ is the lasing wavelength and L is the propagation length of the laser beam along the direction z, $n_2(z)$ is the nonlinear refractive index of the nonlinear medium along the beam path, *I(z)* is the intensity of the laser pulse along the beam path.

Table 6.2 Parameters used in the calculation of B-integral accumulated in BBO crystal

Parameter	Value
Seed pulse energy (E_{seed})	1 μJ
Output pulse energy (E_{output})	1 – 20 mJ
Number of roundtrips	30 – 100
Pulse width (τ)	500 ps
Peak power*	E/ (0.88τ)
Eigenmode radius	1.08 mm
BBO dimension	8×8×25 mm^3

*Assuming sech^2 pulse shape

The BBO crystal in the Pockels cell contributes about 87.3%, and cavity air contributes about 11.5% to the B-integral per roundtrip [210]; the total accumulated B-integral per roundtrip can be estimated by simply rescaling the calculated B-integral in BBO crystal. The amplification process should also be taken into consideration since the pulse energy is amplified after each roundtrip by two reflections on the thin disk. Therefore, the B-integral can be calculated during the amplification process (see Section 3.3.1) using Eq. 6.1 and integrated into the numerical model developed in Section 6.1. Fig. 6.18 shows calculated B-integral values accumulated in BBO crystal as functions of pulse width for different pulse energy intracavity (assuming 70 roundtrips). The typical parameters used in the calculation are shown in Table 6.2. The maximum pulse energy of 20 mJ was also calculated to check the potential of this cavity.

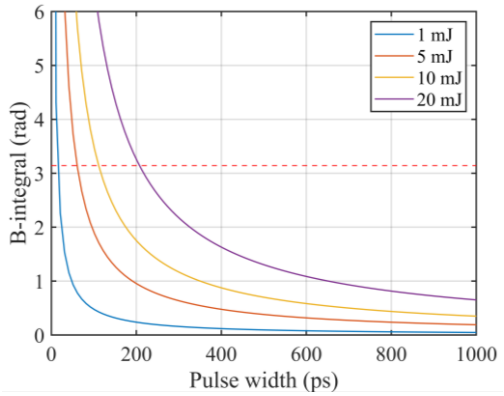

Fig. 6.18 B-integral accumulated in BBO crystal (8×8×25 mm^3) as a function of pulse width for different pulse energy intracavity (assuming 70 roundtrips). The red dashed line indicates the B-integral value of π.

The B-integral accumulated in the BBO crystal for 5 mJ of output pulse energy is calculated to be 0.68 rad for 500 ps pulse width. Therefore, the total B-integral accumulated in the cavity can be estimated to be 0.78 rad, which is much less than π for the safe operation of a regenerative amplifier [204]. In the case of B < 1, the phase distortion of the laser pulse can be neglected [205]. It could be seen from the calculation that this cavity can handle pulse energy up to 20 mJ for 500 ps of pulse width and > 70 roundtrips.

The piezoelectric ringing phenomenon in Pockels cell

Before operating the cavity in regeneration mode, the Pockels cell was tested with a pulse-picking experiment. Pockels cell is an electro-optic (EO) device that consists of an electro-optic crystal, such as Beta barium borate (β-BaB_2O_4, BBO) crystal, Di-deuterium phosphate (KD_2PO_4, KD*P) crystal, through which the laser beam (linear polarized) is transmitted. The polarization direction of the laser beam can be controlled by applying high voltage to the crystal. The basic principle of such a Pockels cell is Pockels Effect: applying a constant or variable voltage (electric field) onto the electro-optic crystal leads to linear changes in the birefringence of the crystal (in contrast to the Kerr Effect, which is quadratic with E) [206]. A Pockels cell, a wave plate, and a polarizer form an electro-optic switch, which is a typical feature of the regenerative amplifier cavity. For such a standing-wave cavity of a regenerative amplifier, as shown in Fig. 6.5, a quarter-wave phase shift (π/2) can be introduced to the laser beam by applying a quarter-wave voltage $V_{\lambda/4}$ on the electro-optic crystal with length L and thickness d in one roundtrip:

$$V_{\lambda/4} = \frac{\lambda d}{4 r_{22} n_0^3 L} \tag{6.2}$$

where n_0 is the refractive index of the nonlinear crystal at the laser wavelength λ and r_{22} The crystal's electro-optic (EO) coefficient corresponds to the transverse Pockels effect [207].

In this thesis, the BBO crystal was selected as the EO crystal due to its high damage threshold (about 2.16 GW/cm^2 @ 1064 nm [208]) and low absorption at around 1 μm wavelength low tendency to piezoelectric ringing compared to other EO crystals. I chose a BBO crystal of

dimension 8×8×25 mm^3 produced by Caston Inc. (Fuzhou, China). The EO coefficient of a BBO crystal is $r_{22} = 2.5\ pm/V$ for the wavelength of 1030 nm [209]. Thus, the quarter-wave voltage required in this work was approximately 7.26 kV.

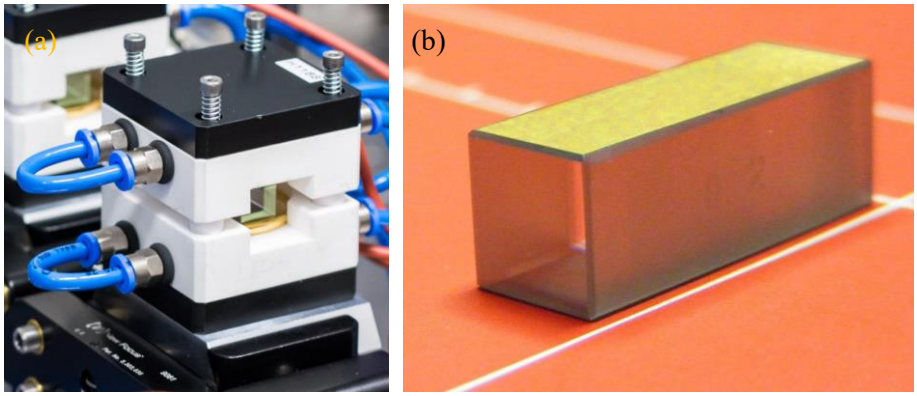

Fig. 6.19 (a) Photo of the water-cooled Pockels cell developed at HiLASE Center [210], (b) a z-cut BBO crystal with Au coated for electrodes on two side surfaces.

In order to avoid thermal depolarization in Pockels cell due to heat generated in BBO crystal working in a high frequency and high average power laser, it is necessary to remove the heat generated by the laser absorption, electrical heating of the electrodes [211] and piezoelectric ringing effect [212][213]. Fig. 6.19(a) shows the second generation of Pockels cell developed at HiLASE by Luděk Švandrlík. The housing of the Pockels cell was made from aluminum oxide (Al_2O_3) ceramics with internal water channels for cooling and a pair of circular Au-coated copper electrodes, which were horizontally oriented in the Pockels cell housing. Four spring-loaded screws were used to fix the Pockels cell.

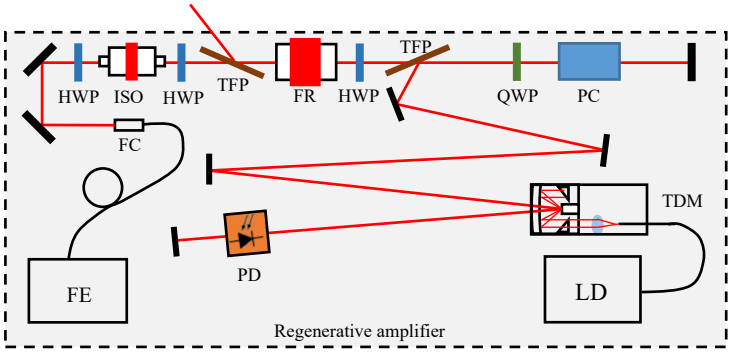

Fig. 6.20 Modified experimental setup for testing the Pockels cell. PD: Photodetector. The ND filter for PD is not shown in the figure. The experiments were carried out without a pump laser.

The optimal quarter-wave voltage of the Pockels cell was optimized by a pulse-picking experiment with the Pockels cell installed in the laser cavity without turning on the pump laser, as shown in Fig. 6.20. The seed pulse train was used as the laser source for the experiment. A photodetector with an ND filter (attenuating the seed laser power to avoid damaging the PD) was placed in the beam path of the laser cavity. With this configuration, pulses were picked up by applying quarter-wave voltage on the Pockels cell. By rotating the angle of the quarter-wave plate, the picked pulses can be injected into the laser cavity and detected by the PD (the rest pulses of the pulse train would be ejected out of the laser cavity) or vice versa.

A 2.5 GHz digital oscilloscope (DSO9254A Digital Storage Oscilloscope from Agilent Technologies), a 2 GHz high-speed biased photodetector (DET025AL from Thorlabs), and a high voltage probe (10076C from Agilent Technologies) were used for the test. During the test, the angle of the quarter-wave plate was tuned so that the picked pulses were ejected out of the cavity. After applying the high voltage on the Pockels cell, tune the angle of the quarter-wave plate and the high voltage. Then the optimal quarter-wave voltage can be obtained by observing the contrast ratio between the unpicked pulses and the ground level where the pulses were ejected, as marked by the red rectangle in Fig. 6.21(a). The optimal quarter-wave voltage was about 6.4 kV when the highest contrast ratio was observed.

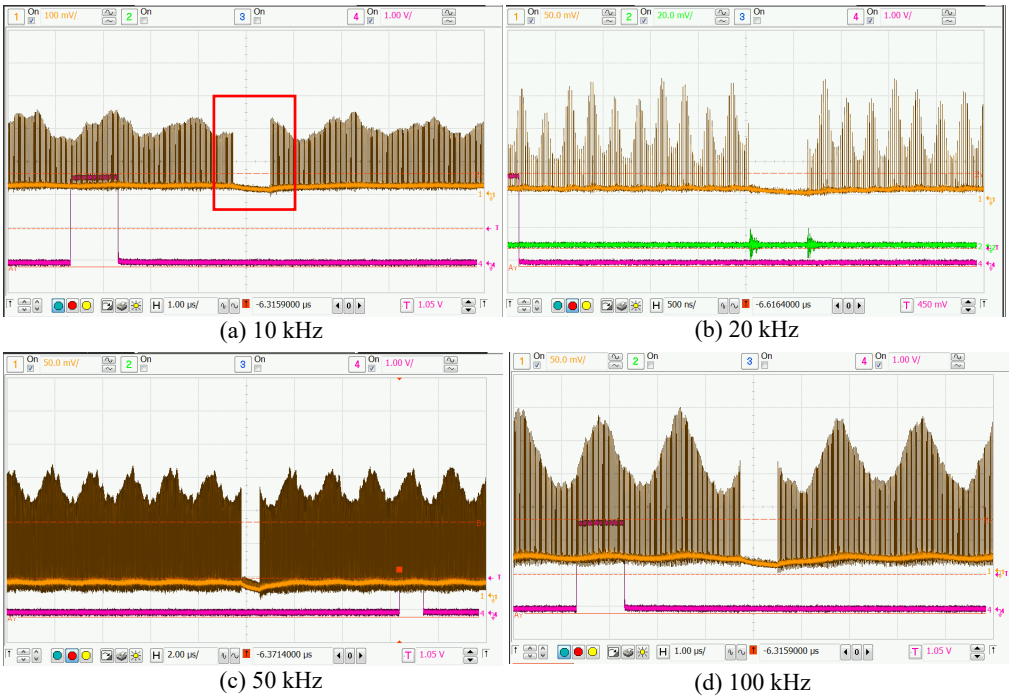

(a) 10 kHz (b) 20 kHz

(c) 50 kHz (d) 100 kHz

Fig. 6.21 Measured pulse trains were influenced by the serious piezoelectric ringing effect of the Pockels cell with different high voltage frequencies during the pulsing picking test. The frequencies of high voltage are (a) 10 kHz, (b) 20 kHz, (c) 50 kHz, (d) 100 kHz, respectively. The purple curves were the high voltage signal sampled from the trigger signal of the Pockels cell driver; the brown curves were the seed pulse train under test. The time difference between the high voltage signal (purple square pulse) and the optical pulses was caused by the delay due to the long cables used between PD, probe, and oscilloscope. The green curve in (b) was the measured high voltage signal with a high voltage probe, indicating the period when the high voltage was applied to the Pockels cell. Green curves were hidden for other measurements.

However, serious piezoelectric ringing effect and its influence on the seed pulse train were observed for every high voltage frequency from 10 kHz to 123 kHz. Fig. 6.21 shows some measured pulse trains influenced by the piezoelectric ringing effect of the Pockels cell with different high voltage frequencies. At some frequencies, the resonance amplitude was about 70% of the maximum amplitude of the seed pulse train, as shown in Fig. 6.21(b). It was then found that the spring-loaded screws could not provide sufficient clamping force to fix the BBO crystal. Thus, the springs were removed, and the Pockels cell was fixed directly with screws. After applying a clamping force of around 5 N on the crystal [210], the serious piezoelectric ringing

was not observed again; the pulse train top was almost flat with a resonant amplitude of less than 3%.

Regeneration operation mode

The seed pulses were injected into the laser cavity in regeneration operation mode. The repetition rate was set to 10.12 kHz. After optimization, the output power of 67.4 W (corresponding to 6.66 mJ pulse energy) was obtained with an amplification time of 1 μs (54 roundtrips) at a pump intensity of 3.82 kW/cm^2. The optical-to-optical conversion efficiency was 41.6%, and the slope efficiency was 53.2%. Fig. 6.22(a) shows the output power of the regenerative amplifier as a function of the pump power. The beam profile of the output laser beam is shown in the inset of Fig. 6.22(a), with an ellipticity of 0.967.

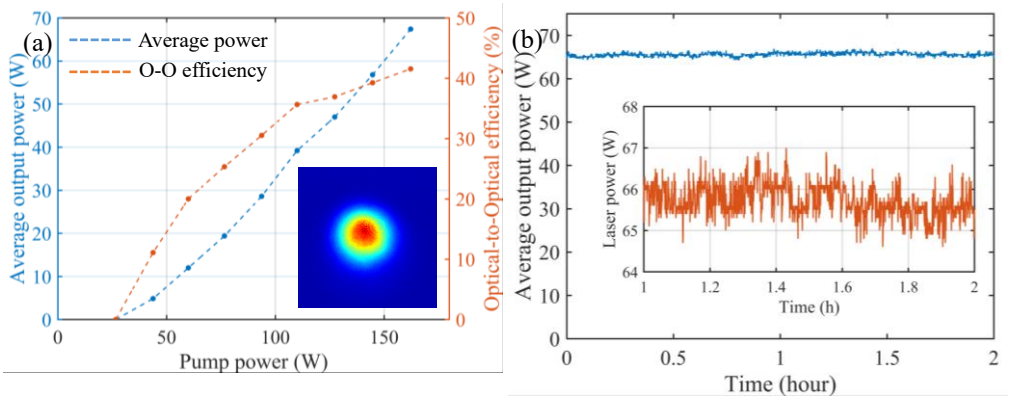

Fig. 6.22 Performance of the regenerative amplifier at a repetition rate of 10.12 kHz (a) the output power and O-O efficiency as functions of the pump power, with maximum O-O the efficiency of 41.6% and slope efficiency of 53.2%. The inset shows the beam profile of the output laser beam with an ellipticity of 0.967. (b) The output power stability was 0.6% (RMS) over 2 hours after warming up. The inset shows a zoom for the stability curve.

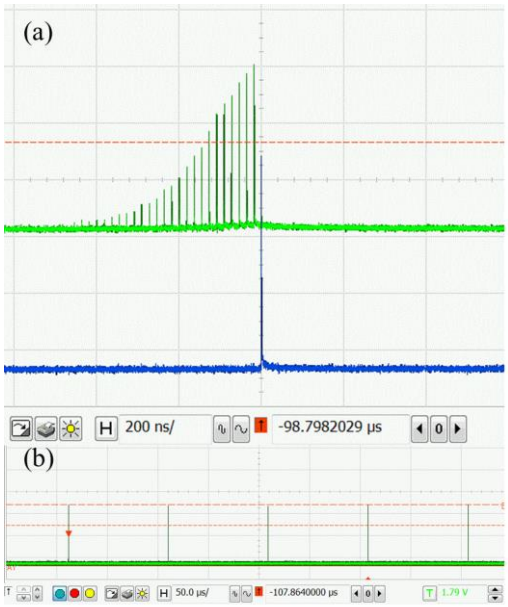

Fig. 6.23 (a) The output pulse (blue) and pulse building-up (green) of the regenerative amplifier for 54 roundtrips, 67 W output power, and (b) the output pulse train.

The pulse energy was sufficient for the user. Therefore, the laser was not scaled up further, although it was still not saturated, as seen from the power curve. The stability of the output

power was measured to be 0.6% (RMS) over 2 hours after warming up the laser (1 hour of warming up time), as shown in Fig. 6.22(b). Fig. 6.23(a) shows the output pulse (blue) and the pulse building-up (green) of the regenerative amplifier measured at the leakage of one cavity mirror. It could be seen from the pulse building-up that the laser was still not saturated. Fig. 6.23(b) shows the output pulse train.

The beam quality of the uncompressed laser pulse was measured and shown in Fig. 6.24(a). The regenerative amplifier operated in fundamental transverse mode with beam quality factors $M^2_{Horizontal}$ = 1.11 and $M^2_{Vertical}$= 1.09 for both the horizontal and vertical axes. Fig. 6.24(b) shows the beam profiles of the near field and far field (focal spot profile, with a plano-convex lens of 500 mm of focal length) measured during the beam quality measurements.

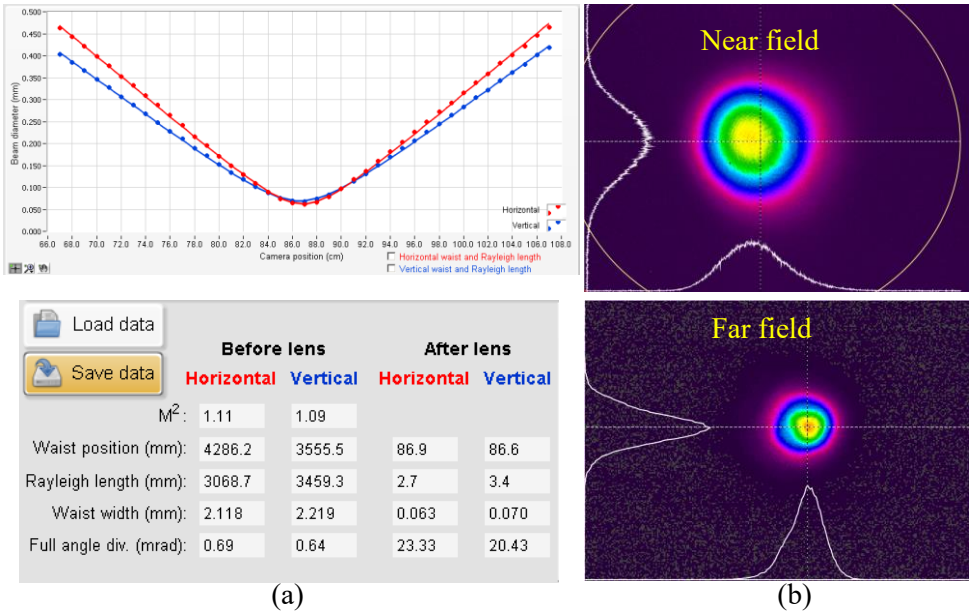

Fig. 6.24 (a) Beam quality of the uncompressed laser pulse at full power output, with $M^2_{Horizontal}$ = 1.11 and $M^2_{Vertical}$= 1.09 for both the horizontal and vertical axes; (b) the beam profiles of near field (top) and far-field (bottom, focal spot profile, with a focusing lens of 500 mm of focal length) measured during the beam quality measurements.

The spectrums of the seed pulse and the uncompressed output beam from the regenerative amplifier were measured and shown in Fig. 6.25. Due to the gain-narrowing effect of the regenerative amplifier, the bandwidth (FWHM) decreased from 3.3 nm (seed pulse) to 1.83 nm (amplified pulse), which corresponded to a transform-limited pulse duration of 853 fs.

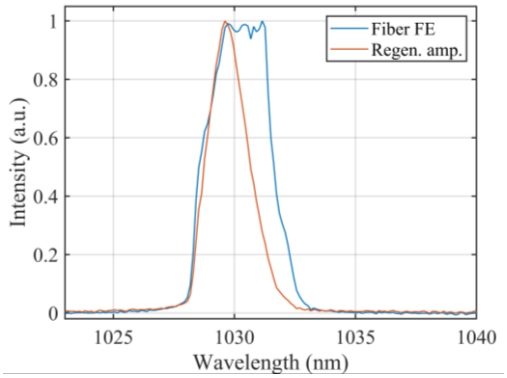

Fig. 6.25 Spectrum of the fiber front-end output (blue, FWHM bandwidth of 3.3 nm) and the regenerative amplifier output (orange, FWHM bandwidth of 1.83 nm).

Bifurcation was observed after running the laser for a few weeks, as shown in Fig. 6.26(a). Bifurcation usually occurs for high roundtrips and leads to an oscillating output pulse energy [214] when the repetition rate is lower than 15 kHz [215]. Simulation results, as shown in Fig. 6.26(b) simulated with the numerical model developed in Section 6.1, shows that the essence of bifurcation is the unbalance between the loss and gain of the laser cavity.

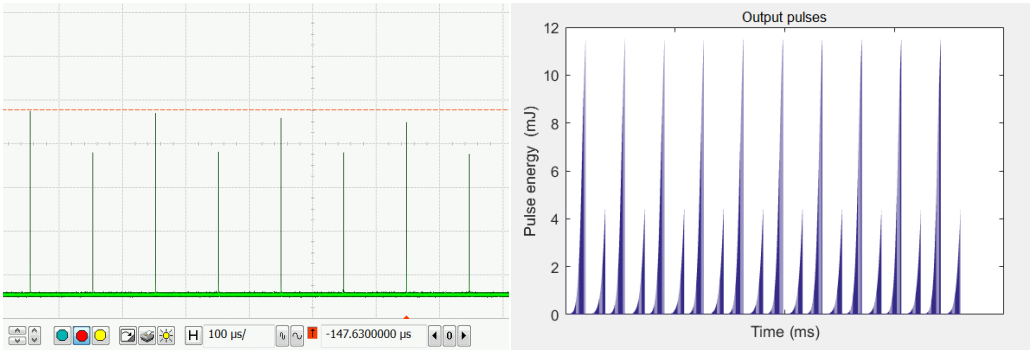

Fig. 6.26 (a) Bifurcation occurred after running the laser for a few weeks, (b) simulated bifurcation with the actual parameters and high cavity loss.

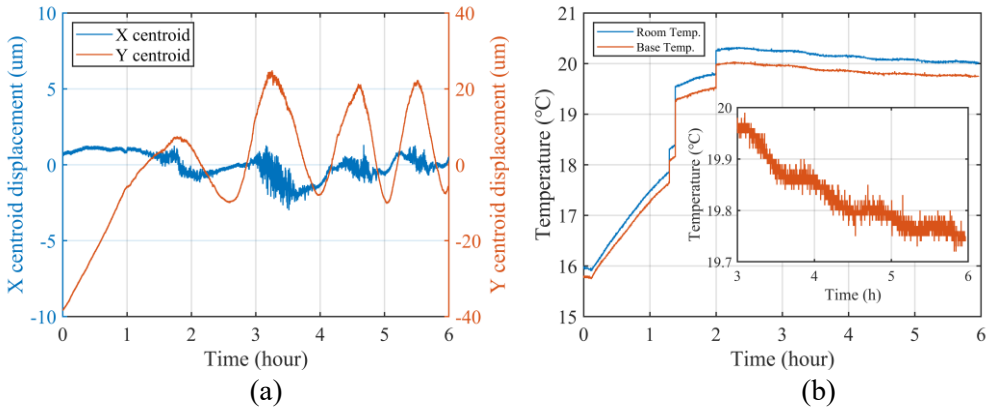

Fig. 6.27 (a) Beam pointing stability of the laser output beam, measured at the output window of the laser box, over 6 hours after turning on the laser, (b) room temperature (blue curve) and temperature of the aluminum base plate (orange curve), measured at the same time by inserting a temperature sensor in the thread hold of the base plate. The inset shows the zoom for the temperature curve.

Further experiments on beam-pointing stability were carried out on the output laser beam. Fig. 6.27(a) shows the beam pointing stability of the laser output for 6 hours (including the warming up period in the first 2 hours). It could be seen that the laser beam fluctuated only ±2 μm in the horizontal orientation (x-axis). However, it periodically fluctuated ±12 μm in the vertical orientation (y-axis) after 2 hours of warming up. Usually, this laser takes about 1 hour to get warm.

It was found that the air conditioner of the laboratory was set to 16℃ after annual maintenance in the morning when the laser was turned on. It was corrected to 20℃ within 2 hours. The recorded room temperature, blue curve in Fig. 6.27(b), shows evidence of the temperature fluctuations. The increased room temperature caused deformation of the aluminum base plate of the laser in the vertical orientation (y-axis), leading to beam pointing shifting in the same direction. Small periodical fluctuations (as shown in the inset of Fig. 6.27(b)) in room temperature and the temperature of the base plate caused periodical deformation of the aluminum base plate within the same period of 1 hour 40 mins. The temperature fluctuations occurred every day. After running the laser for a few weeks, the laser cavity was slightly misaligned due to the slight deformation of the aluminum housing and the misalignment of the mirrors. Therefore, increasing the loss of this laser cavity broke the balance between loss and gain, leading to bifurcation.

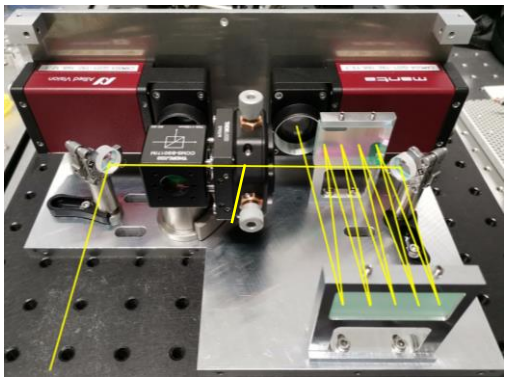

Fig. 6.28 Beam pointing stabilization system

The bifurcation was about 10% of the maximal pulse amplitude, as shown in Fig. 6.26(a)). The bifurcation problem was solved by realigning the laser cavity precisely. In order to keep the balance constant, an active cavity stabilization system (CSS) and a beam stabilization system developed by Jakub Horacek at the HiLASE center were applied to the BIATRI laser. The CSS can actively stabilize the cavity so that the laser power stability can also be maintained. Fig. 6.28 shows the beam sampling box of the BSS. For the stabilization algorithm, two cameras were used to measure the movement of the near-field and far-field beam spots.

6.3.5 Fluctuation-magnification effect in CVBG compressor

A Chirped Volume Bragg Grating (CVBG) was used to compress the amplified laser pulse. The specification of the CVBG is shown in Table 6.3. It provided group delay dispersion (GDD) of 205 ps/nm. The laser beam diameter was expanded to 3 mm ($1/e^2$) to avoid damaging the CVBG due to high peak intensity and clipping by the aperture of CVBG. In order to cool CVBG symmetrically, a water-cooled aluminum housing was designed by Luděk Švandrlík at Hilase, as shown in Fig. 6.29. The CVBG was wrapped with a thin Indium foil to achieve efficient heat dissipation.

Table 6.3 Specification of the Chirped Volume Bragg Grating compressor

Item type	Specification
Central Wavelength (CW), nm	1030.2
Spectral Bandwidth (FWHM), nm	2.59
Diffraction Efficiency, %	85
Clear Aperture (w × h), mm	8.0 × 8.2
Grating Thickness (t), mm	50
Stretching Factor (GDD), ps/nm	~ 205
Stretching Time, ps	~ 500

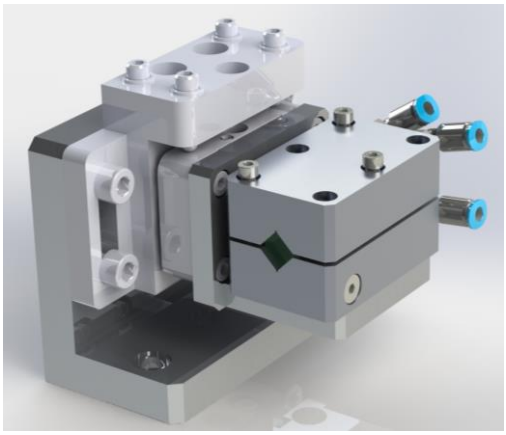

Fig. 6.29 Water-cooled aluminum housing for CVBG compressor. The CVBG was wrapped with a thin Indium foil to achieve efficient heat dissipation.

The pulse duration after compression was 1.88 ps (sech2 fitting). Fig. 6.30(a) shows the autocorrelation trace of the compressed pulse. The maximum laser power after compression was 54 W at a repetition rate of 10 kHz, corresponding to 81% of total compression efficiency.

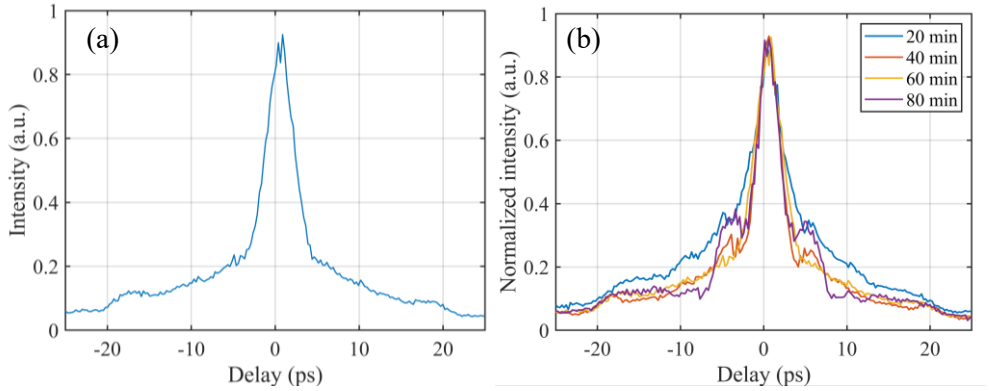

Fig. 6.30 (a) The autocorrelation trace of pulse compressed in CVBG compressor; the pulse width (FWHM) was 1.88 ps ($sech^2$ fitting). (b) Two or more sidebands on the autocorrelation trace appeared. The fitted pulse duration varied between 1.8 ps and 3.5 ps.

However, it was found that the compressed pulse duration slowly fluctuated with full power output. Two or more sidebands on the autocorrelation trace appeared, as shown in Fig. 6.30(b). The fitted pulse duration varied between 1.8 ps and 3.5 ps.

Experimental setup for stability analysis

In order to investigate the origin for such temporal fluctuations in pulse duration, a second harmonic generation (SHG) experimental setup was designed to test the output laser beam. Since second harmonic generation is sensitive to the peak intensity of fundamental laser [216], it is commonly used to evaluate the stability in the peak intensity of laser pulse [217]. It is easy to monitor the stability of the peak intensity of the ultra-fast laser pulse by measuring the long-term stability of its SHG power. Typically, the SHG fluctuation is lower than 2 times the fundamental power fluctuation when there is no extra fluctuation besides SHG, and it could be said that the SHG is stable. The detail of the SHG conversion can be found in literature [218].

The experimental setup is shown in Fig. 6.31. A beam sampler (BS1) sampled the laser pulse under test. A half-wave plate (HWP) and a polarization beam splitter (PBS) were used to attenuate the sampled beam. A second beam sampler (BS2) was used to sample part of the laser beam for autocorrelation measurement. A third beam sampler (BS3) was used to sample part of the laser beam to monitor the fundamental laser's power stability. A plano-convex lens (f = 150mm) was used to focus the fundamental beam into an LBO crystal, which was designed to achieve type I non-critical phase matching for the second harmonic generation. In order to minimize the temperature sensitivity of the LBO crystal, a 2 mm long LBO crystal of type I with larger temperature bandwidth was employed for Second Harmonic Generation. It had a large temperature tolerance range of 4℃ at 99%. The measurements were all carried out in a laboratory environment with a stabilized room temperature of 20±0.25℃. A fourth beam sampler (BS4) was used to sample part of the focused laser beam to the camera (Cam), which was placed at the lens's focal plane to monitor the focal spot. The harmonic laser beam from the LBO crystal was then sent to a second power meter (Pwr2) after two long pass mirrors

(LPM), which had AR coating for the fundamental beam and HR coating at a 45° angle of incidence for the second harmonic beam. Two photodiode power meters (PD300 from Ophir Photonics) were used to monitor the power stability.

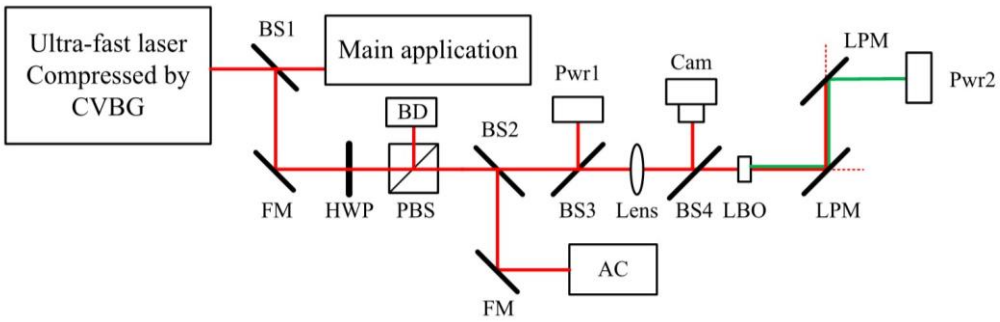

Fig. 6.31 The scheme of the experimental setup. BS: Beam Sampler, FM: Flat Mirror, HWP: Half-Wave Plate, PBS: Polarization Beam Splitter, BD: Beam Dump, AC: Autocorrelator, LPM: Long Pass Mirror, Pwr: Power meter, Cam: Camera.

Instability of the Menlo YLMO oscillator

The power stabilities of the fundamental and the SHG power of Menlo YLMO oscillator were measured after 2 hours of warming up. The result is shown in Fig. 6.32(a). The data was filtered by moving an average of 50 samples only for plotting purposes. The long-term power instability (RMS) of the fundamental power was 0.8% over 2 hours after warming up, while its SHG's long-term power instability (RMS) was 2.1%, which is 2.6 times of the fundamental's. However, the SHG power (green curve) fluctuated with a greater trend than the fundamental (red curve). This was probably caused by the pulse duration fluctuation during running since the beam size did not change. The spectrum of the YLMO fiber oscillator was also measured and processed, as shown in Fig. 6.32(b). There was noticeable periodic spectral modulation over the spectrum, which was a typical characteristic of bound-state solitons in soliton mode-locked fiber laser [219].

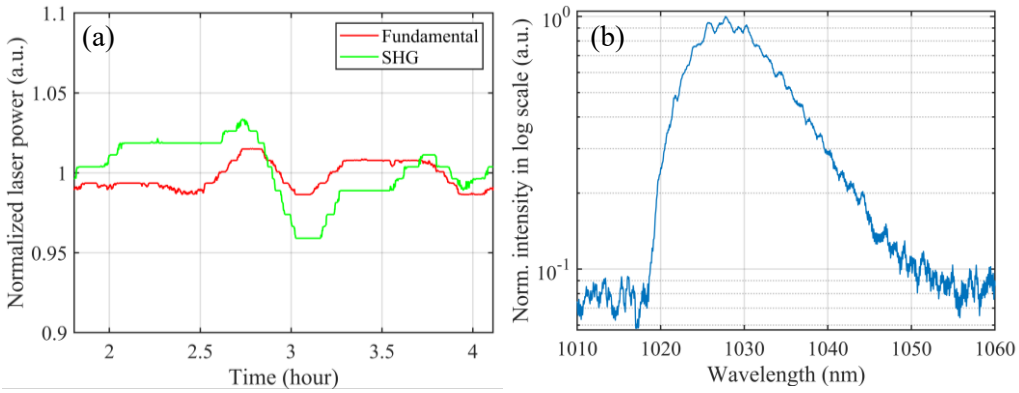

Fig. 6.32 (a) Normalized long-term instability of fundamental (RMS, 0.8%) and second harmonic (RMS, 2.1%) of the Menlo YLMO fiber oscillator over 2 hours after warming up. The data noise was filtered by moving an average of 50 samples only for plotting purposes. (b) The spectrum of the Menlo YLMO fiber oscillator. It was measured by an integrating sphere.

Bound states of solitons of the nonlinear Schrödinger equation are usually formed because two or more fundamental solitons coexist with the same velocity at the same position in the cavity [220]. The spectral modulation indicates that those two or more closely spaced pulses are usually a few tens of picoseconds from each other [200]. Double-pulses from the YLMO

oscillator was observed by fast oscilloscope and fast photodiode, with a time interval of 1.7 ns between two pulses, as shown in Fig. 6.33.

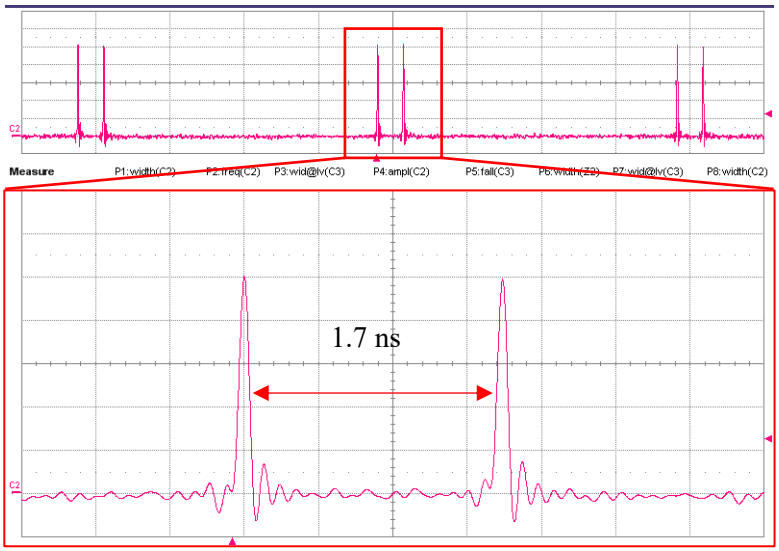

Fig. 6.33 Double pulses were observed from the output of the YLMO oscillator, with a time interval of 1.7 ns between them.

Fluctuation-magnification effect in CVBG compressor

The long-term fluctuations in fundamental power (1H) and its SHG power (2H) were measured over 1.5 hours after warming up the laser system, as shown in Fig. 6.34. In order to minimize the effect of the thermal lens, the average power would be kept within 20 W ~22 W. The pulse energy was scaled from 1.1 mJ to 4 mJ by changing the repetition rate of the thin disk regenerative amplifier from 20 kHz to 5 kHz. The insets of Fig. 6.34(a) and Fig. 6.34(b) show the fast fluctuations over a short period of 18 mins. The fluctuations in fundamental power were within the range of 0.25% ~ 0.35% in both cases for different pulse energies. The fluctuations in the SHG power of the 4 mJ laser pulse were 3.96% for long-term fluctuation and 1.56% for fast fluctuation, respectively. They are 11.3 times and 4.4 times the fluctuations in the fundamental power for the long-term and fast fluctuations, respectively. However, they were only 0.82% (3.2 times) and 0.54% (2 times) for long-term and fast fluctuations for the SHG power of 1.1 mJ laser pulse, respectively. The fluctuations in the 4 mJ case are much higher than in the 1.1 mJ case, and the expected value should be less than 2 times its fluctuation in fundamental power if there is no extra fluctuation.

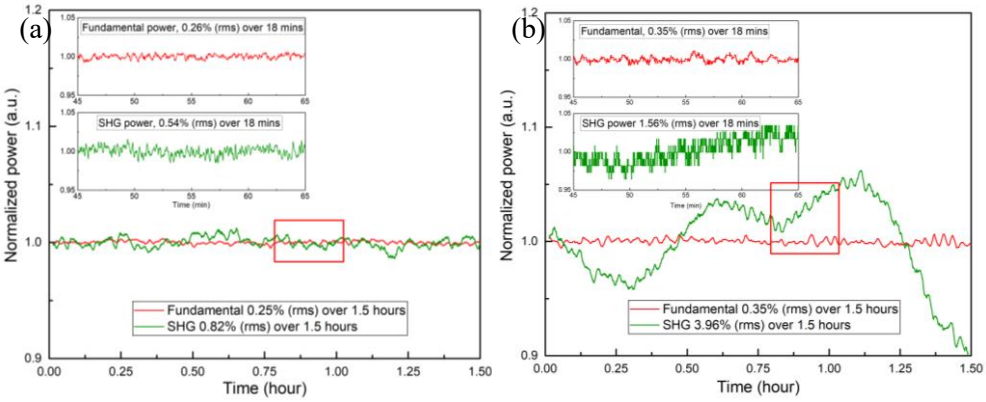

Fig. 6.34 (a) Normalized fluctuations in fundamental power and its SHG power of laser pulse compressed by the CVBG compressor over 1.5 hours after warming up. A moving-average filter of 50 samples filtered the data noise only for plotting purposes. The calculation was done with the original data. The inserts show the detail of the unfiltered fast fluctuation in the selected period of 18mins. The fundamental power fluctuation of 0.25% (RMS) and the SHG power fluctuation of 0.82% (RMS) for pulse energy of 1.1 mJ for 1.5 hours. The insert shows the fundamental power fluctuation of 0.26% (RMS) and the SHG power fluctuation of 0.54% (rms) in 18 mins. (b) The fundamental power fluctuation of 0.37% (RMS) and the SHG power fluctuation of 3.96% (RMS) for pulse energy of 4 mJ for 1.5 hours. The insert shows the fundamental power fluctuation of 0.35% (RMS) and the SHG power fluctuation of 1.56% (RMS) in 18 mins.

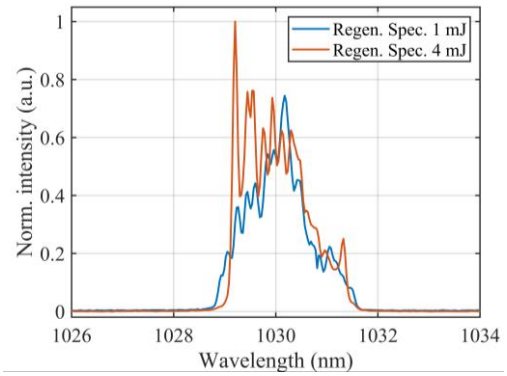

Fig. 6.35 The spectrums of the laser output were measured for pulse energies of 1 mJ (blue curve) and 4 mJ (orange curve). The spectrum was measured with Ocean Optics HR4000 high-resolution spectrometer and Thorlabs integrating sphere IS236A-4.

The spectrums of the laser output were measured for different output pulse energies, as shown in Fig. 6.35. Strong modulation on the spectrum was observed while compressing the pulse with high energy, indicating strong self-phase modulation during the pulse amplification process.

The temporal fluctuations in the compressed pulse duration were logged every 20 mins for 1.5 hours for each measurement. The measured autocorrelation traces are shown in Fig. 3. The fitted pulse duration was around 1.7 ps for the compressed pulse energy of 1.1 mJ, as shown in Fig. 6.36(a). However, the 4 mJ compressed pulse autocorrelation traces varied greatly during the measurement, as shown in Fig. 6.36(b). Sidebands of the autocorrelation traces appeared at some moment, indicating side pulses [221],[222] appeared in this case; therefore, the peak intensity of the main pulse decreased due to the transfer of energy from the main pulse to side pulses

caused by the high Kerr-nonlinearity [203], which would cause temporal fluctuation in the measured pulse duration.

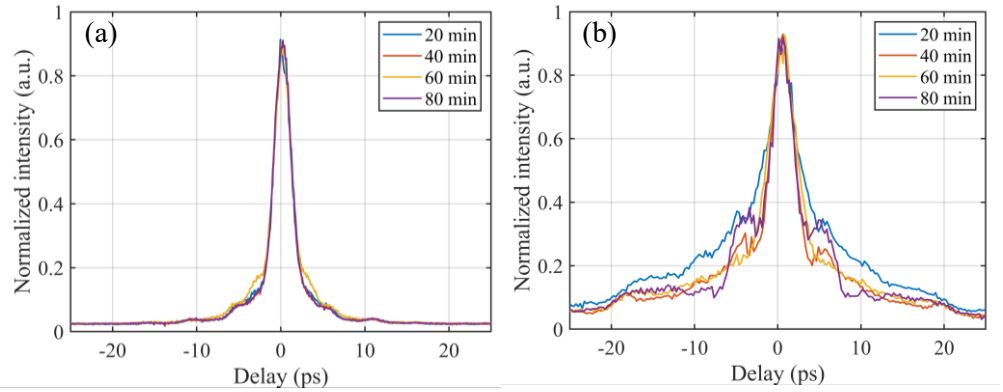

Fig. 6.36 The temporal fluctuations in the autocorrelation of the compressed pulse were also logged every 20 mins during 1.5 hours for a pulse energy of 1.1 mJ (a) and 4.4 mJ (b).

Beam radii in both axes (R_x and R_y) of the focal spot in LBO were also measured for 1.1 mJ pulse and 4 mJ pulse. The beam area (Abeam) was calculated as follows: $A_{beam} = R_x R_y \pi$. To see the curve's trend, the normalized reciprocals of the beam areas (1/beam-area) for 1.5 hours were shown in Fig. 6.37(a), together with the normalized SHG power measured at the same time. From Fig. 6.37(a), the fluctuation in the reciprocals of the beam area (spatial fluctuation) for the 4 mJ pulse had a similar trend as the corresponding fluctuation in SHG power. A similar relation was observed for the 1.1 mJ pulse, although the fluctuations were much smaller.

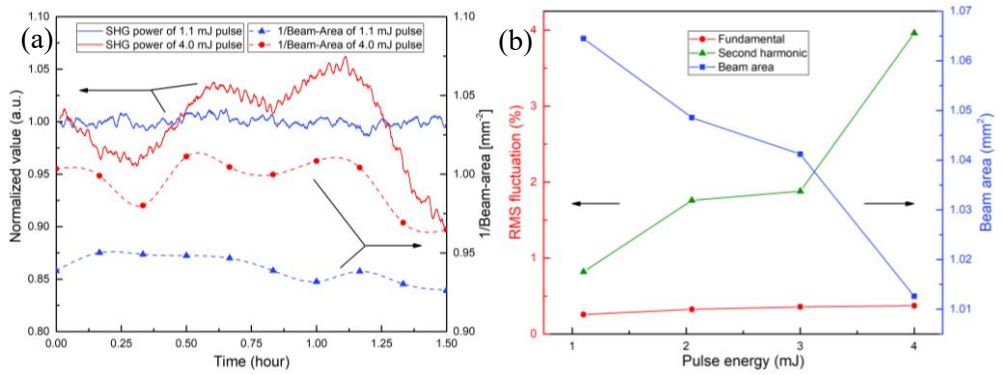

Fig. 6.37 (a) The normalized reciprocals of the beam areas (dash curves, spline fitting) and the normalized SHG power (solid curves) were measured at the same time for 1mJ pulse and 4mJ pulse. (b) The fluctuations in the fundamental power, its SHG power, and the measured beam area are functions of the pulse energy—multiple measurements at these two pulse energy levels generated error bars at 1 mJ and 4 mJ.

The temporal fluctuation caused the spatial fluctuation in the case of high pulse energy due to the Kerr lens in the CVBG compressor at high pulse energy. The 1/beam area shows a similar trend of varying power fluctuation in SHG power. During the measurements, the energy was scaled by changing the repetition rate of the laser, and all other operating parameters were kept the same, like pump power. The average output power was kept at around 20 W to keep the laser running at the same thermal condition. Fig. 6.37 is the evidence of long-term fluctuation due to the Kerr-nonlinearity, even though nonlinear Kerr effects are a transient nonlinear

phenomenon. The high peak intensity in CVBG leads to high Kerr-nonlinearity, which further causes temporal and spatial fluctuations. There is a long-term dynamic process between the Kerr-nonlinearity and the temporal/spatial fluctuations.

Fig. 6.37(b) shows the fluctuations in the fundamental power, its SHG power, and the average beam area as a function of the pulse energy. The fluctuations in SHG power increased by almost 4 times, and the average beam area decreased by > 5.4% when pulse energy increased from 1.1 mJ to 4 mJ, although the fluctuations in fundamental power were almost at the same level. Generally, the fluctuation in peak intensity can be magnified by the CVBG at a high Kerr-nonlinearity.

With Onefive Origami-10 oscillator

In order to further verify the fluctuation-magnification effect in CVBG mentioned above, the YLMO fiber oscillator was replaced by a fiber-coupled Origami-10 solid state oscillator (Onefive GmbH). Table 6.4 shows the specification of Origami-10 oscillator.

Table 6.4 Specification of Origami-10 oscillator from Onefive GmbH

Performance	Value	Unit
Average output power	14.4	mW
Pulse repetition rate	40	MHz
Pulse width	441	fs
Center wavelength	1027.9	nm
Spectra width (FWHM)	10.4	nm
Average power stability (RMS)	< 0.5%	
Pulse-to-pulse stability (RMS)	< 1%	

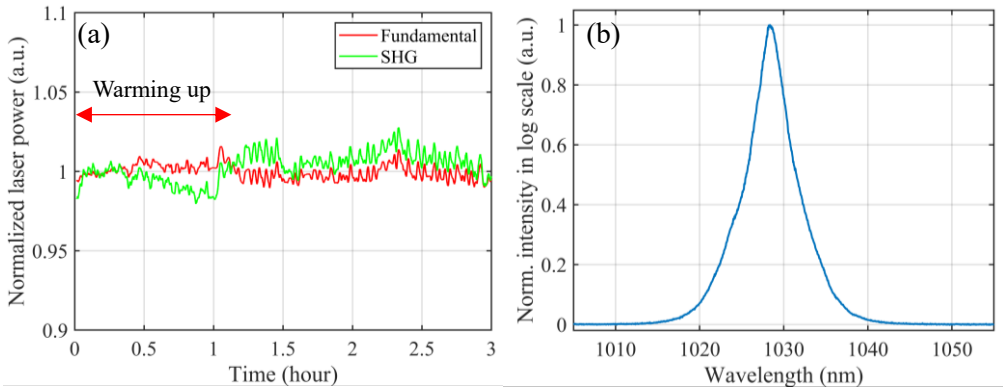

Fig. 6.38 (a) Normalized long-term instability of fundamental (RMS, 0.51%) and second harmonic (RMS, 1.12%) of Onefive Origami-10 oscillator over almost 2 hours after warming up. The data noise was filtered by moving an average of 50 samples. (b) The spectrum of Origami-10 oscillator, measured with integrating sphere.

The measured power stabilities of the fundamental and second harmonic of the Origami-10 oscillator are processed and shown in Fig. 6.38. It took about 70 mins to warm up the laser. Its fundamental laser's long-term power instability (RMS) was 0.51% over almost 2 hours after

warming up, while its SHG power stability was 1.12% at the same time, which is about 2.2 times the former. As shown in Fig. 6.38(a), the pulse duration of the Origami-10 oscillator was very stable; its SHG power (green curve) fluctuated in a similar trend as the fundamental power (red curve). Fig. 6.38(b) shows its spectrum. No spectral modulation was observed.

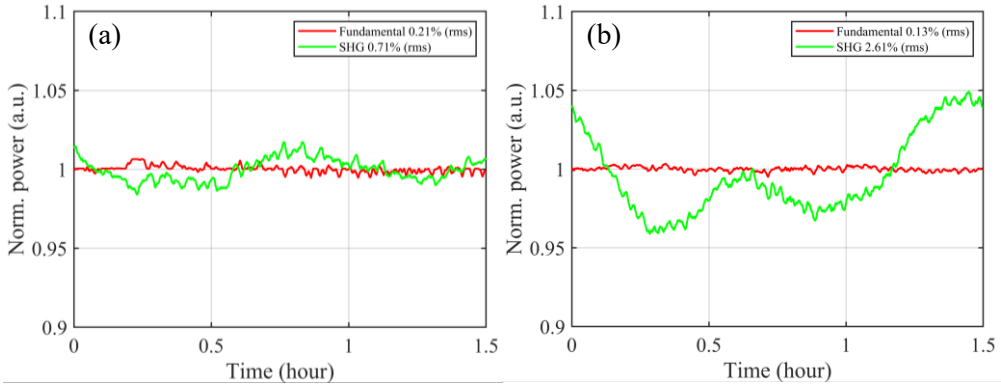

Fig. 6.39 Normalized fluctuations in fundamental power and its SHG power of laser pulse compressed by the CVBG compressor over 1.5 hours after warming up, with Origami-10 oscillator as a seeder. The data noise was filtered by moving an average of 50 samples only for plotting purposes. (a) The fundamental power fluctuation of 0.21% (rms) and the SHG power fluctuation of 0.71% (rms) for pulse energy of 1 mJ for 1.5 hours. (b) The fundamental power fluctuation of 0.13% (rms) and the SHG power fluctuation of 2.61% (rms) for pulse energy of 4 mJ for 1.5 hours.

The TD regenerative amplifier was then measured after replacing the oscillator, after 2 hours of warming up. The measured power stabilities for pulses with energy of 1 mJ and 4 mJ are processed and shown in Fig. 6.39. The long-term power instabilities (RMS) of the fundamental and its SHG power for a pulse energy of 1 mJ, as shown in Fig. 6.39(a), were 0.21% and 0.71%, respectively. When pulse energy was increased to 4 mJ, the long-term SHG power instabilities (RMS) reached 2.61%, as shown in Fig. 6.39(b). It was improved compared to the previous value of 3.96% with the Menlo YLMO oscillator due to improved stability of the seed. However, the fluctuation-magnification effect was still influencing the laser stability.

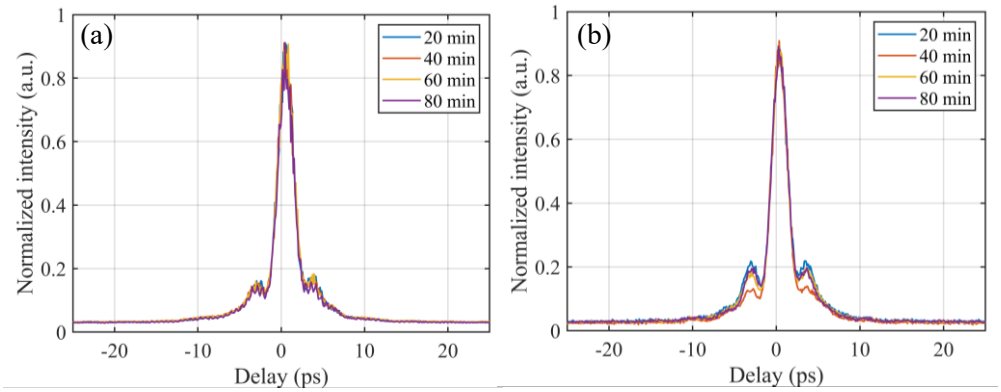

Fig. 6.40 The temporal fluctuations in the autocorrelation of the compressed pulse were also logged every 20 mins during 1.5 hours for a pulse energy of 1 mJ (a) and 4 mJ (b), with the Origami-10 oscillator as a seeder.

The long-term stability of pulse duration was improved for both low-energy pulse and high-energy pulse, as shown in Fig. 6.40. However, temporal fluctuation in the pulse duration was

still observed at the high energy level, as shown in Fig. 6.40(b), indicating the transfer of energy from the main pulse to side pulses and the high accumulated B-integral of the laser pulses in the CVBG. Therefore, the total B-integral accumulated by the laser pulse in the front-end, regenerative amplifier, and CVBG compressor should be reduced as much as possible to obtain a stable laser output. The B-integrals at the wavelength of 1030nm for the above-mentioned experiments were calculated to be 1.81, 3.1, 4.8, and 6.2 for 1 mJ, 2 mJ, 3 mJ, and 4 mJ, respectively.

Conclusion

In general, the fluctuation in peak intensity caused by the bound states of solitons of the fiber oscillator can be magnified by the CVBG at a high Kerr-nonlinearity. The experimental results show that the RMS fluctuation of the SHG power caused by the spatial fluctuation and the temporal fluctuation would be lower than 2% if the B-integral accumulated in the CVBG is lower than π.

6.4 Upgraded version of BIATRI laser

6.4.1 Upgraded design of grating pair compressor

In October 2020, the goal of the BIATRI laser was updated that 10 mJ of pulse energy and 1 ps of pulse duration at the wavelength of 1030 nm were required for the OPA system. With such high energy, it was not recommended to use CVBG as the compressor according to the measurements in previous sections. Transmission grating pairs were recommended to be the new compressor in this case. Since the laser housing had already been manufactured, there was minimal space for installing the new compressor for compressing amplified laser pulse with a pulse duration of 500 ps. In order to fit the Treacy grating compressor into the laser housing, the distance between the grating pairs should be minimized to less than 350 mm. After correctly estimating the pulse duration and distance between gratings using the theory introduced in Section 3.4, the pulse duration of the amplified pulse was decided to be 300 ps so that the grating distance would be 300 mm for the grating parameters listed in Table 6.5.

Table 6.5 Parameters of the transmission grating pair

Item	Value
Angle of incidence (on 1st grating)	18.62°
Grating line density	1800 lines/mm
Grating pair separation	300 mm
Wavelength	1020 – 1040 nm
Littrow angle	71.5°

Two compact grating mounts were designed by Dr. Kohei Hoshimoto to fit the new compressor in the laser housing. Fig. 6.41 shows the grating mounts. The layout of the upgraded laser with the new compressor is shown in Fig. 6.6 in Section 6.1.

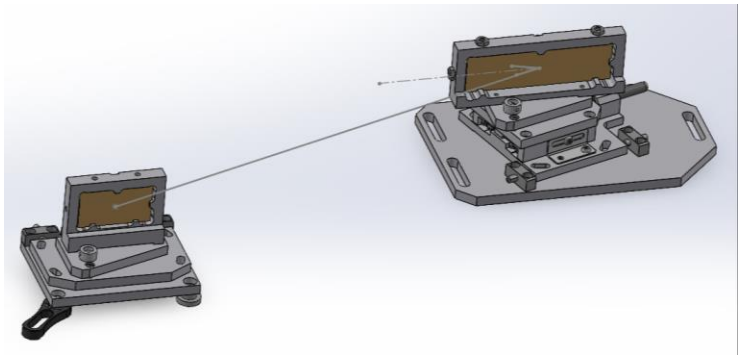

Fig. 6.41 Grating compressors and mounts, designed by Dr. Kohei Hoshimoto.

From the calculation for B-integral shown in Fig. 6.18, the B-integral accumulated in the BBO crystal intra-cavity laser pulse with pulse energy of 10 mJ, pulse duration of 300 ps, and roundtrip numbers of 70 was 1.1 rad, which corresponded to 1.26 rad of B-integral accumulated in the entire laser cavity. Even when the laser pulse was scaled up to 20 mJ, the B-integral accumulated in BBO crystal for roundtrip numbers of 70 was 2.1 rad, corresponding to 2.4 rad of B-integral accumulated in the laser cavity. They were all below π, indicating the laser would still be safe from strong nonlinear effects.

Since the CFBG stretcher used in the previous front end provided negative dispersion, for which the grating compressor cannot compensate. In order to match the dispersion of the grating compressor and avoid the influence caused by the bound-state soliton in the fiber oscillator, the front end, including the fiber oscillator, was redesigned and rebuilt.

6.4.2 Upgraded design of the all-PM-fiber front end

In December 2020, a new version of the all-PM-fiber-based front end, developed by Dr. Liyuan Chen, was accomplished to deliver a stable seed pulse train with 150 mW of average power, 42.7 MHz of repetition rate, 300 ps of pulse duration, and 3.5 nJ of pulse energy. Fig. 6.42 shows the new schematic overview of the upgraded front end. Only one stage of fiber preamplifier was used to amplify the seed pulse train from an all-normal dispersion (ANDi) oscillator, also developed by Dr. Liyuan Chen. Fig. 6.43 shows the photos of the ANDi oscillator and fiber preamplifier. Fig. 6.44 shows the photo of the upgraded main amplifier, including the pulse picker and the new grating compressor.

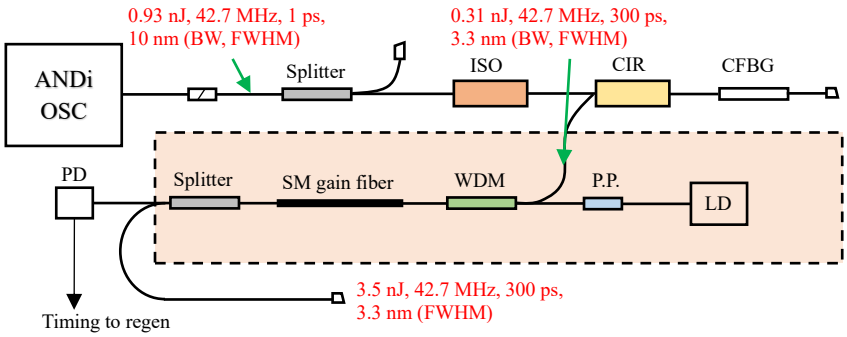

Fig. 6.42 The schematic overview of the upgraded all-PM-fiber-based front end. All the fiber components used in this front end were polarization maintained. ANDi OSC: All-normal dispersion oscillator, ISO: Isolator, CIR: Circulator, CFBG: Chirped Fiber Bragg Grating, WDM: Wavelength Division Multiplexing, P.P.: Pump protector, SM: single mode.

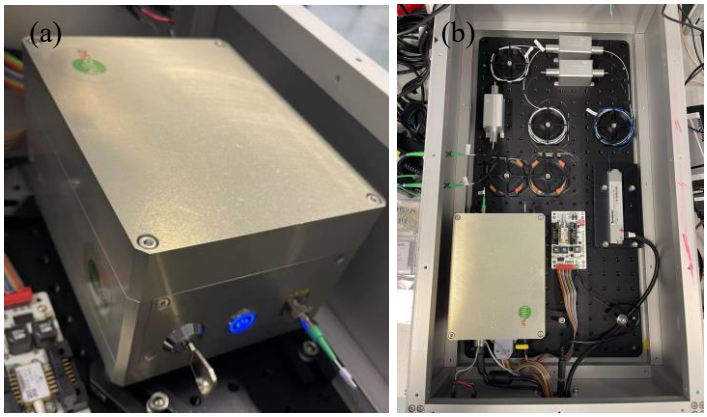

Fig. 6.43 Photos of (a) ANDi Oscillator and (b) fiber preamplifier developed by Dr. Liyuan Chen.

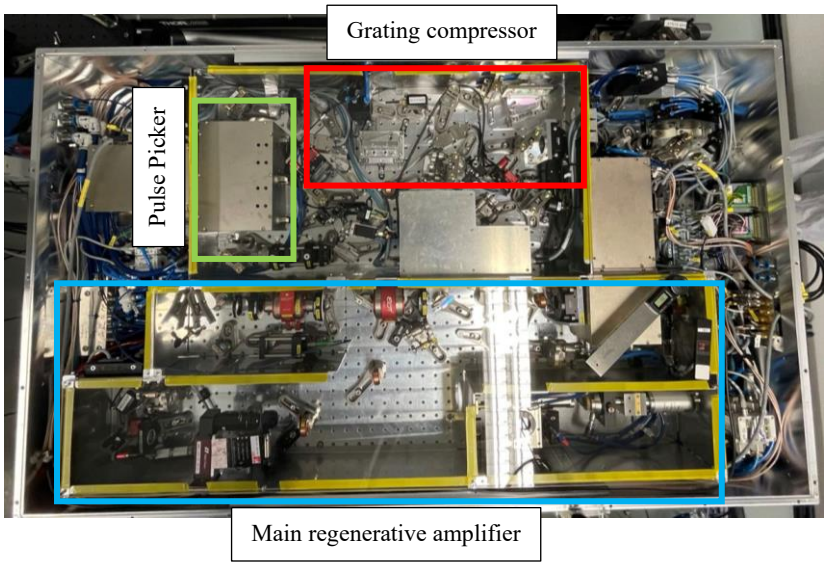

Fig. 6.44 Photo of the upgraded main amplifier, including pulse picker and grating compressor.

6.4.3 Laser performance after upgrading

The laser performance was measured after upgrading. In order to meet the requirement of pulse energy of 10 mJ, the repetition rate was set at 5 kHz, and the average power was measured at 53 W after compression with a compression efficiency of 96%.

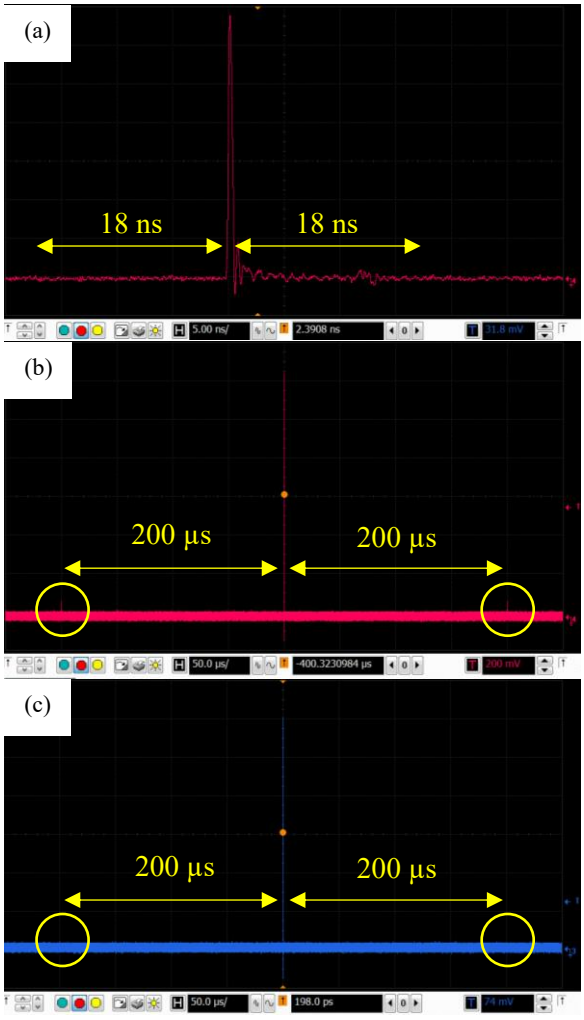

Fig. 6.45 (a) The waveform of the output pulse, no pre-pulse or post-pulse was observed within the 18 ns range before or after the main pulse envelope; (b) the waveform of the output pulse train, small pulses were observed within 200 µs range, corresponding to the repetition rate of 5 kHz, before and after the main pulse with a contrast ratio of 18:1 due to serious bifurcation; (c) the waveform of the output pulse train after pulse picking, the small pulses were abandoned. The contrast ratio of the pulse train was improved to >300:1.

However, bifurcation started when the output power was larger than 20 W, corresponding to 4 mJ of pulse energy. Serious bifurcation was observed at 53 W output power, and the period between pulses was almost doubled (the repetition rate of the output laser pulse was halved to 2.5 kHz). The laser pulse contrast was measured and shown in Fig. 6.45(a). Pre-pulse or post-pulse was not observed within the 18 ns range, the roundtrip time of the laser cavity, before or after the main pulse envelope. The pulse contrast ratio was 152:1. Fig. 6.45(b) shows the measured pulse train. Small pulses were observed and marked by yellow circles in the figure.

The contrast ratio of the pulse train was only 18:1 with small pulses due to serious bifurcation. Since I had designed a pulse picker in the system for the user, I decided to increase the contrast ratio of the pulse train using the pulse picker by picking the pulses with higher pulse energy. Fig. 6.45(c) shows the pulse after pulse picking, and the small pulses were abandoned. The contrast ratio of the pulse train was improved to > 300:1. The output power was 50.2 W after pulse picking at the repetition rate of 2.5 kHz, corresponding to a pulse energy of 20 mJ.

The laser beam was sampled with the previous diagnosing setup shown in Fig. 6.31 to measure the stabilities of the average power of the laser output and the peak intensity of the pulse. Fig. 6.46 shows the normalized fluctuations in the fundamental power and the SHG power of the laser pulses compressed by the grating compressor over 1.5 hours after warming up. The fundamental power fluctuation of 0.56% (rms) and the SHG power fluctuation of 0.80% (rms) over 1.5 hours at full power output. Improvement in SHG power fluctuation compared to the result shown in Fig. 6.39(b) indicates that no nonlinear phenomena occurred during amplification or compression.

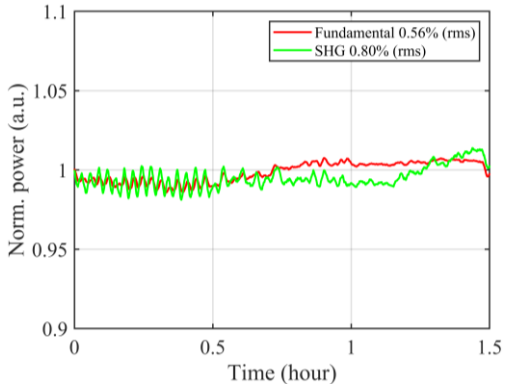

Fig. 6.46 Normalized fluctuations in fundamental power and its SHG power of laser pulse compressed by the CVBG compressor over 1.5 hours after warming up with a new oscillator developed by Dr. Liyuan Chen. The fundamental power fluctuation of 0.56% (rms), and the SHG power fluctuation of 0.80% (rms) over 1.5 hours. The data noise was filtered by moving an average of 50 samples only for plotting purposes.

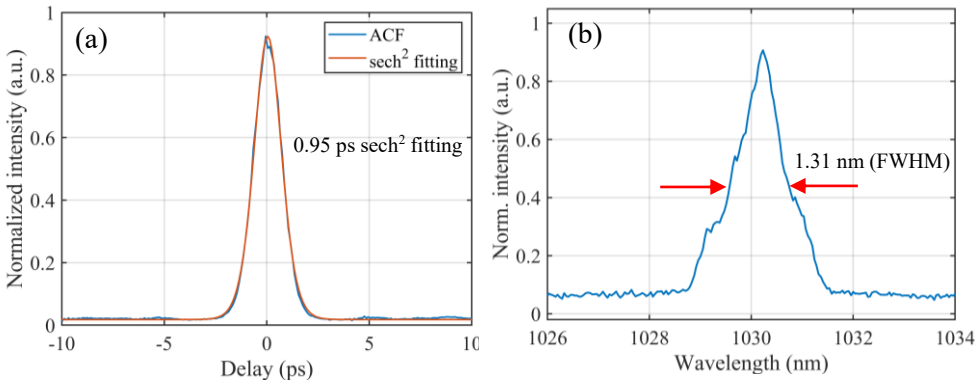

Fig. 6.47 (a) Autocorrelation trace of the output pulse after compression by the grating compressor. The pulse duration was 0.95 ps with $sech^2$ fitting. (B) The output pulse spectrum with a central wavelength of 1030.23 nm and a bandwidth of 1.31 nm (FWHM).

The pulse duration after compression was measured to be 0.95 ps (FWHM), assuming a $sech^2$ shape of the pulse, as shown in Fig. 6.47(a). The spectrum was measured and shown in Fig.

6.47(b), with an FWHM bandwidth of 1.31 nm, corresponding to a transform-limited pulse duration of 0.85 ps (sech^2) and central wavelength of 1030.23 nm. A near transform-limited pulse was obtained with the time-bandwidth product of 0.352.

The beam quality factor M^2 of the output laser was measured homemade M^2 measurement device developed by Dr. Kohei Hashimoto based on a commercial beam profiler (Cinogy CinCam CMOS Nano 1.001). It was measured that M_x^2 = 1.22 in the horizontal direction and M_y^2 = 1.25 in the vertical direction, as shown in Fig. 6.48.

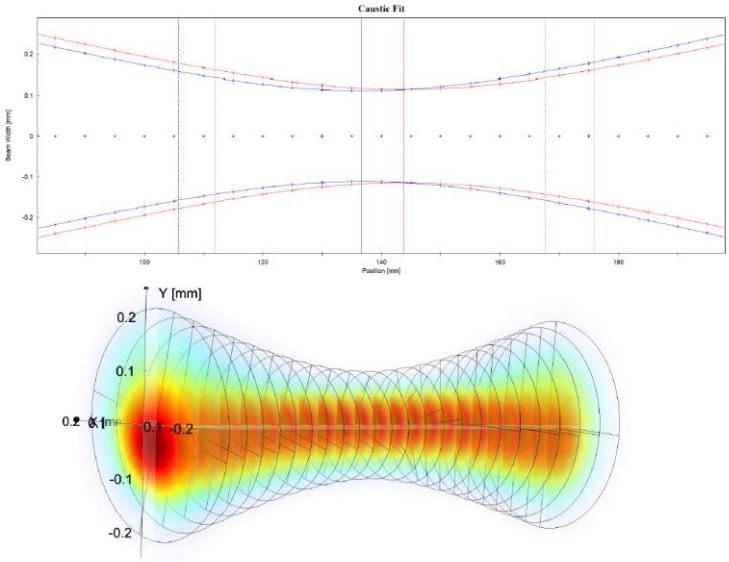

Fig. 6.48 M^2 measurement with M_x^2 = 1.22 at horizontal direction and M_y^2 = 1.25 at vertical direction.

Chapter 7 Application of Mid-IR AO: An Outlook

Much research shows that the wavefront of the pump, signal, and idler beams significantly affect the phase matching and pulse front in OPA systems. Li et al. have experimentally shown that astigmatism in the pump beam is transferred to the idler beam [223]. Chen et al. gave a qualitative description of the pump-to-signal phase transfer effect being proportional to the pump wavefront derivative [224]. Bahk et al. investigated, numerically and experimentally, the effect of the pump beam profile and wavefront on the signal and idler wave in OPAs. Results showed that the signal phase is proportional to the pump and signal wavefront in the phase-matching direction in a non-collinear configuration [225]. The pump-beam wavefront could be transferred to the idler beam more than to the signal beam. However, the transfer to the signal beam cannot be neglected for high-power OPA with large wavefront errors, which could be introduced by the low optical quality of large diameter crystals, defects in the optics, thermal problems of the optical system, self-focusing and self-defocusing in the nonlinear crystal at high energy level [226].

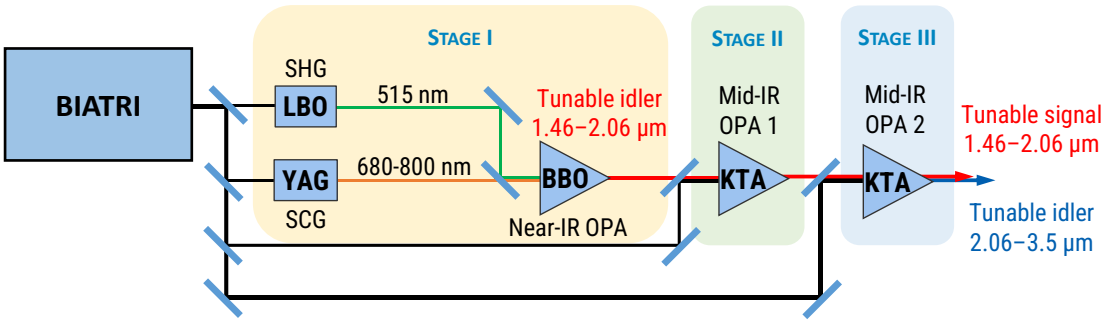

Fig. 7.1 Optical scheme of the mid-IR OPA system pumped by the BIATRI thin disk laser, provided by Dr. Ondrej Novak.

At the HiLASE Centre, the nonlinear optics team led by Dr. Ondrej Novak is currently developing a high-energy mid-IR OPA system pumped by a thin disk laser. As shown in Fig. 7.1, the BIATRI thin disk laser developed in this work will be used as the pump source. The pump beam will be separated into 4 sub-beams, one is used for second-harmonic generation (SHG), and one is used for supercontinuum generation (SCG) in Stage I, where a first tunable near-IR OPA will be built with a BBO crystal as the parametric gain medium. The generated tunable idler beam within the spectral range of 1.46 µm – 2.06 µm will be used as the signal beam for the following mid-IR OPAs, Stage II and Stage III, where Potassium Titanyle Arsenate

(KTiOAsO4) (KTA) crystals will be used as the parametric gain mediums. Amplified tunable signal beam within the spectral range of 1.46 μm – 2.06 μm and tunable idler beam within the spectral range of 2.06 μm – 3.5 μm can be obtained from this OPA system.

In this design, the inherent wavefront aberrations of the pump beam, which are usually caused by the optics, alignment, gratings, and thermal issues in the thin disk laser system, would be mostly transferred to the idler beam of the first near-IR OPA in Stage I. Meanwhile, the optics, LBO, and BBO crystals, especially the long YAG rod, would introduce additional wavefront aberrations to the idler beam. In the following stages, the idler beam will become the signal beam for parametric amplification, which means its wavefront would be less affected, but its phase would be more affected by the pump beam wavefront [223 - 225] in Stage II and Stage III. Fig. 7.2(a) shows the measured Hartmann-gram of the idler beam at wavelength of 2.7 μm of the first OPA (Stage I), which was still under construction and tuning, so that the wavelength was not in the designate spectral range. Fig. 7.2(b) shows the reconstructed wavefront with a wavefront RMS of 1.08λ and P-V value of 4.98λ. It could be seen that the wavefront degraded much after propagating through many optics and crystals in Stage I.

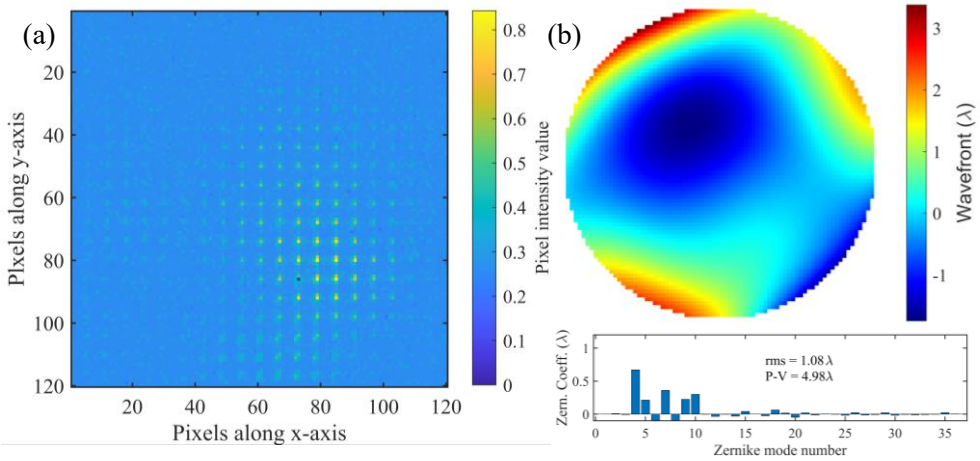

Fig. 7.2 (a) Measured Hartmann-gram of the idler beam at wavelength of 2.7 μm of the first OPA (Stage I), and (b) reconstructed wavefront of the idler beam, with a wavefront RMS of 1.08λ and P-V value of 4.98λ.

In order to improve the phase-matching, efficiency and performance of the OPAs, it is proposed to correct the wavefront for the idler beam (1.46 μm – 2.06 μm) of the Stage I output. The wavefront aberrations transferred from the pump laser and introduced by alignment and crystals could be mitigated to obtain an idler beam with a good wavefront to seed the following OPAs. Fig. 7.3 shows the proposed solution.

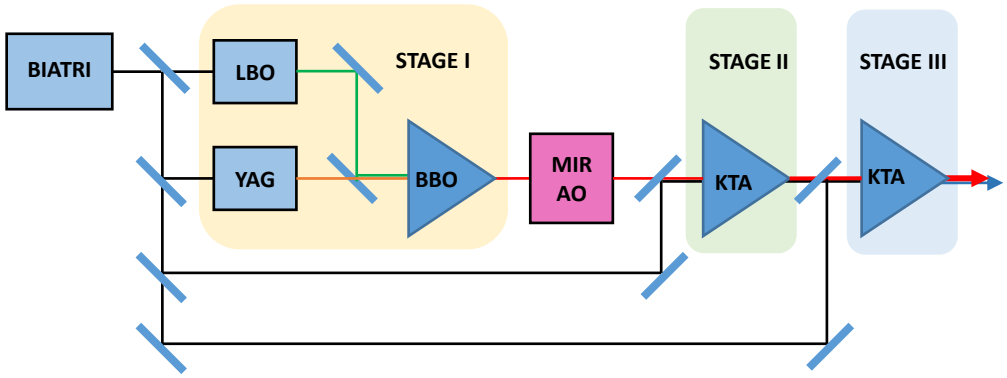

Fig. 7.3 Proposed solutions for wavefront correction for the OPA system: wavefront correction for the idler beam of Stage I with the mid-IR Adaptive Optics system.

Since the OPA system with the above mentioned three stages is still under construction, the application of the mid-IR AO system will be carried out after the accomplishment of the OPA system to improve its performance and investigate the impact of the wavefront on the performance.

Chapter 8 Conclusion

8.1 Summary of the results

The main topics of this thesis were the developments of the mid-IR Adaptive Optics system and high-energy ultrafast thin disk laser system for the BIATRI project at HiLASE Center. Theories of Adaptive Optics and thin disk lasers were introduced in Chapter 2 and Chapter 3.

In Chapter 4 and Chapter 5, I have shown an Adaptive Optics (AO) system developed for a 1.94 μm laser. The AO system consists of a homemade Shack-Hartmann wavefront sensor based on an uncooled Vapor Phase Deposition (VPD) PbSe FPA detector and a silver-coated bimorph piezoelectric deformable mirror coupled in a closed-loop control system. The thermal character of the laser causes an afterimage to be formed on the sensor, especially in the positions of the lenslet-generated focal spots. It introduces a significant error to the centroid detection and causes erroneous wavefront reconstruction. The impact of the thermally induced afterimage on the performance of the AO system was analyzed in detail. The afterimage effect was effectively reduced by dynamic background updating. Using this approach, the residual wavefront RMS was reduced from 0.29 λ to 0.11 λ, and the focal spot diameter was reduced from 2.6 mm (@$1/e^2$) to 0.97 mm (@$1/e^2$). The AO system developed in this work can be easily extended to the mid-IR spectral range (1.5 ~ 5 μm) thanks to the spectral range of the camera. The system will be applied in mid-IR laser applications of the BIATRI project in the near future at HiLASE Center.

In Chapter 6, a thin disk picosecond laser was developed with an all-polarization-maintained fiber front-end as the seeder. Due to the changes in the goal of the BIATRI project, the required pulse energy was changed from 1 mJ to 5 mJ, then to 10 mJ, regardless of the repetition rate. A numerical model was built to simulate the effect on laser performance caused by the Amplified Spontaneous Emission (ASE). It could be used for evaluating the laser performance while designing. In the first design, an all-PM-fiber front-end with three fiber pre-amplifier was built to amplify the seed pulses, a fiber oscillator delivering pulses of 6 nJ pulse energy, 28.6 ps pulse duration at a 50 MHz repetition rate. After the fiber pre-amplifier, the pulse energy was amplified to 1 μJ, the pulse duration was stretched to 500 ps, and the repetition rate was reduced to 1 MHz. The laser pulse energy was amplified to 6.66 mJ at a repetition rate of 10 kHz before

compression. A Chirped Volume Bragg Grating (CVBG) was used to compress the pulse duration to 1.8 ps. However, strong nonlinearity in the CVBG while compressing pulses with high pulse energy caused pulse duration to vary between 1.8 ps and 3.5 ps.

Further experiments were carried out to investigate the origin of the temporal fluctuations of pulse duration. By measuring the SHG of the laser pulse under test, one could estimate the stability of the peak intensity of the laser pulse. It was found that the bound states of solitons in the oscillator would lead to fluctuations in the peak intensity of the seed pulses. Then, the fluctuations in peak intensity can be magnified by the CVBG at high Kerr-nonlinearity. The experimental results show that the RMS fluctuation of the SHG power caused by the spatial fluctuation and the temporal fluctuation would be lower than 2% if the B-integral accumulated in the CVBG is lower than π. In order to solve the instability problem, a new all-PM-fiber front-end was built with home-built All-Normal Dispersion (ANDi) fiber oscillator and one fiber pre-amplifier. A grating pair compressor was designed and built to replace the CVBG compressor to reduce the accumulated nonlinear phase shift experienced by the laser pulses. After upgrading, the laser system delivered a laser beam with an average power of 53 W while the repetition rate was set at 5 kHz. However, strong bifurcation occurred at this repetition rate, halved down to 2.5 kHz. The contrast ratio of the pulse train was only 18:1 due to the bifurcation. The pulse picker was then used to select pulses to increase the contrast ratio of the pulse train to more than 300:1. The output power was 50.2 W after pulse picking at the repetition rate of 2.5 kHz, corresponding to pulse energy of 20 mJ. The power stability of the fundamental laser beam was measured to be 0.56% after warming up.

In comparison, the SHG power stability of the fundamental laser beam was measured to be 0.80%, indicating that the peak intensity of the laser pulse was stable. The pulse duration was measured to be 0.95 ps (FWHM, sech^2 fitting) with an FWHM bandwidth of 1.31 nm. The beam quality factor M^2 of the output laser beam was measured that M_x^2 = 1.22 in the horizontal direction and M_y^2 = 1.25 in the vertical direction.

The thin disk laser developed in this work provides laser pulses with high performance. It will be used as the pump of the Optical Parametric Amplifier (OPA) system, which is under development at the HiLASE center. The AO system developed in this work can be easily extended to the mid-IR spectral range (1 ~ 5 μm) thanks to the spectral range of the camera. The system will be applied in mid-IR laser applications or OPA experiments at the HiLASE center.

8.2 Contribution to the progress of Adaptive Optics and laser science

In the author's opinion, the results achieved in this thesis will contribute to developing mid-IR wavefront controlling for industrial and scientific applications of mid-IR laser sources. New

findings gained during the work will help us further develop mid-IR laser systems and applications at the HiLASE Centre. The main achievements of this work can be summarized as follows:

- An Adaptive Optics System based on the uncooled Vapor Phase Deposition (VPD) PbSe FPA detector with a closed-loop control system has been developed for mid-IR laser sources for the first time. The experiments showed that this system could significantly improve the wavefront of a distorted 1.94 μm laser beam and increase its focusing ability. The system can be extended to the spectral range of 1 ~ 5 μm for various potential applications.
- Fluctuation-magnification effect on the peak intensity of laser pulse caused by the nonlinear Kerr effect in the chirped volume Bragg grating (CVBG) compressor is investigated experimentally for high energy thin disk chirped pulse amplification (CPA) system. Experiments showed that small fluctuations in the peak power of uncompressed pulses cause an increase in temporal and spatial fluctuation due to high Kerr-nonlinearity in the CVBG when B-integral is larger than π. Thus, the initial fluctuation would be magnified by the CVBG compressor.
- A thin disk laser system has been developed, delivering a laser beam at 1030nm with an average power of 50 W at a repetition rate of 2.5 kHz due to bifurcation. The maximum pulse energy was more than 20 mJ. The pulse duration was 0.95 ps (FWHM, sech^2 fitting) with an FWHM bandwidth of 1.31 nm. The beam quality factor M^2 of the output laser beam was measured that M_x^2 = 1.22 in the horizontal direction and M_y^2 = 1.25 in the vertical direction. This laser system is a pump laser of the mid-IR OPA system which the Adaptive Optics in this thesis was developed for.

In conclusion, the objectives of this thesis have been accomplished. I confirm here explicitly that all the results in this thesis were the outcome of my individual work and collaboration with my colleagues. During this work, I authored 2 and co-authored 1 article in peer-reviewed journals, and presented 4 and co-authored 2 international conference contributions with the abovementioned list results.

Appendix 1: Zernike polynomials in polar coordinates

Mode j	Z_n^m	RMS	Zernike polynomial	Meaning
0	Z_0^0	$\sqrt{2}$	1	Piston
1	Z_1^{-1}	2	$r\sin\theta$	Tilt x
2	Z_1^1	2	$r\cos\theta$	Tilt y
3	Z_2^{-2}	$\sqrt{6}$	$r^2\sin 2\theta$	Astigmatism x
4	Z_2^0	$\sqrt{3}$	$2r^2-1$	Defocus
5	Z_2^2	$\sqrt{6}$	$r^2\cos 2\theta$	Astigmatism y
6	Z_3^{-3}	$2\sqrt{2}$	$r^3\sin 3\theta$	Trefoil x
7	Z_3^{-1}	$2\sqrt{2}$	$(3r^3-2r)\sin\theta$	Coma x
8	Z_3^1	$2\sqrt{2}$	$(3r^3-2r)\cos\theta$	Coma y
9	Z_3^3	$2\sqrt{2}$	$r^3\cos 3\theta$	Trefoil y
10	Z_4^{-4}	$\sqrt{10}$	$r^4\sin 4\theta$	Tetrafoil x
11	Z_4^{-2}	$\sqrt{10}$	$(4r^4-3r^2)\sin 2\theta$	Secondary astigmatism x
12	Z_4^0	$\sqrt{5}$	$6r^4-6r^2+1$	Primary spherical
13	Z_4^2	$\sqrt{10}$	$(4r^4-3r^2)\cos 2\theta$	Secondary astigmatism y
14	Z_4^4	$\sqrt{10}$	$r^4\cos 4\theta$	Tetrafoil y
15	Z_5^{-5}	$2\sqrt{3}$	$r^5\sin 5\theta$	Pentafoil x
16	Z_5^{-3}	$2\sqrt{3}$	$(5r^5-4r^3)\sin 3\theta$	Secondary trefoil x
17	Z_5^{-1}	$2\sqrt{3}$	$(10r^5-12r^3+3r)\sin\theta$	Secondary coma x
18	Z_5^1	$2\sqrt{3}$	$(10r^5-12r^3+3r)\cos\theta$	Secondary coma y
19	Z_5^3	$2\sqrt{3}$	$(5r^5-4r^3)\cos 3\theta$	Secondary trefoil y
20	Z_5^5	$2\sqrt{3}$	$r^5\cos 5\theta$	Pentafoil y
21	Z_6^{-6}	$\sqrt{14}$	$r^6\sin 6\theta$	
22	Z_6^{-4}	$\sqrt{14}$	$(6r^6-5r^4)\sin 4\theta$	
23	Z_6^{-2}	$\sqrt{14}$	$(15r^6-20r^4+6r^2)\sin 2\theta$	Tertiary astigmatism x
24	Z_6^0	$\sqrt{7}$	$20r^6-30r^4+12r^2-1$	Secondary spherical
25	Z_6^2	$\sqrt{14}$	$(15r^6-20r^4+6r^2)\cos 2\theta$	Tertiary astigmatism y
26	Z_6^4	$\sqrt{14}$	$(6r^6-5r^4)\cos 4\theta$	
27	Z_6^6	$\sqrt{14}$	$r^6\cos 6\theta$	
28	Z_7^{-7}	4	$r^7\sin 7\theta$	
29	Z_7^{-5}	4	$(7r^7-6r^5)\sin 5\theta$	
30	Z_7^{-3}	4	$(2r^7-30r^5+10r^3)\sin 3\theta$	
31	Z_7^{-1}	4	$(35r^7-60r^5+30r^3-4r)\sin\theta$	
32	Z_7^1	4	$(35r^7-60r^5+30r^3-4r)\cos\theta$	
33	Z_7^3	4	$(2r^7-30r^5+10r^3)\cos 3\theta$	
34	Z_7^5	4	$(7r^7-6r^5)\cos 5\theta$	
35	Z_1^{-1}	4	$r^7\cos 7\theta$	

Appendix 2: MATLAB codes for Zernike polynomials

A 2.1 Zernike polynomials in polar coordinates

```
% Calculate individual Zernike polynomials in polar coordinates
num = 3;      % Zernike mode in single indexing scheme
row = 80;     % The resolution of the Zernike wavefront
column = row; % The resolution of the Zernike wavefront
rad = linspace(0,1,row);        % The radian
ang = linspace(0,2*pi,column);  % The angular
[rho, theta] = meshgrid(rad,ang);
[x,y] = pol2cart(theta,rho);    % Convert polar coordinates to the Cartesian coordinates

cont = 0;
flag = 0;
n = 1;

while cont < num
    for m = -n:2:n
        cont = cont + 1;
        if cont == num
            flag = 1;
            break;
        end
    end
    if flag == 1
        break;
    end
    n = n+1;
end

if m == 0
    deltam = 1;
else
    deltam = 0;
end

Norm = sqrt(2*(n+1)/(1+deltam));  % The normalization constant
Rnm_rho = zeros(size(rho));       % The radial function

for s = 0:(n-abs(m))/2
    Rnm_rho = Rnm_rho + (-1)^s.*prod(1:(n-s))*rho.^(n-2*s)/(prod(1:s)*...
        prod(1:((n + abs(m)) / 2 - s)) * prod(1:((n-abs(m))/2-s)));
end

if m < 0
    Znm = -Norm.*Rnm_rho.*sin(m.*theta);
else
    Znm = Norm.*Rnm_rho.*cos(m.*theta);
end

surf(x,y,Znm);  % Surf the Zernike wavefront
shading interp;
```

A 2.2 Matrix of Zernike polynomials

```
% ZERNIKE_MATRIX create tables for Zernike polynomials up to radial order n.

function Zernike_struct = zernike_matrix(n)

tot = (n + 1)*(n + 2)/2;           % polynomial number, the number of aberration terms
radial_table = zeros(tot, n + 1);  % radial degree
azim_table = zeros(tot, 2);        % azimuthal frequency
jtonm_table = zeros(tot, 2);       % j number with two indexing

radial_table(1, end) = 1;

count = 2;

for ni=1:n
    mi = rem(ni, 2);
    while mi <= ni
        if mi == 0
            radial_table(count, :) = sqrt(ni + 1)*...
                zernike_rho_n_m(ni, mi, n);
            azim_table(count, :) = [0, 0];
            jtonm_table(count, :) = [ni, 0];
            count = count + 1;
        else
            radial_table(count + 0, :) = sqrt(2*(ni + 1))*...
                zernike_rho_n_m(ni, mi, n);
            radial_table(count + 1, :) = sqrt(2*(ni + 1))*...
                zernike_rho_n_m(ni, mi, n);
            if rem(count, 2)
                azim_table(count + 0, :) = [0, mi];
                azim_table(count + 1, :) = [mi, 0];
                jtonm_table(count + 0, :) = [ni, -mi];
                jtonm_table(count + 1, :) = [ni, mi];
            else
                azim_table(count + 0, :) = [mi, 0];
                azim_table(count + 1, :) = [0, mi];
                jtonm_table(count + 0, :) = [ni, mi];
                jtonm_table(count + 1, :) = [ni, -mi];
            end

            count = count + 2;
        end

    mi = mi + 2;
    end
end

Zernike_struct = struct();     % create a empty structure for saving the default data
Zernike_struct.radial_table = radial_table;  % save the radial table in the structure
Zernike_struct.azim_table = azim_table;      % As above
Zernike_struct.jtonm_table = jtonm_table;    % As above
Zernike_struct.ncoeff = tot;

    function z = zernike_rho_n_m(n, m, ord)
        z = zeros(1, ord + 1);
        for s=0:((n - m)/2)
            z(ord + 1 - (n - 2*s)) = ...
                (((-1)^s)*factorial(n - s))/...
                (factorial(s)*factorial((n + m)/2 - s)*...
                factorial((n - m)/2 - s));
        end
    end
end
```

A 2.3 Gradient of the Zernike polynomials (Reconstruction Matrix)

```
% compute the gradient of Z, which is the Reconstruction Matrix (RM)
MatrixA = zeros(2*nSpots,OrderZerCoef);
% Create a zero matrix for saving RM, nSpots is the number of the spots or
% sub-aperture. OrderZerCoef is the order number of the Zernike coefficients
sac = pupil_centre_pix; % pupil center in pixel unit
rbar = SubAperture_radius_m/pupil_radius_m;
% SubAperture_radius_m is the radius of the sub-aperture in meter unit
% pupil_radius_m is the radius of the pupil in meter unit
kk = pupil_radius_m/(pi*(SubAperture_radius_m^2));

for i = 1 : nSpots
    dx1dx2 = (Centers(i, :) - sac)*Camera_pixel_size;
    r = norm(dx1dx2)/(pupil_radius_m);
    % pupil is in canonical coordinates, x points right, y points up
    % ord_centres is in plot coordinates x1 points right, x2 points down
    % atan2(y, x), dx = dx1, dy = -dx2
    gamma = atan2(-dx1dx2(2), dx1dx2(1));
    if r > 1
        throw(MException('Aperture radius is too small, use a larger pupil_radius_m'));
    end

    for zi = 2:ncoeff
        rad_table_row = radialtable(zi, :);
        azim_table_row = azimtable(zi, :);

        [ey, ex] = zernike_gradient(rad_table_row, azim_table_row, r, gamma, rbar);

        % centres, boxes and deltas are in the plot() coordinate system
        % after imshow()!
        % deltas(:) will be [x1; x2] where x1 goes left to right and x2
        % goes top to bottom. So convert again to plot coordinate system.
        % dx1 = kk*dx, dx2 = -kk*dy
        MatrixA(i, zi) = kk*ex;
        MatrixA(i + nSpots, zi) = -kk*ey;
      end
  end
```

```
function [Ey, Ex] = zernike_gradient(radrow, azimrow, r, gamma, rbar)

% r is in [0 1]
% rbar is in [0 1]

assert(r >= 0 && r < 1);
assert(rbar > 0 && rbar < 1);

rhoindefint1 = polyint([polyder(radrow) 0]);
rhoindefint2 = polyint(radrow);

if r > rbar
    thetas = gamma + ...
        [acos(sqrt(r^2 - rbar^2)/r), - acos(sqrt(r^2 - rbar^2)/r)];

    theta_a = min(thetas);
    theta_b = max(thetas);
    assert(theta_b > theta_a);

    rho_a = @(x) r*cos(x - gamma) - ...
        sqrt(r^2.*cos(x - gamma).^2 - (r^2 - rbar^2));
    rho_b = @(x) r*cos(x - gamma) + ...
        sqrt(r^2.*cos(x - gamma).^2 - (r^2 - rbar^2));
else
    theta_a = 0;
    theta_b = 2*pi;

    rho_a = @(x) 0*x;
    rho_b = @(x) r*cos(x - gamma) + ...
        sqrt(r^2.*cos(x - gamma).^2 - (r^2 - rbar^2));
```

```
end

rhoint1a = @(x) polyval(rhoindefint1, rho_a(x));
rhoint1b = @(x) polyval(rhoindefint1, rho_b(x));
rhoint2a = @(x) polyval(rhoindefint2, rho_a(x));
rhoint2b = @(x) polyval(rhoindefint2, rho_b(x));

psi = zernike_radialfun(azimrow);
psider = zernike_radialderfun(azimrow);

integrandx = @(x) ...
    (rhoint1b(x) - rhoint1a(x)).*psi(x).*cos(x) - ...
    (rhoint2b(x) - rhoint2a(x)).*psider(x).*sin(x);

integrandy = @(x) ...
    (rhoint1b(x) - rhoint1a(x)).*psi(x).*sin(x) + ...
    (rhoint2b(x) - rhoint2a(x)).*psider(x).*cos(x);

Ex = integral(integrandx, theta_a, theta_b);
Ey = integral(integrandy, theta_a, theta_b);
End
```

Appendix 3: MATLAB codes for wavefront reconstruction

A 3.1 MATLAB code for generating absolute reference grid

```
function [ActiveImg,Cen_GridX Cen_GridY] = Ref_Grid(Img_filtered)
% automaticaly searching for the center of the image and
% generate the reference grid
PixelNumberPerPitch = 6 ;
XStart = size(Img_filtered,2)/2; % set a center at the center of the image
YStart = size(Img_filtered,1)/2; %
Spacing = 5; % 6x6 size = spacing + 1
CenRange = Img_filtered(YStart:YStart+Spacing, XStart:XStart+Spacing); % get this part out of
the processed image
[y,x] = find(CenRange == max(CenRange(:))); % find the max value of this area, and locate it
xOrigin = x(1,1)+XStart;  % This should be the centroid of the reference grid
yOrigin = y(1,1)+YStart;  % This will be used to calibrate the reference grid, used to offset
the spots
x_rest = mod(xOrigin,PixelNumberPerPitch) - PixelNumberPerPitch/2; %get the remainder of the
centroid over pitch size,
y_rest = mod(yOrigin,PixelNumberPerPitch) - PixelNumberPerPitch/2; %then shift it to half of a
pitch

if x_rest<0 %if the remainder is negative, add one pitch to make it positive
    x_rest = x_rest+6;
end
if y_rest<0
    y_rest = y_rest+6;
end

% get the image in the active area
x_start = round(x_rest);
y_start = round(y_rest);
%get the end index of the active area
x_end = x_start + 19*6 +5; % restrict the array within 20x20 size
y_end = y_start + 19*6 +5; % restrict the array within 20x20 size
% if the start value is zero, make it start from 1
if x_rest == 0
    x_start = x_start+6;
    %then shift 1 pixel backwards
    x_end = x_start + 19*6 + 5; % restrict the array within 20x20 size
end
if y_rest ==0
    y_start = y_start+6;
    %then shift 1 pixel backwards
    y_end = y_start + 19*6 + 5;% restrict the array within 20x20 size
end

%get the active area in the grid
ActiveImg = Img_filtered(y_start:y_end,x_start:x_end);

%Generate a mesh grid as reference
[GridX,GridY] = meshgrid(1:6:120,1:6:120);
GridX = GridX - 1; % offset the center since the meshgrid start from 1,
GridY = GridY - 1;

Cen_GridX = GridX + PixelNumberPerPitch/2;  %generate the centroid of reference grid
Cen_GridY = GridY + PixelNumberPerPitch/2;
```

A 3.2 MATLAB code for dividing image into equal-sized sub-images

This code is cited here for the convenience of the reader. The original code can be found in the reference [176].

```
function outCell=mat2tiles(inArray,varargin)
%MAT2TILES - breaks up an array into a cell array of adjacent sub-arrays of
%equal sizes
%
%   C=mat2tiles(X,D1,D2,D3,...,Dn)
%   C=mat2tiles(X,[D1,D2,D3,...,Dn])
%
%will produce a cell array C containing adjacent chunks of the array X,
%with each chunk of dimensions D1xD2xD3x...xDn. If a dimensions Di does
%not divide evenly into size(X,i), then the chunks at the upper boundary of
%X along dimension i will be truncated.
%
%It is permissible for the Di to be given value Inf. When this is done, it is
%equivalent to setting Di=size(X,i).
%
%If n < ndims(X), then the unspecified dimensions Dj, n<j<=ndims(X) will be
%set to size(X,i).
%
%If n > ndims(X), the the extra dimensions Dj, j>ndims(X) will  be ignored.
%
%EXAMPLE 1: Split a 28x28 matrix into 4x7 sub-matrices
%
%     >> A=rand(28); C=mat2tiles(A,[4,7])
%
%     C =
%
%         [4x7 double]    [4x7 double]    [4x7 double]    [4x7 double]
%         [4x7 double]    [4x7 double]    [4x7 double]    [4x7 double]
%         [4x7 double]    [4x7 double]    [4x7 double]    [4x7 double]
%         [4x7 double]    [4x7 double]    [4x7 double]    [4x7 double]
%         [4x7 double]    [4x7 double]    [4x7 double]    [4x7 double]
%         [4x7 double]    [4x7 double]    [4x7 double]    [4x7 double]
%         [4x7 double]    [4x7 double]    [4x7 double]    [4x7 double]
%
%EXAMPLE 2: Split a 20x20x6 array into 20x6x3 sub-arrays. This example
%illustrates how 'Inf' can be used to indicate that one of the sub-array
%dimensions is to be the same as in the original array, in this case size(A,1)=20.
%
%     >> A=rand(20,20,6);
%
%     >> C=mat2tiles(A,[Inf,6,3])   %equivalent to mat2tiles(A,[20,6,3])
%
%     C(:,:,1) =
%
%         [20x6x3 double]    [20x6x3 double]    [20x6x3 double]    [20x2x3 double]
%
%     C(:,:,2) =
%
%         [20x6x3 double]    [20x6x3 double]    [20x6x3 double]    [20x2x3 double]
%
%The example also shows a situation where the original array does not
%divide evenly into sub-arrays of the specified size. Note therefore that
%some boundary sub-chunks are 20x2x3.
tileSizes=[varargin{:}];
N=length(tileSizes);
Nmax=ndims(inArray);
if N<Nmax
    tileSizes=[tileSizes,inf(1,Nmax-N)];
elseif N>Nmax
    tileSizes=tileSizes(1:Nmax);
```

```
end
N=Nmax;
C=cell(1,N);
for ii=1:N %loop over the dimensions
    dim=size(inArray,ii);
    T=min(dim, tileSizes(ii));
    if T~=floor(T) || T<=0
        error 'Tile dimension must be a strictly positive integer or Inf'
    end
    nn=( dim / T );
    nnf=floor(nn);

    resid=[];
    if nnf~=nn
        nn=nnf;
        resid=dim-T*nn;
    end
    C{ii}=[ones(1,nn)*T,resid];
end
outCell=mat2cell(inArray,C{:});
```

A 3.3 MATLAB code for estimating beam profile

```
app.BeamProfile = zeros(size(app.Sub_ActiveImg));
% create a zero matrix.
% app.Sub_ActiveImg is the cell arry of sub-apertures obtained by mat2tiles
for nn = 1:400
    app.BeamProfile(nn) = sum(app.Sub_ActiveImg{nn},'all');
    % summing each sub-aperture
end
[Xq,Yq] = meshgrid(1:1:120);
BP = interp2(app.GridX,app.GridY,app.BeamProfile, Xq, Yq, 'cubic');
% apply interpolation
imagesc(app.BeamProfile2D,Xq, Yq, BP,'EdgeColor', 'interp');
% show the estimated beam profile
```

Appendix 4: Published peer-reviewed papers

7958 Vol. 61, No. 27 / 20 September 2022 / Applied Optics Research Article

applied optics

Adaptive optics system for a short wavelength mid-IR laser based on a Shack–Hartmann wavefront sensor and analysis of thermal noise impacts

Huang Zhou,[1,2,*] Jan Pilar,[2] Martin Smrz,[2] Liyuan Chen,[2] Miroslav Čech,[1] and Tomas Mocek[2]

[1]Czech Technical University in Prague, Faculty of Nuclear Sciences and Physical Engineering, Brehova 7, 115 19 Prague, Czech Republic
[2]HiLASE Centre, Institute of Physics of the Czech Academy of Sciences, Institute of Physics, Za Radnici 828, 252 41, Dolni Brezany, Czech Republic
*Corresponding author: huang.zhou@hilase.cz

Received 20 May 2022; revised 23 August 2022; accepted 30 August 2022; posted 30 August 2022; published 15 September 2022

We present an adaptive optics (AO) system for a 1.94-μm laser source. Our system consists of a home-made Shack–Hartmann wavefront sensor and silver-coated bimorph deformable mirror operating in a closed-loop control scheme. The wavefront sensor used an uncooled vapor phase deposition PbSe focal-plane array for the actual light sensing. An effect of thermal afterimage was found to be reducing the centroid detection precision significantly. The effect was analyzed in detail and finally has been dealt with by updating the background calibration. System stability was increased by reduction of control modes. The system functionality and stability were demonstrated by improved focal spot quality. By replacing some of the used optics, the range of the demonstrated mid-IR AOS could be extended to cover the spectral range of 1–5 μm. To the best of our knowledge, it is the first AO system built specifically for mid-IR laser wavefront correction. © 2022 Optica Publishing Group

https://doi.org/10.1364/AO.464676

1. INTRODUCTION

Laser sources operating in the short-wavelength mid-IR (2–5 μm) spectral region have numerous applications, such as generation of attosecond pulses, high harmonics towards the X-ray range [1], and medical treatment [2]. It can be used to generate powerful broadband few-cycle mid-IR radiation [3]. Wavefront sensing and shaping technologies have been widely used to analyze and diagnose the high-power ultrafast laser systems in visible and near-IR spectral regions for decades [4,5]. In the past decade, the interest in wavefront correction moved towards the mid-IR region as more mid-IR laser sources are reaching the market, and more mid-IR applications are appearing.

The wavefront sensor is the key part of the adaptive optics (AO) system. Various kinds of detectors have been employed for the mid-IR wavefront detection, such as cooled InSb focal-plane-array (FPA) detectors [6], the cooled mercury cadmium telluride (MCT) detector [7], the pyroelectric detector based on lithium tantalate [8], and the broadband microbolometer [9–11]. Indirect detecting techniques, which convert the image from mid IR to near IR or visible are also proposed to exploit high contrast optical switching in vanadium oxide thin-film layers [12,13]. Wavefront correctors, such as bimorph deformable mirrors (DM) [14], a piston-actuated DM [15], a membrane DM [16], and the microelectromechanical system [17], are widely used to correct the wavefront errors in the AO system. Various AO systems have been developed with different wavefront sensors and correctors for astronomical observations [18–20]. In this paper, we provide an AO system solution for the short-wavelength mid-IR (2–5-μm) spectral region. We employed an uncooled vapor phase deposition (VPD) PbSe FPA [21,22] as the detector for the home-made Shack–Hartmann wavefront sensor (SHWFS) and a silver-coated bimorph piezoelectric deformable mirror in the closed-loop control system.

2. SHWFS FOR MID-IR WAVELENGTH

The SHWFS uses a lenslet array to divide the incoming beam into an array of subapertures, each of which is focused onto the camera sensor. A planar wavefront incident on the lenslet array and focused on the camera sensor will generate a regularly spaced grid of focal spots. A distorted wavefront will cause individual spots to be displaced from the optical axis of each lenslet. The shift of each spot's centroid is proportional to the local slope of the wavefront at the location of the corresponding lenslet.

1559-128X/22/277958-08 Journal © 2022 Optica Publishing Group

Table 1. Main Parameters of the TACHYON 16K Camera

Detector type	VPD PbSe FPA
FPA format	128 × 128 pixels
Pixel size	50 µm (square format)
Dimension of sensor	6.4 × 6.4 (mm)
Spectral range	Mid-IR 1–5 µm
Peak wavelength of detection	3.7 µm
Frame rate (maximum)	2000 fps (full resolution)
Cooled housing	Air-cooled housing
Color type	Monochrome

The wavefront is then reconstructed from the found slope values [23].

When choosing suitable detector technology to fulfill the requirements of the wavefront correction applications in the optical parametric amplifier (OPA) system under developing at the HiLASE laser facility, we surveyed the options and assessed their specifics. Cooled InSb FPA or MCT detectors require complicated cooling systems, which increase the complexity and cost [6,7]. The pyroelectric detector has a larger pixel size of >80 µm [8], which limits the resulting sensor parameters or raises additional space requirements. The indirect wavefront sensing using vanadium oxide as the optical switch has a high detecting threshold of around 144 mW/cm^2. Moreover, the contrast and resolution of the detected image highly depends on the pulse length and laser intensity [12,13]. Lastly, the broadband microbolometer has a small pixel size of around 15 µm and high spatial resolution, it is also rather expensive (>20 000 USD) significantly increasing the overall cost of the AO system.

In this paper, a Tachyon 16K camera, which uses a VPD PbSe FPA sensor [21,22] from the NIT company is selected as the detector for mid-IR radiation. The VPD PbSe FPA detector is monolithically integrated with the corresponding Si-complementary metal-oxide semiconductor (-CMOS) circuitry. The main advantage of using the VPD PbSe technology is using a big area and complex substrates. This makes it unique as it combines all the main requirements demanded for a volume-ready technology: affordable processing, good reproducibility and homogeneity, Si-CMOS compatible and fast processing speed [24]. The main parameters of this camera are listed in Table 1.

Due to the low spatial resolution of the VPD PbSe FPA, here are some considerations for selecting the proper lenslet array for the mid-IR SHWFS: (1) The target wavelength is around 2 µm; (2) the spatial resolution; (3) the dynamic range which is the maximum wavefront slope measurable by one subaperture; (4) the sensitivity, which is inversely proportional to the minimum wavefront slope measurable. In order to have a detectable focal spot centroid on the sensor, the focal spot diameter ($1/e^2$) of the subaperture should be larger than the pixel size (50 µm). The main parameters of the selected lenslet array are listed in Table 2.

With this lenslet array, the resolution of the SHWFS subaperture is 6 × 6 pixels, and the spatial resolution of the SHWFS is 20 × 20 subapertures. The total pixels in the active area are 120 × 120 pixels. Due to the small size of each lenslet, we

Table 2. Main Parameters of the Lenslet Array from Edmund Optics

Part number	64–476
Type	Square lenslet array
Type of optics	Planoconvex
Lens profile	Spherical
Substrate material	IR-fused silica
Radius R (mm)	2.35
Thickness (mm)	1.20
Pitch (µm)	300.00
Effective focal length (mm)	5.10
Dimensions (mm)	10.0 × 10.0
Wavelength range (nm)	200–2200
Coating	Uncoated

assume a plane wavefront in each subaperture. Therefore, the Airy disk is used to estimate the focal spot diameter ($1/e^2$) as [25]

$$D_{\text{Airy}} = 2 \times 0.82 \frac{\lambda f}{d}, \tag{1}$$

where D_{Airy} is the $1/e^2$ diameter of the Airy disk, λ is the wavelength of the radiation under test, f is the focal length of the lenslet, and d is the diameter of the subaperture (pitch).

Thus, the focal spot diameter is 54 µm ($1/e^2$) for a 1.9-µm laser beam. The dynamic range, which is the maximum detectable wavefront slope without correction of algorithm [26] can be calculated by

$$\theta_{\max} = \frac{1}{2f} D_{\text{sub}}, \tag{2}$$

where D_{sub} is the subaperture size.

In this paper, the $\theta_{\max}$ for an individual subaperture is 29.4 mrad. The minimum detectable wavefront slope $\theta_{m\epsilon}$ can be calculated by

$$\theta_{m\epsilon = \frac{d_{\min}}{f}}, \tag{3}$$

where $d_{\min}$ is the minimum detectable spot displacement.

Typically, $d_{\min}$ is determined by the pixel size of the detector, the centroid algorithm, etc. The measurement sensitivity in this paper is $1/\theta_{m\epsilon} = 1/0.09$ mrad^{-1} with a minimum detectable displacement of 0.01 pixel, which is our estimation based on estimations for similar algorithms. A photograph of the developed mid-IR SHWFS is shown in the left-bottom corner of Fig. 1. The camera features an active cooler for temperature management.

3. EXPERIMENTAL SETUPS

The SHWFS was first calibrated by a spherical wavefront originating from a single-mode fiber, using an absolute calibration method [27] as shown in the experimental setup in Fig. 1. We employed a tip of the single-mode fiber of a 1550-nm fiber laser as a source of a virtually aberration-free diverging spherical wave. The distance to the wavefront sensor was carefully measured, and the resulting image on the wavefront sensor was recorded. From the known parameters of the diverging wave, we could calibrate the parameters relevant to the wavefront sensor's scaling,

7960 Vol. 61, No. 27 / 20 September 2022 / Applied Optics Research Article

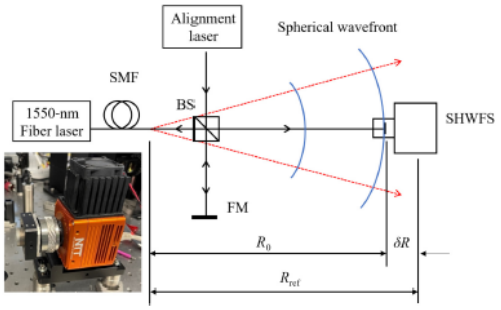

Fig. 1. Calibration setup. SMF: single-mode fiber; BS: beam splitter; SHWFS; FM: flat mirror. R_{ref}: reference radius of curvature of the wavefront, R_0: actual radius of curvature of the wavefront, δR: difference between the reference and the actual radius of curvature. The blue curves indicate the diverging spherical wave. The red dashed lines indicate the propagating direction of the spherical wave. The alignment laser and BS will be removed during measuring after precise alignment. The inset shows the home-made SHWFS.

such as a lenslet array distance from the light-sensitive part of the sensor, which is difficult to measure in practice. Additional details about the technique can be found in the references [27]. An alignment laser source and respective coupling beam splitter were used only for the alignment procedure and were not present for the actual measurement.

Figure 2(a) shows the Shack–Hartmann pattern of one measurement captured by the home-made SHWFS and processed by our own developed MATLAB App. The wavefront was reconstructed by a modal reconstruction method using Zernike polynomials [28,29]. Figures 2(b) and 2(c) show one of the measured and reconstructed wavefronts of the 1550-nm fiber laser during the calibration procedure. The defocus term indicates a diverging wavefront. The SHWFS was available for wavefront measurement after precise calibration.

The experimental setup used for the AO system characterization is shown in Fig. 3. A closed-loop control scheme [30–34] had been used in our mid-IR AO system. A Tm fiber laser emitting at the wavelength of 1940 nm was used as the mid-IR source. The Tm-doped fiber laser was collimated with a fiber collimator. An attenuator consisting of a HWP and a PBS was installed after the output to decrease the output power. Two DiMs coated with high reflectivity at 1940 nm and high transfer at 780 nm were used to couple out the pump light from the 1940-nm mid-IR laser beam. The residual pump light was present due to the Tm fiber laser specifics. A telescope consisting of two convex lenses with focal lengths of $f_1 = 100$ mm and $f_2 = 800$ mm were used to expand the beam diameter to 17 mm $(1/e^2)$ to cover most of the center part of the DM. The DM used in this paper was a piezoelectric bimorph mirror with 64 actuators from dynamic optics. It is coated with protected silver coating, suitable for wide spectral range applications, and its clear aperture is 30 mm. The bimorph technology was chosen from a variety of DM technologies based on several aspects. First, it is potentially suitable for high-power laser beams thanks to its ability to integrate multilayer coating. Second, it is suitable for correction of thermal aberration thanks to its natural

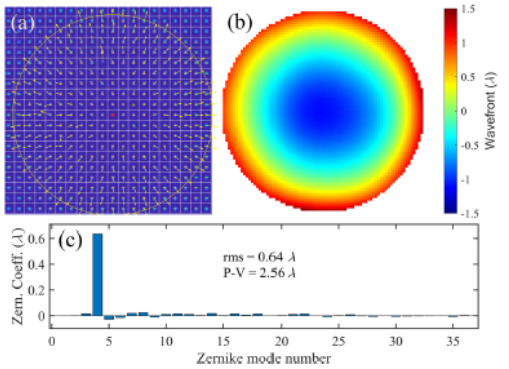

Fig. 2. (a) Hartmann gram obtained by the home-made SHWFS and processed by the MATLAB App developed at the HiLASE Centre. The yellow circle indicates the unit circle of the sampled wavefront, and the yellow arrows indicate the wavefront slopes. (b) Reconstructed wavefront from the measured Shack–Hartmann pattern and (c) its Zernike coefficients. Zernike modes are indexed in the single indexing scheme; the same for the other figures in this paper. The defocus term indicates the diverging wavefront.

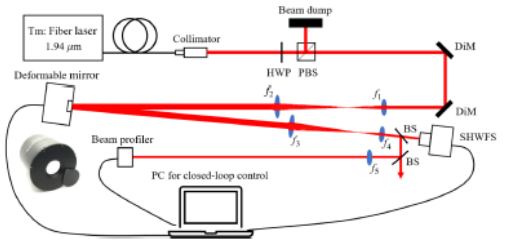

Fig. 3. Experimental setup of the AO system for 1.94-μm Tm: fiber laser. Half-wave plate (HWP); polarization BS (PBS); dichroic mirror (DiM); SHWFS; BS. The inset is a photograph of the DM.

flexing properties. Third, it is a cost-effective technology with high-speed control ability.

A second telescope formed by two convex lenses with focal lengths of $f_3 = 500$ mm and $f_4 = 200$ mm was used as an optical relay system to image the DM onto the SHWFS, while maintaining the optical properties of the wavefront under test. Therefore, a good linearity between the wavefront controlling and the wavefront response can be ensured. The beam diameter after the second telescope was 6.8 mm $(1/e^2)$. The DM and the lenslet array of the SHWFS are placed on the conjugated planes of the optical relay system. Two beam splitters were used to get a low-power beam for measurements of the wavefront and the focal spot (far field). The beam profiler used in this paper is a WinCamD based on a broadband microbolometer from the DATARAY company. It has a large spectral range from 2 to 16 μm. Its pixel size is 17 μm × 17 μm and 10.88 × 8.16 mm sensor size. The focusing lens with a focal length of $f_5 = 1.5$ m was used to have a large focal spot size covering more pixels of the beam profiler for detailed analysis of the profile.

Research Article Vol. 61, No. 27 / 20 September 2022 / Applied Optics 7961

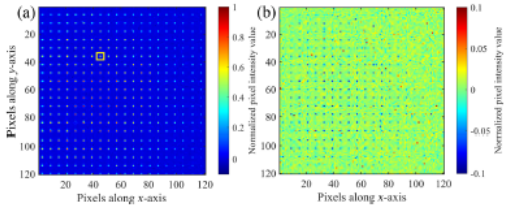

Fig. 4. (a) Hartmann gram while the 1.94-μm laser beam was incident on the Tachyon 16 K camera. (b) The afterimage was captured when blocking the laser beam after 10-s exposition of the camera. The area marked by yellow rectangle is one subaperture. Both images are shown with a jet color map, and the color bar indicates the normalized pixel intensity value after subtracting the thermal noise.

4. THERMAL SPECIFICS OF THE SHWFS

During tests on the experimental setup (Fig. 1), it was found that the accumulated thermal noise of the Tachyon 16K camera can affect the wavefront measurement accuracy with a thresholding center of gravity or a weighted center of gravity centroiding technique [35,36]. The sensor displayed an afterimagelike thermal noise, which is an image that continues to appear in the eyes after a period of exposure to the original image. Figure 4(a) shows the Hartmann gram captured while a 1.94-μm laser beam incident on the Tachyon 16K camera. The afterimage observed is shown in Fig. 4(b). It was taken after a 10-s laser exposure to the camera. Prior to this measurement, an image of thermal noise was captured with the camera internal mechanical shutter closed. Such a thermal noise image was then subtracted from the following measurements.

The thermal afterimage was caused by the sampled beam focal spots on the sensor. We found that the afterimage generates on the order of seconds after being exposed to the laser beam. Higher incident intensities lead to shorter accumulating times of the afterimage.

The wavefronts were measured continuously with the time interval of 2 s for 120 s to see the impacts of the thermally induced afterimage on the centroid detection. The results are shown in Fig. 5. The subaperture marked by the yellow rectangle in Fig. 4(a) was chosen for analysis. Figure 5(a) shows the distribution of the focal spot centroids detected during 120 s. The change in color of the focal spot centroids is related to the iteration number. It shows the trend of the centroid shift caused by the afterimage The centroid distribution root-mean square (rms) is 0.16 pixels and 0.24 pixels for the x and y axes, respectively. Figure 5(b) shows the time development of the x-tilt Zernike coefficient during 120 s. It could be seen that the x-tilt coefficient increased steadily in time. Figures 5(c) and 5(d) show the reconstructed wavefronts of the first and the last measurements.

The TACHYON 16K camera has an integrated physical shutter which can be controlled remotely. This allows easy update of the background every few seconds, effectively subtracting the afterimage with it. The response time of the physical shutter is tested to be about 50 ms, effectively adding a 100-ms delay to the control system for each background update every 2 s. Since the current bandwidth of the closed-loop AO system was only 10–20 Hz on the MATLAB platform, no obvious

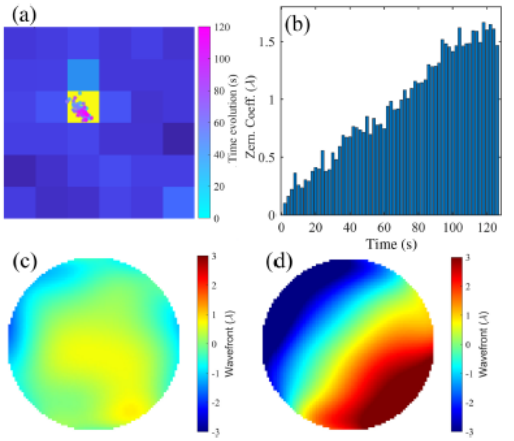

Fig. 5. (a) Distribution of the calculated centroids of the focal spots detected during the 120 s in the subaperture. The background image is the first captured image of the subaperture (6 × 6 pixels) in a jet color map. The colors of the spots varying from cyan to magenta indicate the recording sequence from the first to the last centroids. (b) Bar plot of the Zernike coefficients of the x-tilt term of each reconstructed wavefront as a function of time during 120 s. The measured wavefront of the first (c) and the last (d) capturings.

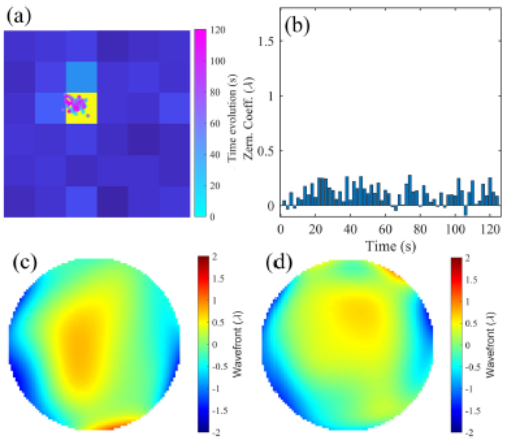

Fig. 6. (a) Distribution of the calculated centroids of the focal spots detected during the 120 s in the subaperture. The colors of the spots varying from cyan to magenta indicate the recording sequence from the first to the last centroids. (b) Bar plot of the Zernike coefficients of the x-tilt term of each reconstructed wavefront as a function of time during 120 s. The measured wavefront of the first (c) and the last (d) capturings.

impact, such as frozen frames or interrupting of the closed loop, to the AO system had been observed. It would be expected that the impact would be observed at a bandwidth higher than 20 Hz. With dynamic updating of the background, the detected centroid distribution was more uniform as shown in Fig. 6(a) with the rms reduced to 0.11 pixel and 0.15 pixel for the x and y

7962 Vol. 61, No. 27 / 20 September 2022 / Applied Optics Research Article

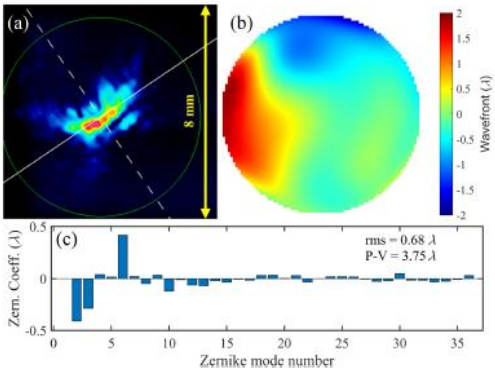

Fig. 7. (a) Focal spot profile with dimensions of 2.59 mm × 1.2 mm (at $1/e^2$) and 1.48 mm × 0.42 mm (at FWHM), (b) the wavefront and (c) its Zernike coefficients measured when replacing the DM with a flat silver-coated mirror. The wavefront rms was 0.68λ, the peak-to-valley (P-V) was 3.75λ (at 1.94 μm).

axes, respectively. The Zernike coefficient of the x-tilt term was showing improved stability, and wavefront variations decreased [Figs. 6(c) and 6(d)].

Prior to starting the AO system, the initial wavefront and the focal spot profile were measured by replacing the DM with a standard silver-coated mirror with a flatness of rms $< \lambda/6$ (at 632 nm). Figure 7 shows the initial wavefront and the focal spot profile after the focusing lens f_5. The distortion of the wavefront and focal spot profile was mainly caused by the fiber collimator of the laser source, the usage of singlet lenses and the imperfect alignment of the optical system. Telescopes for a 1.94-μm laser with such large beam diameter can be aligned with the help of the inaccurate mid-IR liquid crystal detector card. The rms value of the wavefront was 0.47λ, and P-V was 3.75λ (at 1.94 μm).

After characterization of the initial wavefront and focal spot profile of the experimental setup (Fig. 1), the DM was installed back to the AO system. Then calibration of the AO system was carried out to obtain the control matrix for closed-loop control. We used the influence functions scheme in which the characteristic DM response to the action of each single actuator is measured. The closed loop was then started, and the rms of residual wavefront was logged as a function of time/iteration

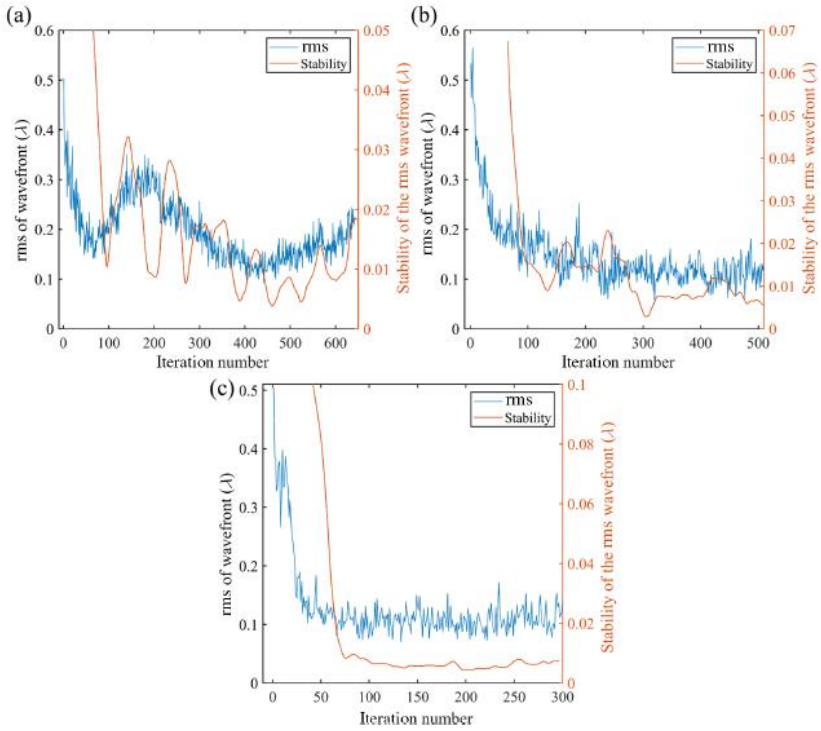

Fig. 8. (a) The residual wavefront rms was logged as function of the iteration number of the closed-loop control system without dynamic updating of the background and (b) with dynamic updating of the background with the time interval of 2 s. The wavefront corrections were performed for all 35 Zernike terms. (c) The residual wavefront rms was logged as function of the iteration number of the closed-loop control system with dynamic updating of the background with the time interval of 2 s. The wavefront correction was performed for the first 10 Zernike terms. The orange curve shows the stability of the control system performance by calculating the standard deviation of every 50 values of the wavefront rms.

Research Article Vol. 61, No. 27 / 20 September 2022 / Applied Optics 7963

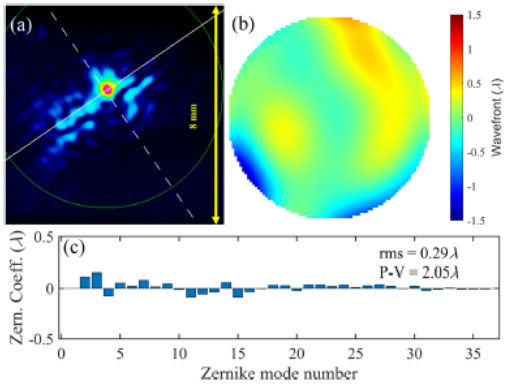

Fig. 9. (a) Focal spot profile with diameters of 2.61 mm (at $1/e^2$) and 0.51 mm (at FWHM), (b) the residual wavefront rms and (c) its Zernike coefficients after running 650 iterations without dynamic updating of the background. The wavefront rms was 0.29λ, and the P-V was 2.05λ (at 1.94 μm).

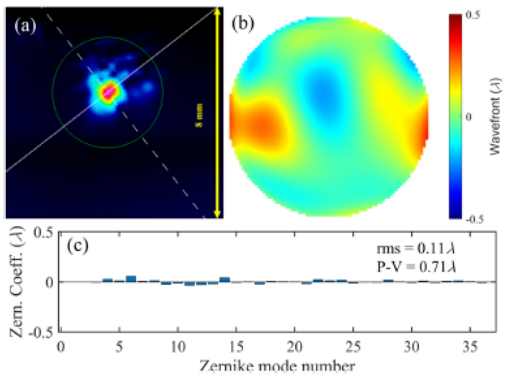

Fig. 10. (a) Focal spot profile with diameters of 1.26 mm (at $1/e^2$) and 0.52 mm (at FWHM), (b) the residual wavefront rms and (c) its Zernike coefficients after correcting the first 35 Zernike terms (without piston), with dynamic updating of the background. The residual wavefront rms was 0.11λ, and the P-V value was 0.71λ (at 1.94 μm).

number. We compared the case without dynamic updating of the thermal background with the case where thermal background is updated during the closed loop as shown in Figs. 8(a) and 8(b), respectively. From Fig. 8(a), it could be seen that without dynamic updating of the background, the residual wavefront rms initially decreased to 0.16λ after 70 iterations (about 7 s), but it did not remain stable was fluctuating presumably due to the thermal error buildup as indicated by the rms stability curve, which was performed by calculating the standard deviation of every 50 values of the wavefront rms. Figure 9 shows the focal spot profile and the residual wavefront after running 650 iterations, without dynamic updating of the background. The residual wavefront rms was 0.29λ, and the P-V value was 2.05λ (at 1.94 μm). The focal spot diameter was 2.6 mm (at

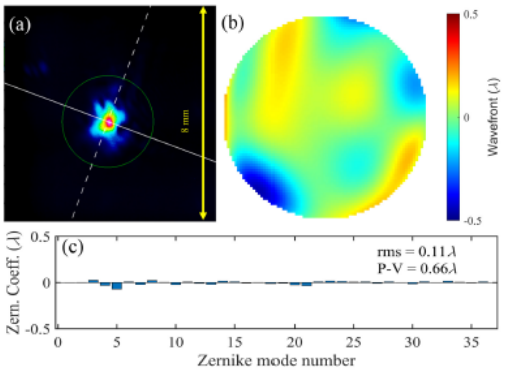

Fig. 11. (a) Focal spot profile with diameters of 0.97 mm (at $1/e^2$) and 0.54 mm (at FWHM), (b) the residual wavefront rms, and (c) its Zernike coefficients after correcting the first 10 Zernike terms (without piston) with dynamic updating of the background. The residual wavefront rms was 0.11λ, and the P-V value was 0.66λ (at 1.94 μm).

$1/e^2$) and 0.51 mm (at FWHM) with a lens of focal length $f_5 = 1.5$ m.

Figure 8(b) shows the result with dynamic updating of the background with the time interval of 2 s, which was selected as a compromise between the ability to mitigate the thermal afterimage; whereas keeping the loop speed high. The residual wavefront rms decreased from 0.54λ to 0.15λ after 100 iterations (about 12 s). The rms was stable within the range of $0.1\lambda - 0.18\lambda$ after 220 iterations (about 25 s). The stability curve indicates stable performance with less oscillations. The equidistant ripples on the stability curve were caused by the background updates every 2 s.

When correcting the first 35 Zernike terms (without a piston), the residual wavefront rms was 0.11λ, and the P-V value was 0.71λ (at 1.94 μm). The focal spot profile diameter was reduced to 1.26 mm (at $1/e^2$) and 0.52 mm (at FWHM). The results are shown in Fig. 10.

However, the focal spot profile was further improved to diameters of 0.97 mm (at $1/e^2$) and 0.54 mm (at FWHM); whereas, correcting only the first 10 Zernike terms (the first three radial orders of aberrations without piston) as shown in Fig. 11. The residual wavefront rms was 0.11λ and the P-V of 0.66λ (at 1.94 μm). The residual wavefront rms decreased from 0.5λ to 0.12λ after 50 iterations (about 6 s) and then remained stable within the range of $0.10\lambda - 0.15\lambda$ [see Fig. 8(c)]. The AO system corrected the wavefront faster when correcting only the first 10 Zernike terms, and it became more stable with smaller ripples. We found the control loop running faster and more stable when only the first 10 Zernike terms were used. The speed increase is intuitively related to the lower computational load. We attribute the stability increase to the fact that most of the focus-degrading aberrations were within those 10 terms, and so they were included in the correction loop. Since the higher orders were much weaker as shown in Fig. 7(c), their signal-to-noise ratio could be relatively more influenced by the thermal afterimage. Therefore, correcting those terms could have led

to a virtual aberration correction causing random focal spot degradations and wavefront rms fluctuation.

5. CONCLUSION

In this paper, we have shown an AO system developed for the 1.94-μm laser. The AO system consists of a home-made Shack–Hartmann wavefront sensor based on an uncooled VPD PbSe FPA detector and a silver-coated bimorph piezoelectric deformable mirror coupled in a closed-loop control system. The thermal character of the laser causes the afterimage being formed on the sensor especially in the positions of the lenslet-generated focal spots. It introduces a significant error to the centroid detection and causes erroneous wavefront reconstruction. The impact of the thermally induced afterimage on the performance of the AO system was analyzed in detail. The afterimage effect was effectively reduced by dynamic background updating. By using this approach, the residual wavefront rms was reduced from 0.29λ to 0.11λ, and the focal spot diameter was reduced from 2.6 to 0.97 mm (at $1/e^2$). The AO system developed in this paper can be easily extended to the mid-IR spectral range (1–5 μm) thanks to the spectral range of the camera. The system will be applied in mid-IR laser applications or OPA experiments in the near future at the HiLASE laser facility.

Funding. European Regional Development Fund and the State Budget of the Czech Republic (CZ.02.1.01/0.0/0.0/15_006/0000674); European Union's Horizon 2020 Research and Innovation Programme (739573).

Disclosures. The authors declare that there are no conflicts of interest related to this article.

Data availability. Data underlying the results presented in this paper are not publicly available at this time but may be obtained from the authors upon reasonable request.

REFERENCES

1. F. Silva, S. M. Teichmann, S. L. Cousin, M. Hemmer, and J. Biegert, "Spatiotemporal isolation of attosecond soft X-ray pulses in the water window," Nat. Commun. **6**, 6611 (2015).
2. S. Gravas, A. Bachmann, O. Reich, C. G. Roehrborn, P. J. Gilling, and J. De La Rosette, "Critical review of lasers in benign prostatic hyperplasia (BPH)," BJU Int. **107**, 1030–1043 (2011).
3. T. Kanai, P. Malevich, S. S. Kangaparambil, K. Ishida, M. Mizui, K. Yamanouchi, H. Hoogland, R. Holzwarth, A. Pugzlys, and A. Baltuska, "Parametric amplification of 100 fs mid-infrared pulses in $ZnGeP_2$ driven by a Ho:YAG chirped-pulse amplifier," Opt. Lett. **42**, 683–686 (2017).
4. Z. Guo, L. Yu, W. Li, Z. Gan, and X. Liang, "Wavefront evolution of the signal beam in Ti: sapphire chirped pulse amplifier," Chin. Phys. B **28**, 014203 (2019).
5. V. Y. Zavalova and A. V. Kudryashov, "Shack-Hartmann wavefront sensor for laser beam analyses," Proc. SPIE **4493**, 277–284 (2002).
6. L. Shkedy, T. Markovitz, Z. Calahorra, I. Hirsh, and I. Shtrichman, "Megapixel digital InSb detector for midwave infrared imaging," Opt. Eng. **50**, 061008 (2011).
7. C. Robert, V. Michau, B. Fleury, S. Magli, and L. Vial, "Mid-infrared Shack-Hartmann wavefront sensor fully cryogenic using extended source for endoatmospheric applications," Opt. Express **20**, 15636–15653 (2012).
8. E. L. Maweza, L. Gailele, H. J. Strauss, I. Litvin, A. Forbes, and A. Dudley, "Shaping and detecting mid-IR light with a spatial light modulator," in *Advanced Solid-State Lasers* (Optical Society of America, 2016), paper JTh2A-15.
9. S. Velghe, D. Brahmi, W. Boucher, B. Wattellier, N. Guérineau, R. Haïdar, and J. Primot, "MWIR and LWIR wavefront sensing with quadri-wave lateral shearing interferometry," Proc. SPIE **7300**, 73000T (2009).
10. B. Fieque, A. Crastes, O. Legras, and J.-L. Tissot, "MWIR uncooled microbolometer: a way to increase the number of applications," Proc. SPIE **5783**, 531–538 (2005).
11. B. D. Oelrich, A. Crastes, C. I. Underwood, and S. Mackin, "Low-cost mid-wave IR microsatellite imager concept based on uncooled technology," Proc. SPIE **5570**, 209–217 (2004).
12. S. Bonora, U. Bortolozzo, S. Residori, R. Balu, and P. V. Ashrit, "Mid-IR to near-IR image conversion by thermally induced optical switching in vanadium dioxide," Opt. Lett. **35**, 103–105 (2010).
13. S. Bonora, G. Beydaghyan, A. Haché, and P. V. Ashrit, "Mid-IR laser beam quality measurement through vanadium dioxide optical switching," Opt. Lett. **38**, 1554–1556 (2013).
14. R. Bastaits, D. Alaluf, M. Horodinca, I. Romanescu, I. Burda, G. Martic, G. Rodrigues, and A. Preumont, "Segmented bimorph mirrors for adaptive optics: segment design and experiment," Appl. Opt. **53**, 6635–6642 (2014).
15. R. H. Freeman and J. E. Pearson, "Deformable mirrors for all seasons and reasons," Appl. Opt. **21**, 580–588 (1982).
16. S. Bonora and L. Poletto, "Push-pull membrane mirrors for adaptive optics," Opt. Express **14**, 11935–11944 (2006).
17. T. G. Bifano, J. Perreault, R. K. Mali, and M. N. Horenstein, "Microelectromechanical deformable mirrors," IEEE J. Sel. Top. Quantum Electron. **5**, 83–89 (1999).
18. L. Jolissaint and S. Kendrew, "Modeling the chromatic correction error in adaptive optics: application to the case of mid-infrared observations in dry to wet atmospheric conditions," in *1st AO4ELT Conference-Adaptive Optics for Extremely Large Telescopes, EDP Sciences* (2010), p. 05021.
19. M. R. Chun, J. Elias, B. Ellerbroek, T. Bond, M. Liang, R. Clare, A. Tokunaga, M. Richter, and L. Daggert, "MIRAO: a mid-IR adaptive optics system design for TMT," Proc. SPIE **6272**, 252–261 (2006).
20. S. Hippler, M. Feldt, T. Bertram, W. Brandner, F. Cantalloube, B. Carlomagno, O. Absil, A. Obereder, I. Shatokhina, and R. Stuik, "Single conjugate adaptive optics for the ELT instrument METIS," Exp. Astron. **47**, 65–105 (2019).
21. G. Vergara, R. Gutiérrez, L. J. Gómez, *et al.*, "Fast uncooled low density FPA of VPD PbSe," Proc. SPIE **7298**, 775–782 (2009).
22. G. Vergara, R. Linares-Herrero, R. Gutiérrez-Álvarez, C. Fernández-Montojo, L. J. Gómez, V. Villamayor, A. Baldasano-Ramírez, and M. T. Montojo, "4.1-The first uncooled (no thermal) MWIR FPA monolithically integrated with a Si-CMOS ROIC: a 80 × 80 VPD PbSe FPA," in *Proceedings IRS²* (2013), pp. 71–75.
23. R. G. Lane and M. Tallon, "Wave-front reconstruction using a Shack–Hartmann sensor," Appl. Opt. **31**, 6902–6908 (1992).
24. G. Vergara, R. Linares Herrero, R. Gutiérrez-Álvarez, M. T. Montojo, C. Fernández-Montojo, A. Baldasano-Ramírez, and G. Fernández-Berzosa, "VPD PbSe technology fills the existing gap in uncooled low-cost and fast IR imagers," Proc. SPIE **8012**, 80121Q (2011).
25. C. W. Merkle, S. P. Chong, A. M. Kho, J. Zhu, A. Dubra, and V. J. Srinivasan, "Visible light optical coherence microscopy of the brain with isotropic femtoliter resolution *in vivo*," Opt. Lett. **43**, 198–201 (2018).
26. H. Shinto, Y. Saita, and T. Nomura, "Shack–Hartmann wavefront sensor with large dynamic range by adaptive spot search method," Appl. Opt. **55**, 5413–5418 (2016).
27. A. Chernyshov, U. Sterr, F. Riehle, J. Helmcke, and J. Pfun, "Calibration of a Shack–Hartmann sensor for absolute measurements of wavefronts," Appl. Opt. **44**, 6419–6425 (2005).
28. I. Mochi and K. A. Goldberg, "Modal wavefront reconstruction from its gradient," Appl. Opt. **54**, 3780–3785 (2015).
29. V. Lakshminarayanan and A. Fleck, "Zernike polynomials: a guide," J. Mod. Opt. **58**, 545–561 (2011).
30. S.-Y. Cheng, W.-J. Liu, S.-Q. Chen, L.-Z. Dong, P. Yang, and B. Xu, "Comparison between iterative wavefront control algorithm and direct gradient wavefront control algorithm for adaptive optics system," Chin. Phys. B **24**, 084214 (2015).
31. B. Dong and M. J. Booth, "Wavefront control in adaptive microscopy using Shack-Hartmann sensors with arbitrarily shaped pupils," Opt. Express **26**, 1655–1669 (2018).

32. B. L. Ellerbroek and T. A. Rhoadarmer, "Adaptive wavefront control algorithms for closed loop adaptive optics," Math. Comput. Model. **33**, 145–158 (2001).
33. J.-P. Zou, B. Wattellier, and B. Tyson, *Adaptive Optics for High-Peak-Power Lasers–An Optical Adaptive Closed-Loop Used for High-Energy Short-Pulse Laser Facilities: Laser Wave-Front Correction and Focal-Spot Shaping* (Intech, 2012).
34. A. R. Ganesan, P. Arulmozhivarman, D. Mohan, A. Kumar, and A. K. Gupta, "Design and development of a closed loop adaptive optics system for wavefront sensing and control," J. Opt. **34**, 67–81 (2005).
35. S. Thomas, T. Fusco, A. Tokovinin, M. Nicolle, V. Michau, and G. Rousset, "Comparison of centroid computation algorithms in a Shack–Hartmann sensor," Mon. Not. R. Astron. Soc. **371**, 323–336 (2006).
36. A. Vyas, M. B. Roopashree, and B. R. Prasad, "Optimization of existing centroiding algorithms for Shack Hartmann sensor," arXiv:0908.4328 (2009).

Experimental study on the fluctuation–magnification effect of chirped volume Bragg grating compressor in high-energy, ultrafast, thin-disk chirped pulse amplification system

Huang Zhou,[a,b,*] Ondrej Novak,[a] Martin Smrž,[a,b] Liyuan Chen,[b] Lukáš Roškot,[a,b] Bianka Csanaková,[a] Michal Chyla,[b] Miroslav Čech,[a] and Tomáš Mocek[b]

[a]Czech Technical University in Prague, Faculty of Nuclear Sciences and Physical Engineering, Prague, Czech Republic

[b]Czech Academy of Sciences, Institute of Physics, HiLASE Center, Dolni Brezany, Czech Republic

Abstract. The fluctuation–magnification effect on the peak intensity of a laser pulse caused by the nonlinear Kerr effect in the chirped volume Bragg grating (CVBG) compressor is investigated experimentally for a high-energy, thin-disk, chirped pulse amplification system. The nonlinear Kerr effect occurs at the blue end, and the accumulated nonlinear phase shift (B-integral) in the CVBG rises with the increase of laser pulse energy. Experiments show that small fluctuations in peak power of uncompressed pulses cause increasing of the temporal fluctuation and spatial fluctuation due to high Kerr-nonlinearity in the CVBG when B-integral is larger than π. Thus the initial fluctuation would be magnified by the CVBG compressor. © *2022 Society of Photo-Optical Instrumentation Engineers (SPIE)* [DOI: 10.1117/1.OE.61.XX.XXXXXX]

Keywords: fluctuation–magnification; chirped volume Bragg grating; thin-disk laser; B-integral; nonlinear Kerr effects.

Paper 20220391G received Apr. 15, 2022; accepted for publication Sep. 26, 2022.

1 Introduction

Ultrafast laser sources have been applied in various fields in scientific research and industry, such as laser micromachining,[1] laser welding,[2] laser shock peening,[3] and laser materials processing. In the past few decades, the chirped pulse amplification (CPA)[4] technique, which amplifies the temporally stretched pulse and then compresses the pulse to accomplish both high peak power and transform-limited pulse, extends the application areas of the ultrafast laser source. Diffraction grating-based compressor and the chirped volume Bragg grating (CVBG) compressors are commonly used for ultrafast pulse compression. The former provides larger dispersion and wider bandwidth of spectrum; the latter provides compactness, robustness, and relatively lower sensitivity to mechanical vibrations and optical misalignment.[5] Thanks to these properties of the CVBG, it has been widely used in applied ultrafast laser systems in recent years. Smrž et al.[6] compressed 100 kHz, sub-1-mJ pulses at 1030 nm by the CVBG to 1.9 ps. von Grafenstein et al.[7] applied the CVBG to compress a 2-μm CPA source with 55 mJ, 4.3 ps pulses at a kHz repetition rate. Štěpánková et al.[8] did a detailed experimental investigation on high-power CVBG compressor, which was performed with a 216-W thin-disk laser system of 1030 nm, 92-kHz repetition rate, and 2-ps pulse duration. CVBG has also been used for pulse stretching or compression in fiber CPA, obtaining transform limited pulses.[9,10] High-energy ultrafast pulse of millijoule pulse energy and <400 fs pulse duration has also been achieved with CVBG utilized in bulk CPA system.[11,12]

*Address all correspondence to Huang Zhou, huang.zhou@hilase.cz

0091-3286/2022/$28.00 © 2022 SPIE

The CVBG is bulky material made of photo-thermal-refractive glass of a few centimeters in length. When ultrafast laser pulse with high peak intensity propagates through a CVBG, the total on-axis nonlinear phase shift (B-integral) of the laser pulse accumulated during a CVBG round-trip can be high and non-negligible. Therefore, nonlinear Kerr effect induced by high nonlinear phase shift would bring additional instability to dynamically changing properties of compressed laser pulses, leading to damage on the device components due to self-focusing on the worst case, chirp, and spectral broadening due to self-phase modulation (SPM),[13] changing of beam divergence and beam diameter by an introduced Kerr lens,[14] etc. Increasing the beam diameter to reduce the B-integral is a commonly used in laser engineering.

In this work, we experimentally investigated the fluctuation–magnification effect on the peak intensity of a laser pulse caused by the nonlinear Kerr effect in the CVBG compressor. Experiments show that small fluctuations in peak power of uncompressed pulses cause increasing of the spatial fluctuation and the temporal fluctuation with the increasing of pulse energy due to the high nonlinear Kerr effect in the CVBG compressor.

2 Experimental Setup

The experimental setup is shown in Fig. 1. A thin-disk regenerative amplifier is used as the pulse source. Its parameters are shown in Table 1. The laser pulse is compressed to ~1.7 ps by the CVBG, whose parameters are shown in Table 2. The laser pulse is sampled by a beam sampler (BS1). A half-wave plate (HWP) and a polarization beam splitter (PBS) are used to attenuate the

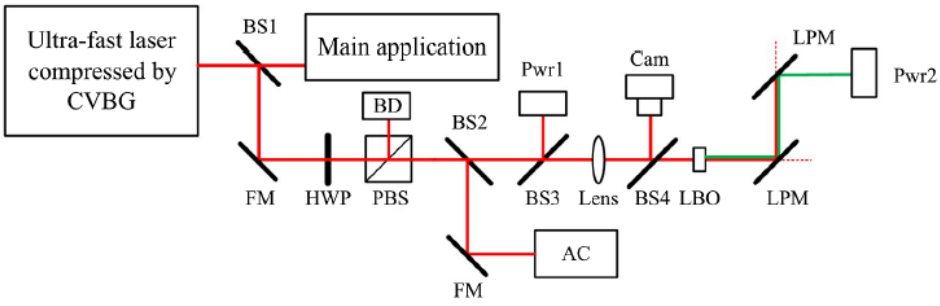

Fig. 1 The scheme of the experimental setup. BS: beam sampler, FM: flat mirror, HWP: half-wave plate, PBS: polarization beam splitter, BD: beam dump, AC: autocorrelator, LPM: long-pass mirror, Pwr: Power meter, and Cam: Camera.

Table 1 Parameters of the laser pulse for simulation.

Item type	Value
Center wavelength (nm)	1030
Spectral bandwidth (FWHM) (nm)	1.65
Average power (W)	20
Repetition rate (kHz)	5 to 20
Pulse energy (mJ)	1 to 4
Pulse duration (uncompressed) (ps)	500
Pulse duration (compressed) (ps)	1.0
Beam diameter ($1/10^2$) (mm)	3.5
Beam divergence (half angle) (mrad)	0.2
M2 beam quality	<1.12

Table 2 Parameters of the CVBG for simulation.

Item type	Value
Center wavelength (nm)	1030
Spectral bandwidth (FWHM) (nm)	2.59
Diffraction efficiency (%)	85
Grating aperture ($w \times h$) (mm)	8×8
Length (mm)	50
Stretching factor (ps/nm)	205
Stretching time (ps)	500

sampled beam. A second beam sampler (BS2) is used to sample part of the laser beam for autocorrelation measurement. A third beam sampler (BS3) is used to sample part of the laser beam for monitoring the power stability of the fundamental laser. A lens ($f = 150$ mm) is used to focus the fundamental beam into an Lithium triborate (LiB_3O_5) (LBO) crystal, which is designed to achieve type I noncritical phase matching for the second harmonic generation (SHG). In order to minimize the temperature sensitivity of LBO crystal, a 2-mm-long LBO crystal of type I with larger temperature bandwidth is employed for SHG. It has a large temperature tolerance range of 4°C at 99%. The measurements were all carried out in a laboratory environment with a stabilized room temperature of $20 \pm 0.25^{\circ}$C. A fourth beam sampler (BS4) is used to sample part of the focused laser beam to the camera (Cam), which is placed at the focal plane of the lens, for monitoring the focal spot. The harmonic laser beam from the LBO crystal is then sent to a second power meter (Pwr2) after two long-pass mirror (LPM), which has AR coating for the fundamental beam and HR coating at 45-deg angle of incidence for the second harmonic beam. Two photodiode power meters (PD300 from Ophir Photonics) are used for monitoring the power stability.

3 Results and Discussion

The long-term fluctuations in fundamental power (1H) and its SHG power (2H) were measured over 1.5 h after warming up of the laser system, as shown in Fig. 2. The pulse energy was scaled

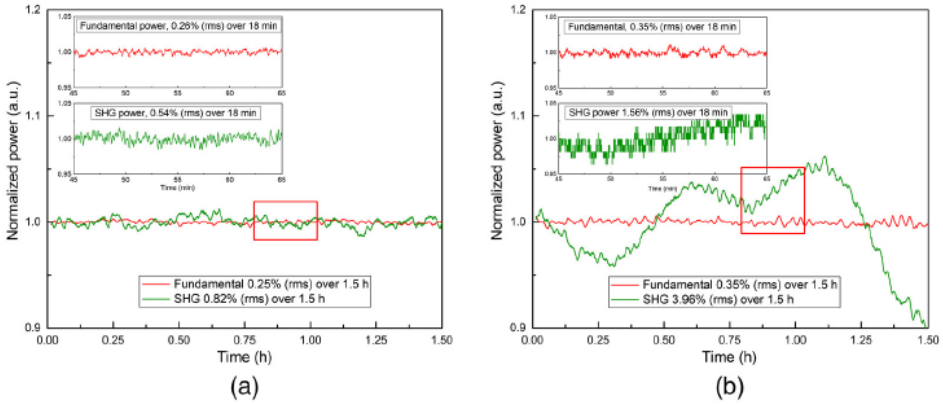

Fig. 2 (a) Normalized fluctuations in fundamental power and its SHG power of laser pulse compressed by the CVBG compressor for pulse energy of 1.1 mJ over 1.5 h after warming up. The data noise was filtered by a moving-average filter of 50 samples only for plotting purpose. The insets show the detail of the unfiltered fast fluctuation in the selected period of 18 min. (b) The fundamental power fluctuation and the SHG power fluctuation for pulse energy of 4 mJ for 1.5 h. The insets show the fundamental power fluctuation and the SHG power fluctuation in 18 min.

by changing the repetition rate of the thin-disk regenerative amplifier so that the average power would be kept within 20 to 22 W. Therefore, the thermal lens would be similar for different pulse energies and could be neglected in this model. The insets of Figs. 2(a) and 2(b) show the fast fluctuations in a short period of 18 min. The fluctuations in fundamental power were within the range of 0.25% to 0.35% in both cases for different pulse energies. The fluctuations in the SHG power of the 4-mJ laser pulse were 3.96% for long-term fluctuation and 1.56% for fast fluctuation, respectively. They are 11.3 times and 4.4 times of the fluctuations in the fundamental power for the long-term fluctuation and fast fluctuation, respectively. However, they were only 0.82% (3.2 times) and 0.54% (2 times) for both fluctuations for 1.1 mJ laser pulse, respectively. The fluctuations in 4 mJ case are much higher than 1.1 mJ case and the expected value, which should be <2 times of its fluctuation in fundamental power when there is no extra fluctuation.

The B-integrals at the wavelength of 1030 nm are calculated to be 1.81, 3.1, 4.8, and 6.2 for 1, 2, 3, and 4 mJ, respectively. The temporal fluctuations in the compressed pulse duration were also logged every 20 min during 1.5 h for each measurement. The measured autocorrelation traces are shown in Fig. 3. The fitted pulse duration was around 1.7 ps with an rms fluctuation of <0.5% (rms) for the compressed pulse energy of 1.1 mJ, as shown in Fig. 3(a). However, the autocorrelation traces for 4 mJ compressed pulse varied a lot during the measurement, as shown in Fig. 3(b). Sidebands appeared at some moment indicating side pulses[15] appeared in this case, therefore, the peak intensity of the main pulse decreased due to the transfer of energy from the main pulse to side pulses caused by the high Kerr-nonlinearity on long-term time scale,[15] which would cause temporal fluctuation in pulse duration.

Beam radii in both axes (R_x and R_y) of the focal spot in LBO were also measured for 1.1 and 4 mJ pulse. The beam area (A_{beam}) was calculated as: $A_{\text{beam}} = R_x R_y \pi$. To see the trend of the curve, the normalized reciprocals of the beam areas (1/beam area) for 1.5 h were shown in Fig. 4(a), together with the normalized SHG power measured at the same time. From Fig. 4(a), the fluctuation in the reciprocals of the beam area (spatial fluctuation) for 4 mJ pulse had a similar trend as the corresponding fluctuation in SHG power. A similar relation was observed for the 1.1-mJ pulse, although the fluctuations were much smaller. The spatial fluctuation in the case of high pulse energy was caused by the temporal fluctuation due to Kerr lens in CVBG compressor at high pulse energy. The 1/beam area shows similar trend of varying as the power fluctuation in SHG power. During the measurements, the energy was scaled by changing the repetition rate of the laser, and all other operating parameters, such as pump power, are kept the same. The output average power had been kept at around 20 W to keep the laser running at the same thermal condition. Figure 4 shows the evidence of long-term fluctuation due to the Kerr-nonlinearity, even though nonlinear Kerr effects are transient nonlinear phenomenon. The high peak intensity in CVBG leads to high Kerr-nonlinearity that further causes temporal and

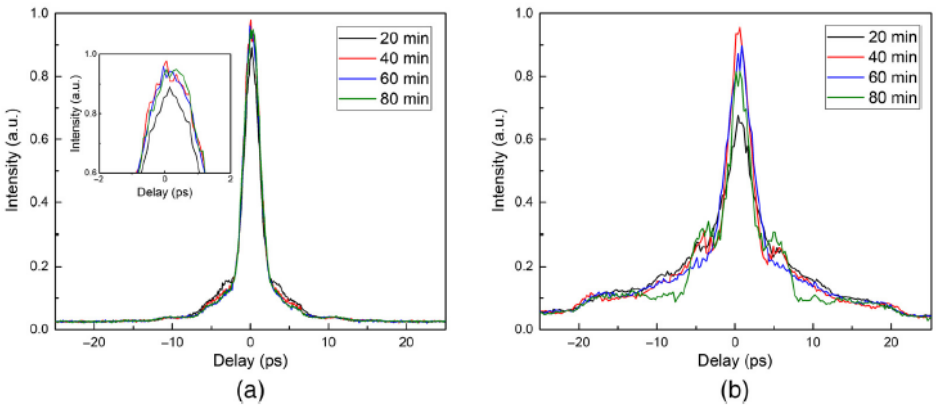

Fig. 3 The temporal fluctuations in the autocorrelation of the compressed pulse were also logged every 20 min during 1.5 h for pulse energy of (a) 1.1 mJ and (b) 4.4 mJ. The inset of (a) shows the detail of the peak of the autocorrelation traces.

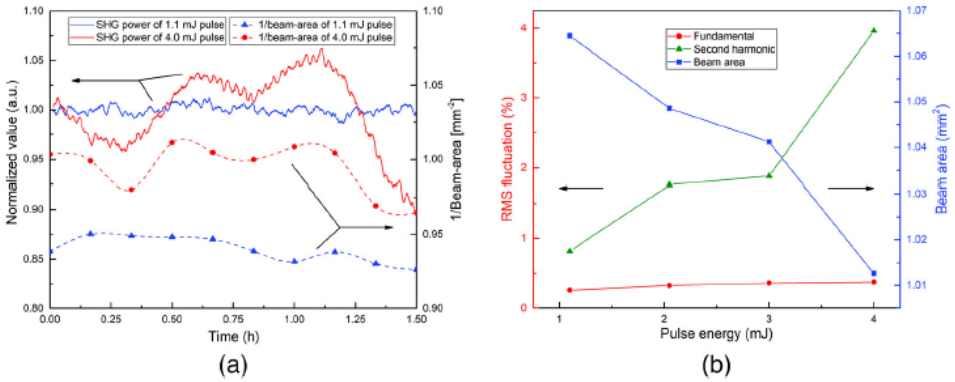

Fig. 4 (a) The normalized reciprocals of the beam areas (dash curves, spline fitting) and the normalized SHG power (solid curves) measured at the same time for 1 and 4 mJ pulse. (b) The fluctuations in the fundamental power and its SHG power, and the measured beam area as functions of the pulse energy.

spatial fluctuations. There is a long-term dynamic process between the Kerr-nonlinearity and the temporal/spatial fluctuations.

Figure 4(b) shows the fluctuations in the fundamental power and its SHG power and the average beam area as a function of the pulse energy. The fluctuations in SHG power increased by almost 4 times and the average beam area decreased by >5.4% when pulse energy increased from 1.1 to 4 mJ, although the fluctuations in fundamental power were almost at the same level.

In general, the fluctuation in peak intensity can be magnified by the CVBG at a high Kerr-nonlinearity. The experimental results show that the rms fluctuation of the SHG power caused by the spatial fluctuation and the temporal fluctuation would be lower than 2% if the B-integral accumulated in the CVBG is lower than π.

4 Conclusion

In this paper, we have experimentally investigated the fluctuation-magnification effect on the peak intensity of a laser pulse caused by the Kerr-nonlinearity in the CVBG compressor. Experiments show that small fluctuations in peak power of uncompressed pulses cause increasing in spatial fluctuation and temporal fluctuation due to the Kerr-nonlinearity in the CVBG when B-integral is larger than π. In order to avoid the fluctuation in peak intensity, it is necessary to decrease the B-integral by expanding the laser beam diameter for high-energy pulse to keep B-integral lower than π as suggested.

Acknowledgments

The authors thank their colleagues for discussion and for providing support during the experiments. This paper was financed by European Regional Development Fund (Award No. CZ.02.1.01/0.0/0.0/15_003/0000445), the State Budget of the Czech Republic (Award No. CZ.02.1.01/0.0/0.0/15_006/0000674), and European Union's Horizon 2020 Research and Innovation Program (Award No. 739573).

References

1. R. R. Gattass and E. Mazur, "Femtosecond laser micromachining in transparent materials," *Nat. Photonics* **2**, 219–225 (2008).
2. R. M. Carter et al., "Picosecond laser welding of similar and dissimilar materials," *Appl. Opt.* **53**, 4233–4238 (2014).
3. S. Petronic et al., "Picosecond laser shock peening of nimonic 263 at 1064 nm and 532 nm wavelength," *Metals* **6**(3), 1–14 (2016).

4. D. Strickland and G. Mourou, "Compression of amplified chirped optical pulses," *Opt. Commun.* **56**, 219–221 (1985).
5. S. Cho et al., "Numerical analysis of beam distortion induced by thermal effects in chirped volume Bragg grating compressors for high-power lasers," *J. Opt. Soc. Am. B* **37**, 3874–3881 (2020).
6. M. Smrž et al., "Amplification of picosecond pulses to 100 W by an Yb:YAG thin-disk with CVBG compressor," *Proc. SPIE* **9513**, 951304 (2015).
7. L. von Grafenstein et al., "Ho:YLF chirped pulse amplification at kilohertz repetition rates —43 ps pulses at 2 μm with GW peak power," *Opt. Lett.* **41**, 4668–4671 (2016).
8. D. Štěpánková et al., "Experimental study on compression of 216-W laser pulses below 2 ps at 1030 nm with chirped volume Bragg grating," *Appl. Opt.* **59**, 7938–7944 (2020).
9. K. H. Liao et al., "Large-aperture chirped volume Bragg grating based fiber CPA system," *Opt. Express* **15**(8), 4876–4882 (2007).
10. T. Bartulevicius et al., "Compact fiber CPA system based on a CFBG stretcher and CVBG compressor with matched dispersion profile," *Opt. Express* **25**(17), 19856–19862 (2017).
11. M. Loeser et al., "Compact millijoule Yb^{3+}:CaF_2 laser with 162 fs pulses," *Opt. Express* **29**(6), 9199–9206 (2021).
12. C. P. João et al., "Dispersion compensation by two-stage stretching in a sub-400 fs, 1.2 mJ Yb: CaF_2 amplifier," *Opt. Express* **22**(9), 10097–10104 (2014).
13. T. Schreiber et al., "Influence of pulse shape in self-phase-modulation-limited chirped pulse fiber amplifier systems," *J. Opt. Soc. Am. B* **24**, 1809–1814 (2007).
14. B. Yu et al., "Impact of nonlinear Kerr effect on the focusing performance of optical lens with high-intensity laser incidence," *Appl. Sci.* **10**, 1–17 (2020).
15. D. N. Schimpf et al., "The impact of spectral modulations on the contrast of pulses of nonlinear chirped-pulse amplification systems," *Opt. Express* **16**(14), 10664–10674 (2008).

Biographies of the authors are not available.

References

1. R. R. Gattass and E. Mazur, "Femtosecond laser micromachining in transparent materials," Nat. Photonics 2, 219-225 (2008).https://doi.org/10.1038/nphoton.2008.47
2. R. M. Carter, J. Chen, J. D. Shephard, R. R. Thomson, and D. P. Hand, "Picosecond laser welding of similar and dissimilar materials," Appl. Opt. 53, 4233 (2014). https://doi.org/10.1364/AO.53.004233
3. S. Petronic, T. Sibalija, M. Burzic, S. Polic, K. Colic, and D. Milovanovic, "Picosecond laser shock peening of nimonic 263 at 1064 nm and 532 nm wavelength," Metals (Basel). 6, 1–14 (2016). https://doi.org/10.3390/met6030041
4. D. Strickland and G. Mourou, "Compression of amplified chirped optical pulses," Opt. Commun. 56, 219–221 (1985). https://doi.org/10.1016/0030-4018(85)90120-8
5. S. Cho, O. Novák, M. Smrž, A. Lucianetti, T. J. Yu, and T. Mocek, "Numerical analysis of beam distortion induced by thermal effects in chirped volume Bragg grating compressors for high-power lasers," J. Opt. Soc. Am. B 37, 3874 (2020). https://doi.org/10.1364/JOSAB.409434
6. M. Smrž, M. Chyla, O. Novák, T. Miura, A. Endo, and T. Mocek, "Amplification of picosecond pulses to 100 W by an Yb:YAG thin-disk with CVBG compressor," High-Power, High-Energy, High-Intensity Laser Technol. II 9513, 951304 (2015). https://doi.org/10.1117/12.2178900
7. L. von Grafenstein, M. Bock, D. Ueberschaer, U. Griebner, and T. Elsaesser, "Ho:YLF chirped pulse amplification at kilohertz repetition rates – 43 ps pulses at 2 μm with GW peak power," Opt. Lett. 41, 4668 (2016). https://doi.org/10.1364/OL.41.004668
8. D. Štěpánková, J. Mužík, O. Novák, L. Roškot, V. Smirnov, L. Glebov, M. Jelínek, M. Smrž, A. Lucianetti, and T. Mocek, "Experimental study on compression of 216-W laser pulses below 2 ps at 1030 nm with chirped volume Bragg grating," Appl. Opt. 59, 7938 (2020). https://doi.org/10.1364/AO.400415

9. K.H. Liao, M.-Y. Cheng, E. Flecher, V. I. Smirnov, L. B. Glebov, and A. Galvanauskas. "Large-aperture chirped volume Bragg grating based fiber CPA system," Optics express 15, no. 8 (2007). https://doi.org/10.1364/OE.15.004876

10. T. Bartulevicius, S. Frankinas, A. Michailovas, R. Vasilyeu, V. Smirnov, F. Trepanier, and N. Rusteika. "Compact fiber CPA system based on a CFBG stretcher and CVBG compressor with matched dispersion profile," Optics express 25, no. 17 (2017). https://doi.org/10.1364/OE.25.019856

11. M.Loeser, C. Bernert, D. Albach, K. Zeil, U. Schramm, and M. Siebold. "Compact millijoule Yb 3+: CaF 2 laser with 162 fs pulses," Optics Express 29, no. 6 (2021). https://doi.org/10.1364/OE.418319

12. C.P. João, H. Pires, L. Cardoso, T. Imran, and G. Figueira. "Dispersion compensation by two-stage stretching in a sub-400 fs, 1.2 mJ Yb: CaF 2 amplifier," Optics express 22, no. 9 (2014). https://doi.org/10.1364/OE.22.010097

13. T. Schreiber, D. Schimpf, D. Müller, F. Röser, J. Limpert, and A. Tünnermann, "Influence of pulse shape in self-phase-modulation-limited chirped pulse fiber amplifier systems," J. Opt. Soc. Am. B 24, 1809 (2007). https://doi.org/10.1364/JOSAB.24.001809

14. B. Yu, Z. Lin, X. Chen, W. Qiu, and J. Pu, "Impact of nonlinear kerr effect on the focusing performance of optical lens with high-intensity laser incidence," Appl. Sci. 10, 1–17 (2020). https://doi.org/10.3390/app10061945

15. D. N. Schimpf, E. Seise, J. Limpert, and A. Tünnermann, "The impact of spectral modulations on the contrast of pulses of nonlinear chirped-pulse amplification systems," Opt. Express 16, 16664 (2008). https://doi.org/10.1364/OE.16.010664

Biographies for the authors are not available.

Publications of the author related to this work

Publications in peer-reviewed journals

[A1] **Huang Zhou**, Jan Pilar, Martin Smrz, Liyuan Chen, Miroslav Cech, and Tomas Mocek. "Adaptive optics system for short wavelength mid-IR laser based on a Shack–Hartmann wavefront sensor and analysis of thermal noise impacts," Applied Optics, Vol. 61, No. 26 (2022). DOI: 10.1364/AO.464676

[A2] **Huang Zhou**, Ondrej Novak, Martin Smrž, Liyuan Chen, Lukáš Roškot, Bianka Csanaková, Michal Chyla, Miroslav Čech, Tomáš Mocek. "Experimental study on the fluctuation-magnification effect of CVBG compressor in high energy ultrafast thin-disk CPA system," Optical Engineering, 61(10), 106103 (2022), DOI: 10.1117/1.OE.61.10.106103

[A3] Liyuan Chen, Jaroslav Huynh, **Huang Zhou**, Michal Chyla, Martin Smrž, and Tomáš Mocek. "Generating 84 fs, 4 nJ directly from an Yb-doped fiber oscillator by optimization of the net dispersion." Laser Physics 29, no. 6 (2019): 065105. DOI: 10.1088/1555-6611/ab0feb

Conference proceedings

[A4] **Huang Zhou**, Michal Chyla, Siva Sankar Nagisetty, Liyuan Chen, Akira Endo, Martin Smrz, and Tomas Mocek. "A practical model of thin disk regenerative amplifier based on analytical expression of ASE lifetime." In *Photonics, Devices, and Systems VII*, vol. 10603, pp. 6-11. SPIE, 2017. DOI: 10.1117/12.2292319

[A5] Denisa Štěpánková, **Huang Zhou**, Seryeyohan Cho, Jiří Mužík, Ondřej Novák, Martin Smrž, and Tomáš Mocek. "Influence of the CVBG compressor on output parameters of high-power and high-energy laser beam." In *Advanced Solid State Lasers, pp. JM3A-1*. Optical Society of America, 2021. DOI: 10.1364/ASSL.2021.JM3A.1

Conference without proceedings

[A6] **Huang Zhou**, Michal Chyla, Jakub Horacek, Pavel Crha, Jiri Muzik, Ondrej Novak, Martin Smrz, and Tomas Mocek. "100 W industrial thin disk regenerative amplifier," In *International Conference on Advanced Laser Technologies (ALT)* HiLASE-O-3, 2019. DOI: 10.24411/9999-011A-2019-00201

[A7] **Huang Zhou**, Michal Chyla, Pavel Crha, Jakub Horacek, Pavel Crha, Jiri Muzik,

Ondrej Novak, Martin Smrz, and Tomas Mocek. “100 W TRL-6 thin-disk laser for industrial applications,” In *Optics + Optoelectronics*, SPIE, 3-4 April 2019, Prague.

[A8] **Huang Zhou**, Jan Pilar, Martin Smrz, and Tomas Mocek. “ Adaptive optics system for mid-IR laser source,” In *The XXIII International Symposium on High-Power Laser Systems and Applications*, 13-16 June 2022, Prague.

Additional work by the author

Conference proceedings

[A9] Michal Chyla, Siva S. Nagisetty, Patricie Severova, **Huang Zhou**, Martin Smrz, Akira Endo, and Tomas Mocek. "Generation of 1-J bursts with picosecond pulses from Perla B thin-disk laser system." In *Solid State Lasers XXVII: Technology and Devices*, vol. 10511, pp. 90-98. SPIE, 2018. DOI: 10.1117/12.2291386

List of Figures

Fig. 2.1 Principles of shearing interferometry wavefront measurements ..... - 5 -
Fig. 2.2 Optical schematics of the Hartmann test and Shack-Hartmann sensor ..... - 6 -
Fig. 2.3 Optical schematic of a pyramid WFS ..... - 7 -
Fig. 2.4 Cross section of a bimorph deformable mirror. ..... - 8 -
Fig. 2.5 Electrostatic membrane mirror section view and the active membrane region. ..... - 9 -
Fig. 2.6 Principles of MEMS deformable mirrors ..... - 10 -
Fig. 2.7 Principle of Shack-Hartmann wavefront sensor ..... - 10 -
Fig. 2.8 Focal spot and its centroid on the sub-aperture on the camera sensor ..... - 11 -
Fig. 2.9 Definition of the dynamic range of the wavefront sensor. ..... - 11 -
Fig. 2.10 Eq. (2.9) expression using matrix notation ..... - 13 -
Fig. 2.11 Southwell geometry for wavefront reconstruction ..... - 14 -
Fig. 2.12 Polar coordinates and the relationship with Cartesian coordinates ..... - 15 -
Fig. 2.13 Surface plots of the Zernike polynomial sequence up to 6 orders ..... - 17 -
Fig. 2.14 Calibration procedure of the AO system ..... - 20 -
Fig. 2.15 (a) Open-loop control system, (b) Closed-loop control system. ..... - 23 -
Fig. 3.1 Principle of chirped pulse amplification (CPA) ..... - 26 -
Fig. 3.2 Principle of thin disk laser ..... - 27 -
Fig. 3.3 Thin disk regenerative amplifier with a linear cavity ..... - 28 -
Fig. 3.4 Principle of Amplified Spontaneous Emission (ASE) in thin disk medium ..... - 31 -
Fig. 3.5 The geometry for computing the ASE flux ..... - 31 -
Fig. 3.6 (a) Chirped volume Bragg grating. (b) uniform volume Bragg grating ..... - 33 -
Fig. 3.7 Refractive index change in a uniform and chirped fiber Bragg grating. ..... - 34 -
Fig. 3.8 Treacy-type compressor and Martinez-type stretcher ..... - 35 -
Fig. 3.9 Principle of Optical Parametric Amplification ..... - 36 -
Fig. 3.10 Phase-matching for a non-collinear and collinear OPA ..... - 37 -
Fig. 4.1 Tachyon 16K camera for detecting mid-IR wavelength (1 – 5 μm) ..... - 39 -
Fig. 4.2 The normalized spectral detectivity of VPD PbSe TACHYON 16K FPA. ..... - 40 -
Fig. 4.3 Internal transmission curves for common laser optics materials ..... - 41 -
Fig. 4.4 The home-made mid-IR Shack-Hartmann wavefront sensor. ..... - 42 -
Fig. 4.5 Flowchart of the wavefront measurement algorithm. ..... - 43 -
Fig. 4.6 Closed-loop control system for mid-IR AO system. ..... - 44 -
Fig. 4.7 The piezoelectric bimorph deformable mirror from Dynamic Optics ..... - 45 -

Fig. 4.8 Flowchart of the algorithm for measuring the Influence Functions Matrix. ..... - 47 -
Fig. 4.9 Flowchart of the algorithm for the closed-loop control. ..... - 48 -
Fig. 4.10 User interface for the wavefront measurement ..... - 49 -
Fig. 4.11 Tabs of the AO controlling part of the user interface ..... - 50 -
Fig. 5.1 Calibration setup ..... - 52 -
Fig. 5.2 Experiment setup of the spherical wavefront measurement ..... - 52 -
Fig. 5.3 The Hartmann-gram of the 1030 nm laser beam ..... - 53 -
Fig. 5.4 The snapshot of the PhotonLoop software ..... - 53 -
Fig. 5.5 The report of the measured wavefront ..... - 54 -
Fig. 5.6 Processed image with my wavefront reconstruction algorithm. ..... - 54 -
Fig. 5.7 The reproduced wavefront measured by Dynamic Optics WFS, and the reconstructed wavefront processed by my MATLAB code.. ..... - 55 -
Fig. 5.8 The difference of the reproduced and reconstructed wavefront ..... - 55 -
Fig. 5.9 Experiment setup for calibrating the home-mode wavefront sensor ..... - 56 -
Fig. 5.10 Relative positions of the camera sensor and the lenslet array ..... - 56 -
Fig. 5.11 (a) The Hartmann-gram caused by mismatching between the lenslet array and the sensor, (b) the wrongly reconstructed wavefront. ..... - 57 -
Fig. 5.12 (a) The Hartmann-gram with the precise matching between the lenslet array and the sensor. (b) The correctly reconstructed wavefront. ..... - 57 -
Fig. 5.13 Measuring the curvature of the wavefront ..... - 59 -
Fig. 5.14 The processed Hartmann-gram image captured during calibration. ..... - 59 -
Fig. 5.15 The measured data and its second-order polynomial fitting. ..... - 60 -
Fig. 5.16 Reconstructed wavefront and its Zernike Coefficients.. ..... - 60 -
Fig. 5.17 Background noise captured without incident laser beam before warming up.. - 61 -
Fig. 5.18 (a) The Hartmann-gram image was captured with an incident laser beam before the camera warmed up ..... - 62 -
Fig. 5.19 Background noise captured without incident laser beam after warming up. ... - 62 -
Fig. 5.20 The corresponding Hartman-gram image and the intensity profile ..... - 62 -
Fig. 5.21 The corresponding Hartman-gram image and the intensity profile ..... - 63 -
Fig. 5.22 The background image without incident laser input, after subtracting the background noise after warming up ..... - 63 -
Fig. 5.23 The corresponding Hartman-gram image and the intensity profile ..... - 63 -
Fig. 5.24 Thermal afterimage captured after 10 seconds laser exposure to the camera. . - 64 -
Fig. 5.25 Thermal afterimage captured after 10 seconds laser exposure to the camera, with background noise subtracted. ..... - 65 -
Fig. 5.26 The Hartmann-gram image and the distribution of the centroids ..... - 66 -
Fig. 5.27 Bar-plot of the Zernike coefficients of the x-tilt term in 120 seconds. ..... - 66 -
Fig. 5.28 The wavefront and the Zernike coefficients of the first and last captures. ..... - 66 -

Fig. 5.29 (a) The centroid distribution in 120 seconds in the sub-aperture. (b) Bar-plot of the Zernike coefficients of the x-tilt term in 120 seconds ..... - 67 -
Fig. 5.30 The wavefront and the Zernike coefficients of the first and last captures, with dynamically updating the thermal background..... - 67 -
Fig. 5.31 The Hartman-gram image and the intensity profile captured with dynamic updating of the thermal background..... - 68 -
Fig. 5.32 The experimental setup of the AO system for 1.94 μm laser ..... - 69 -
Fig. 5.33 Photo of the experimental setup..... - 69 -
Fig. 5.34 Influence Functions produced by the action of each actuator over the DM..... - 70 -
Fig. 5.36 Reproduction of the first 9 Zernike mode shapes 72
Fig. 5.37 The initial wavefront and its Zernike coefficients of the 1.94 μm laser beam. - 73 -
Fig. 5.38 The residual wavefront RMS was logged as a function of the iteration number of the AO system, without dynamic updating of the background, for 35 Zernike terms.... - 74 -
Fig. 5.39 Residual wavefront RMS and its Zernike coefficients after running 650 iterations without dynamic updating of the background ..... - 75 -
Fig. 5.40 Residual wavefront RMS was logged as a function of the iteration number of the closed-loop control system, with dynamic updating of the background with the time interval of 2 seconds for 35 Zernike terms ..... - 75 -
Fig. 5.41 Residual wavefront RMS and its Zernike coefficients after running 500 iterations, with dynamic updating of the background with the time interval of 2 seconds for 35 Zernike terms ..... - 76 -
Fig. 5.42 Residual wavefront RMS was logged as a function of the iteration number of the closed-loop control system, with dynamic updating of the background with the time interval of 5 seconds for 35 Zernike terms ..... - 77 -
Fig. 5.43 Residual wavefront RMS and its Zernike coefficients after running 400 iterations, with dynamic updating of the background with the time interval of 5 seconds for 35 Zernike terms ..... - 77 -
Fig. 5.44 Residual wavefront RMS was logged as a function of the iteration number of the closed-loop control system, with dynamic updating of the background with the time interval of 2 seconds for the first 15 Zernike terms..... - 78 -
Fig. 5.45 Residual wavefront RMS and its Zernike coefficients, with dynamic updating of the background with the time interval of 2 seconds for the first 15 Zernike terms..... - 79 -
Fig. 5.46 Residual wavefront RMS was logged with dynamic updating of the background with the time interval of 2 seconds, for the first 10 Zernike terms..... - 79 -
Fig. 5.47 Residual wavefront RMS and its Zernike coefficients, with dynamic updating of the background with the time interval of 2 seconds for the first 15 Zernike terms..... - 80 -
Fig. 6.1 Simplified layout of the thin disk regenerative amplifier used in the model. .... - 82 -
Fig. 6.2 The schematic block diagram of the simulation..... - 83 -

Fig. 6.3 Simulated pulse building up in the regenerative amplifier..... - 84 -
Fig. 6.4 (a) The experimental data and the simulated data with different loss factors, (b) the loss factor increased nonlinearly with pump intensity..... - 85 -
Fig. 6.5 The schematic overview of the first design of the BIATRI laser system, with a regenerative amplifier and CVBG pulse compressor..... - 86 -
Fig. 6.6 The schematic overview of the upgraded design of the BIATRI laser system... - 87 -
Fig. 6.7 The schematic overview of the first design of the front end..... - 88 -
Fig. 6.8 Performance of YLMO oscillator from Menlo Systems company..... - 89 -
Fig. 6.9 First design of the front end..... - 89 -
Fig. 6.10 Long-term stability of the front-end for 6 hours..... - 90 -
Fig. 6.11 Yb:YAG thin disk used in the regenerative amplifier..... - 91 -
Fig. 6.12 DILAS IS45.4MP pump diode laser..... - 91 -
Fig. 6.13 The eigenmode's beam radius vs. the laser cavity length..... - 93 -
Fig. 6.14 The eigenmode beam radius on the thin disk..... - 94 -
Fig. 6.15 The stability map of the laser cavity..... - 94 -
Fig. 6.16 The constructed laser cavity for testing..... - 95 -
Fig. 6.17 Average power and optical efficiency for CW operation mode..... - 95 -
Fig. 6.18 B-integral accumulated in BBO crystal. ..... - 97 -
Fig. 6.19 The water-cooled Pockels cell developed at HiLASE Center..... - 98 -
Fig. 6.20 Modified experimental setup for testing the Pockels cell..... - 98 -
Fig. 6.21 Pulse trains influenced by the serious piezoelectric ringing effect..... - 99 -
Fig. 6.22 Performance of the regenerative amplifier at a repetition rate of 10.12 kHz . - 100 -
Fig. 6.23 The output pulse and pulse building-up of the regenerative amplifier..... - 100 -
Fig. 6.24 Beam quality of the uncompressed laser pulse at full power output..... - 101 -
Fig. 6.25 Spectrum of the fiber front-end and the regenerative amplifier..... - 102 -
Fig. 6.26 Bifurcation occurred after running the laser for a few weeks..... - 102 -
Fig. 6.27 Beam pointing stability of the laser output beam..... - 102 -
Fig. 6.28 Beam pointing stabilization system..... - 103 -
Fig. 6.29 Water-cooled aluminum housing for CVBG compressor..... - 104 -
Fig. 6.30 The autocorrelation trace of pulse compressed in CVBG compressor..... - 105 -
Fig. 6.31 The scheme of the experimental setup..... - 106 -
Fig. 6.32 Normalized long-term instability of fundamental and SHG of the Menlo YLMO fiber oscillator over 2 hours after warming up..... - 106 -
Fig. 6.33 Double pulses were observed from YLMO oscillator..... - 107 -
Fig. 6.34 Normalized fluctuations in fundamental power and its SHG power of laser pulse compressed by the CVBG compressor over 1.5 hours after warming up..... - 108 -
Fig. 6.35 The spectrums of the laser output for 1 mJ and 4 mJ pulses..... - 108 -
Fig. 6.36 The temporal fluctuations in the autocorrelation of the compressed pulse were

logged every 20 mins during 1.5 hours for 1.1 mJ and 4.4 mJ pulses..... - 109 -
Fig. 6.37 The normalized reciprocals of the beam areas and the SHG power measured for 1mJ and 4mJ pulses..... - 109 -
Fig. 6.38 Normalized long-term instability of fundamental and SHG of Onefive Origami-10 oscillator over almost 2 hours after warming up. ..... - 110 -
Fig. 6.39 Normalized fluctuations in fundamental power and SHG power of laser pulse compressed by the CVBG compressor over 1.5 hours after warming up, with Origami-10 oscillator as a seeder..... - 111 -
Fig. 6.40 The temporal fluctuations in the autocorrelation of the compressed pulse were logged every 20 mins in 1.5 hours, with the Origami-10 oscillator ..... - 111 -
Fig. 6.41 Grating compressors and mounts, designed by Dr. Kohei Hoshimoto. ..... - 113 -
Fig. 6.42 The schematic overview of the upgraded all-PM-fiber-based front end..... - 114 -
Fig. 6.43 ANDi Oscillator and fiber preamplifier developed by Dr. Liyuan Chen. ..... - 114 -
Fig. 6.44 The upgraded main amplifier. ..... - 114 -
Fig. 6.45 The waveform of the output pulse..... - 115 -
Fig. 6.46 Normalized fluctuations in fundamental power and SHG power of laser pulse compressed by the CVBG compressor over 1.5 hours with a new oscillator..... - 116 -
Fig. 6.47 Autocorrelation trace of the pulse compressed by the grating compressor.... - 116 -
Fig. 6.48 M^2 measurement..... - 117 -
Fig. 7.1 Optical scheme of the mid-IR OPA system..... - 118 -
Fig. 7.2 Hartmann-gram and wavefront of the output of Stage I of the OPA system…..- 119-
Fig. 7.3 Proposed solutions for wavefront correction for the OPA system ..... - 120 -

List of Tables

Table 4.1 Main parameters of TACHYON 16K camera ..... - 40 -
Table 4.2 Main parameters of lenslet array from Edmund ..... - 41 -
Table 4.3 Main parameters of the deformable mirror from Dynamic Optics. ..... - 44 -
Table 6.1 Parameters used in the model ..... - 83 -
Table 6.2 Parameters used in the calculation of B-integral accumulated in BBO crystal ... - 96 -
Table 6.3 Specification of the Chirped Volume Bragg Grating compressor..... - 104 -
Table 6.4 Specification of Origami-10 oscillator from Onefive GmbH ..... - 110 -
Table 6.5 Parameters of the transmission grating pair..... - 112 -

Bibliography

[1] Francisco Silva, Stephan M. Teichmann, Seth L. Cousin, Michael Hemmer, and Jens Biegert. "Spatiotemporal isolation of attosecond soft X-ray pulses in the water window." *Nature communications* 6, no. 1 (2015): 1-6.

[2] Stavros Gravas, Alexander Bachmann, Oliver Reich, Claus G. Roehrborn, Peter J. Gilling, and Jean De La Rosette. "Critical review of lasers in benign prostatic hyperplasia (BPH)." BJU international 107, no. 7 (2011): 1030-1043.

[3] Tsuneto Kanai, Pavel Malevich, Sarayoo Sasidharan Kangaparambil, Kakuta Ishida, Makoto Mizui, Kaoru Yamanouchi, Heinar Hoogland, Ronald Holzwarth, Audrius Pugzlys, and Andrius Baltuska. "Parametric amplification of 100 fs mid-infrared pulses in ZnGeP 2 driven by a Ho: YAG chirped-pulse amplifier." *Optics letters* 42, no. 4 (2017): 683-686.

[4] Theresa Buberl. "Towards next-generation molecular fingerprinting." PhD diss., lmu, 2021.

[5] P. P. Sorokin, and M. J. Stevenson. "Stimulated infrared emission from trivalent uranium." *Physical Review Letters* 5, no. 12 (1960): 557.

[6] Stuart D. Jackson "Towards high-power mid-infrared emission from a fibre laser." *Nature photonics* 6, no. 7 (2012): 423-431.

[7] Vincent Fortin, Martin Bernier, Souleymane T. Bah, and Réal Vallée. "30 W fluoride glass all-fiber laser at 2.94 μm." *Optics Letters* 40, no. 12 (2015): 2882-2885.

[8] M. Yu Koptev, E. A. Anashkina, A. V. Andrianov, V. V. Dorofeev, A. F. Kosolapov, S. V. Muravyev, and A. V. Kim. "Widely tunable mid-infrared fiber laser source based on soliton self-frequency shift in microstructured tellurite fiber." *Optics letters* 40, no. 17 (2015): 4094-4097.

[9] Jas S. Sanghera, L. Brandon Shaw, and Ishwar D. Aggarwal. "Chalcogenide glass-fiber-based mid-IR sources and applications." *IEEE Journal of selected topics in quantum electronics* 15, no. 1 (2009): 114-119.

[10] Shigeki Tokita, Mayu Hirokane, Masanao Murakami, Seiji Shimizu, Masaki Hashida, and Shuji Sakabe. "Stable 10 W Er: ZBLAN fiber laser operating at 2.71–2.88 μm." *Optics letters* 35, no. 23 (2010): 3943-3945.

[11] Majid Ebrahim-Zadeh, and Irina T. Sorokina, eds. *Mid-infrared coherent sources and applications*. Springer Science & Business Media, 2007.

[12] Irina T. Sorokina, and Konstantin L. Vodopyanov, eds. *Solid-state mid-infrared laser sources*. Vol. 89. Springer Science & Business Media, 2003.

[13] Hari P. Nair, Rodolfo Salas, Nathaniel T. Sheehan, Scott J. Maddox, and Seth R. Bank. "3.4 μm diode lasers employing Al-free GaInAsSb/GaSb MQW active regions at 20° C." In *71st Device Research Conference*, pp. 187-188. IEEE, 2013.

[14] W. Z. Shen, K. Wang, L. F. Jiang, X. G. Wang, S. C. Shen, H. Z. Wu, and P. J. McCann. "Study of band structure in PbSe/PbSrSe quantum wells for midinfrared laser applications." *Applied Physics Letters* 79, no. 16 (2001): 2579-2581.

[15] Allan Wirth. "Ophthalmic instrument having Hartmann wavefront sensor with extended source." U.S. Patent 6,595,642, issued July 22, 2003.

[16] Martin J Booth. "Adaptive optics in microscopy." *Philosophical Transactions of the Royal Society A: Mathematical, Physical and Engineering Sciences* 365, no. 1861 (2007): 2829-2843.

[17] Robert K Tyson. "Bit-error rate for free-space adaptive optics laser communications." *JOSA A* 19, no. 4 (2002): 753-758.

[18] Clélia Robert , Vincent Michau, Bruno Fleury, Serge Magli, and Laurent Vial. "Mid-infrared Shack-Hartmann wavefront sensor fully cryogenic using extended source for endoatmospheric applications." *Optics express* 20, no. 14 (2012): 15636-15653.

[19] Horace W. Babcock. "The possibility of compensating astronomical seeing." *Publications of the Astronomical Society of the Pacific* 65, no. 386 (1953): 229-236.

[20] Laird M. Close, Beth Biller, William F. Hoffmann, Phil M. Hinz, John H. Bieging, Francois Wildi, Michael Lloyd-Hart et al. "Mid-infrared imaging of the post-asymptotic giant branch star AC Herculis with the Multiple Mirror Telescope adaptive optics system." The Astrophysical Journal 598, no. 1 (2003): L35.

[21] William F. Hoffmann, Joseph L. Hora, Giovanni G. Fazio, Lynne K. Deutsch, and Aditya Dayal. "MIRAC2: a mid-infrared array camera for astronomy." In *Infrared Astronomical Instrumentation*, vol. 3354, pp. 647-658. SPIE, 1998.

[22] Andrew J. Skemer, Philip M. Hinz, William F. Hoffmann, Laird M. Close, Sarah Kendrew, Richard J. Mathar, Remko Stuik, Thomas P. Greene, Charles E. Woodward, and Michael S. Kelley. "A Direct Measurement of Atmospheric Dispersion in N-band Spectra: Implications for Mid-IR Systems on ELTs1." *Publications of the Astronomical Society of the Pacific* 121, no. 882 (2009): 897.

[23] Mark R. Chun, Jay Elias, Brent Ellerbroek, Tim Bond, Ming Liang, Richard Clare, Alan Tokunaga, Matt Richter, and Larry Daggert. "MIRAO: a mid-IR adaptive optics system design for TMT." In *Advances in Adaptive Optics II*, vol. 6272, pp. 252-261. SPIE, 2006.

[24] Stefan Hippler, Markus Feldt, Thomas Bertram, Wolfgang Brandner, Faustine Cantalloube, Brunella Carlomagno, Olivier Absil, Andreas Obereder, Iuliia Shatokhina, and Remko Stuik. "Single conjugate adaptive optics for the ELT instrument METIS." *Experimental Astronomy* 47, no. 1 (2019): 65-105.

[25] Bernhard R. Brandl, Tibor Agócs, Gabby Aitink-Kroes, Thomas Bertram, Felix Bettonvil, Roy Van Boekel, Olivier Boulade et al. "Status of the mid-infrared E-ELT imager and spectrograph METIS." In *Ground-based and Airborne Instrumentation for Astronomy VI*, vol. 9908, p. 990820. International Society for Optics and Photonics, 2016.

[26] Byron M. Welsh, Brent L. Ellerbroek, Michael C. Roggemann, and Timothy L. Pennington. "Fundamental performance comparison of a Hartmann and a shearing interferometer wave-front sensor." *Applied optics* 34, no. 21 (1995): 4186-4195.

[27] J. L. Gardner. "Wave-front curvature in a Fizeau wavemeter." *Optics Letters* 8, no. 2 (1983): 91-93.

[28] Daniel Malacara, ed. *Optical shop testing*. Vol. 59. John Wiley & Sons, 2007.

[29] M. E. Riley, and M. A. Gusinow. "Laser beam divergence utilizing a lateral shearing interferometer." *Applied Optics* 16, no. 10 (1977): 2753-2756.

[30] Shunsuke Yokozeki, and Kazuo Ohnishi. "Spherical aberration measurement with shearing interferometer using Fourier imaging and moiré method." *Applied optics* 14, no. 3 (1975): 623-627.

[31]P. Hariharan, and D. Sen. "Radial shearing interferometer." *Journal of Scientific Instruments* 38, no. 11 (1961): 428.

[32] M. V. R. K. Murty. "A compact radial shearing interferometer based on the law of refraction." *Applied Optics* 3, no. 7 (1964): 853-857.

[33] J. Primot, and L. Sogno. "Achromatic three-wave (or more) lateral shearing interferometer." *JOSA A* 12, no. 12 (1995): 2679-2685.

[34] J-C. Chanteloup. "Multiple-wave lateral shearing interferometry for wave-front sensing." *Applied optics* 44, no. 9 (2005): 1559-1571.

[35] Sabrina Velghe , Jérôme Primot, Nicolas Guérineau, Mathieu Cohen, and Benoit Wattellier. "Wave-front reconstruction from multidirectional phase derivatives generated by multilateral shearing interferometers." *Optics letters* 30, no. 3 (2005): 245-247.

[36] B. Wattellier, M. Cohen, P. D'Oliveira, G. Doumy, P. Monot, and F. Reau. "New precompensation scheme for best focusing of a 30-fs femtosecond 10-TW laser beam using a four-wave lateral shearing interferometer." In *CLEO/Europe. 2005 Conference on Lasers and Electro-Optics Europe, 2005.*, p. 172. IEEE, 2005.

[37] Jan Pilar, Ondrej Slezak, Pawel Sikocinski, Martin Divoky, Magdalena Sawicka, Stefano Bonora, Antonio Lucianetti, Tomas Mocek, and Helena Jelinkova. "Design and optimization of an adaptive optics system for a high-average-power multi-slab laser (HiLASE)." *Applied Optics* 53, no. 15 (2014): 3255-3261.

[38] Benjamin C.Platt, and Roland Shack. "History and principles of Shack-Hartmann wavefront sensing." *Journal of refractive surgery* 17, no. 5 (2001): S573-S577.

[39] Benjamin C. Platt. *Instruments for Measuring Properties of Infrared Transmitting Optical Materials*. The University of Arizona, 1976.

[40] Mingliang Xia, Chao Li, Lifa Hu, Zhaoliang Cao, Quanquan Mu, and Xuan Li. "Shack-Hartmann wavefront sensor with large dynamic range." Journal of Biomedical Optics 15, no. 2 (2010): 026009.

[41] Huy Tuong Cao, Sebastian WS Ng, Minkyun Noh, Aidan Brooks, Fabrice Matichard, and Peter J. Veitch. "Enhancing the dynamic range of deformable mirrors with compression bias." Optics Express 28, no. 26 (2020): 38480-38490.

[42] Hyuck Choo, and Richard S. Muller. "Addressable microlens array to improve dynamic range of Shack–Hartmann sensors." Journal of microelectromechanical systems 15, no. 6 (2006): 1555-1567.

[43] Vyas Akondi, and Alfredo Dubra. "Shack-Hartmann wavefront sensor optical dynamic range." *Optics Express* 29, no. 6 (2021): 8417-8429.

[44] Thomas Godin, Michael Fromager, Emmanuel Cagniot, Marc Brunel, and Kamel Aït-Ameur. "Reconstruction-free wavefront measurements with enhanced sensitivity." In Optical Micro-and Nanometrology V, vol. 9132, pp. 128-135. SPIE, 2014.

[45] Alice M. Nightingale, and Stanislav V. Gordeyev. "Shack-Hartmann wavefront sensor image analysis: a comparison of centroiding methods and image-processing techniques." Optical Engineering 52, no. 7 (2013): 071413.

[46] M. Nicolle, T. Fusco, G. Rousset, and V. Michau. "Improvement of Shack–Hartmann wave-front sensor measurement for extreme adaptive optics." Optics letters 29, no. 23 (2004): 2743-2745.

[47] S. Thomas, T. Fusco, A. Tokovinin, M. Nicolle, V. Michau, and G. Rousset. "Comparison of centroid computation algorithms in a Shack–Hartmann sensor." Monthly Notices of the Royal Astronomical Society 371, no. 1 (2006): 323-336.

[48] Khalid M. Hosny. "Fast computation of accurate Zernike moments." Journal of Real-Time Image Processing 3, no. 1 (2008): 97-107.

[49] Carlos M. Correia. "Advanced control laws for the new generation of AO systems." In Adaptive Optics Systems VI, vol. 10703, pp. 527-537. SPIE, 2018.

[50] Roberto Ragazzoni. "Pupil plane wavefront sensing with an oscillating prism." *Journal of modern optics* 43, no. 2 (1996): 289-293.

[51] Iuliia Shatokhina, Victoria Hutterer, and Ronny Ramlau. "Review on methods for wavefront reconstruction from pyramid wavefront sensor data." *Journal of Astronomical Telescopes, Instruments, and Systems* 6, no. 1 (2020): 010901.

[52] Charlotte Z. Bond, Sylvain Cetre, Scott Lilley, Peter Wizinowich, Dimitri Mawet, Mark Chun, Edward Wetherell et al. "Adaptive optics with an infrared pyramid wavefront sensor at Keck." *Journal of Astronomical Telescopes, Instruments, and Systems* 6, no. 3 (2020): 039003.

[53] Adriano Ghedina, Massimo Cecconi, Roberto Ragazzoni, Jacopo Farinato, Andrea Baruffolo, Giuseppe Crimi, Emiliano Diolaiti et al. "On-sky test of the pyramid wavefront sensor." In *Adaptive Optical System Technologies II*, vol. 4839, pp. 869-877. International Society for Optics and Photonics, 2003.

[54] Roberto Ragazzoni, Emiliano Diolaiti, and Elise Vernet. "A pyramid wavefront sensor with no dynamic modulation." *Optics communications* 208, no. 1-3 (2002): 51-60.

[55] D. Peter, M. Feldt, Th Henning, S. Hippler, J. Aceituno, L. Montoya, J. Costa, and B. Dorner. "PYRAMIR: exploring the on-sky performance of the world's first near-infrared pyramid wavefront sensor." *Publications of the Astronomical Society of the Pacific* 122, no. 887 (2009): 63.

[56] Fernando Quirós-Pacheco, Guido Agapito, Armando Riccardi, Simone Esposito, Miska Le Louarn, and Enrico Marchetti. "Performance simulation of the ERIS pyramid wavefront sensor module in the VLT adaptive optics facility." In *Adaptive Optics Systems III*, vol. 8447, pp. 1830-1841. SPIE, 2012.

[57] Aurea Garcia-Rissmann, and Miska Le Louarn. "Performance evaluation of a SCAO system for a 42-m telescope using the pyramid wavefront sensor." In *Adaptive Optics Systems II*, vol. 7736, p. 773648. International Society for Optics and Photonics, 2010.

[58] Lior Shkedy, Tuvy Markovitz, Zipora Calahorra, Itay Hirsh, and Itay Shtrichman. "Megapixel digital InSb detector for midwave infrared imaging." *Optical Engineering* 50, no. 6 (2011): 061008.

[59] Clélia Robert , Vincent Michau, Bruno Fleury, Serge Magli, and Laurent Vial. "Mid-infrared Shack-Hartmann wavefront sensor fully cryogenic using extended source for endoatmospheric applications." *Optics express* 20, no. 14 (2012): 15636-15653.

[60] Eric Costard, P. Bois, Alfredo De Rossi, A. Nedelcu, Olivier Cocle, François-Hugues Gauthier, and Francis Audier. "QWIP detectors and thermal imagers." *Comptes Rendus Physique* 4, no. 10 (2003): 1089-1102.

[61] D. L. Smith, and C. Mailhiot. "Proposal for strained type II superlattice infrared detectors." *Journal of Applied Physics* 62, no. 6 (1987): 2545-2548.

[62] S. Abdollahi Pour , EK-W. Huang, G. Chen, Abbas Haddadi, B-M. Nguyen, and Manijeh Razeghi. "High operating temperature midwave infrared photodiodes and focal plane arrays based on type-II InAs/GaSb superlattices." *Applied Physics Letters* 98, no. 14 (2011): 143501.

[63] Elijah L. Maweza, L. Gailele, Hencharl J. Strauss, Ihar Litvin, Andrew Forbes, and A. Dudley. "Shaping and detecting mid-IR light with a Spatial Light Modulator." In *Advanced Solid State Lasers*, pp. JTh2A-15. Optical Society of America, 2016.

[64] Sabrina Velghe, Djamel Brahmi, William Boucher, Benoit Wattellier, Nicolas Guérineau, Riad Haïdar, and Jérôme Primot. "MWIR and LWIR wavefront sensing with quadri-wave lateral shearing interferometry." In *Infrared Imaging Systems: Design, Analysis, Modeling, and Testing XX*, vol. 7300, p. 73000T. International Society for Optics and Photonics, 2009.

[65] Bruno Fieque, Arnaud Crastes, Olivier Legras, and Jean-Luc Tissot. "MWIR uncooled microbolometer: a way to increase the number of applications." In *Infrared Technology and Applications XXXI*, vol. 5783, pp. 531-538. SPIE, 2005.

[66] Brian D. Oelrich, Arnaud Crastes, Craig I. Underwood, and Stephen Mackin. "Low-cost mid-wave IR microsatellite imager concept based on uncooled technology." In *Sensors, Systems, and Next-Generation Satellites VIII*, vol. 5570, pp. 209-217. International Society for Optics and Photonics, 2004.

[67] S. Bonora, U. Bortolozzo, S. Residori, R. Balu, and P. V. Ashrit. "Mid-IR to near-IR image conversion by thermally induced optical switching in vanadium dioxide." *Optics letters* 35, no. 2 (2010): 103-105.

[68] S. Bonora, G. Beydaghyan, A. Haché, and P. V. Ashrit. "Mid-IR laser beam quality measurement through vanadium dioxide optical switching." *Optics Letters* 38, no. 9 (2013): 1554-1556.

[69] Christina CC Willis, Joshua D. Bradford, Lawrence Shah, and Martin C. Richardson. "Measurement of wavefront distortions resulting from incidence of high-power 2 μm laser light." In *CLEO: 2011-Laser Science to Photonic Applications*, pp. 1-2. IEEE, 2011.

[70] Renaud Bastaits, David Alaluf, Mihaita Horodinca, Iulian Romanescu, Ioan Burda, Grégory Martic, Gonçalo Rodrigues, and André Preumont. "Segmented bimorph mirrors for adaptive optics: segment design and experiment." *Applied optics* 53, no. 29 (2014): 6635-6642.

[71] Stefano Bonora , and Luca Poletto. "Push-pull membrane mirrors for adaptive optics." *Optics express* 14, no. 25 (2006): 11935-11944.

[72] Thomas G. Bifano, Julie Perreault, R. Krishnamoorthy Mali, and Mark N. Horenstein. "Microelectromechanical deformable mirrors." *IEEE Journal of selected topics in quantum electronics* 5, no. 1 (1999): 83-89.

[73] Gordon D. Love, Janet S. Fender, and Sergio R. Restaino. "Adaptive wavefront shaping with liquid crystals." Optics and Photonics news 6, no. 10 (1995): 16-21.

[74] A. V. Kudryashov, J. Gonglewski, S. Browne, and R. Highland, “Liquid crystal phase modulator for adaptive optics. Temporal performance characterization,” Opt. Comm. **141**, 247–252 (1997).

[75] Yu Ning, Wenhan Jiang, Ning Ling, and Changhui Rao. "Response function calculation and sensitivity comparison analysis of various bimorph deformable mirrors." *Optics Express* 15, no. 19 (2007): 12030-12038.

[76] David A. Horsley, Hyunkyu Park, Sophie P. Laut, and John S. Werner. "Characterization of a bimorph deformable mirror using stroboscopic phase-shifting interferometry." *Sensors and Actuators A: Physical* 134, no. 1 (2007): 221-230.

[77] Jianqiang Ma, Lei Tian, Yan Li, Zongfeng Yang, Yuguo Cui, and Jiaru Chu. "Hysteresis compensation of piezoelectric deformable mirror based on Prandtl–Ishlinskii model." *Optics Communications* 416 (2018): 94-99.

[78] Gilles Cheriaux, Jean-Philippe Rousseau, Frédéric Burgy, Jean-Christophe Sinquin, Jean-Marie Lurçon, and Claude Guillemard. "Monomorph large aperture adaptive optics for high peak-power femtosecond lasers." In *Adaptive Optics for Laser Systems and Other Applications*, vol. 6584, p. 658405. International Society for Optics and Photonics, 2007.

[79] S. Bonora, I. Capraro, L. Poletto, M. Romanin, C. Trestino, and P. Villoresi. "Fast wavefront active control by a simple DSP-Driven deformable mirror." Review of Scientific Instruments 77, no. 9 (2006): 0034-6748.

[80] S. Bonora, U. Bortolozzo, G. Naletto, and S. Residori. "Innovative membrane deformable mirrors." *Topics in*

Adaptive Optics (2012).

[81] Boston Micromachines Corporation. https://bostonmicromachines.com/

[82] Thomas Bifano. "MEMS deformable mirrors." *Nature photonics* 5, no. 1 (2011): 21-23.

[83] Conrad William Merkle, Shau Poh Chong, Aaron Michael Kho, Jun Zhu, Alfredo Dubra, and Vivek Jay Srinivasan. "Visible light optical coherence microscopy of the brain with isotropic femtoliter resolution in vivo." Optics letters 43(2), 198-201 (2018).

[84] Vyas Akondi, and Alfredo Dubra. "Shack-Hartmann wavefront sensor optical dynamic range." *Optics Express* 29, no. 6 (2021): 8417-8429.

[85] Hironobu Shinto, Yusuke Saita, and Takanori Nomura. "Shack–Hartmann wavefront sensor with large dynamic range by adaptive spot search method." *Applied Optics* 55, no. 20 (2016): 5413-5418.

[86] E. Kewei, Chen Zhang, Mengyang Li, Zhao Xiong, and Dahai Li. "Wavefront reconstruction algorithm based on Legendre polynomials for radial shearing interferometry over a square area and error analysis." *Optics Express* 23, no. 16 (2015): 20267-20279.

[87] J. Pilar *et al.*, "Design and optimization of an adaptive optics system for a high-average-power multi-slab laser (HiLASE)," *Applied Optics,* vol. 53, no. 15, pp. 3255-3261, MAY 20 2014 2014.

[88] David L. Fried. "Least-square fitting a wave-front distortion estimate to an array of phase-difference measurements." *JOSA* 67, no. 3 (1977): 370-375.

[89] William H Southwell. "Wave-front estimation from wave-front slope measurements." *JOSA* 70, no. 8 (1980): 998-1006.

[90] Weiyao Zou, and Jannick P. Rolland. "Quantifications of error propagation in slope-based wavefront estimations." *JOSA A* 23, no. 10 (2006): 2629-2638.

[91] Guang-ming Dai. "Modal wave-front reconstruction with Zernike polynomials and Karhunen–Loève functions." *JOSA A* 13, no. 6 (1996): 1218-1225.

[92] Virendra N. Mahajan. "Zernike circle polynomials and optical aberrations of systems with circular pupils." *Applied optics* 33, no. 34 (1994): 8121-8124.

[93] Vasudevan Lakshminarayanan, and Andre Fleck. "Zernike polynomials: a guide." *Journal of Modern Optics* 58, no. 7 (2011): 545-561.

[94] Frits Zernike. "Diffraction theory of the knife-edge test and its improved form, the phase-contrast method." *Monthly Notices of the Royal Astronomical Society* 94 (1934): 377-384.

[95] V. N. Mahajan. Orthonormal Polynomials in Wavefront Analysis. In Handbook of Optics, 3rd ed.; McGraw-Hill: New York, 2010; Vol 2, Part 3, Chapter 11.

[96] Robert J. Noll. "Zernike polynomials and atmospheric turbulence." *JOsA* 66, no. 3 (1976): 207-211.

[97] M. Born and E. Wolf, Principles of Optics (Cambridge University Press, 1999), 7th ed.

[98] V. N. Mahajan, "Zernike polynomials and aberration balancing," Proc. SPIE 5173, 1–17 (2003).

[99] S. Thomas, T. Fusco, A. Tokovinin, M. Nicolle, V. Michau, and G. Rousset. "Comparison of centroid computation algorithms in a Shack–Hartmann sensor." *Monthly Notices of the Royal Astronomical Society* 371, no. 1 (2006): 323-336.

[100] Akondi Vyas, M. B. Roopashree, and B. R. Prasad. "Optimization of existing centroiding algorithms for Shack Hartmann sensor." *arXiv preprint arXiv:0908.4328* (2009).

[101] Olivier Lardière, Rodolphe Conan, Richard Clare, Colin Bradley, and Norbert Hubin. "Performance comparison of centroiding algorithms for laser guide star wavefront sensing with extremely large telescopes." *Applied Optics* 49, no. 31 (2010): G78-G94.

[102] K. L. Baker, and M. M. Moallem. "Iteratively weighted centroiding for Shack-Hartmann wave-front sensors." *Optics express* 15, no. 8 (2007): 5147-5159.

[103] M. Nicolle, T. Fusco, G. Rousset, and V. Michau. "Improvement of Shack–Hartmann wave-front sensor measurement for extreme adaptive optics." *Optics letters* 29, no. 23 (2004): 2743-2745.

[104] T. Fusco, M. Nicolle, G. Rousset, V. Michau, J.-L. Beuzit, and D. Mouillet, "Optimisation of a Shack-Hartmann-based wave-front sensor for XAO system," SPIE 5490, 1155 (2004).

[105] Martin Booth, Tony Wilson, Hong-Bo Sun, Taisuke Ota, and Satoshi Kawata. "Methods for the

characterization of deformable membrane mirrors." *Applied optics* 44, no. 24 (2005): 5131-5139.

[106] Karen Hampson, and Martin Booth. "Calibration and Closed-Loop Control of Deformable Mirrors Using Direct Sensing." (2020). Retrieved from https://aomicroscopy.org/dm-calibration-direct-sensing

[107] Kirk Baker. "Singular value decomposition tutorial." *The Ohio State University* 24 (2005).

[108] Donald T. Gavel. "Suppressing anomalous localized waffle behavior in least squares wavefront reconstructors." In *Adaptive Optical System Technologies II*, vol. 4839, pp. 972-980. International Society for Optics and Photonics, 2003.

[109] Herrmann, Jan. "Cross coupling and aliasing in modal wave-front estimation." *JOSA* 71, no. 8 (1981): 989-992.

[110] Jason Porter, Hope Queener, Julianna Lin, Karen Thorn, and Abdul AS Awwal. *Adaptive optics for vision science: Principles, practices, design, and applications*. John Wiley & Sons, 2006.

[111] Ruppel, Thomas, Shihao Dong, Frédéric Rooms, Wolfgang Osten, and Oliver Sawodny. "Feedforward control of deformable membrane mirrors for adaptive optics." IEEE Transactions on Control Systems Technology 21, no. 3 (2012): 579-589.

[112] G. F. Franklin, J. D. Powell, M. Workman. *Digital Control of Dynamic Systems*, 3rd ed. New York: Addison-Wesley, 1997.

[113] Theodore H. Maiman. "Stimulated optical radiation in ruby." (1960): 493-494.

[114] J. E. Murray, and W. H. Lowdermilk. "Nd: YAG regenerative amplifier." *Journal of Applied Physics* 51, no. 7 (1980): 3548-3556.

[115] W. H. Lowdermilk, and J. E. Murray. "The multipass amplifier: Theory and numerical analysis." *Journal of Applied Physics* 51, no. 5 (1980): 2436-2444.

[116] Donna Strickland, and Gerard Mourou. "Compression of amplified chirped optical pulses." *Optics communications* 55, no. 6 (1985): 447-449.

[117] Matthew C. Asplund, Jeremy A. Johnson, and James E. Patterson. "The 2018 Nobel Prize in Physics: optical tweezers and chirped pulse amplification." *Analytical and bioanalytical chemistry* 411, no. 20 (2019): 5001-5005.

[118] Adolf Giesen, H. Hügel, A. Voss, K. Wittig, U. Brauch, and H. Opower. "Scalable concept for diode-pumped high-power solid-state lasers." *Applied Physics B* 58, no. 5 (1994): 365-372.

[119] Jens Mende, J. Speiser, G. Spindler, Willy L. Bohn, and Adolf Giesen. "Mode dynamics and thermal lens effects of thin-disk lasers." In *Solid State Lasers XVII: Technology and Devices*, vol. 6871, p. 68710M. International Society for Optics and Photonics, 2008.

[120] Jens Mende, Elke Schmid, Jochen Speiser, Gerhard Spindler, and Adolf Giesen. "Thin disk laser: power scaling to the kW regime in fundamental mode operation." In *Solid State Lasers XVIII: Technology and Devices*, vol. 7193, pp. 493-504. SPIE, 2009.

[121] Adolf Giesen. "Thin disk lasers–power scalability and beam quality." *Laser Technik Journal* 2, no. 2 (2005): 42-45.

[122] Christian Vorholt, and Ulrich Wittrock. "Intra-cavity pumped Yb: YAG thin-disk laser with 1.74% quantum defect." *Optics Letters* 40, no. 20 (2015): 4819-4822.

[123] Birgit Weichelt, Andreas Voss, Marwan Abdou Ahmed, and Thomas Graf. "Enhanced performance of thin-disk lasers by pumping into the zero-phonon line." *Optics letters* 37, no. 15 (2012): 3045-3047.

[124] Walter Koechner. *Solid-state laser engineering*. Vol. 1. Springer, 2013.

[125] Michael Schulz. “High Energy High Repetition-Rate Thin-Disk Amplifier for OPCPA Pumping”. No. DESY-2013-00751. DOOR-User, (2013).

[126] Jochen Speiser. "Scaling of thin-disk lasers—influence of amplified spontaneous emission." JOSA B 26(1), 26-35 (2009).

[127] Hiroaki Furuse, Haik Chosrowjan, Junji Kawanaka, Noriaki Miyanaga, Masayuki Fujita, and Yasukazu Izawa. "ASE and parasitic lasing in thin disk laser with anti-ASE cap." *Optics Express* 21, no. 11 (2013): 13118-13124.

[128] Mu Wang, Guangzhi Zhu, Xiao Zhu, Yongqian Chen, Jing Dong, Hailin Wang, and Yefeng Qian. "Thickness optimization for an anti-ASE cap in a thin disk laser considering dioptric power and aberration-induced

loss." *JOSA B* 35, no. 3 (2018): 583-592.

[129] K. Ertel, S. Banerjee, P. Mason et al., “Optimising the efficiency of pulsed diode pumped Yb:YAG laser amplifiers for ns pulse generation,” Optics Express, 19(27), 26610-26626 (2011).

[130] D. D. Lowenthal and J. M. Eggleston, “ASE Effects in Small Aspect Ratio Laser Oscillators and Amplifiers with Non-Saturable Losses,” IEEE J. of Quantum Electronics, 22(8), 1165-1173 (1986).

[131] Drew A. Copeland. "Amplified Spontaneous Emission (ASE) Models and Approximations for Thin–Disk Laser Modeling." Proc. of SPIE 8599, 85991P-1-24 (2013).

[132] Dmitrii Kouznetsov, Jean-François Bisson, and Kenichi Ueda. "Scaling laws of disk lasers." Optical materials 31(5), 754-759 (2009).

[133] Huang Zhou, Michal Chyla, Siva Sankar Nagisetty, Liyuan Chen, Akira Endo, Martin Smrz, and Tomas Mocek. "A practical model of thin disk regenerative amplifier based on analytical expression of ASE lifetime." In *Photonics, Devices, and Systems VII*, vol. 10603, p. 1060303. International Society for Optics and Photonics, 2017.

[134] Garry McCracken, and Peter Stott. Fusion: the energy of the universe. Academic Press, 2012.

[135] Edmond Treacy. "Optical pulse compression with diffraction gratings." *IEEE Journal of quantum Electronics* 5, no. 9 (1969): 454-458.

[136] O. E. Martinez, J. P. Gordon, and R. L. Fork. "Negative group-velocity dispersion using refraction." *JOSA A* 1, no. 10 (1984): 1003-1006.

[137] R. L. Fork, O. E. Martinez, and J. P. Gordon. "Negative dispersion using pairs of prisms." *Optics letters* 9, no. 5 (1984): 150-152.

[138] G. Imeshev, I. Hartl, and M. E. Fermann, “Chirped pulse amplification with a nonlinearly chirped fiber Bragg grating matched to the Treacy compressor,” Opt. Lett. 29(7), 679–681 (2004).

[139] Sergiy Kaim, Sergiy Mokhov, Boris Y. Zeldovich, and Leonid B. Glebov. "Stretching and compressing of short laser pulses by chirped volume Bragg gratings: analytic and numerical modeling." Optical Engineering 53, no. 5 (2013): 051509.

[140] Oleksiy Andrusyak, Lionel Canioni, Ion Cohanoshi, Martin Delaigue, Eugeniu Rotari, Vadim Smirnov, and Leonid Glebov. "Sectional chirped volume Bragg grating compressors for high-power chirped-pulse amplification." In *Solid State Lasers XIX: Technology and Devices*, vol. 7578, p. 75781A. International Society for Optics and Photonics, 2010.

[141] Leonid B. Glebov, Vadim Smirnov, Eugeniu Rotari, Ion Cohanoschi, Larissa Glebova, Oleg V. Smolski, Julien Lumeau, Christopher Lantigua, and Alexei Glebov. "Volume-chirped Bragg gratings: monolithic components for stretching and compression of ultrashort laser pulses." *Optical Engineering* 53, no. 5 (2014): 051514.

[142] Herwig Kogelnik. "Coupled wave theory for thick hologram gratings." In *Landmark Papers On Photorefractive Nonlinear Optics*, pp. 133-171. 1995.

[143] Igor V. Ciapurin, Leonid B. Glebov, and Vadim I. Smirnov. "Modeling of phase volume diffractive gratings, part 1: transmitting sinusoidal uniform gratings." *Optical Engineering* 45, no. 1 (2006): 015802.

[144] Igor V. Ciapurin, Vadim Smirnov, Derrek R. Drachenberg, George B. Venus, and Leonid B. Glebov. "Modeling of phase volume diffractive gratings, part 2: reflecting sinusoidal uniform gratings, Bragg mirrors." *Optical Engineering* 51, no. 5 (2012): 058001.

[145] Kai-Hsiu Liao, Ming-Yuan Cheng, Emilie Flecher, Vadim I. Smirnov, Leonid B. Glebov, and Almantas Galvanauskas. "Large-aperture chirped volume Bragg grating based fiber CPA system." *Optics express* 15, no. 8 (2007): 4876-4882.

[146] Yan Mao, Xingpeng Yan, and Weifeng Wang. "Principle and Design of Chirped Fiber Grating." In *Journal of Physics: Conference Series*, vol. 1653, no. 1, p. 012011. IOP Publishing, 2020.

[147] J. A. R. Williams, I. Bennion, K. Sugden, and N. J. Doran. "Fibre dispersion compensation using a chirped in-fibre Bragg grating." *Electronics Letters* 30, no. 12 (1994): 985-987.

[148] İsa Navruz, and Ahmet Altuncu. "Design of a chirped fiber Bragg grating for use in wideband dispersion compensation." In *New Trends In Computer Networks*, pp. 114-123. 2005.

[149] Edmond Treacy. "Optical pulse compression with diffraction gratings." *IEEE Journal of quantum*

Electronics 5, no. 9 (1969): 454-458.

[150] O. E. Martinez, J. P. Gordon, and R. L. Fork. "Negative group-velocity dispersion using refraction." *JOSA A* 1, no. 10 (1984): 1003-1006.

[151] O. E. Martinez. "3000 times grating compressor with positive group velocity dispersion: Application to fiber compensation in 1.3-1.6 μm region." *IEEE Journal of Quantum Electronics* 23, no. 1 (1987): 59-64.

[152] Ivan Vladimirovich Yakovlev. "Stretchers and compressors for ultra-high power laser systems." *Quantum Electronics* 44, no. 5 (2014): 393.

[153] Zhaoyang Li, Shigeki Tokita, Satoshi Matsuo, Keiichi Sueda, Takashi Kurita, Toshiyuki Kawasima, and Noriaki Miyanaga. "Scattering pulse-induced temporal contrast degradation in chirped-pulse amplification lasers." *Optics Express* 25, no. 18 (2017): 21201-21215.

[154] T. Oksenhendler, and N. Forget. *Pulse shaping techniques theory and experimental implementation for femtosecond pulses*. ISBN 978–953–7619–80–0, 2010.

[155] Parametric Amplification. https://www.rp-photonics.com/parametric_amplification.html

[156] Parametric Nonlinearities. https://www.rp-photonics.com/parametric_nonlinearities.html

[157] Giordmaine, Joseph Anthony, and Robert C. Miller. "Tunable coherent parametric oscillation in $LiNbO_3$ at optical frequencies." *Physical Review Letters* 14, no. 24 (1965): 973.

[158] Baumgartner, R., and R. Byer. "Optical parametric amplification." *IEEE Journal of Quantum Electronics* 15, no. 6 (1979): 432-444.

[159] Guenther, Bob D., and Duncan Steel, eds. Encyclopedia of modern optics. Academic Press, 2018.

[160] Manzoni, Cristian, and Giulio Cerullo. "Design criteria for ultrafast optical parametric amplifiers." *Journal of Optics* 18, no. 10 (2016): 103501.

[161] Ciriolo, Anna G., Matteo Negro, Michele Devetta, Eugenio Cinquanta, Davide Faccialà, Aditya Pusala, Sandro De Silvestri, Salvatore Stagira, and Caterina Vozzi. "Optical parametric amplification techniques for the generation of high-energy few-optical-cycles IR pulses for strong field applications." Applied Sciences 7, no. 3 (2017): 265.

[162] Dabu, Razvan. "Femtosecond laser pulses amplification in crystals." *Crystals* 9, no. 7 (2019): 347.

[163] Franken, P. A., and J. F. Ward. "Optical harmonics and nonlinear phenomena." *Reviews of Modern Physics* 35, no. 1 (1963): 23.

[164] Fattahi, Hanieh. "Yb: YAG-pumped, few-cycle optical parametric amplifiers." *High Energy and Short Pulse Lasers* (2016): 55-72.

[165] Kanai, Tsuneto, Pavel Malevich, Sarayoo Sasidharan Kangaparambil, Kakuta Ishida, Makoto Mizui, Kaoru Yamanouchi, Heinar Hoogland, Ronald Holzwarth, Audrius Pugzlys, and Andrius Baltuska. "Parametric amplification of 100 fs mid-infrared pulses in ZnGeP 2 driven by a Ho: YAG chirped-pulse amplifier." Optics letters 42, no. 4 (2017): 683-686.

[166] Kanai, T., Y. Lee, M. Seo, and D. E. Kim. "A 17-W, mid-IR parametric amplifier driven by a Yb: YAG thin-disk laser and its application to high harmonic generation in solids." In Journal of Physics: Conference Series, vol. 1412, no. 7, p. 072038. IOP Publishing, 2020.

[167] Popmintchev, Tenio, Ming-Chang Chen, Dimitar Popmintchev, Paul Arpin, Susannah Brown, Skirmantas Ališauskas, Giedrius Andriukaitis et al. "Bright coherent ultrahigh harmonics in the keV x-ray regime from mid-infrared femtosecond lasers." *science* 336, no. 6086 (2012): 1287-1291.

[168] Metzger, Thomas, Alexander Schwarz, Catherine Yuriko Teisset, Dirk Sutter, Alexander Killi, Reinhard Kienberger, and Ferenc Krausz. "High-repetition-rate picosecond pump laser based on a Yb: YAG disk amplifier for optical parametric amplification." *Optics letters* 34, no. 14 (2009): 2123-2125.

[169] Heinrich, Alexander-Cornelius, Jonathan Fischer, Dominik-Pascal Ertel, Alfred Leitenstorfer, and Daniele Brida. "High Power Optical Parametric Amplifier Driven by a Sub-ps Yb: Thin-Disk System." In *High Intensity Lasers and High Field Phenomena*, pp. HT1A-2. Optica Publishing Group, 2018.

[170] Wang, Jing, Peng Yuan, Dongfang Zhang, Guoqiang Xie, Kainan Xiong, Xiaoniu Tu, Yanqing Zheng, Jingui Ma, and Liejia Qian. "Direct ultrafast parametric amplification pumped by a picosecond thin-disk laser." *arXiv preprint arXiv:2206.07929* (2022).

[171] G. Vergara, G., R. Gutiérrez, L. J. Gómez, V. Villamayor, M. Álvarez, M. C. Torquemada, M. T. Rodrigo et

al. "Fast uncooled low density FPA of VPD PbSe." In *Infrared Technology and Applications XXXV*, vol. 7298, pp. 775-782. SPIE, 2009.

[172] TACHYON 16K Camera specifications. https://www.niteurope.com/en/tachyon-16k/

[173] G. Vergara, R. Linares-Herrero, R. Gutiérrez-Álvarez, M. T. Montojo, C. Fernández-Montojo, A. Baldasano-Ramírez, and G. Fernández-Berzosa. "VPD PbSe technology fills the existing gap in uncooled low-cost and fast IR imagers." In *Infrared Technology and Applications XXXVII*, vol. 8012, p. 80121Q. International Society for Optics and Photonics, 2011.

[174] Common Laser Optics Materials. https://www.edmundoptics.com/knowledge-center/application-notes/lasers/common-laser-optics-materials/

[175] Introduction of App Designer. https://www.mathworks.com/products/matlab/app-designer.html

[176] Matt J (2022). MAT2TILES: divide array into equal-sized sub-arrays (https://www.mathworks.com/matlabcentral/fileexchange/35085-mat2tiles-divide-array-into-equal-sized-sub-arrays), MATLAB Central File Exchange.

[177] Zou, Ji-Ping, Benoit Wattellier, and Bob Tyson. Adaptive optics for high-peak-power lasers–an optical adaptive closed-loop used for high-energy short-pulse laser facilities: laser wave-front correction and focal-spot shaping. Intech, 2012.

[178] Zeng, Jun, Pierre Mahou, Marie-Claire Schanne-Klein, Emmanuel Beaurepaire, and Delphine Débarre. "3D resolved mapping of optical aberrations in thick tissues." *Biomedical optics express* 3, no. 8 (2012): 1898-1913.

[179] Biesheuvel, R. S., A. J. E. M. Janssen, P. Pozzi, and S. F. Pereira. "Implementation and benchmarking of a crosstalk-free method for wavefront Zernike coefficients reconstruction using Shack-Hartmann sensor data." *OSA Continuum* 1, no. 2 (2018): 581-603.

[180] ZERNIKE MODES & DEFORMABLE MIRRORS. https://www.jpe-innovations.com/precision-point/zernike-modes-deformable-mirrors/

[181] Alexander Chernyshov, Uwe Sterr, Fritz Riehle, Jürgen Helmcke, and Johannes Pfund. "Calibration of a Shack–Hartmann sensor for absolute measurements of wavefronts." *Applied optics* 44, no. 30 (2005): 6419-6425.

[182] Jinsheng Yang, Ling Wei, Hongli Chen, Xuejun Rao, and Changhui Rao. "Absolute calibration of Hartmann-Shack wavefront sensor by spherical wavefronts." *Optics communications* 283, no. 6 (2010): 910-916.

[183] Alexander N. Nikitin, Ilya Galaktionov, Julia Sheldakova, Alexis Kudryashov, Nikolay Baryshnikov, Dmitrii Denisov, Valerii Karasik, and Alexey Sakharov. "Absolute calibration of a Shack-Hartmann wavefront sensor for measurements of wavefronts." In *Photonic Instrumentation Engineering VI*, vol. 10925, pp. 118-125. SPIE, 2019.

[184] Lingfeng Chen, Xusheng Zhang, Jiaming Lin, and Dingguo Sha. "Signal-to-noise ratio evaluation of a CCD camera." *Optics & Laser Technology* 41, no. 5 (2009): 574-579.

[185] Signal to Noise Ratio (SNR). https://svi.nl/Signal-to-Noise-Ratio

[186] Bo Dong, Linus Holm, and Min Bao. "Cortical mechanisms for afterimage formation: Evidence from interocular grouping." *Scientific reports* 7, no. 1 (2017): 1-13.

[187] B. L. Ellerbroek, and T. A. Rhoadarmer. "Adaptive wavefront control algorithms for closed loop adaptive optics." *Mathematical and Computer modelling* 33, no. 1-3 (2001): 145-158.

[188] Ji-Ping Zou, Benoit Wattellier, and Bob Tyson. Adaptive optics for high-peak-power lasers–an optical adaptive closed-loop used for high-energy short-pulse laser facilities: laser wave-front correction and focal-spot shaping. Intech, 2012.

[189] A. R. Ganesan, P. Arulmozhivarman, D. Mohan, Ashok Kumar, and A. K. Gupta. "Design and development of a closed loop adaptive optics system for wavefront sensing and control." *Journal of Optics* 34, no. 2 (2005): 67-81.

[190] Zhengxiong Zhu, Yan Li, Junjie Chen, Jianqiang Ma, and Jiaru Chu. "Development of a unimorph deformable mirror with water cooling." *Optics Express* 25, no. 24 (2017): 29916-29926.

[191] Michael Schulz. “High Energy High Repetition-Rate Thin-Disk Amplifier for OPCPA Pumping”. No. DESY-2013-00751. DOOR-User, (2013).

[192] Martin Smrz, Michal Chyla, Ondrej Novak, Taisuke Miura, Akira Endo, Tomas Mocek. "Amplification of

picosecond pulses to 100 W by an Yb: YAG thin-disk with CVBG compressor." Proc. SPIE 9513, 951304-1-7 (2015).

[193] D. J. Twitchen, C. S. J. Pickles, S. E. Coe, R. S. Sussmann, and C. E. Hall. "Thermal conductivity measurements on CVD diamond." *Diamond and related materials* 10, no. 3-7 (2001): 731-735.

[194] Changli Li, Rui Liu, Faquan Gong, Yong Jia, Songwen Deng, Yuqi Jin, and Gang Li. "Theoretical calculation and experimental study on absorption properties of Yb: YAG crystal applied in thin disk laser." *Optik* 130 (2017): 511-516.

[195] Martin Smrž, Taisuke Miura, Michal Chyla, Siva Nagisetty, Ondřej Novák, Akira Endo, and Tomáš Mocek. "Suppression of nonlinear phonon relaxation in Yb: YAG thin disk via zero phonon line pumping." *Optics letters* 39, no. 16 (2014): 4919-4922.

[196] Michal Chyla, Taisuke Miura, Martin Smrz, Patricie Severova, Ondrej Novak, Akira Endo, and Tomas Mocek. "Zero-phonon-line pumped 1 kHz Yb: YAG thin-disk regenerative amplifier." In *Solid State Lasers XXII: Technology and Devices*, vol. 8599, p. 85991Q. International Society for Optics and Photonics, 2013.

[197] Introduction of reZonator. http://rezonator.orion-project.org/

[198] Norman Hodgson, and Horst Weber. *Laser Resonators and Beam Propagation: Fundamentals, Advanced Concepts, Applications*. Vol. 108. Springer, 2005.

[199] Binghua Su, Junwen Xue, Lu Sun, Huiyuan Zhao, and Xuedan Pei. "Generalised ABCD matrix treatment for laser resonators and beam propagation." *Optics & Laser Technology* 43, no. 7 (2011): 1318-1320.

[200] Jiri Muzik, Michal Chyla, Siva S. Nagisetty, Taisuke Miura, Klaus Mann, Akira Endo, and Tomas Mocek. "Precise curvature measurement of Yb: YAG thin disk." In *Optics and Measurement Conference 2014*, vol. 9442, p. 94420X. International Society for Optics and Photonics, 2015.

[201] J. Mende, E. Schmid, J. Speiser, G. Spindler, and A. Giesen, “Thin disk laser: power scaling to the kW regime in fundamental mode operation”, in *Solid State Lasers XVIII: Technology and Devices*, W. A. Clarkson, N. Hodgson, and R. K. Shori, Eds., International Society for Optics and Photonics, vol. 7193, SPIE, 2009, pp. 493 –504

[202] T. Metzger, “High-repetition-rate picosecond pump laser based on an Yb:YAG disk amplifier for optical parametric amplification”, Ph.D. dissertation, Technischen Universität Berlin, 2009.

[203] *LAYERTEC catalog – Common laser types*, http://www.layertec.de/files/catalog/2020/LAYERTEC_Optics_And_Coatings_Common_Laser_Types.pdf, Accessed: 2021-05-28.

[204] A. E. Siegman, *Lasers*. University Science Books, 1986, ISBN: 9780935702118.

[205] H. Injeyan and G. D. Goodno, *High Power Laser Handbook,* 1st ed. The McGraw-Hill Companies, Inc., 2011, ISBN: 9780071609012.

[206] R. Paschotta, article on 'Pockels effect' in the Encyclopedia of Laser Physics and Technology, 1. edition October 2008, Wiley-VCH, ISBN 978-3-527-40828-3

[207] Walter Koechner. *Solid-state laser engineering*. Vol. 1. Springer, 2013.

[208] G. C. Bhar, A. K. Chaudhary, P. Kumbhakar, A. M. Rudra, and S. C. Sabarwal. "A comparative study of laser-induced surface damage thresholds in BBO crystals and effect of impurities." *Optical Materials* 27, no. 1 (2004): 119-123.

[209] Mustapha Abarkan, Jean-Paul Salvestrini, M. D. Fontana, and M. Aillerie. "Frequency and wavelength dependences of electro-optic coefficients in inorganic crystals." *Applied Physics B* 76, no. 7 (2003): 765-769.

[210] Jiří Mužík, Development of High-Repetition-Rate Picosecond Thin-Disk Lasers. Doctoral thesis. 2021, Czech Technical University in Prague.

[211] Robert Goldstein. "Pockels cell primer." *Laser Focus* 34, no. 1 (1968).

[212] Giedrius Sinkevicius, and Algirdas Baskys. "Investigation of piezoelectric ringing frequency response of beta barium borate crystals." *Crystals* 9, no. 1 (2019): 49.

[213] G. Sinkevicius, A. Baskys, and N. Paulauskas. "Influence of the piezoelectric ringing on the temperature of the beta barium borate crystal." *Acta Phys. Pol. A* 134, no. 2 (2018): 535-538.

[214] Andreas Deutschmann, Tobias Flöry, Katharina Schrom, Vinzenz Stummer, Andrius Baltuška, and Andreas Kugi. "Bifurcation suppression in regenerative amplifiers by active feedback methods." *Optics Express* 28, no. 2 (2020): 1722-1737.

[215] Juan Hugo García-López, Rider Jaimes-Reátegui, Samuel Mardoqueo Afanador-Delgado, Ricardo Sevilla-Escoboza, Guillermo Huerta-Cuéllar, Didier López-Mancilla, Roger Chiu-Zarate, Carlos Eduardo Castañeda-Hernández, and Alexander Nikolaevich Pisarchik. "Experimental and Numerical Study of an Optoelectronics Flexible Logic Gate Using a Chaotic Doped Fiber Laser." *Recent Development in Optoelectronic Devices* (2018): 97-114.

[216] D. A. Shelestov, V. E. Karasik, K. I. Koshelev, V. A. Lazarev, and A. B. Pnev, "Improved technique for picosecond pulse duration measurement based on second harmonic generation," J. Phys. Conf. Ser. 584, 1–5 (2015).

[217] M. A. Tunes, C. G. Schön, and N. U. Wetter, "Pulse-to-pulse stability analysis in a frequency-doubled, q-switched Nd:YAG rod-laser," in Instrumentation, Metrology, and Standards for Nanomanufacturing, Optics, and Semiconductors VII (2013), Vol. 8819, p. 88190G.

[218] B.E. Saleh, and M.C. Teich, Fundamentals of photonics (2019).

[219] Ai-Ping Luo, Hao Liu, Nian Zhao, Xu-Wu Zheng, Meng Liu, Rui Tang, Zhi-Chao Luo, and Wen-Cheng Xu. "Observation of three bound states from a topological insulator mode-locked soliton fiber laser." IEEE Photonics Journal 6, no. 4 (2014): 1-8.

[220] D. Y. Tang, W. S. Man, Hwa Yaw Tam, and P. D. Drummond. "Observation of bound states of solitons in a passively mode-locked fiber laser." Physical Review A 64, no. 3 (2001): 033814.

[221] T. Schreiber, D. Schimpf, D. Müller, F. Röser, J. Limpert, and A. Tünnermann, "Influence of pulse shape in self-phase-modulation-limited chirped pulse fiber amplifier systems," J. Opt. Soc. Am. B 24, 1809 (2007).

[222] Damian N. Schimpf, Enrico Seise, Jens Limpert, and Andreas Tünnermann. "The impact of spectral modulations on the contrast of pulses of nonlinear chirped-pulse amplification systems." Optics Express 16, no. 14 (2008): 10664-10674.

[223] Li, Wenkai, Yun Chen, Yanyan Li, Yi Xu, Xiaoyang Guo, Jun Lu, and Yuxin Leng. "Astigmatism transfer phenomena in the optical parametric amplification process." *Applied Physics B* 123, no. 1 (2017): 1-7.

[224] Y. Chen, Y. Zhou, G. Jiang, and L. Wang, “Numerical simulations of transfer of spatial beam aberrations in optical parametric chirped-pulse amplification,” Adv. Condens. Matter Phys. 2018, 5731938 (2018).

[225] Bahk, S-W., I. A. Begishev, R. Roides, C. Mileham, R. Cuffney, C. Feng, B. M. Webb et al. "Effect of the pump beam profile and wavefront on the amplified signal wavefront in optical parametric amplifiers." *Optics Express* 30, no. 8 (2022): 12995-13008.

[226] DeSalvo, Richard, David J. Hagan, Mansoor Sheik-Bahae, Gt Stegeman, Eric W. Van Stryland, and Herman Vanherzeele. "Self-focusing and self-defocusing by cascaded second-order effects in KTP." *Optics letters* 17, no. 1 (1992): 28-30.